The Dissertation Committee for Arash Fathi
certifies that this is the approved version of the following dissertation:

Full-waveform inversion in three-dimensional PML-truncated elastic media: theory, computations, and field experiments

Committee:

Loukas F. Kallivokas, Supervisor

Clinton N. Dawson

Leszek F. Demkowicz

Omar Ghattas

Lance Manuel

Kenneth H. Stokoe II

Full-waveform inversion in three-dimensional PML-truncated elastic media: theory, computations, and field experiments

by

Arash Fathi, B.Sc., M.Sc.

DISSERTATION

Presented to the Faculty of the Graduate School of
The University of Texas at Austin
in Partial Fulfillment
of the Requirements
for the Degree of

DOCTOR OF PHILOSOPHY

THE UNIVERSITY OF TEXAS AT AUSTIN
May 2015

I don’t tell the murky world

to turn pure.

I purify myself

and check my reflection

in the water of the valley brook.

Ryōkan

Acknowledgments

This dissertation would not have been possible without the help of many others. I would like to express my sincere gratitude and appreciation to my doctoral advisor, Professor Loukas F. Kallivokas, for his assistance, ingenuity, and supervision of this work. I am thankful to Professors Clint Dawson, Leszek Demkowicz, Omar Ghattas, Lance Manuel, and Kenneth Stokoe, for serving on my dissertation committee, and for their valuable comments. I also wish to thank Babak Poursartip, Georg Stadler, Sezgin Kucukcoban, Pranav Karve, and Chanseok Jeong, for their continuous support, and fruitful discussions, and Farn-Yuh Menq, Y.-C. Lin and Changyoung Kim, for assisting with the field experiments, processing of the SASW test results, and the CPT tests, respectively.

Partial support for my research has been provided by the National Science Foundation under grant award CMMI-0619078 and through an Academic Alliance Excellence grant between the King Abdullah University of Science and Technology in Saudi Arabia (KAUST) and the University of Texas at Austin. This support is gratefully acknowledged.

Full-waveform inversion in three-dimensional PML-truncated elastic media: theory, computations, and field experiments

Arash Fathi, Ph.D.
The University of Texas at Austin, 2015

Supervisor: Loukas F. Kallivokas

We are concerned with the high-fidelity subsurface imaging of the soil, which commonly arises in geotechnical site characterization and geophysical explorations. Specifically, we attempt to image the spatial distribution of the Lamé parameters in semi-infinite, three-dimensional, arbitrarily heterogeneous formations, using surficial measurements of the soil's response to probing elastic waves. We use the complete waveforms of the medium's response to drive the inverse problem. Specifically, we use a partial-differential-equation (PDE)-constrained optimization approach, directly in the time-domain, to minimize the misfit between the observed response of the medium at select measurement locations, and a computed response corresponding to a trial distribution of the Lamé parameters. We discuss strategies that lend algorithmic robustness to the proposed inversion schemes. To limit the computational domain to the size of interest, we employ perfectly-matched-layers (PMLs).

The PML is a buffer zone that surrounds the domain of interest, and enforces the decay of outgoing waves.

In order to resolve the forward problem, we present a hybrid finite element approach, where a displacement-stress formulation for the PML is coupled to a standard displacement-only formulation for the interior domain, thus leading to a computationally cost-efficient scheme. We discuss several time-integration schemes, including an explicit Runge-Kutta scheme, which is well-suited for large-scale problems on parallel computers.

We report numerical results demonstrating stability and efficacy of the forward wave solver, and also provide examples attesting to the successful reconstruction of the two Lamé parameters for both smooth and sharp profiles, using synthetic records. We also report the details of two field experiments, whose records we subsequently used to drive the developed inversion algorithms in order to characterize the sites where the field experiments took place. We contrast the full-waveform-based inverted site profile against a profile obtained using the Spectral-Analysis-of-Surface-Waves (SASW) method, in an attempt to compare our methodology against a widely used concurrent inversion approach. We also compare the inverted profiles, at select locations, with the results of independently performed, invasive, Cone Penetrometer Tests (CPTs).

Overall, whether exercised by synthetic or by physical data, the full-waveform inversion method we discuss herein appears quite promising for the robust subsurface imaging of near-surface deposits in support of geotechnical site characterization investigations.

Table of Contents

List of Tables

List of Figures

Chapter 1

Introduction

A high-fidelity image of the near-surface deposits has practical significance in the safe design of critical infrastructure components, such as bridges, hospitals, nuclear power plants, etc. In current practice, both invasive and non-invasive techniques are used. Among the non-invasive techniques, wave-based approaches, whether via elastic, acoustic, or electromagnetic waves, are dominant. Currently, the majority of the wave-based techniques rely on simplifying assumptions that limit their applicability. For instance, the widely-used Spectral-Analysis-of-Surface-Waves (SASW) method, relies on a one-dimensional assumption that result in a horizontally layered profile for the soil. Similarly, the Multichannel-Analysis-of-Surface-Waves (MASW) method, though more versatile than the SASW method, falls short of reconstructing heterogeneous three-dimensional images. By contrast, full-waveform inversion techniques are inherently three- (or two-) dimensional, and can accommodate arbitrary heterogeneity automatically.

This dissertation presents a systematic framework for the high-fidelity imaging of the soil, in the context of geotechnical site characterization. The goal is to image the arbitrarily heterogeneous material profile of a probed site, using complete waveforms of its response to interrogating elastic waves, originating from the ground surface. To this end, the response of the soil medium to active sources is collected by receivers dispersed over the formation's surface. Arriving at a material profile is then accomplished by minimizing the misfit between the collected response at receiver locations, and a computed response corresponding to a trial distribution of the material parameters. The misfit minimization problem is constrained by the wave physics of the forward problem, resulting in a PDE-constrained optimization problem.

Imaging near-surface deposits brings additional difficulties, typically not encountered in exploration geophysics, or medical imaging. Since in geotechnical site characterization, one, typically, deals with a semi-infinite, (relatively) small domain, an accurate domain termination tool seems necessary, and may play a critical role in obtaining a reliable material profile. In this vein, and in the presence of heterogeneity, using Perfectly-Matched-Layers (PMLs) for domain termination is the best available option, and is thus used in this work.

1.1 Background

The robust, high-fidelity subsurface imaging of the soil relies on two key components: a) the forward problem, where a wave simulation tool for semi-infinite domains is needed[1]; and b) the inverse problem, where a full-waveform inversion approach is used for the misfit minimization. The solution of the inverse problem, typically, necessitates an iterative process, which requires repeated solutions of the

---

[1] We use PMLs for domain truncation.

forward problem, thereby accentuating the importance of an efficient and accurate forward simulator. We review next key developments in both the forward and inverse problems, in order to place the present work in context.

1.1.1 The perfectly-matched-layer (PML)

Numerical simulation of elastic waves in unbounded heterogeneous media has important applications in various fields, such as seismology [1], soil-structure interaction [2, 3], seismic imaging [4], wave-based enhanced oil recovery [5–7], and site characterization [8]. To keep the computation feasible, one needs to limit the extent of the computational domain. This entails considering appropriate conditions at the truncation boundaries such that, under ideal conditions, the boundaries become invisible to the outgoing waves. Perfectly-matched-layers (PML) appear to be among the best choices for domain truncation owing, especially, to their ability to handle heterogeneity. From a practical standpoint, implementing PML in existing codes is also easier than competitive alternatives [9, 10]. The PML is a buffer zone that enforces attenuation of propagating and evanescent waves. The PML's properties vary gradually, from a perfectly matched interface, through a progressively attenuative medium, to, usually, a fixed termination at the buffer zone's end[2].

The PML was first introduced by Bérenger for electromagnetic waves [13]. Later, it was interpreted as a mapping of the physical coordinates onto the complex space, referred to as complex coordinate stretching [14–16]. The interpretation al-

---

[2] Other termination conditions are also possible, including local non-reflecting boundary conditions [11, 12].

lowed the further development and adoption of the PML in elastodynamics [17, 18], for the linearized Euler equations [19], for Helmholtz equations [9], in poroelasticity [20], and elsewhere.

Bérenger's original development, and many other early formulations, were based on field-splitting, which partitions a physical variable into components parallel and perpendicular to the truncation boundary; this technique alters the structure of the underlying differential equations and results in a manyfold increase of the number of unknowns. Gedney [21] proposed an unsplit formulation for electromagnetic waves, citing preservation of the Maxwellian structure, and computational efficiency among the main advantages. Abarbanel and Gottlieb showed that Bérenger's split-form is only weakly well-posed[3], and therefore is prone to instability [23]. This motivated the development of strongly well-posed unsplit formulations [24]; however, it turned out that the dynamical system associated with the unsplit form suffers from degeneracy at quiescent state, which renders the scheme unstable, and further manipulation of the equations is necessary to ensure stability [25].

In elastodynamics, Duru and Kreiss [26] proposed a well-posed discretely-stable unsplit formulation, and mentioned that the first-order split-form is only weakly hyperbolic[4] [27]. Among other unsplit formulations, we refer to [28–30] where the authors' motivation stemmed primarily from exploring alternative forms, rather than address stability. All these developments used finite differences for spatial discretization, and exploited explicit time-stepping. Among unsplit-field finite element

---

[3] See [22] for definition of well-posedness, and hyperbolicity.

[4] Strong hyperbolicity is a desirable property and guarantees well-posedness.

developments, Basu and Chopra [2] presented an, almost, displacement-only procedure that relies on stress-histories and needs the evaluation of an internal force vector at every time step, as is typically done in plasticity, via an implicit time-marching scheme based on unsymmetric matrices. Later, Basu [31] extended this work to three-dimensional problems, using mass-lumping and explicit time-stepping. Martin et al. [32] developed a computationally efficient procedure that couples a velocity-stress convolutional PML (CPML) in an *ad hoc* manner with a displacement-only formulation in the interior domain for two-dimensional problems. The CPML formulation was used to circumvent instabilities observed when waves travel along the interface between the PML and the interior domain, when the standard PML stretching function is used. Recently, Kucukcoban and Kallivokas [33] developed a symmetric displacement-stress formulation, using mixed-field finite elements for the PML, coupled with standard displacement-only finite elements for the interior domain, using the standard Newmark method for time integration. We remark that implicit time-stepping can become challenging for large-scale three-dimensional problems and should be avoided if possible.

The literature on split-field elastodynamics is rich. This approach is particularly attractive because, normally, it does not use convolutions or auxiliary variables. However, it almost always results in using mixed schemes, i.e., treating velocity and stress components (or a similar combination) as unknowns over the entire domain. Table 1.1 summarizes key developments in time-domain elastodynamics based on four categories: split- or unsplit-field formulation, and finite difference or finite/spectral element implementation.

Table 1.1: PML developments in time-domain elastodynamics.

	Split-field	**Unsplit-field**
FD	Chew and Liu[17]	Wang and Tang [30]
	Hastings et al. [34]	Drossaert and Giannopoulos [28]
	Liu [35]	Komatitsch and Martin [29]
	Collino and Tsogka [18]	Duru and Kreiss [26]
FE/SE	Collino and Tsogka [18]	Basu and Chopra [2]
	Bécache et al. [36]	Martin et al. [32]
	Festa and Nielsen [37]	Basu [31]
	Komatitsch and Tromp [38]	Kucukcoban and Kallivokas [33]
	Cohen and Fauqueux [39]	
	Festa and Vilotte [40]	
	Meza-Fajardo and Papageorgiou [41]	

Differences between various PML formulations are not only due to the split or unsplit formulation and numerical implementation, but also on the choice of coordinate stretching function. The classical stretching function has been criticized for allowing spurious growths in numerical simulations in two dimensions, when waves impinge at grazing incidence on the PML interface. These growths have been loosely attributed to a zero-frequency singularity in the classical stretching function, and have been, reportedly, alleviated by using a complex-frequency-shifted (CFS) stretching function, which removes the singularity [28]. However the CFS-PML loses its absorptive competence at low frequencies [42]. Meza-Fajardo and Papageorgiou [41] proposed a multi-axial stretching approach and demonstrated its successful performance for waves impinging on the PML at grazing incidence, as well as for problems involving anisotropy. In [43, 44], it was reported that the M-PML is not perfectly-matched at the interface; however, later on, Meza-Fajardo and Papageorgiou showed that the multi-axial perfectly-matched-layer (M-PML) is indeed perfectly-matched in Bérenger's sense, and it provides domain truncations that are at least as accurate as the classical PML, when the latter is stable [45]. In a more recent study, Ping et al. [46] have shown results according to which M-PML may perform less accurately than the classical PML. Our own experience, both in two-dimensional and three-dimensional simulations, is also more in accordance with Ping et al. [46]. It also seems that the original M-PML development is mathematically inconsistent due to the improper definition of the Jacobian of the transformation. We discuss this issue in Section 2.6. Herein, we opt for classical stretching functions for their simplicity, satisfactory performance when parametrized carefully, and their accuracy in low frequencies, which is important in site characterization problems [8]. We also discuss how our formulation can accommodate the multi-axial stretching through simple modifications.

1.1.2 Full-waveform inversion (FWI)

Seismic inversion refers to the process of identification of material properties in geological formations [47–49]. The problem arises predominantly in exploration geophysics [50–53] and geotechnical site characterization [8]; it belongs to the broader class of inverse medium problems: waves, whether of acoustic, elastic, or electromagnetic nature, are used to interrogate a medium, and the medium's response to the probing is subsequently used to image the spatial distribution of properties (e.g., Lamé parameters, or wave velocities) [54–56]. Mathematically, algorithmically, and computationally, inverse medium problems are challenging, especially, when no *a priori* constraining assumption is made on the spatial variability of the medium's properties. The challenges are further compounded when the underlying physics is time-dependent, and involves more than a single distributed parameter to be inverted for, as in seismic inversion.

Due to the complexity of the inverse problem at hand, most techniques to date rely on simplifying assumptions, aiming at rendering a solution to the problem more tractable. These assumptions can be divided into four categories: a) assumptions regarding the dimensionality of the problem, whereby the original problem is reduced to a two-dimensional [8, 57], or a one-dimensional problem [58]; b) assuming that the dominant portion of the wave energy on the ground surface is transported through Rayleigh waves, and thus, disregarding other wave types, such as compressional and shear waves, as is the case in the Spectral-Analysis-of-Surface-Waves (SASW) and its variants (MASW) [59]; c) inverting for only one parameter, as is done in [60–63], where inversion was attempted only for the shear wave velocity, assuming the compressional wave velocity (or an equivalent counterpart) is known; and d) assumptions concerning the truncation boundaries, which are oftentimes, grossly simplified due to the complexity associated with the rigorous treatment of these boundaries [64]. Over the past decade, continued advances in both algorithms and computer architectures have allowed the gradual removal of the limitations of existing methodologies. However, a robust methodology, especially for the time-dependent elastic case remains, by and large, elusive.

Among the recent works on inversion, which are similar in character to ours, we refer to Pratt et al. [65] who considered two-dimensional acoustic inversion in the frequency domain, and Epanomeritakis et al. [61] where full-waveform inversion has attempted for three-dimensional time-domain elastodynamics, where a simple boundary condition was used for domain truncation. Kang and Kallivokas [56] considered the problem for the two-dimensional time-domain acoustic case, and used PMLs to accurately account for domain truncation. Kucukcoban [57] extended the work of Kang and Kallivokas to two-dimensional elastodynamics, and reported successful reconstruction of the two Lamé parameters for models involving synthetic data. Recently, Bramwell [66] used a discontinuous Petrov-Galerkin (DPG) method in the frequency domain, endowed with PMLs, for seismic tomography problems, advocating the DPG scheme over conventional continuous Galerkin methods, since it results in less numerical pollution.

This dissertation extends the work of Kucukcoban [57] to three-dimensional elastodynamics. We remark that PMLs add significant complexity to the solution of both the forward and the inverse problem. Moreover, since we target three-dimensional problems, using scalable parallel algorithms is essential.

1.2 Present approach

In this dissertation, we discuss a systematic framework for the numerical resolution of the inverse medium problem, directly in the time-domain, in the context of geotechnical site characterization. As discussed in the introduction, the goal is to image the arbitrarily heterogeneous material profile of a probed soil medium, using complete waveforms[5] of its response to interrogating elastic waves, originating from

---

[5] Using the complete waveform (complete recorded response) results in a full-waveform inversion approach.

the ground surface. To this end, the response of the soil medium to active sources (Vibroseis equipment) is collected by receivers (geophones) dispersed over the formation's surface, as shown in Figure 1.1(a). Arriving at a material profile is then accomplished by minimizing the difference between the collected response at receiver locations, and a computed response corresponding to a trial distribution of the material parameters. Due to the heterogeneity, we use PMLs for domain termination, as the best available option. Figure 1.1 shows the prototype computational model, where the physical domain has been replaced by a computational domain terminated by PMLs at the truncation boundaries.

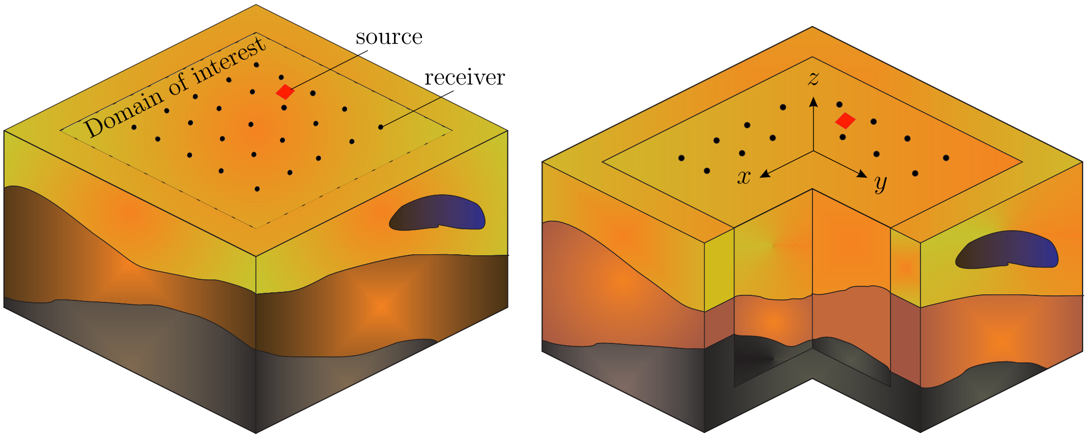

(a)

(b)

Figure 1.1: Problem definition: (a) interrogation of a heterogeneous semi-infinite domain by an active source; and (b) computational model truncated from the semi-infinite medium via the introduction of PMLs.

In order to address all the difficulties outlined earlier, we integrate recent advances in several areas. Specifically, we use (a) a parallel, state-of-the-art wave simulation tool for domains terminated by PMLs [67]; (b) a partial-differential-equation

(PDE)-constrained optimization framework through which the minimization of the difference between the collected response at receiver locations and a computed response corresponding to a trial distribution of the material properties is attained [68]; (c) regularization schemes to alleviate the ill-posedness inherent in inverse problems; (d) continuation schemes that lend algorithmic robustness [56]; and (e) a biasing scheme that accelerates the convergence of the λ-profile for robust simultaneous inversion of both Lamé parameters [57].

1.3 Contributions

This work builds and improves upon the Ph.D. dissertation of Sezgin Kucukcoban in two-dimensional elastic full-waveform inversion [57]. Key contributions of the present development are listed below.

In three dimensions:

- Developing a new PML formulation for the simulation of elastic waves in three-dimensional, arbitrarily heterogeneous, semi-infinite media, where a stress-displacement formulation for the PML, is coupled with a standard displacement-only formulation for the interior domain. This hybrid treatment leads to a computationally cost-efficient scheme. The formulation builds and improves upon a recently developed two-dimensional scheme [33]. However, it is restructured, and modified, to accommodate explicit time-stepping, which makes it suitable for large-scale problems on parallel computers [67].
- Presenting a robust full-waveform inversion methodology for three-dimensional,

arbitrarily heterogeneous, PML-truncated, elastic formations, leading to the successful reconstruction of the spatially-distributed Lamé parameters. A consistent finite element approach was used throughout. The accuracy of the discrete gradients, computed from this scheme, are verified by comparing them with directional finite differences [69]. The developed framework was used for the three-dimensional characterization of the NEES@UCSB site in Garner Valley, CA [70].

In two dimensions:

- Developing a discretize-then-optimize scheme for the accurate computation of the discrete gradients of the discrete objective functional. Accordingly, the objective functional is discretized first, followed by differentiation, to yield discrete gradients, which can then be used in a gradient-based optimization scheme [8].
- Developing a practical procedure to accommodate field data, which are inherently three-dimensional, into two-dimensional full-waveform-inversion-based codes. Designing and conducting a field experiment at the Hornsby Bend site in Austin, TX, whose records were subsequently used to drive the inversion algorithms in order to characterize the site where the experiment took place [8].

1.4 Dissertation outline

The rest of this dissertation is organized as follows:

Chapter 2 presents a new PML formulation for the simulation of elastic waves in three-dimensional, arbitrarily heterogeneous domains. We begin with reviewing key ideas for developing a PML, and discuss complex coordinate stretching. Then, we present a stress-displacement formulation for the PML, which leads to a third-order-in-time semi-discrete form. We discuss how this formulation can be coupled with a standard displacement-only formulation for the interior domain, thus leading to a computationally cost-efficient scheme. We discuss several time-marching schemes. In particular, we discuss an explicit, fourth-order, Runge-Kutta scheme which is well-suited for large-scale problems on parallel computers. In Section 2.5, we discuss an alternative formulation for the PML that leads to a symmetric semi-discrete form. In Section 2.6 we show how our formulation can accommodate multi-axial PML (M-PML), by simple modifications. Lastly, we provide numerical experiments demonstrating stability and efficacy of the proposed formulations.

In Chapter 3, we consider the inverse medium problem in three-dimensional, PML-truncated domains, using full-waveforms. We cast the associated inverse problem, as a misfit minimization problem, using the apparatus of PDE-constrained optimization to impose the forward wave propagation equations, followed by computing the optimality system. Next, we discuss strategies that alleviate ill-posedness, and lend algorithmic robustness to our proposed inversion scheme. By using a numerical experiment, we verify the accuracy of the gradients computed via the control problems, by comparing them with directional finite differences. We present numerical experiments demonstrating successful reconstruction of the two Lamé parameters for smooth and sharp profiles, using noise-free and also highly-noisy synthetic data.

In Chapter 4, we discuss a full-waveform inversion methodology for site characterization, using field data. We start by reviewing the two-dimensional forward wave propagation in PML-truncated domains, followed by presenting a robust approach to tackle the associated inverse medium problem. We then report on the design and data processing of a field experiment, whose records were used along with the presented two-dimensional framework, to obtain the compressional, and shear wave velocity profile of the site where the experiment took place. Next, we compare the profiles with those obtained from the SASW method, and invasive Cone Penetrometer Tests (CPTs). Lastly, we use the methodology described in Chapter 3 for the three-dimensional site characterization of the NEES site in Garner Valley, CA.

We conclude with summary remarks in Chapter 5, and suggest future directions.

Chapter 2

Simulation of wave motion in three-dimensional PML-truncated heterogeneous media

In this chapter, we discuss the development and parallel implementation of an unsplit-field, displacement-stress PML formulation, using mixed-field finite elements for the PML, which when coupled with a standard displacement-only finite element formulation for the interior domain, leads to the efficient simulation of wave motion in physically unbounded, three-dimensional, arbitrarily heterogeneous elastic media. The hybrid treatment of coupling a mixed-field PML with a single-field interior-domain leads to optimal computational cost and allows for ready incorporation of the PML in existing closed-domain standard finite element codes, by simply attaching the matrices corresponding to the PML buffer. The resulting semi-discrete form is unsymmetric and third-order in time. Using spectral elements, we render the mass matrix diagonal and exploit explicit time-stepping via the Runge-Kutta method. We also present an alternative formulation, which results in a fully symmetric discrete form, at the expense of utilizing an implicit time-marching scheme. We discuss how the standard Newmark scheme can also be used for time integration. This work builds and improves upon recent developments [33, 71] in two-dimensional elastodynamics.

2.1 Complex-coordinate-stretching

In this section, we briefly review the key features of the PML. Part of the material discussed here is not new; however, it is provided to allow for context and completeness.

2.1.1 Key idea

The key idea in constructing a PML is based on analytic continuation of solutions of wave equations. This amounts to mapping the spatial coordinates onto the complex space, using the, so-called, stretching functions. For instance, one-dimensional outgoing waves propagate according to $u^{out}(x,t) = e^{-ik(x-ct)}$, where k is the wavenumber, and c denotes wave speed. After applying the mapping[1] $x \mapsto \zeta(x) + \frac{1}{i\omega}\,\eta(x)$, we obtain $u^{out}_{\text{PML}}(x,t) = e^{-ik(\zeta(x)-ct)}e^{-\eta(x)/c}$, where the latter term enforces spatial attenuation. A similar argument also holds for evanescent waves.

In practice, the PML has a limited thickness (see Fig. 2.1), and is terminated with a fixed boundary. Therefore, reflections (i.e., incoming waves) could develop when outgoing waves hit the fixed boundary of the PML layer. In our one-dimensional example, $u^{inc}_{\text{PML}}(x,t) = e^{ik(\zeta(x)+ct)}e^{\eta(x)/c}$. Since $\eta(x)$ is a positive, monotonically increasing function of x, reflected waves also get attenuated, due to decreasing x. Hence, the PML attenuates both outgoing and incoming waves.

We briefly discuss the principal components required for constructing a PML.

---

[1] $\zeta(x), \eta(x)$ are positive, monotonically increasing functions of x.

Referring to Fig. 2.1, let s denote the coordinate variable normal to the interface of the interior domain with the PML. For the interior domain it holds $0 < s < s_0$, whereas for the PML $s_0 < s < s_t$; L_{PML} denotes the thickness of the PML layer, and n_s is the outward unit normal at the interface, pointing away from the interior domain. The physical coordinate s is mapped (or "stretched") to $\tilde{s}$ within the PML region according to

$$s \mapsto \tilde{s} = s_o + \int_{s_o}^{s} \lambda_s(s', \omega)\, ds', \tag{2.1}$$

where ω denotes circular frequency, and λ_s is the, so-called, stretching funcion.

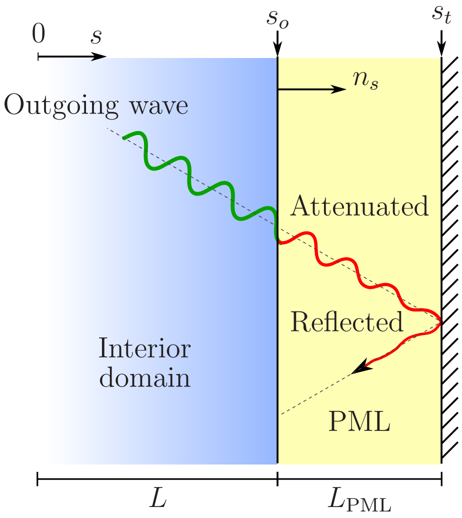

Figure 2.1: A PML truncation boundary in the direction of coordinate s.

The classical PML results from choosing the stretching function according to

$$\lambda_s(s, \omega) = \alpha_s(s) + \frac{1}{i\omega}\beta_s(s), \tag{2.2}$$

where α_s is the scaling function, which stretches the coordinate variable s, whereas β_s is the attenuation function, which enforces the amplitude decay of propagating waves[2]. For evanescent waves, α_s improves amplitude decay by elongating the real coordinate variable s. For the interface to be "invisible" to the waves entering the PML (perfect matching), $\alpha_s|_{s=s_0} = 1$, and $\beta_s|_{s=s_0} = 0$. Moreover, α_s and β_s are positive, non-decreasing functions of s. Finally, applying the fundamental theorem of calculus to (2.1), there results

$$\frac{d\tilde{s}}{ds} = \frac{d}{ds}\int_{s_o}^{s} \lambda_s(s', \omega)\, ds' = \lambda_s(s, \omega). \tag{2.3}$$

Hence, we obtain the following derivative rule between the stretched coordinate system, and the physical coordinate system

$$\frac{d(\cdot)}{d\tilde{s}} = \frac{1}{\lambda_s(s, \omega)}\frac{d(\cdot)}{ds}. \tag{2.4}$$

The PML governing equations are naturally written in the stretched coordinate system. We frequently use (2.4) to express the PML equations in the physical coordinate system.

2.1.2 Choice of stretching functions

The main requirements for the stretching functions are a) perfect matching at the interface; b) positive non-decreasing variability; and c) a gradual and smoothly

---

[2] In our one-dimensional example, we used the notation $\zeta(x) = \int_0^x \alpha(x')dx'$, and $\eta(x) = \int_0^x \beta\,(x')\,dx'$.

varying profile. The last requirement is particularly important for numerical discretization, since, for adequate resolution, a sharply varying profile requires a finer mesh than a smoother profile. A widely adopted form that satisfies these requirements is given in terms of polynomials, as in

$$\alpha_s(s) = 1 + \alpha_o \left[\frac{(s - s_o) n_s}{L_{\text{PML}}} \right]^m, \qquad s_o \leq s \leq s_t, \tag{2.5a}$$

$$\beta_s(s) = \beta_o \left[\frac{(s - s_o) n_s}{L_{\text{PML}}} \right]^m, \qquad s_o \leq s \leq s_t, \tag{2.5b}$$

where α_0 and β_0 are user-tunable parameters that control amplitude decay, and m denotes polynomial degree.

For one-dimensional problems, prior to discretization, β_0 can be shown to be

$$\beta_0 = \frac{(m+1)\ c_p}{2\ L_{\text{PML}}} \log \left(\frac{1}{R} \right), \tag{2.6}$$

where R is the amount of reflection from the fixed PML boundary, and c_p is the P-wave velocity. In practice, however, selecting appropriate values for α_0 and β_0 is not straightforward. The choice depends on the problem at hand, mesh resolution, and, it typically, needs a few experiments to be optimized. We remark that the performance of the PML relies heavily on its careful parameterization [11, 33].

We also worked with the following trigonometric profiles that are smoother than polynomials; however, we did not observe any compelling improvement.

$$\alpha_s(s) = 1 + \frac{\alpha_o}{2}\left[1 + \sin\Big(\pi\Big(\frac{|s-s_o|}{L_{\text{PML}}} - \frac{1}{2}\Big)\Big)\right], \qquad s_o \le s \le s_t, \tag{2.7a}$$

$$\beta_s(s) = \frac{\beta_o}{2}\left[1 + \sin\Big(\pi\Big(\frac{|s-s_o|}{L_{\text{PML}}} - \frac{1}{2}\Big)\Big)\right], \qquad s_o \le s \le s_t. \tag{2.7b}$$

2.2 Three-dimensional unsplit-field PML

The linear elastic wave equation, in the absence of body forces, can be written as the following system

$$\mathbf{div}\,\mathcal{S}^T = \rho\ddot{\mathbf{u}}, \tag{2.8a}$$

$$\mathcal{S} = \mu\left[\nabla\mathbf{u} + (\nabla\mathbf{u})^T\right] + \lambda(\operatorname{div}\mathbf{u})\mathcal{I}, \tag{2.8b}$$

where (2.8a) represents conservation of linear momentum, and (2.8b) is the combined constitutive and kinematic equations; $\mathcal{S}$ represents the Cauchy stress tensor, $\mathbf{u}$ is the displacement vector, ρ denotes mass density of the medium, λ and μ are the two Lamé parameters, $\mathcal{I}$ is the second-order identity tensor, and a dot $(\dot{\ })$ denotes differentiation with respect to time of the subtended variable.

To derive the corresponding PML equations, we first Fourier-transform (2.8) with respect to the time variable. Writing the resulting differential equations in the stretched coordinate system affords the sought-after spatial decaying property. These equations can then be expressed in the physical coordinate system by using (2.4). Finally, exploiting the inverse Fourier transform results in the corresponding time-domain equations.

2.2.1 Frequency-domain equations

We Fourier-transform (2.8) with respect to the time variable; there results:

$$\begin{aligned} \mathbf{div}\,\hat{\mathcal{S}}^T &= (i\omega)^2 \rho \hat{\mathbf{u}}, && \text{(2.9a)} \\ \hat{\mathcal{S}} &= \mu \left[\nabla \hat{\mathbf{u}} + (\nabla \hat{\mathbf{u}})^T \right] + \lambda (\operatorname{div} \hat{\mathbf{u}}) \mathcal{I}, && \text{(2.9b)} \end{aligned}$$

where a caret $(\hat{\ })$ denotes the Fourier transform of the subtended variable, and spatial and frequency dependency of the variables are suppressed for brevity. We focus on (2.9a) first, and express it in the stretched coordinate system by replacing x, y, and z with $\tilde{x}$, $\tilde{y}$, and $\tilde{z}$, respectively. For clarity, we use the unabridged notation:

$$\begin{aligned} \frac{\partial \hat{\mathcal{S}}_{xx}}{\partial \tilde{x}} + \frac{\partial \hat{\mathcal{S}}_{yx}}{\partial \tilde{y}} + \frac{\partial \hat{\mathcal{S}}_{zx}}{\partial \tilde{z}} &= (i\omega)^2 \rho \ \hat{u}_x, && \text{(2.10a)} \\ \frac{\partial \hat{\mathcal{S}}_{xy}}{\partial \tilde{x}} + \frac{\partial \hat{\mathcal{S}}_{yy}}{\partial \tilde{y}} + \frac{\partial \hat{\mathcal{S}}_{zy}}{\partial \tilde{z}} &= (i\omega)^2 \rho \ \hat{u}_y, && \text{(2.10b)} \\ \frac{\partial \hat{\mathcal{S}}_{xz}}{\partial \tilde{x}} + \frac{\partial \hat{\mathcal{S}}_{yz}}{\partial \tilde{y}} + \frac{\partial \hat{\mathcal{S}}_{zz}}{\partial \tilde{z}} &= (i\omega)^2 \rho \ \hat{u}_z, && \text{(2.10c)} \end{aligned}$$

where $\mathcal{S}_{ij}$, and u_i, denote stress tensor, and displacement vector components, respectively. Equation (2.10) can be expressed in the physical (un-stretched) coordinate system by using (2.4); thus, we obtain:

$$\frac{1}{\lambda_x}\frac{\partial \hat{\mathbb{S}}_{xx}}{\partial x} + \frac{1}{\lambda_y}\frac{\partial \hat{\mathbb{S}}_{yx}}{\partial y} + \frac{1}{\lambda_z}\frac{\partial \hat{\mathbb{S}}_{zx}}{\partial z} = (i\omega)^2 \rho \ \hat{u}_x, \tag{2.11a}$$

$$\frac{1}{\lambda_x}\frac{\partial \hat{\mathbb{S}}_{xy}}{\partial x} + \frac{1}{\lambda_y}\frac{\partial \hat{\mathbb{S}}_{yy}}{\partial y} + \frac{1}{\lambda_z}\frac{\partial \hat{\mathbb{S}}_{zy}}{\partial z} = (i\omega)^2 \rho \ \hat{u}_y, \tag{2.11b}$$

$$\frac{1}{\lambda_x}\frac{\partial \hat{\mathbb{S}}_{xz}}{\partial x} + \frac{1}{\lambda_y}\frac{\partial \hat{\mathbb{S}}_{yz}}{\partial y} + \frac{1}{\lambda_z}\frac{\partial \hat{\mathbb{S}}_{zz}}{\partial z} = (i\omega)^2 \rho \ \hat{u}_z. \tag{2.11c}$$

Multiplying (2.11) through by $\lambda_x \lambda_y \lambda_z$ results in

$$\mathbf{div}\left(\hat{\mathbb{S}}^T \Lambda\right) = (i\omega)^2 \rho \ \lambda_x \lambda_y \lambda_z \ \hat{\mathbf{u}}, \tag{2.12}$$

where the stretching tensor Λ is defined as

$$\begin{aligned}\Lambda = \begin{bmatrix} \lambda_y\lambda_z & 0 & 0 \\ 0 & \lambda_x\lambda_z & 0 \\ 0 & 0 & \lambda_x\lambda_y \end{bmatrix} &= \begin{bmatrix} \alpha_y\alpha_z & 0 & 0 \\ 0 & \alpha_x\alpha_z & 0 \\ 0 & 0 & \alpha_x\alpha_y \end{bmatrix} \\ &+ \frac{1}{(i\omega)} \begin{bmatrix} \alpha_y\beta_z + \alpha_z\beta_y & 0 & 0 \\ 0 & \alpha_x\beta_z + \alpha_z\beta_x & 0 \\ 0 & 0 & \alpha_x\beta_y + \alpha_y\beta_x \end{bmatrix} \\ &+ \frac{1}{(i\omega)^2} \begin{bmatrix} \beta_y\beta_z & 0 & 0 \\ 0 & \beta_x\beta_z & 0 \\ 0 & 0 & \beta_x\beta_y \end{bmatrix} = \Lambda_e + \frac{1}{i\omega}\Lambda_p + \frac{1}{(i\omega)^2}\Lambda_w. \end{aligned} \tag{2.13}$$

We remark that within the interior domain, Λ_e reduces to the identity tensor, whereas Λ_p and Λ_w vanish identically. Substituting (2.13) and (2.2) in (2.12), rearranging and grouping similar terms, results in

$$\mathbf{div}\left(\hat{\mathbb{S}}^T \Lambda_e + \frac{1}{i\omega}\hat{\mathbb{S}}^T \Lambda_p + \frac{1}{(i\omega)^2}\hat{\mathbb{S}}^T \Lambda_w\right) = \rho\left[(i\omega)^2 a\hat{\mathbf{u}} + i\omega b\hat{\mathbf{u}} + c\hat{\mathbf{u}} + \frac{d}{i\omega}\hat{\mathbf{u}}\right], \tag{2.14}$$

where

$$\begin{aligned} a &= \alpha_x\ \alpha_y\ \alpha_z, \\ b &= \alpha_x\ \alpha_y\ \beta_z + \alpha_x\ \alpha_z\ \beta_y + \alpha_y\ \alpha_z\ \beta_x, \\ c &= \alpha_x\ \beta_y\ \beta_z + \alpha_y\ \beta_z\ \beta_x + \alpha_z\ \beta_y\ \beta_x, \\ d &= \beta_x\ \beta_y\ \beta_z. \end{aligned} \tag{2.15}$$

Multiplying (2.14) by $i\omega$, we obtain

$$\mathbf{div}\left(i\omega\hat{\mathcal{S}}^T\Lambda_e + \hat{\mathcal{S}}^T\Lambda_p + \frac{1}{i\omega}\hat{\mathcal{S}}^T\Lambda_w\right) = \rho\left[(i\omega)^3 a\hat{\mathbf{u}} + (i\omega)^2 b\hat{\mathbf{u}} + i\omega c\hat{\mathbf{u}} + d\hat{\mathbf{u}}\right]. \tag{2.16}$$

Next, we focus our attention on the combined constitutive and kinematic equations (2.9b). Writing (2.9b) in the stretched coordinate system, and using (2.4) to express it in the physical coordinate system, there results

$$\begin{aligned} \hat{\mathcal{S}} = \mu\left\{(\nabla\hat{\mathbf{u}})\begin{bmatrix}\frac{1}{\lambda_x} & 0 & 0\\ 0 & \frac{1}{\lambda_y} & 0\\ 0 & 0 & \frac{1}{\lambda_z}\end{bmatrix} + \begin{bmatrix}\frac{1}{\lambda_x} & 0 & 0\\ 0 & \frac{1}{\lambda_y} & 0\\ 0 & 0 & \frac{1}{\lambda_z}\end{bmatrix}(\nabla\hat{\mathbf{u}})^T\right\} \\ + \lambda\Big(\frac{1}{\lambda_x}\frac{\partial\hat{u}_x}{\partial x} + \frac{1}{\lambda_y}\frac{\partial\hat{u}_y}{\partial y} + \frac{1}{\lambda_z}\frac{\partial\hat{u}_z}{\partial z}\Big)\mathcal{I}. \end{aligned} \tag{2.17}$$

Multiplying (2.17) by $\lambda_x\lambda_y\lambda_z$ results in

$$\lambda_x\lambda_y\lambda_z\hat{\mathcal{S}} = \mu\left[\nabla\hat{\mathbf{u}}\ \Lambda + \Lambda\,(\nabla\hat{\mathbf{u}})^T\right] + \lambda\,\mathrm{div}(\Lambda\hat{\mathbf{u}})\mathcal{I}, \tag{2.18}$$

where the stretching tensor Λ is defined in (2.13). Multiplying (2.18) by $(i\omega)^2$ and using (2.13), and (2.2), rearranging and grouping similar terms, we obtain

$$
\begin{aligned}
(i\omega)^2 a\hat{\mathcal{S}} + i\omega b\hat{\mathcal{S}} + c\hat{\mathcal{S}} + \frac{1}{i\omega} d\hat{\mathcal{S}} &= \mu(i\omega)^2 \left[(\nabla\hat{\mathbf{u}})\Lambda_e + \Lambda_e(\nabla\hat{\mathbf{u}})^T\right] \\
&\quad + \mu\ i\omega \left[(\nabla\hat{\mathbf{u}})\Lambda_p + \Lambda_p(\nabla\hat{\mathbf{u}})^T\right] + \mu \left[(\nabla\hat{\mathbf{u}})\Lambda_w + \Lambda_w(\nabla\hat{\mathbf{u}})^T\right] \\
&\quad + \lambda(i\omega)^2 \operatorname{div}(\Lambda_e\hat{\mathbf{u}})\mathcal{I} + \lambda\ i\omega \operatorname{div}(\Lambda_p\hat{\mathbf{u}})\mathcal{I} + \lambda \operatorname{div}(\Lambda_w\hat{\mathbf{u}})\mathcal{I}. \qquad (2.19)
\end{aligned}
$$

Equations (2.16) and (2.19) constitute the corresponding frequency-domain momentum, and combined constitutive and kinematic equations in the stretched coordinate system, respectively. They possess the desired spatial decaying property.

2.2.2 Time-domain equations

In this section, we apply the inverse Fourier transform to (2.16) and (2.19) to obtain the corresponding time-domain equations. This operation is rather simple due to the specific choice of the stretching function (2.2). We use

$$
\mathcal{F}^{-1}\left[\frac{\hat{g}(\omega)}{i\omega}\right] = \int_0^t g(\tau)d\tau, \qquad (2.20)
$$

where $\mathcal{F}^{-1}$ denotes the inverse Fourier transform operator[3], and $g(t)$ is a sufficiently regular function. Applying the inverse Fourier transform to (2.16) and (2.19), we obtain

---

[3] In general, $\mathcal{F}^{-1}\left[\frac{\hat{g}(\omega)}{i\omega}\right] = \int_0^t g(\tau)d\tau - \pi\hat{g}(0)\delta(\omega)$, but, it can be shown that since, by construction, the overall development excludes $\omega = 0$, the inverse transform reduces to (2.20) [71].

$$\mathbf{div}\left[\dot{\mathcal{S}}^T\Lambda_e + \mathcal{S}^T\Lambda_p + \left(\int_0^t \mathcal{S}^T d\tau\right)\Lambda_w\right] = \rho\left(a\dddot{\mathbf{u}} + b\ddot{\mathbf{u}} + c\dot{\mathbf{u}} + d\mathbf{u}\right), \tag{2.21a}$$

$$\begin{aligned}
&a\ddot{\mathcal{S}} + b\dot{\mathcal{S}} + c\mathcal{S} + d\left(\int_0^t \mathcal{S} d\tau\right) = \\
&\mu\left[(\nabla\ddot{\mathbf{u}})\Lambda_e + \Lambda_e(\nabla\ddot{\mathbf{u}})^T + (\nabla\dot{\mathbf{u}})\Lambda_p + \Lambda_p(\nabla\dot{\mathbf{u}})^T + (\nabla\mathbf{u})\Lambda_w + \Lambda_w(\nabla\mathbf{u})^T\right] + \\
&\lambda\left[\mathrm{div}(\Lambda_e\ddot{\mathbf{u}}) + \mathrm{div}(\Lambda_p\dot{\mathbf{u}}) + \mathrm{div}(\Lambda_w\mathbf{u})\right]\mathcal{I}.
\end{aligned} \tag{2.21b}$$

The set of integro-differential equations (2.21) can be expressed as a set of only partial differential equations, upon introducing the auxiliary variable $\mathbf{S}(\mathbf{x}, t)$, which may be interpreted as the stress history tensor [71, 72]:

$$\mathbf{S}(\mathbf{x}, t) = \int_0^t \mathcal{S}(\mathbf{x}, \tau) d\tau. \tag{2.22a}$$

Clearly,

$$\dot{\mathbf{S}}(\mathbf{x}, t) = \mathcal{S}(\mathbf{x}, t), \qquad \ddot{\mathbf{S}}(\mathbf{x}, t) = \dot{\mathcal{S}}(\mathbf{x}, t), \qquad \dddot{\mathbf{S}}(\mathbf{x}, t) = \ddot{\mathcal{S}}(\mathbf{x}, t). \tag{2.22b}$$

Substituting (2.22) in (2.21), we obtain

$$\mathbf{div}\left(\ddot{\mathbf{S}}^T\Lambda_e + \dot{\mathbf{S}}^T\Lambda_p + \mathbf{S}^T\Lambda_w\right) = \rho\left(a\dddot{\mathbf{u}} + b\ddot{\mathbf{u}} + c\dot{\mathbf{u}} + d\mathbf{u}\right), \tag{2.23a}$$

$$\begin{aligned}
&a\dddot{\mathbf{S}} + b\ddot{\mathbf{S}} + c\dot{\mathbf{S}} + d\mathbf{S} = \\
&\mu\left[(\nabla\ddot{\mathbf{u}})\Lambda_e + \Lambda_e(\nabla\ddot{\mathbf{u}})^T + (\nabla\dot{\mathbf{u}})\Lambda_p + \Lambda_p(\nabla\dot{\mathbf{u}})^T + (\nabla\mathbf{u})\Lambda_w + \Lambda_w(\nabla\mathbf{u})^T\right] + \\
&\lambda\left[\mathrm{div}(\Lambda_e\ddot{\mathbf{u}}) + \mathrm{div}(\Lambda_p\dot{\mathbf{u}}) + \mathrm{div}(\Lambda_w\mathbf{u})\right]\mathcal{I}.
\end{aligned} \tag{2.23b}$$

Equations (2.23) constitute the corresponding time-domain PML momentum, and combined constitutive and kinematic equations.

2.3 Hybrid finite element implementation

In this section, we discuss an efficient finite element technique for transient elastodynamics in PML-truncated domains. We use a method-of-lines approach, where we exploit a Galerkin method for spatial discretization, thus, obtaining a third-order, continuous-in-time system of ordinary differential equations. Various methods exist for time-integration of such systems. We discuss three techniques that seem suitable for practical applications.

2.3.1 Spatial discretization

The PML equations (2.23) can be used both for the interior domain and the PML buffer zone, since by construction, they reduce to (2.8) in the interior domain. This unified treatment amounts to considering stress and displacement components as unknowns in both the interior domain and the PML buffer zone. While feasible in principle, as is done in most PML formulations to date, we opt for a hybrid treatment, originally developed in [33] for two-dimensional problems, where the interior domain is treated with a standard displacement-only formulation, coupled with the PML equations in the buffer zone. This approach results in substantial reduction in computational cost compared to mixed-field formulations cast over the entire domain. It also makes the modification of existing interior-domain elastodynamic codes straightforward, since, one needs to only add the PML-related forms, whereas for the most part, the general structure of such codes remains intact.

Accordingly, find $\mathbf{u}(\mathbf{x}, t)$ in $\Omega^{\mathrm{RD}} \cup \Omega^{\mathrm{PML}}$, and $\mathbf{S}(\mathbf{x}, t)$ in Ω^{PML} (see Fig. 2.2 for domain and boundary designations), where $\mathbf{u}$ and $\mathbf{S}$ reside in appropriate function spaces, and:

$$\mathbf{div}\left\{\mu\left[\nabla\dot{\mathbf{u}} + (\nabla\dot{\mathbf{u}})^T\right] + \lambda(\operatorname{div}\dot{\mathbf{u}})\mathcal{I}\right\} + \dot{\mathbf{b}} = \rho\dddot{\mathbf{u}} \qquad \text{in } \Omega^{\mathrm{RD}} \times \mathsf{J}, \tag{2.24a}$$

$$\mathbf{div}\left(\ddot{\mathbf{S}}^T\Lambda_e + \dot{\mathbf{S}}^T\Lambda_p + \mathbf{S}^T\Lambda_w\right) = \rho\left(a\dddot{\mathbf{u}} + b\ddot{\mathbf{u}} + c\dot{\mathbf{u}} + d\mathbf{u}\right) \qquad \text{in } \Omega^{\mathrm{PML}} \times \mathsf{J}, \tag{2.24b}$$

$$\begin{aligned}
&a\dddot{\mathbf{S}} + b\ddot{\mathbf{S}} + c\dot{\mathbf{S}} + d\mathbf{S} = \\
&\mu\left[(\nabla\ddot{\mathbf{u}})\Lambda_e + \Lambda_e(\nabla\ddot{\mathbf{u}})^T + (\nabla\dot{\mathbf{u}})\Lambda_p + \Lambda_p(\nabla\dot{\mathbf{u}})^T + (\nabla\mathbf{u})\Lambda_w + \Lambda_w(\nabla\mathbf{u})^T\right] + \\
&\lambda\left[\operatorname{div}(\Lambda_e\ddot{\mathbf{u}}) + \operatorname{div}(\Lambda_p\dot{\mathbf{u}}) + \operatorname{div}(\Lambda_w\mathbf{u})\right]\mathcal{I} \qquad \text{in } \Omega^{\mathrm{PML}} \times \mathsf{J}.
\end{aligned} \tag{2.24c}$$

The system is initially at rest, and subject to the following boundary and interface conditions:

$$\left\{\mu\left[\nabla\dot{\mathbf{u}} + (\nabla\dot{\mathbf{u}})^T\right] + \lambda(\operatorname{div}\dot{\mathbf{u}})\mathcal{I}\right\}\mathbf{n}^+ = \dot{\boldsymbol{g}}_n \qquad \text{on } \Gamma_{\mathrm{N}}^{\mathrm{RD}} \times \mathsf{J}, \tag{2.25a}$$

$$(\ddot{\mathbf{S}}^T\Lambda_e + \dot{\mathbf{S}}^T\Lambda_p + \mathbf{S}^T\Lambda_w)\mathbf{n}^- = \mathbf{0} \qquad \text{on } \Gamma_{\mathrm{N}}^{\mathrm{PML}} \times \mathsf{J}, \tag{2.25b}$$

$$\mathbf{u} = \mathbf{0} \qquad \text{on } \Gamma_{\mathrm{D}}^{\mathrm{PML}} \times \mathsf{J}, \tag{2.25c}$$

$$\mathbf{u}^+ = \mathbf{u}^- \qquad \text{on } \Gamma^{\mathrm{I}} \times \mathsf{J}, \tag{2.25d}$$

$$\left\{\mu\left[\nabla\dot{\mathbf{u}} + (\nabla\dot{\mathbf{u}})^T\right] + \lambda(\operatorname{div}\dot{\mathbf{u}})\mathcal{I}\right\}\mathbf{n}^+ + (\ddot{\mathbf{S}}^T\Lambda_e + \dot{\mathbf{S}}^T\Lambda_p + \mathbf{S}^T\Lambda_w)\mathbf{n}^- = 0 \quad \text{on } \Gamma^{\mathrm{I}} \times \mathsf{J}, \tag{2.25e}$$

where temporal and spatial dependencies are suppressed for brevity; Ω^{RD} denotes the interior (regular) domain, Ω^{PML} represents the region occupied by the PML buffer zone, Γ^{I} is the interface boundary between the interior and PML domains, $\Gamma_{\mathrm{N}}^{\mathrm{RD}}$ and $\Gamma_{\mathrm{N}}^{\mathrm{PML}}$ denote the free (top surface) boundary of the interior domain and PML, respectively, and $\mathsf{J} = (0, T]$ is the time interval of interest. In (2.24a), $\mathbf{b}$ denotes body force per unit volume.

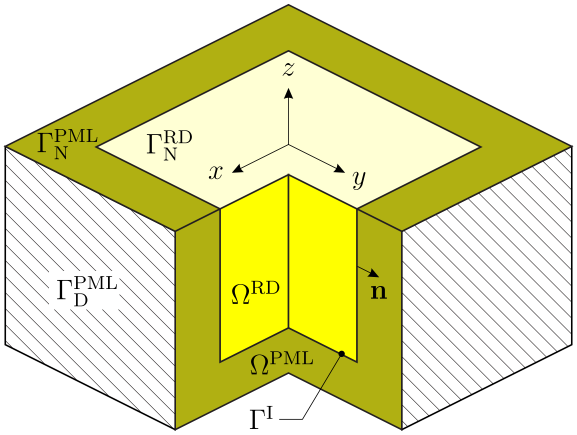

Figure 2.2: PML-truncated semi-infinite domain.

We remark that the temporal differentiation in (2.24a) is necessary for the boundary integrals that result from the weak form of (2.24a) and (2.24b) to cancel out; this is manifested in (2.25e) and enforces the balance of tractions at the interface of the interior domain and the PML. Moreover, (2.25d) implies continuity of displacements at the interface; (2.25a) specifies tractions ($\boldsymbol{g}_n$) on the top surface of the interior domain, and (2.25b) implies traction-free boundary condition on the top PML surface. We consider fixed boundaries for the PML on the sides and at the bottom, as indicated by (2.25c); other possibilities also exist but they seem to have little influence on performance [11, 12].

Next, we seek a weak solution, corresponding to the strong form of (2.24) and (2.25), in the Galerkin sense. Specifically, we take the inner products of (2.24a) and (2.24b) with (vector) test function $\mathbf{w}(\mathbf{x})$, and integrate by parts over their corresponding domains. Incorporating (2.25d-2.25e) eliminates the interface boundary terms and results in (2.26a). Next, we take the inner product of (2.24c) with (tensor) test function $\mathbf{T}(\mathbf{x})$; there results (2.26b). There are other possibilities for deriving a weak form that corresponds to the strong form (2.24) and (2.25). We refer to [73] for further details.

Accordingly, find $\mathbf{u} \in \mathbf{H}^1(\Omega) \times \mathsf{J}$, and $\mathbf{S} \in \mathcal{L}^2(\Omega) \times \mathsf{J}$, such that:

$$\begin{aligned}
&\int\limits_{\Omega^{\mathrm{RD}}} \nabla \mathbf{w} : \left\{ \mu \left[\nabla \dot{\mathbf{u}} + (\nabla \dot{\mathbf{u}})^T \right] + \lambda (\operatorname{div} \dot{\mathbf{u}}) \mathcal{J} \right\} \, \mathrm{d}\Omega + \int\limits_{\Omega^{\mathrm{PML}}} \nabla \mathbf{w} : \left(\ddot{\mathbf{S}}^T \Lambda_e + \dot{\mathbf{S}}^T \Lambda_p + \mathbf{S}^T \Lambda_w \right) \, \mathrm{d}\Omega \\
&+ \int\limits_{\Omega^{\mathrm{RD}}} \mathbf{w} \cdot \rho \ddot{\mathbf{u}} \, \mathrm{d}\Omega + \int\limits_{\Omega^{\mathrm{PML}}} \mathbf{w} \cdot \rho \left(a \dddot{\mathbf{u}} + b \ddot{\mathbf{u}} + c \dot{\mathbf{u}} + d \mathbf{u} \right) \, \mathrm{d}\Omega = \int\limits_{\Gamma^{\mathrm{RD}}_{\mathrm{N}}} \mathbf{w} \cdot \dot{\boldsymbol{g}}_n \, \mathrm{d}\Gamma + \int\limits_{\Omega^{\mathrm{RD}}} \mathbf{w} \cdot \dot{\mathbf{b}} \, \mathrm{d}\Omega,
\end{aligned} \tag{2.26a}$$

$$\begin{aligned}
&\int\limits_{\Omega^{\mathrm{PML}}} \mathbf{T} : \left(a \dddot{\mathbf{S}} + b \ddot{\mathbf{S}} + c \dot{\mathbf{S}} + d \mathbf{S} \right) \, \mathrm{d}\Omega \\
&= \int\limits_{\Omega^{\mathrm{PML}}} \mathbf{T} : \mu \left[(\nabla \ddot{\mathbf{u}}) \Lambda_e + \Lambda_e (\nabla \ddot{\mathbf{u}})^T + (\nabla \dot{\mathbf{u}}) \Lambda_p + \Lambda_p (\nabla \dot{\mathbf{u}})^T + (\nabla \mathbf{u}) \Lambda_w + \Lambda_w (\nabla \mathbf{u})^T \right] \\
&+ \mathbf{T} : \lambda \left[\operatorname{div}(\Lambda_e \ddot{\mathbf{u}}) + \operatorname{div}(\Lambda_p \dot{\mathbf{u}}) + \operatorname{div}(\Lambda_w \mathbf{u}) \right] \mathcal{J} \, \mathrm{d}\Omega,
\end{aligned} \tag{2.26b}$$

for every $\mathbf{w} \in \mathbf{H}^1(\Omega)$ and $\mathbf{T} \in \mathcal{L}^2(\Omega)$, where $\boldsymbol{g}_n \in \mathbf{L}^2(\Omega) \times \mathsf{J}$, and $\mathbf{b} \in \mathbf{L}^2(\Omega) \times \mathsf{J}$. Function spaces for scalar- (v), vector- ($\mathbf{v}$), and tensor-valued ($\mathcal{A}$) functions are defined as

$$L^2(\Omega) = \left\{ v\colon \int_\Omega |v|^2 d\mathbf{x} < \infty \right\}, \tag{2.27a}$$

$$\mathbf{L}^2(\Omega) = \left\{ \mathbf{v}\colon \mathbf{v} \in (L^2(\Omega))^3 \right\}, \tag{2.27b}$$

$$\mathcal{L}^2(\Omega) = \left\{ \mathcal{A}\colon \mathcal{A} \in (L^2(\Omega))^{3\times3} \right\}, \tag{2.27c}$$

$$H^1(\Omega) = \left\{ v\colon \int_\Omega \left(|v|^2 + |\nabla v|^2 \right) d\mathbf{x} < \infty,\ v|_{\Gamma_{\mathrm{D}}^{\mathrm{PML}}} = 0 \right\}, \tag{2.27d}$$

$$\mathbf{H}^1(\Omega) = \left\{ \mathbf{v}\colon \mathbf{v} \in (H^1(\Omega))^3 \right\}. \tag{2.27e}$$

In order to resolve (2.26) numerically, we use standard finite-dimensional subspaces. Specifically, we introduce finite-dimensional subspaces $\boldsymbol{\Xi}_h \subset \mathbf{H}^1(\Omega)$ and $\boldsymbol{\Upsilon}_h \subset \mathcal{L}^2(\Omega)$, with basis functions $\boldsymbol{\Phi}$ and $\boldsymbol{\Psi}$, respectively. We then approximate $\mathbf{u}(\mathbf{x}, t)$ with $\mathbf{u}_h(\mathbf{x}, t) \in \boldsymbol{\Xi}_h \times \mathsf{J}$, and $\mathbf{S}(\mathbf{x}, t)$ with $\mathbf{S}_h(\mathbf{x}, t) \in \boldsymbol{\Upsilon}_h \times \mathsf{J}$, as detailed below

$$\mathbf{u}_h(\mathbf{x}, t) = \begin{bmatrix} \boldsymbol{\Phi}^T(\mathbf{x})\mathbf{u}_x(t) \\ \boldsymbol{\Phi}^T(\mathbf{x})\mathbf{u}_y(t) \\ \boldsymbol{\Phi}^T(\mathbf{x})\mathbf{u}_z(t) \end{bmatrix}, \tag{2.28a}$$

$$\mathbf{S}_h(\mathbf{x}, t) = \begin{bmatrix} \boldsymbol{\Psi}^T(\mathbf{x})\mathbf{S}_{xx}(t) & \boldsymbol{\Psi}^T(\mathbf{x})\mathbf{S}_{xy}(t) & \boldsymbol{\Psi}^T(\mathbf{x})\mathbf{S}_{xz}(t) \\ \boldsymbol{\Psi}^T(\mathbf{x})\mathbf{S}_{yx}(t) & \boldsymbol{\Psi}^T(\mathbf{x})\mathbf{S}_{yy}(t) & \boldsymbol{\Psi}^T(\mathbf{x})\mathbf{S}_{yz}(t) \\ \boldsymbol{\Psi}^T(\mathbf{x})\mathbf{S}_{zx}(t) & \boldsymbol{\Psi}^T(\mathbf{x})\mathbf{S}_{zy}(t) & \boldsymbol{\Psi}^T(\mathbf{x})\mathbf{S}_{zz}(t) \end{bmatrix}. \tag{2.28b}$$

In a similar fashion, we approximate the test functions, $\mathbf{w}(\mathbf{x})$ with $\mathbf{w}_h(\mathbf{x}) \in \boldsymbol{\Xi}_h$, and $\mathbf{T}(\mathbf{x})$ with $\mathbf{T}_h(\mathbf{x}) \in \boldsymbol{\Upsilon}_h$; therefore:

$$\mathbf{w}_h(\mathbf{x}) = \begin{bmatrix} \mathbf{w}_x^T \boldsymbol{\Phi}(\mathbf{x}) \\ \mathbf{w}_y^T \boldsymbol{\Phi}(\mathbf{x}) \\ \mathbf{w}_z^T \boldsymbol{\Phi}(\mathbf{x}) \end{bmatrix}, \tag{2.29a}$$

$$\mathbf{T}_h(\mathbf{x}) = \begin{bmatrix} \mathbf{T}_{xx}^T \boldsymbol{\Psi}(\mathbf{x}) & \mathbf{T}_{xy}^T \boldsymbol{\Psi}(\mathbf{x}) & \mathbf{T}_{xz}^T \boldsymbol{\Psi}(\mathbf{x}) \\ \mathbf{T}_{yx}^T \boldsymbol{\Psi}(\mathbf{x}) & \mathbf{T}_{yy}^T \boldsymbol{\Psi}(\mathbf{x}) & \mathbf{T}_{yz}^T \boldsymbol{\Psi}(\mathbf{x}) \\ \mathbf{T}_{zx}^T \boldsymbol{\Psi}(\mathbf{x}) & \mathbf{T}_{zy}^T \boldsymbol{\Psi}(\mathbf{x}) & \mathbf{T}_{zz}^T \boldsymbol{\Psi}(\mathbf{x}) \end{bmatrix}. \tag{2.29b}$$

Incorporating (2.28-2.29) into (2.26), results in the following semi-discrete form

$$\mathbf{M}\dddot{\mathbf{d}} + \mathbf{C}\ddot{\mathbf{d}} + \mathbf{K}\dot{\mathbf{d}} + \mathbf{G}\mathbf{d} = \dot{\mathbf{f}}, \tag{2.30}$$

where spatial and temporal dependencies are suppressed for brevity, and system matrices, $\mathbf{M}$, $\mathbf{C}$, $\mathbf{K}$, $\mathbf{G}$, and vectors $\mathbf{d}$ and $\mathbf{f}$, are defined as

$$\mathbf{M} = \begin{bmatrix} \bar{\mathbf{M}}_{\mathrm{RD}} + \bar{\mathbf{M}}_a & \mathbf{0} \\ \mathbf{0} & \mathbf{N}_a \end{bmatrix}, \qquad \mathbf{C} = \begin{bmatrix} \bar{\mathbf{M}}_b & \bar{\mathbf{A}}_{eu} \\ -\bar{\mathbf{A}}_{el}^T & \mathbf{N}_b \end{bmatrix}, \tag{2.31a}$$

$$\mathbf{K} = \begin{bmatrix} \bar{\mathbf{K}}_{\mathrm{RD}} + \bar{\mathbf{M}}_c & \bar{\mathbf{A}}_{pu} \\ -\bar{\mathbf{A}}_{pl}^T & \mathbf{N}_c \end{bmatrix}, \qquad \mathbf{G} = \begin{bmatrix} \bar{\mathbf{M}}_d & \bar{\mathbf{A}}_{wu} \\ -\bar{\mathbf{A}}_{wl}^T & \mathbf{N}_d \end{bmatrix}, \tag{2.31b}$$

$$\mathbf{d} = \begin{bmatrix} \mathbf{u}_h & \mathbf{S}_h \end{bmatrix}^T, \qquad \mathbf{f} = \begin{bmatrix} \bar{\mathbf{f}}_{\mathrm{RD}} & \mathbf{0} \end{bmatrix}^T, \tag{2.31c}$$

where subscript RD refers to the interior (regular) domain, and $\mathbf{M}_{\mathrm{RD}}$, $\mathbf{K}_{\mathrm{RD}}$, and $\mathbf{f}_{\mathrm{RD}}$, correspond to the standard mass matrix, stiffness matrix, and vector of nodal forces in the interior domain, respectively, and a bar indicates their extension to encompass all the displacement degrees-of-freedom[4]; $\mathbf{u}_h$ and $\mathbf{S}_h$ comprise the vector of nodal

---

[4] This is merely a formalism to arrive at a unified, yet informative, matrix representation. For instance, we take $\mathbf{K}_{\mathrm{RD}}$ and extend it by adding zero entries corresponding to the $\mathbf{u}_h$ components of the PML buffer. This makes the matrix-vector operation $\bar{\mathbf{K}}_{\mathrm{RD}}\ \mathbf{u}_h$ meaningful, where, now, $\mathbf{u}_h$ contains the displacement degrees-of-freedom of the entire domain.

displacements and stresses. Moreover, $\mathbf{u}_h$ is partitioned such that its first entries belong solely to the interior domain, followed by those on the interface boundary between the interior domain and the PML buffer, and finally those that are located only within the PML. The rest of the submatrices in (2.31) correspond to the PML buffer zone (see Fig. 2.3 for a schematic partitioning, and Appendix A.1 for submatrix definitions; the dotted line in Fig. 2.3 separates displacement from stress degrees-of-freedom).

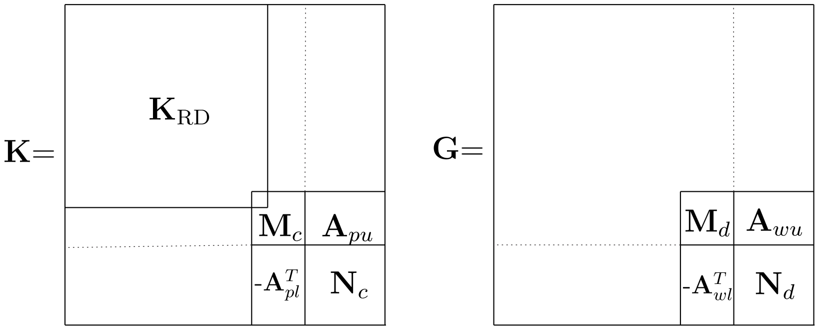

Figure 2.3: Partitioning of submatrices in (2.31b).

We remark that the upper-left corner blocks of $\mathbf{M}$ and $\mathbf{K}$ correspond to the mass and stiffness matrices of a standard displacement-only formulation, as depicted in Fig. 2.3. This implies that in order to accommodate PML capability into existing codes, one needs to account only for the submatrices on the lower-right blocks of $\mathbf{M}$, $\mathbf{C}$, $\mathbf{K}$, $\mathbf{G}$.

The matrix $\mathbf{M}$ has a block-diagonal structure (see (A.2a)-(A.2c)); thus, it can be diagonalized if one employs spectral elements, which then enables explicit time integration of (2.30): this is discussed in Section 2.4.

Notice that the semi-discrete form (2.30) is not symmetric. In fact, a block-diagonal structure for $\mathbf{M}$ comes at the price of losing symmetry. Alternatively, one may preserve symmetry of the matrices in the semi-discrete form at the expense of losing the block-diagonal form of $\mathbf{M}$, and thus the ability for explicit time integration. We discuss this alternative formulation in Section 2.5.

2.3.2 Discretization in time

In this section, we discuss various possibilities of integrating the semi-discrete form (2.30) in time. One may apply a time-marching scheme directly to (2.30), which is third-order in time, or, exploit a more common scheme by first expressing (2.30) as a second- or first-order in time system, via the introduction of auxiliary vectors.

Time-integration can be accomplished by working with either (2.30) or one of its second- or first-order system counterparts, or, alternatively, one may (analytically) integrate (2.30) in time first, to obviate the temporal differentiation of the forcing vector. Assuming the system is initially at rest, there results

$$\mathbf{M}\ddot{\mathbf{d}} + \mathbf{C}\dot{\mathbf{d}} + \mathbf{K}\mathbf{d} + \mathbf{G}\bar{\mathbf{d}} = \mathbf{f}, \tag{2.32a}$$

$$\bar{\mathbf{d}} = \int_0^t \mathbf{d}(\tau)|_{\mathrm{PML}}\, d\tau, \tag{2.32b}$$

where $\bar{\mathbf{d}}$ is the vector of history terms. Equation (2.32) can be integrated via an extended Newmark method as outlined in Appendix B.2. The scheme is implicit and requires matrix factorization.

We remark that $\bar{\mathbf{d}}$ contains displacement and stress degrees-of-freedom that are associated with the PML buffer *only* ; therefore, its size is much smaller than $\mathbf{d}$ (Fig. 2.3).

Alternatively, (2.32) can be expressed as a second-order system

$$\mathbf{M}\ddot{\mathbf{d}} + \mathbf{C}\dot{\mathbf{d}} + \mathbf{K}\mathbf{d} + \mathbf{G}\bar{\mathbf{d}} = \mathbf{f}, \tag{2.33a}$$

$$\dot{\bar{\mathbf{d}}} = \mathbf{d}|_{\mathrm{PML}}. \tag{2.33b}$$

In matrix notation, (2.33) reads

$$\begin{bmatrix} \mathbf{M} & \mathbf{0} \\ \mathbf{0} & \mathbf{0} \end{bmatrix} \begin{bmatrix} \ddot{\mathbf{d}} \\ \ddot{\bar{\mathbf{d}}} \end{bmatrix} + \begin{bmatrix} \mathbf{C} & \mathbf{0} \\ \mathbf{0} & \mathbf{I} \end{bmatrix} \begin{bmatrix} \dot{\mathbf{d}} \\ \dot{\bar{\mathbf{d}}} \end{bmatrix} + \begin{bmatrix} \mathbf{K} & \mathbf{G} \\ -\mathbf{I} & \mathbf{0} \end{bmatrix} \begin{bmatrix} \mathbf{d} \\ \bar{\mathbf{d}} \end{bmatrix} = \begin{bmatrix} \mathbf{f} \\ \mathbf{0} \end{bmatrix}, \tag{2.34}$$

where now a standard Newmark scheme may be utilized to integrate (2.34); or, alternatively

$$\begin{bmatrix} \mathbf{M} & \mathbf{0} \\ \mathbf{0} & \mathbf{I} \end{bmatrix} \begin{bmatrix} \ddot{\mathbf{d}} \\ \ddot{\bar{\mathbf{d}}} \end{bmatrix} + \begin{bmatrix} \mathbf{C} & \mathbf{0} \\ -\mathbf{I} & \mathbf{0} \end{bmatrix} \begin{bmatrix} \dot{\mathbf{d}} \\ \dot{\bar{\mathbf{d}}} \end{bmatrix} + \begin{bmatrix} \mathbf{K} & \mathbf{G} \\ \mathbf{0} & \mathbf{0} \end{bmatrix} \begin{bmatrix} \mathbf{d} \\ \bar{\mathbf{d}} \end{bmatrix} = \begin{bmatrix} \mathbf{f} \\ \mathbf{0} \end{bmatrix}, \tag{2.35}$$

where the resulting system can be integrated explicitly, provided that $\mathbf{M}$ is diagonal, as we discuss in Section 2.4.

One may also express (2.32) as a first-order system

$$\frac{d}{dt} \begin{bmatrix} \mathbf{x}_0 \\ \mathbf{x}_1 \\ \mathbf{M}\mathbf{x}_2 \end{bmatrix} = \begin{bmatrix} \mathbf{0} & \mathbf{I} & \mathbf{0} \\ \mathbf{0} & \mathbf{0} & \mathbf{I} \\ -\mathbf{G} & -\mathbf{K} & -\mathbf{C} \end{bmatrix} \begin{bmatrix} \mathbf{x}_0 \\ \mathbf{x}_1 \\ \mathbf{x}_2 \end{bmatrix} + \begin{bmatrix} \mathbf{0} \\ \mathbf{0} \\ \mathbf{f} \end{bmatrix}, \tag{2.36}$$

where $\mathbf{x}_0 = \bar{\mathbf{d}}$, $\mathbf{x}_1 = \mathbf{d}$, and $\mathbf{x}_2 = \dot{\mathbf{d}}$. Various standard explicit schemes could then be used, provided that $\mathbf{M}$ is diagonal [74]. Here, we favor an explicit fourth-order Runge-Kutta (RK-4) method. Based on various numerical experiments we performed, we found out that, for the RK-4, $\Delta t < 0.8\frac{\Delta x}{c_p}$ ensures stability on uniform grids, where Δx is the minimum distance between two grid points, and c_p is the maximum compressional wave velocity over an element. If, for a certain choice of time step, a simulation with displacement-only finite elements is stable, then, the associated simulation involving the PML is also stable with the same time step. In other words, the introduction of the PML does not impose a more onerous time step choice than an interior elastodynamics problem would require.

2.4 Spectral elements and explicit time integration

Hyperbolic initial-value-problems are, in general, advanced in time by using explicit methods [22, 75]. This obviates the need for "inverting" a large linear system, typically encountered in implicit schemes. Moreover, explicit schemes naturally lend themselves to parallel computation, which is essential when dealing with large-scale simulations in three-dimensional problems. In this section, we discuss how the matrix $\mathbf{M}$ in the semi-discrete form (2.30) may be diagonalized, thus, enabling explicit time-stepping via the techniques discussed in Section 2.3.2.

The simplest way of obtaining (discrete) diagonal mass-like matrices, is by mass-lumping, as was done in [31, 76] where the authors used linear elements[5]. To

---

[5] By contrast to classical Galerkin finite elements, a finite difference formulation automatically yields diagonal mass-like matrices; see [74] for instance.

achieve high-order accuracy, however, one may use nodal spectral elements, where numerical integration (quadrature rule) is based on the same nodes that polynomial interpolation is carried out [77, 78]. This results in (discrete) diagonal mass-like matrices, which are high-order accurate, depending on the degree of the interpolating polynomial. Herein, we use quadratic hexahedral elements (27-noded) with a Legendre-Gauss-Lobatto quadrature rule (Table 2.1).

Table 2.1: Legendre-Gauss-Lobatto quadrature rule.

Element	Location of nodes	Location of integration points	Weights
Quadratic	±1.0	±1.0	1/3
	0.0	0.0	4/3

An m point Legendre-Gauss-Lobatto rule integrates polynomials of degree up to and including $2m$ - 3, exactly [77]. However, to compute mass-like matrices, one needs to integrate terms with $\mathbf{\Phi}\mathbf{\Phi}^T$-like components, where $\mathbf{\Phi}$ is the vector of Lagrange interpolating polynomials (see A.1). Having m interpolation nodes results in polynomials of degree m - 1. The tensor products then involve terms of degree $2m$ - 2; thus, the approach relies on under-integration in order to return a diagonal mass-like matrix. Herein, we use the Legendre-Gauss-Lobatto rule to compute all the submatrices presented in (2.31).

We remark that integration of mass-like matrices must be done consistently. This means that the same quadrature rule must be used to compute $\mathbf{M}_{\text{RD}}$, $\mathbf{M}_i, \mathbf{N}_i$, $i = a, b, c, d$ in (2.31), therefore, rendering all these matrices diagonal. Choosing a scheme that diagonalizes the mass-like matrix $\mathbf{M}$ in (2.31), whether done by conventional mass lumping, or, via spectral elements, while not applying the same scheme uniformly to all mass-like matrices, will result in instabilities, as it has also been reported in [31, 79].

2.5 A symmetric formulation

In Section 2.2, we discussed a non-symmetric PML formulation that can be integrated explicitly in time. In this section, we discuss an alternative formulation, that results in a symmetric semi-discrete form, which would require an implicit time-integration scheme due to a non-diagonal mass-like matrix. The key difference with the Section 2.2 formulation is the handling of the combined constitutive and kinematic equations. To this end, we keep the equilibrium equation in (2.8a) intact, but express (2.8b) in a different form.

Similar to what was done in [57], we start with the constitutive and kinematic equations in the time domain

$$\mathcal{S} = \mathcal{C}[\mathcal{E}], \tag{2.37a}$$

$$\mathcal{E} = \frac{1}{2}\left[\nabla\mathbf{u} + (\nabla\mathbf{u})^T\right], \tag{2.37b}$$

where $\mathcal{E}$ is the strain tensor, and $\mathcal{C}$ is the fourth-order constitutive tensor. For an isotropic medium, $\mathcal{C}[\mathcal{E}] = 2\mu\mathcal{E} + \lambda(\mathrm{tr}\mathcal{E})\mathcal{I}$. Taking the Fourier transform of (2.37), there results:

$$\hat{\mathcal{S}} = \mathcal{C}[\hat{\mathcal{E}}], \tag{2.38a}$$

$$\hat{\mathcal{E}} = \frac{1}{2}\left[\nabla\hat{\mathbf{u}} + (\nabla\hat{\mathbf{u}})^T\right]. \tag{2.38b}$$

Writing (2.38b) in the stretched coordinate system and using (2.4), we obtain:

$$\hat{\mathcal{E}} = \frac{1}{2}\left\{(\nabla\hat{\mathbf{u}})\begin{bmatrix}\frac{1}{\lambda_x} & 0 & 0\\ 0 & \frac{1}{\lambda_y} & 0\\ 0 & 0 & \frac{1}{\lambda_z}\end{bmatrix} + \begin{bmatrix}\frac{1}{\lambda_x} & 0 & 0\\ 0 & \frac{1}{\lambda_y} & 0\\ 0 & 0 & \frac{1}{\lambda_z}\end{bmatrix}(\nabla\hat{\mathbf{u}})^T\right\}. \tag{2.39}$$

Multiplying (2.39) by $\lambda_x\lambda_y\lambda_z$ results in

$$\lambda_x\lambda_y\lambda_z\hat{\mathcal{E}} = \frac{1}{2}\left[(\nabla\hat{\mathbf{u}})\Lambda + \Lambda(\nabla\hat{\mathbf{u}})^T\right]. \tag{2.40}$$

Multiplying (2.40) by $(i\omega)^2$ and using (2.13) and (2.2), we obtain

$$\begin{aligned}(i\omega)^2 a\hat{\mathcal{E}} + i\omega b\hat{\mathcal{E}} + c\hat{\mathcal{E}} + \frac{1}{i\omega}d\hat{\mathcal{E}} &= \frac{1}{2}(i\omega)^2\left[(\nabla\hat{\mathbf{u}})\Lambda_e + \Lambda_e(\nabla\hat{\mathbf{u}})^T\right]\\ &+ \frac{1}{2}i\omega\left[(\nabla\hat{\mathbf{u}})\Lambda_p + \Lambda_p(\nabla\hat{\mathbf{u}})^T\right] + \frac{1}{2}\left[(\nabla\hat{\mathbf{u}})\Lambda_w + \Lambda_w(\nabla\hat{\mathbf{u}})^T\right]. \end{aligned}\tag{2.41}$$

Equation (2.41) constitutes the corresponding frequency-domain kinematic equation in the stretched coordinate system. Taking the inverse Fourier transform of (2.38a) and (2.41), there results

$$\mathcal{S} = \mathcal{C}[\mathcal{E}], \tag{2.42a}$$

$$a\ddot{\mathcal{E}} + b\dot{\mathcal{E}} + c\mathcal{E} + d\left(\int_0^t \mathcal{E}\, d\tau\right) = \\ \frac{1}{2}\left[(\nabla\ddot{\mathbf{u}})\Lambda_e + \Lambda_e(\nabla\ddot{\mathbf{u}})^T + (\nabla\dot{\mathbf{u}})\Lambda_p + \Lambda_p(\nabla\dot{\mathbf{u}})^T + (\nabla\mathbf{u})\Lambda_w + \Lambda_w(\nabla\mathbf{u})^T\right]. \tag{2.42b}$$

Combining the resulting constitutive equation (2.42a) with the kinematic equation (2.42b), and using the auxiliary variables introduced in (2.22), we obtain

$$\mathcal{D}\left[\left(a\dddot{\mathbf{S}} + b\ddot{\mathbf{S}} + c\dot{\mathbf{S}} + d\mathbf{S}\right)\right] = \\ \frac{1}{2}\left[(\nabla\ddot{\mathbf{u}})\Lambda_e + \Lambda_e(\nabla\ddot{\mathbf{u}})^T + (\nabla\dot{\mathbf{u}})\Lambda_p + \Lambda_p(\nabla\dot{\mathbf{u}})^T + (\nabla\mathbf{u})\Lambda_w + \Lambda_w(\nabla\mathbf{u})^T\right], \tag{2.43}$$

where $\mathcal{D}$ is the compliance tensor ($\mathcal{E} = \mathcal{D}[\mathcal{S}]$). Equation (2.43) constitutes the PML combined constitutive and kinematic equations, which is equivalent to (2.23b).

Next, similar to what we did in Section 2.3.1, we take the inner product of (2.43) with (tensor) test function $\mathbf{T}(\mathbf{x}) \in \mathcal{L}^2(\Omega)$; there results:

$$\int\limits_{\Omega^{\text{PML}}} \mathbf{T} : \mathcal{D}\left(a\dddot{\mathbf{S}} + b\ddot{\mathbf{S}} + c\dot{\mathbf{S}} + d\mathbf{S}\right)\, \mathrm{d}\Omega \\ = \frac{1}{2}\int\limits_{\Omega^{\text{PML}}} \mathbf{T} : \left[(\nabla\ddot{\mathbf{u}})\Lambda_e + \Lambda_e(\nabla\ddot{\mathbf{u}})^T + (\nabla\dot{\mathbf{u}})\Lambda_p + \Lambda_p(\nabla\dot{\mathbf{u}})^T + (\nabla\mathbf{u})\Lambda_w + \Lambda_w(\nabla\mathbf{u})^T\right] \mathrm{d}\Omega. \tag{2.44}$$

Upon discretization of (2.26a) and (2.44) via (2.28)-(2.29), we obtain a semi-discrete form

$$\mathbf{M}_s\dddot{\mathbf{d}} + \mathbf{C}_s\ddot{\mathbf{d}} + \mathbf{K}_s\dot{\mathbf{d}} + \mathbf{G}_s\mathbf{d} = \dot{\mathbf{f}}, \tag{2.45}$$

with the following definition for system matrices

$$\mathbf{M}_s = \begin{bmatrix} \bar{\mathbf{M}}_{\mathrm{RD}} + \bar{\mathbf{M}}_a & \mathbf{0} \\ \mathbf{0} & -\mathbf{N}_a \end{bmatrix}, \qquad \mathbf{C}_s = \begin{bmatrix} \bar{\mathbf{M}}_b & \bar{\mathbf{A}}_e \\ \bar{\mathbf{A}}_e^T & -\mathbf{N}_b \end{bmatrix}, \tag{2.46a}$$

$$\mathbf{K}_s = \begin{bmatrix} \bar{\mathbf{K}}_{\mathrm{RD}} + \bar{\mathbf{M}}_c & \bar{\mathbf{A}}_p \\ \bar{\mathbf{A}}_p^T & -\mathbf{N}_c \end{bmatrix}, \qquad \mathbf{G}_s = \begin{bmatrix} \bar{\mathbf{M}}_d & \bar{\mathbf{A}}_w \\ \bar{\mathbf{A}}_w^T & -\mathbf{N}_d \end{bmatrix}, \tag{2.46b}$$

$$\mathbf{d} = \begin{bmatrix} \mathbf{u}_h & \mathbf{S}_h \end{bmatrix}^T, \qquad \mathbf{f} = \begin{bmatrix} \bar{\mathbf{f}}_{\mathrm{RD}} & \mathbf{0} \end{bmatrix}^T, \tag{2.46c}$$

where a bar denotes matrix extension to encompass all the displacement degrees-of-freedom; $\mathbf{M}_i,\ i = a, b, c, d$ are PML matrices defined in (A.2b), and $\mathbf{N}_i,\ i = a, b, c, d$, $\mathbf{A}_i,\ i = e, p, w$ are defined in (A.7) and (A.8), respectively. Moreover, similar to what we did in Section 2.3.2, (2.45) can be expressed similarly to (2.32) by taking into account (2.32b), therefore, obviating the temporal differentiation of the forcing term:

$$\mathbf{M}_s\ddot{\mathbf{d}} + \mathbf{C}_s\dot{\mathbf{d}} + \mathbf{K}_s\mathbf{d} + \mathbf{G}_s\bar{\mathbf{d}} = \mathbf{f}. \tag{2.47}$$

System matrices defined in (2.46a)-(2.46b) are now symmetric and indefinite by contrast to (2.31a)-(2.31b). They can become positive definite if one multiplies their lower blocks by a minus sign, at the expense of losing symmetry. We refer to [33, 80] for details.

We remark that $\mathbf{N}_a$ in $\mathbf{M}$ is a block penta-diagonal matrix; this entails an implicit time-integration scheme for the semi-discrete form. The extended Newmark method outlined in Appendix B.2 could then be used for time-stepping, which then necessitates factorization of a symmetric matrix.

2.6 Generalization for multi-axial perfectly-matched-layers

The aforementioned derivations are based on using the classical stretching function (2.2), where stretching is enforced only in the direction perpendicular to the PML interface. It has been reported that, in two dimensions, and under certain parameterizations, this stretching function creates spurious growths when waves travel along the interface, thus leading to numerical instability. In an attempt to stabilize the PML (in 2D), Meza-Fajardo and Papageorgiou [41] proposed coordinate-stretching in all directions within the PML buffer, leading to the, so-called, multi-axial PML (M-PML).

Herein, we show that by making minimal modifications, our framework can also accommodate the M-PML. We focus on the "right" PML buffer zone first, i.e., the volume contained in $x_0 \leq x \leq x_t$ (see Fig. 2.1 with s replaced by x); extending the ideas to the zones where two or three layers intersect is straightforward, and can be accomplished by using superposition. We stretch the physical coordinates according to

$$\tilde{x} = x_0 + \int_{x_0}^{x} \left[\alpha_x(x') + \frac{1}{i\omega}\beta_x(x') \right] dx', \tag{2.48a}$$

$$\tilde{y} = y_0 + \int_{y_0}^{y} \left[\alpha_y(x) + \frac{1}{i\omega}\beta_y(x) \right] dy', \tag{2.48b}$$

$$\tilde{z} = z_0 + \int_{z_0}^{z} \left[\alpha_z(x) + \frac{1}{i\omega}\beta_z(x) \right] dz'. \tag{2.48c}$$

where $\alpha_y, \alpha_z, \beta_y$, and β_z are functions of x only, and are defined as

$$\alpha_y(x) = 1 + \varrho\ \alpha_o \left[\frac{(x - x_o)n_x}{L_{\text{PML}}} \right]^m, \qquad \beta_y(x) = \varrho\ \beta_x(x), \tag{2.49a}$$

$$\alpha_z(x) = 1 + \varrho\ \alpha_o \left[\frac{(x - x_o)n_x}{L_{\text{PML}}} \right]^m, \qquad \beta_z(x) = \varrho\ \beta_x(x), \tag{2.49b}$$

where ϱ is a proportionality constant, and n_x is the outward unit normal at the interface, similar to n_s in Fig. 2.1; α_x and β_x are defined in (2.5). We remark that α_y, α_z would have been reduced to one, and β_y, β_z would have been identically zero, in the right buffer, had we used the classical stretching. Applying the fundamental theorem of calculus to (2.48), results in

$$\lambda_x := \frac{\partial \tilde{x}}{\partial x} = \alpha_x(x) + \frac{1}{i\omega}\beta_x(x), \tag{2.50a}$$

$$\lambda_y := \frac{\partial \tilde{y}}{\partial y} = \alpha_y(x) + \frac{1}{i\omega}\beta_y(x), \tag{2.50b}$$

$$\lambda_z := \frac{\partial \tilde{z}}{\partial z} = \alpha_z(x) + \frac{1}{i\omega}\beta_z(x). \tag{2.50c}$$

These are the stretching functions the authors used in [45]. However, the definition of the stretched gradient operator in equation (3) in [45] requires additional terms, which the authors had not included. For example, the derivative with respect to $\tilde{x}$ should read

$$\frac{\partial(\ )}{\partial\tilde{x}} = \frac{\partial(\ )}{\partial x}\frac{\partial x}{\partial\tilde{x}} + \frac{\partial(\ )}{\partial y}\frac{\partial y}{\partial\tilde{x}} + \frac{\partial(\ )}{\partial z}\frac{\partial z}{\partial\tilde{x}} \tag{2.51a}$$

$$= \frac{1}{\lambda_x}\frac{\partial(\ )}{\partial x} - \frac{\lambda_{yx}}{\lambda_x\lambda_y}\frac{\partial(\ )}{\partial y} - \frac{\lambda_{zx}}{\lambda_x\lambda_z}\frac{\partial(\ )}{\partial z}, \tag{2.51b}$$

instead of the expression given in [45], which reads

$$\frac{\partial(\ )}{\partial\tilde{x}} = \frac{1}{\lambda_x}\frac{\partial(\ )}{\partial x}. \tag{2.52a}$$

In (2.51) above, the cross-derivative terms are defined as

$$\lambda_{yx} := \frac{\partial\tilde{y}}{\partial x} = \left(\frac{\partial}{\partial x}\alpha_y(x) + \frac{1}{i\omega}\frac{\partial}{\partial x}\beta_y(x)\right)(y - y_0), \tag{2.53a}$$

$$\lambda_{zx} := \frac{\partial\tilde{z}}{\partial x} = \left(\frac{\partial}{\partial x}\alpha_z(x) + \frac{1}{i\omega}\frac{\partial}{\partial x}\beta_z(x)\right)(z - z_0). \tag{2.53b}$$

In other words, it seems that in [41, 45], the authors have not accounted properly for the Jacobian. Thus, there are at least two possible forms of the M-PML: the *uncorrected* form in [41, 45], and the *corrected* form, which accounts for the cross-derivatives. Interestingly, numerical experiments we performed in two dimensions with the corrected form yielded small, but non-negligible reflections from the interface. By contrast, the *uncorrected* form yielded better results, despite its unsound mathematical foundation. This has led us to adopt the approach taken in [41, 45]; accordingly, the equation pertaining to the conservation of linear momentum in the stretched coordinate system becomes

$$\mathbf{div}\left(\hat{\mathbb{S}}^T\Lambda\right) - \hat{\mathbb{S}}^T\,\mathbf{div}\,\Lambda = (i\omega)^2\rho\ \lambda_x\lambda_y\lambda_z\ \hat{\mathbf{u}}, \tag{2.54}$$

which results in the following strong form

$$\begin{aligned} &\mathbf{div}\left(\ddot{\mathbf{S}}^T\Lambda_e + \dot{\mathbf{S}}^T\Lambda_p + \mathbf{S}^T\Lambda_w\right) - \left(\ddot{\mathbf{S}}^T\,\mathbf{div}\,\Lambda_e + \dot{\mathbf{S}}^T\,\mathbf{div}\,\Lambda_p + \mathbf{S}^T\,\mathbf{div}\,\Lambda_w\right) \\ &\qquad = \rho\left(a\dddot{\mathbf{u}} + b\ddot{\mathbf{u}} + c\dot{\mathbf{u}} + d\mathbf{u}\right). \end{aligned} \tag{2.55}$$

The structure of the formulation pertaining to the combined constitutive and kinematic equation in the stretched coordinate system we previously discussed remains unaltered. Hence, for accommodating the M-PML, one only needs to replace (2.24b) in the strong form of the equations with (2.55), which, in turn, changes the definition of submatrices $\mathbf{A}_{eu}, \mathbf{A}_{pu}$, and $\mathbf{A}_{wu}$ in (2.31). The new definition of these submatrices for the M-PML case are given in Appendix A.3.

2.7 Numerical Experiments

We present three numerical experiments to test the accuracy and efficacy of our hybrid formulation. The first example involves a homogeneous half-space; the second one is a horizontally layered medium with an ellipsoidal inclusion. The last example compares various formulations discussed in Sections 2.3.2 and 2.5. We compare our results against an enlarged domain[6] solution with fixed boundaries, obtained via a standard displacement-only formulation, which may be viewed as

---

[6] denoted by Ω^{ED}, such that $\Omega^{\mathrm{RD}} \subset \Omega^{\mathrm{ED}}$.

a reference solution. Due to the fixed boundaries of the enlarged domain model, reflection occurs at these boundaries; hence, we limit the comparison time up to the arrival of the reflected waves to the regular domain.

In the first two examples, we apply a surface traction on the medium, with a Ricker pulse time signature, defined as

$$\mathrm{T_p}(t) = \frac{(0.25u^2 - 0.5)e^{-0.25u^2} - 13e^{-13.5}}{0.5 + 13e^{-13.5}} \quad \text{with} \;\; 0 \le t \le \frac{6\sqrt{6}}{\omega_r}, \tag{2.56}$$

such that

$$u = \omega_r t - 3\sqrt{6}, \tag{2.57}$$

where ω_r $(= 2\pi f_r)$ denotes the characteristic central circular frequency of the pulse. Here, we take $f_r = 15$ Hz, and the load has an amplitude of 1 kPa. The pulse time-history, and its corresponding Fourier spectrum are shown in Fig. 2.4.

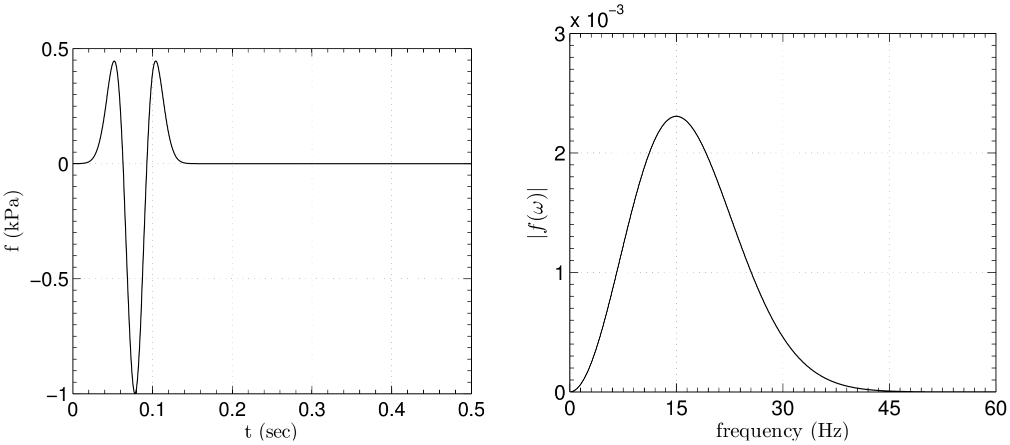

Figure 2.4: Ricker pulse time history and its Fourier spectrum.

In order to quantify the performance of our PML formulation, we consider two metrics: (a) time-history comparisons at select nodes via evaluation of a time-dependent Euclidean norm of the error, relative to the reference solution; and (b) decay of the total energy within the regular domain.

We define the time-dependent Euclidean norm of the relative error at a point $\mathbf{x} \in \Omega^{\mathrm{RD}}$ as

$$e(\mathbf{x}, t) = \frac{\|\mathbf{u}(\mathbf{x}, t) - \mathbf{u}_{\mathrm{ED}}(\mathbf{x}, t)\|_2}{\max\limits_{t} \|\mathbf{u}_{\mathrm{ED}}(\mathbf{x}, t)\|_2}, \tag{2.58}$$

where $\mathbf{u}_{\mathrm{ED}}(\mathbf{x}, t)$ represents the enlarged domain solution, and the Euclidean norm of a vector $\mathbf{u}(\mathbf{x}, t) = [u_x(\mathbf{x}, t), u_y(\mathbf{x}, t), u_z(\mathbf{x}, t)]^T$ is defined as

$$\|\mathbf{u}(\mathbf{x}, t)\|_2 = \sqrt{\big(u_x(\mathbf{x}, t)\big)^2 + \big(u_y(\mathbf{x}, t)\big)^2 + \big(u_z(\mathbf{x}, t)\big)^2}. \tag{2.59}$$

The energy introduced into the system through the loading is carried via waves, which then enter the PML buffer and attenuate. Therefore, an effective PML ought to result in the rapid decay of energy. The total energy of the system can be computed at any time via

$$E_t(t) = \frac{1}{2} \int\limits_{\Omega^{\mathrm{RD}}} \rho(\mathbf{x}) \left[\dot{\mathbf{u}}^T(\mathbf{x}, t) \dot{\mathbf{u}}(\mathbf{x}, t)\right] \, \mathrm{d}\Omega + \frac{1}{2} \int\limits_{\Omega^{\mathrm{RD}}} \left[\boldsymbol{\sigma}^T(\mathbf{x}, t) \boldsymbol{\epsilon}(\mathbf{x}, t)\right] \, \mathrm{d}\Omega, \tag{2.60}$$

where $\dot{\mathbf{u}}$ denotes the velocity vector, and $\boldsymbol{\sigma}$ and $\boldsymbol{\epsilon}$ are stress and strain vectors, respectively. We compute and compare energy only within the regular domain. Moreover,

$E_t(t)$ can also be used as a stability indicator since one expects that the total energy decays monotonically for a stable formulation.

2.7.1 Homogeneous media

We consider a homogeneous half-space with shear wave velocity $c_s = 500$ m/s, Poisson's ratio $\nu = 0.25$, and mass density $\rho = 2000$ kg/m^3, which, after truncation, is reduced to a cubic computational domain of length and width 100 m × 100 m, and 50 m depth. A 12.5 m-thick PML is placed at the truncation boundaries, as shown in Fig. 2.5. Two excitations are considered: a vertical stress load (vertical excitation), and a horizontal traction along the x axis (horizontal excitation). The excitations have the Ricker pulse temporal variation (Fig. 2.4), and are applied on the surface of the medium over a region (-1.25 m $\leq x, y \leq 1.25$ m). We carry out the simulation for each excitation separately. The interior and PML domains are discretized by quadratic hexahedral spectral elements (i.e., 27-noded bricks, and quadratic-quadratic pairs of approximation for displacement and stress components in the PML) of size 1.25 m. For the PML parameters, we choose $\alpha_o = 5$, $\beta_o = 866\ s^{-1}$, and a quadratic profile for the attenuation functions, i.e., $m = 2$. Using the 4$^{\text{th}}$-order explicit Runge-Kutta method, discussed in B.1, with a time step of $\Delta t = 0.0006$ s, we compute the response for 2 s using the hybrid formulation corresponding to (2.36).

We also compute a reference solution, via a standard displacement-only formulation, for an enlarged domain of size 440 m × 440 m × 220 m, with fixed boundaries, using the same element type and size discussed above. For this example, P-wave velocity is $c_p = 866$ m/s. Therefore, it takes 0.45 s for the P-wave generated

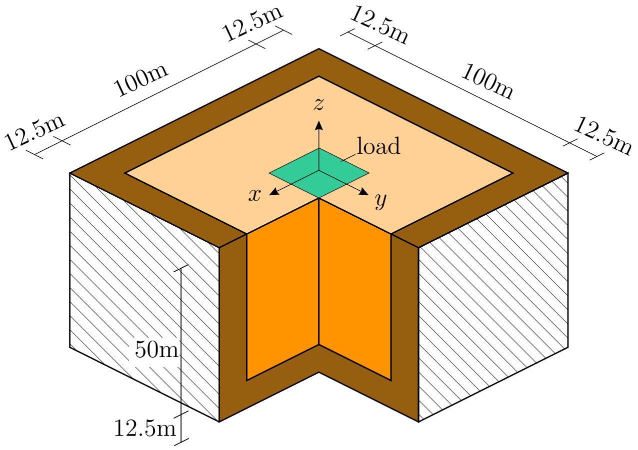

Figure 2.5: PML-truncated semi-infinite homogeneous media.

by the stress load, which is applied at the center of the surface, to hit the fixed boundaries and return to the regular domain. We use the 4th-order explicit Runge-Kutta method, with $\Delta t = 0.0006$ s for time-stepping and compute the response for 0.45 s. Table 2.2 summarizes the discretization details of the two considered models[7].

Table 2.2: Discretization details of the hybrid-PML and enlarged domain models.

	elements	nodes	unknowns
hybrid-PML	500,000	4,080,501	24,228,426
enlarged-domain	21,807,104	175,449,825	521,884,704

Figure 2.6 displays snapshots of the total displacement at two different times for the vertical excitation. The left figure shows waves at an evolving stage, while the figure on the right demonstrates absorption of waves in the PML region. Figure 2.7 shows the corresponding wave motion for the horizontal excitation. No discernible

---

[7] We developed a code in Fortran, using PETSc [81] to facilitate parallel implementation.

reflections can be observed from the PML interface, nor any residuals from the fixed-end boundaries, indicating satisfactory performance of the PML.

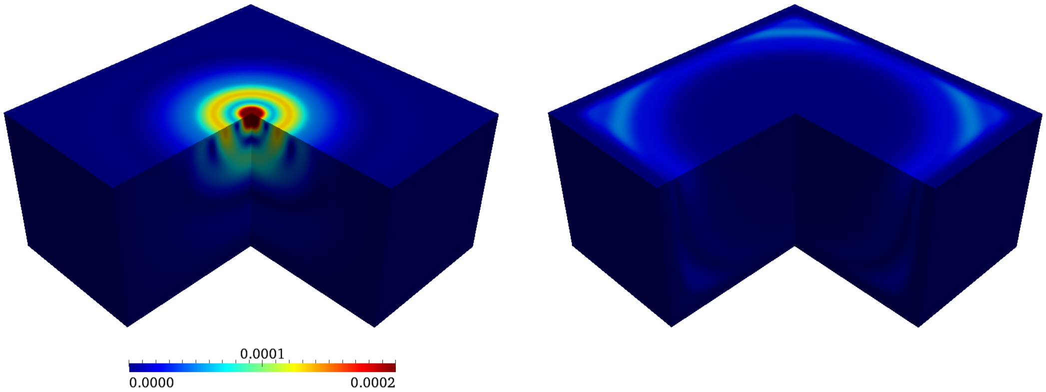

Figure 2.6: Snapshots of total displacement taken at $t = 0.111$ s, 0.219 s (vertical excitation).

We compare time histories of the hybrid PML formulation against the reference solution at select points. The location of these points are summarized in Table 2.3; the maximum relative error at each of these sampling points, computed using (2.58), is presented in the fifth and the sixth column, for the vertical and horizontal excitations, respectively. The relative error is very small and demonstrates the efficacy and success of the approach.

Figures 2.8 and 2.9 display comparison of the two responses, due to the vertical and horizontal excitation, at various sampling points. The agreement is excellent; the PML has effectively absorbed waves with practically no reflections. The response is causal, effectively dies out at around $t = 0.35$ s at all the considered points, and is free from spurious reflections.

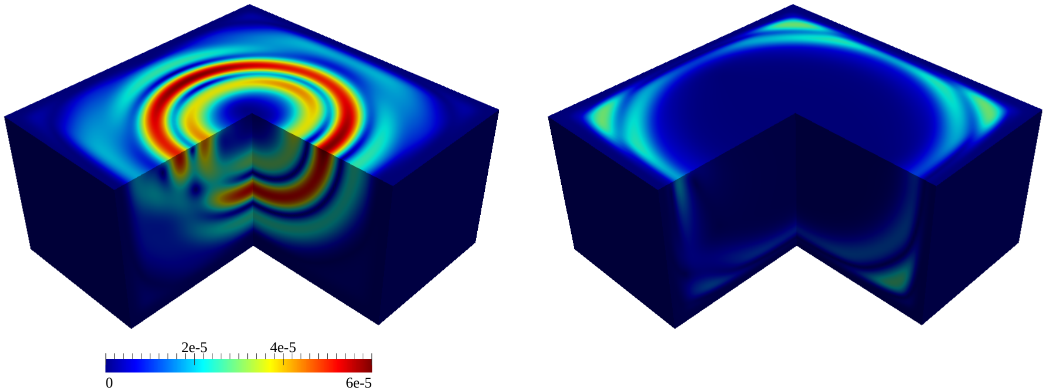

Figure 2.7: Snapshots of total displacement taken at $t = 0.147$ s, 0.219 s (horizontal excitation).

Table 2.3: Relative error at sampling points between hybrid-PML and enlarged domain solutions.

sample point	x	y	z	error (homogeneous) vertical excitation	error (homogeneous) horizontal excitation	error (heterogeneous) vertical excitation
sp_1	0	0	0	1.17×10^{-12}	8.77×10^{-13}	4.61×10^{-10}
sp_2	+50	0	0	2.52×10^{-8}	2.34×10^{-8}	6.07×10^{-7}
sp_3	+50	0	-25	2.89×10^{-9}	4.12×10^{-8}	2.87×10^{-6}
sp_4	+50	0	-50	1.46×10^{-7}	1.42×10^{-7}	7.03×10^{-6}
sp_5	0	0	-50	9.86×10^{-9}	2.51×10^{-9}	1.41×10^{-5}
sp_6	+50	+50	0	3.26×10^{-7}	2.16×10^{-7}	1.86×10^{-6}
sp_7	+50	+50	-25	5.50×10^{-8}	1.18×10^{-7}	6.72×10^{-6}
sp_8	+50	+50	-50	5.08×10^{-7}	5.25×10^{-7}	6.44×10^{-6}

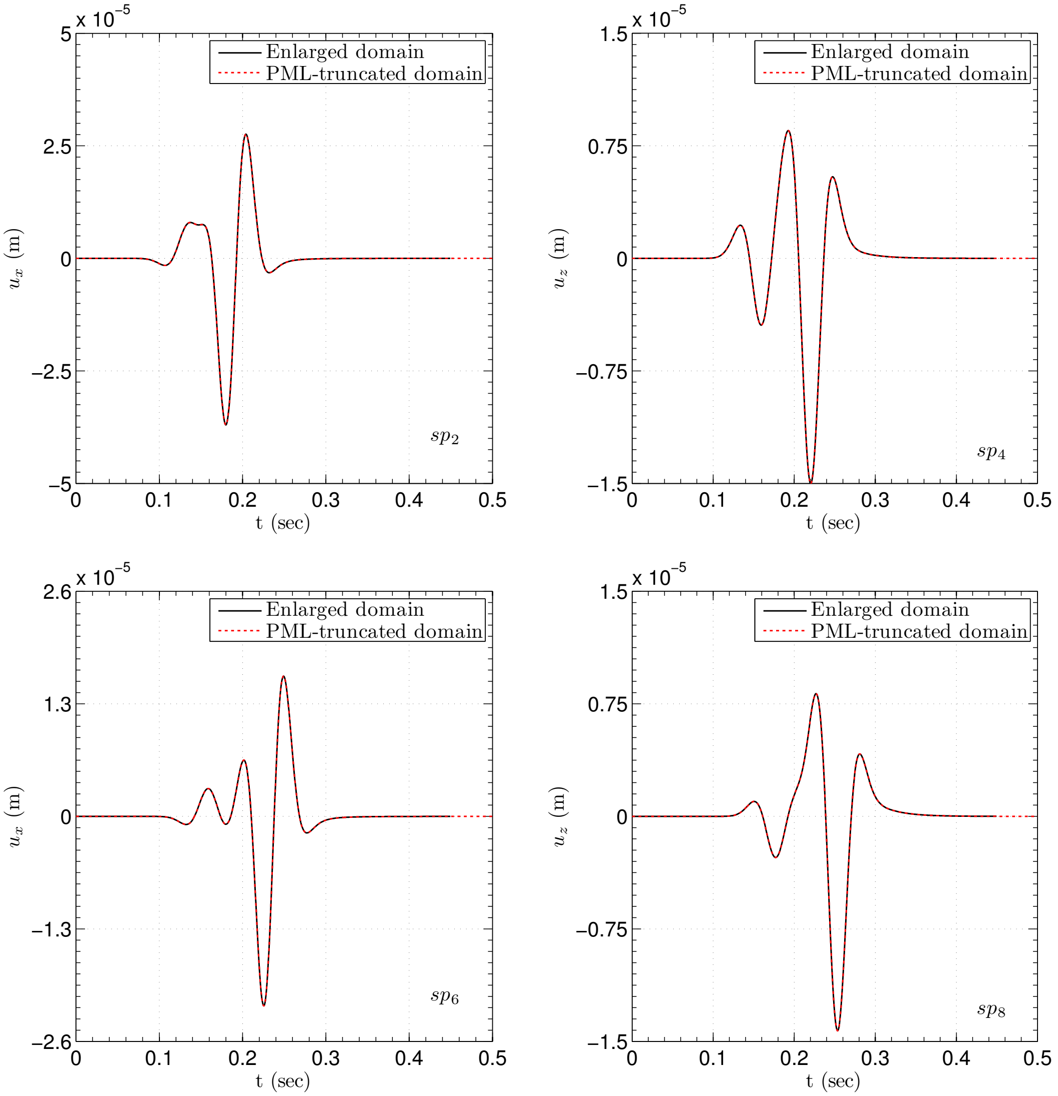

Figure 2.8: Comparison of displacement time histories between the enlarged and PML-truncated domain solutions at the sp_2, sp_4, sp_6, and sp_8 sampling points (homogeneous case, vertical excitation).

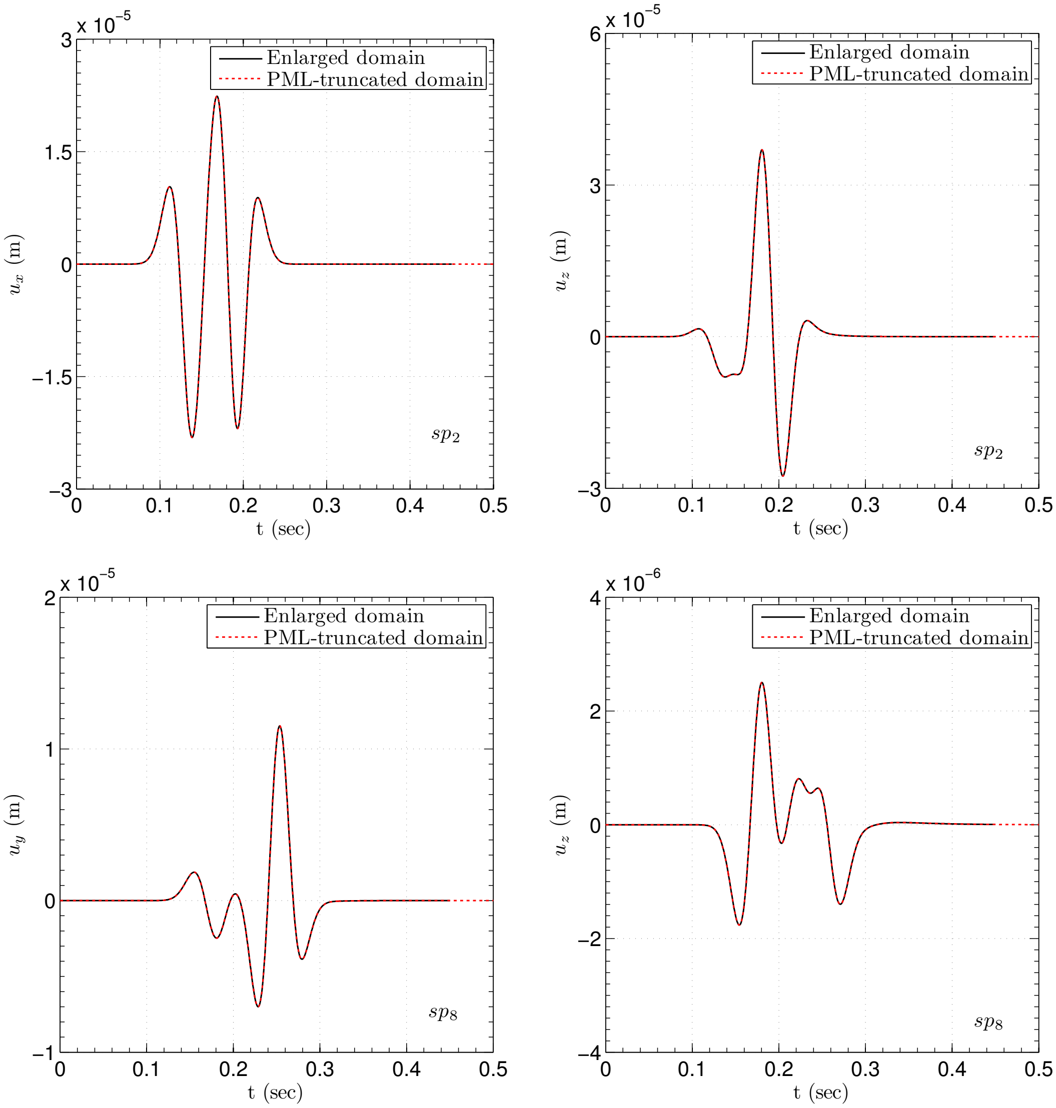

Figure 2.9: Comparison of displacement time histories between the enlarged and PML-truncated domain solutions at the sp_2 and sp_8 sampling points (homogeneous case, horizontal excitation).

Figure 2.10 shows the normalized error time history (2.58) due to the vertical excitation for two distinct locations: sp_3 and sp_8. Figure 2.11 shows the corresponding error time history for the horizontal excitation. Among all the considered locations, sp_8 has the highest error, which is only 5.08×10^{-7} for the vertical excitation, and 5.25×10^{-7} for the horizontal excitation.

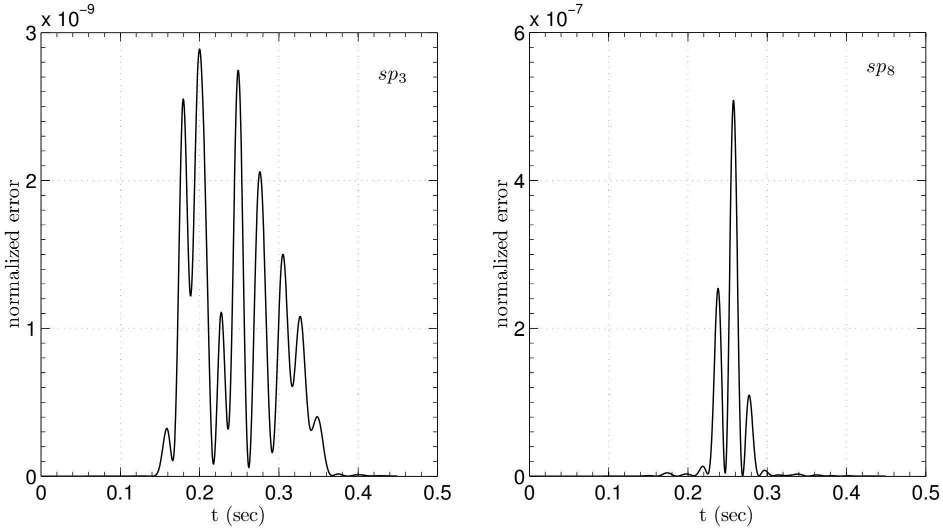

Figure 2.10: Relative error time history $e(\mathbf{x}, t)$ at various sampling points (homogeneous case, vertical excitation).

The total energy decay within the regular domain, due to the vertical excitation, is plotted in Figure 2.12, both in standard and semi-logarithmic scale for various values of β_o. Due to the limited size of the enlarged domain model, we compare the enlarged domain solution with the set of the PML solutions for various β_o only up to 0.45 s, since for $t > 0.45$ s, the reflections from the enlarged domain's fixed boundaries would have traveled back to the regular domain. The agreement is excellent and no difference can be observed. For $\beta_o = 866\ s^{-1}$, the total reduction in

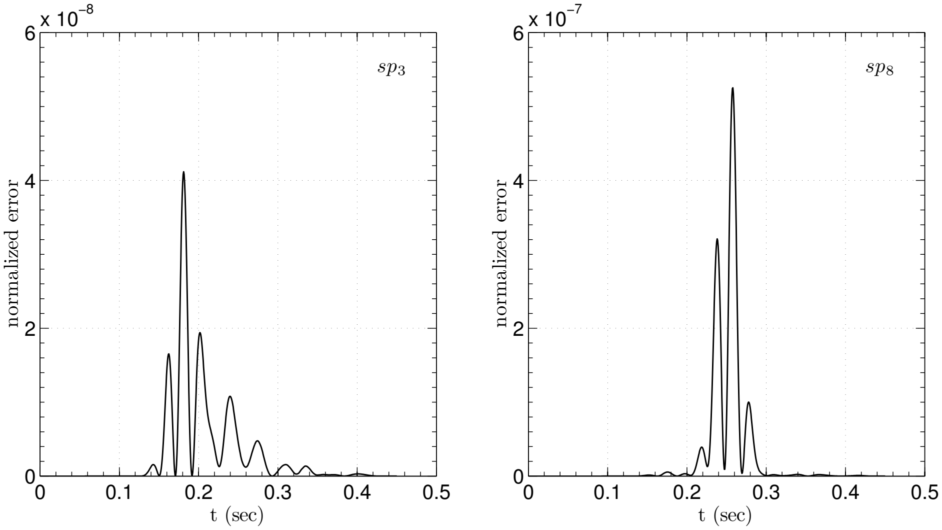

Figure 2.11: Relative error time history $e(\mathbf{x}, t)$ at various sampling points (homogeneous case, horizontal excitation).

energy, relative to its peak value, is 14 orders of magnitude. The decay is sharp and smooth, without any discernible reflections, indicating the effectiveness and health of the PML. Figure 2.13 displays the corresponding decay of energy curves due to the horizontal excitation. As can be seen from the standard scale plot, most of the energy travels out of the interior domain quickly, and gets absorbed in the PML effectively.

To illustrate the stability of the formulation, we run the simulation for 50,000 time steps. The total energy decay is displayed in Fig. 2.14 and shows no numerical instability during the simulation time.

We remark that we also used M-PML terminations to conduct this numerical experiment. While the results are satisfactory in general, they are not as accurate as when using PML terminations. In fact, for all the sampling points of Table 2.3,

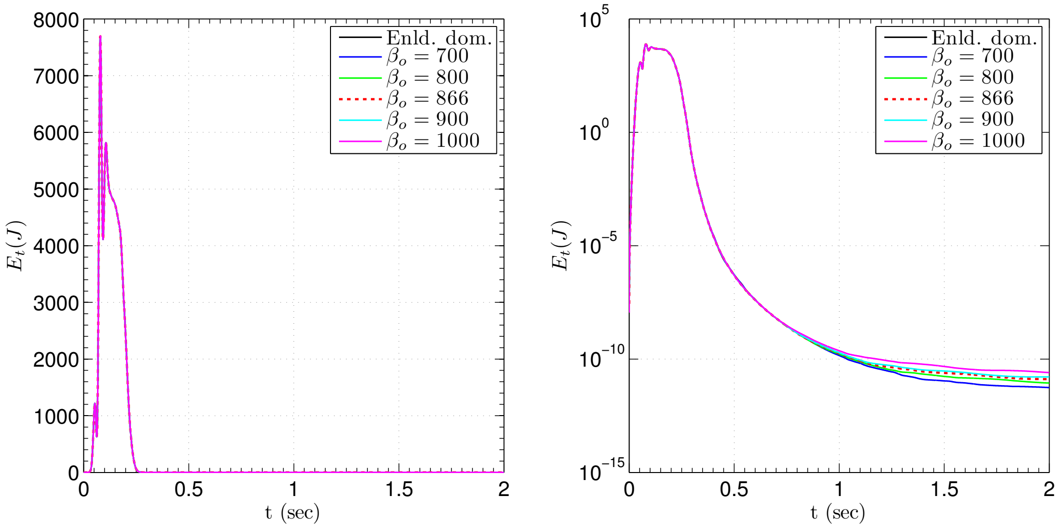

(a) standard scale

(b) logarithmic scale

Figure 2.12: Total decay of energy within the regular domain for various values of β_o (homogeneous case, vertical excitation).

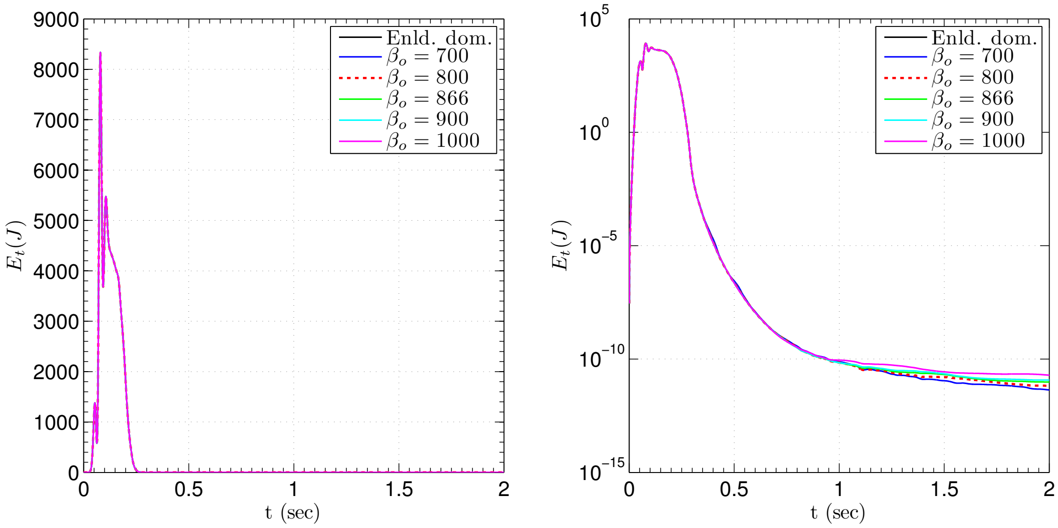

(a) standard scale

(b) logarithmic scale

Figure 2.13: Total decay of energy within the regular domain for various values of β_o (homogeneous case, horizontal excitation).

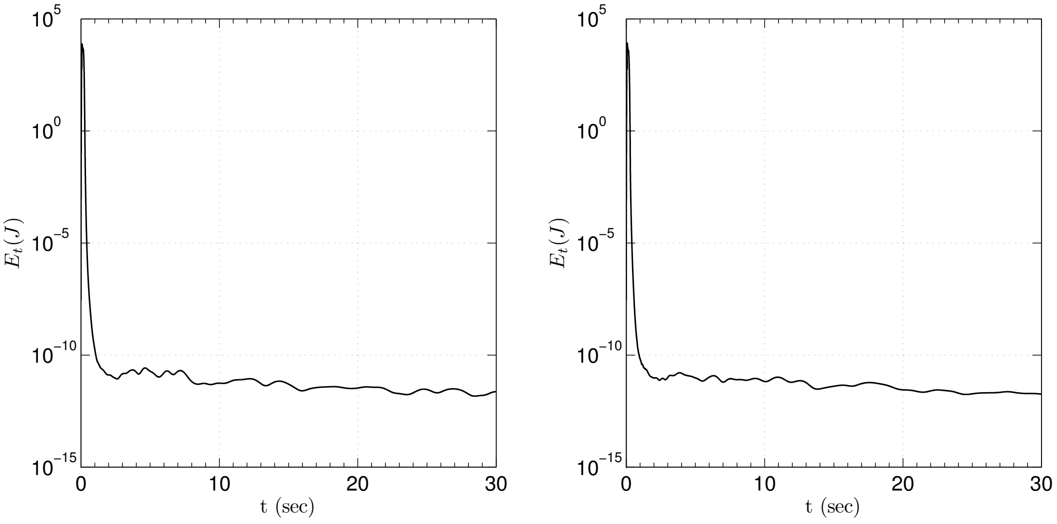

(a) vertical excitation (b) horizontal excitation

Figure 2.14: Total decay of energy within the regular domain for $\beta_o = 866\ s^{-1}$ (homogeneous case).

the relative error remained less than 1%, except at the corner point sp_8 where the relative error is about 5%. We do not report the M-PML-based results in detail pending comprehensive investigations.

2.7.2 Heterogeneous media

In the second example, we study the performance of our hybrid-PML formulation for a heterogeneous medium. We consider a 100 m × 100 m × 50 m layered medium with an ellipsoidal inclusion, where a 12.5 m-thick PML is placed at its truncation boundaries, as shown in Fig. 2.15. The properties of the medium are

$$c_s(z) = \begin{cases} 400 \text{ m/s}, & \text{for } -20 \text{ m} \leq z \leq 0 \text{ m}, \\ 500 \text{ m/s}, & \text{for } -50 \text{ m} \leq z < -20 \text{ m}, \\ 600 \text{ m/s}, & \text{for ellipsoidal inclusion}, \end{cases} \tag{2.61}$$

with mass density $\rho = 2000$ kg/m^3, and Poisson's ratio $\nu = 0.25$; the ellipsoidal inclusion occupies the region $(\frac{x-25}{15})^2 + (\frac{y-25}{5})^2 + (\frac{z+20}{5})^2 \leq 1$. The material properties at the interfaces Γ^{I} are extended into the PML buffer. A vertical stress load, with the Ricker pulse temporal signature, is applied on the surface of the medium over a region (-1.25 m $\leq x, y \leq 1.25$ m). The problem is discretized with quadratic hexahedral elements of size 1.25 m. The PML parameters are taken as $\alpha_o = 5$, $\beta_o = 500\ s^{-1}$, and $m = 2$. To resolve the motion we use the first-order system (2.36), and a 4$^{\text{th}}$-order explicit Runge-Kutta method, with a time step of $\Delta t = 0.00048$ s.

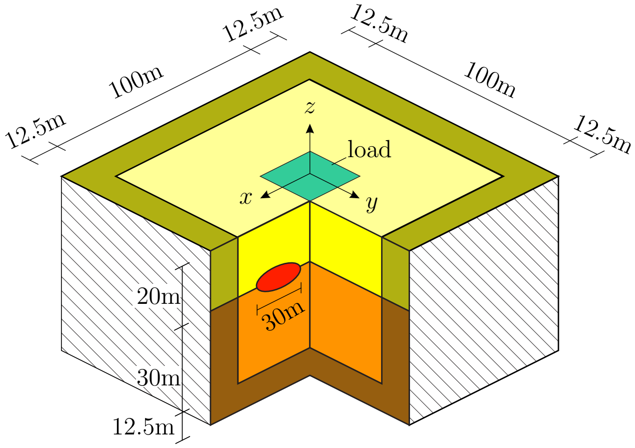

Figure 2.15: PML-truncated semi-infinite heterogeneous media.

Next, a reference solution is computed by using an enlarged domain, with size and spatial discretization properties similar to the previous example, and a time step of $\Delta t = 0.00048$ s. Table 2.2 summarizes the spatial discretization details of the problem.

To assess the performance of our hybrid PML formulation, we compare displacement time histories at select locations against the enlarged domain solution. The sampling points, with their corresponding relative error computed via (2.58) are summarized in the last column of Table 2.3. The relative error values are higher than the previous example, which was a homogeneous medium, but still, they are very low. In fact, the highest relative error, which corresponds to sp_8, is only 1.41×10^{-5}, which is very small in practical applications.

Snapshots of the total displacement at two different times are displayed in Fig. 2.16. The figure on the left shows waves at an evolving stage, while the right figure indicates absorption of waves in the PML buffer zone. Notice that no discernible reflections can be seen from the PML interfaces, nor any residuals from the fixed-end boundaries, a visual indication of satisfactory performance of the PML for domains involving heterogeneous material properties. Figure 2.17 depicts the complex wave pattern around the ellipsoidal inclusion on a cross-section through the domain situated at 20 m from the surface going through the ellipsoid's midplane.

Various components of displacement time-histories for the enlarged domain and the hybrid PML simulations are displayed in Fig. 2.18 for select sampling points. The agreement is excellent. The response effectively dies out at around 0.45 s. The relative error time histories are shown in Fig. 2.19 and indicate satisfactory performance of the PML.

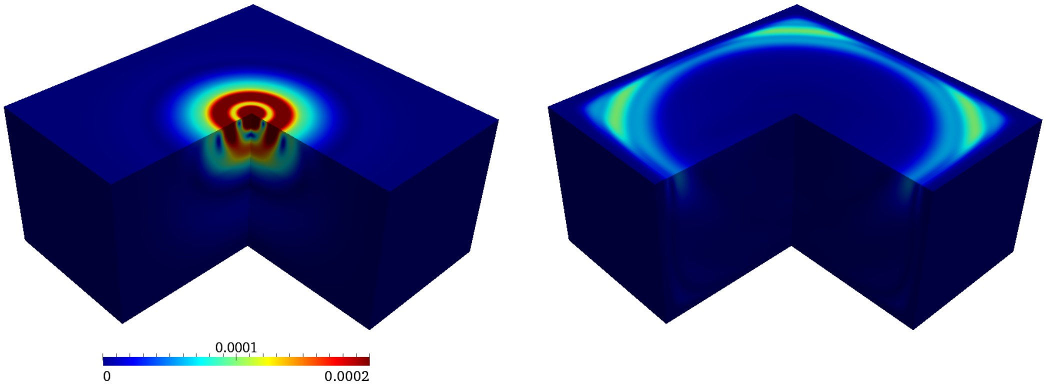

Figure 2.16: Snapshots of total displacement taken at $t = 0.111$ s, 0.225 s.

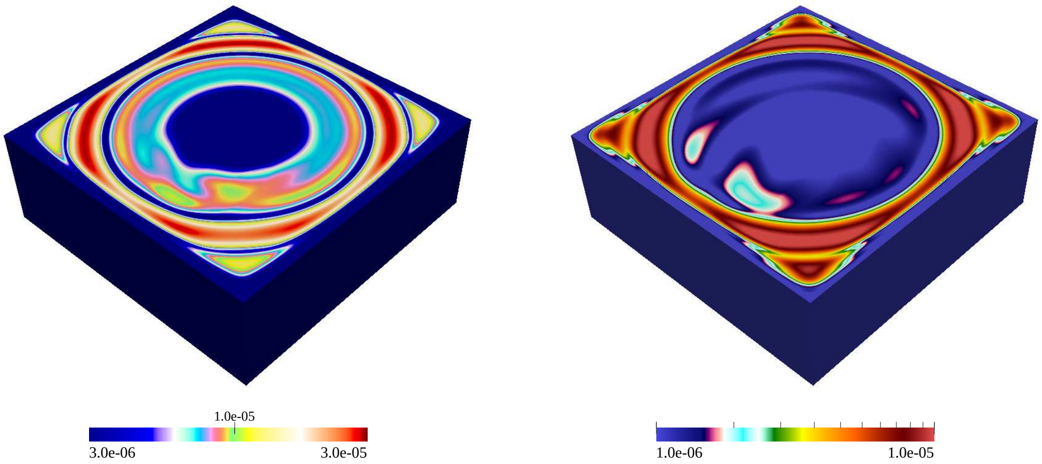

Figure 2.17: Snapshots of total displacement taken at $t = 0.233$ s, and 0.290 s, on the $z = -20$ m domain cross-section.

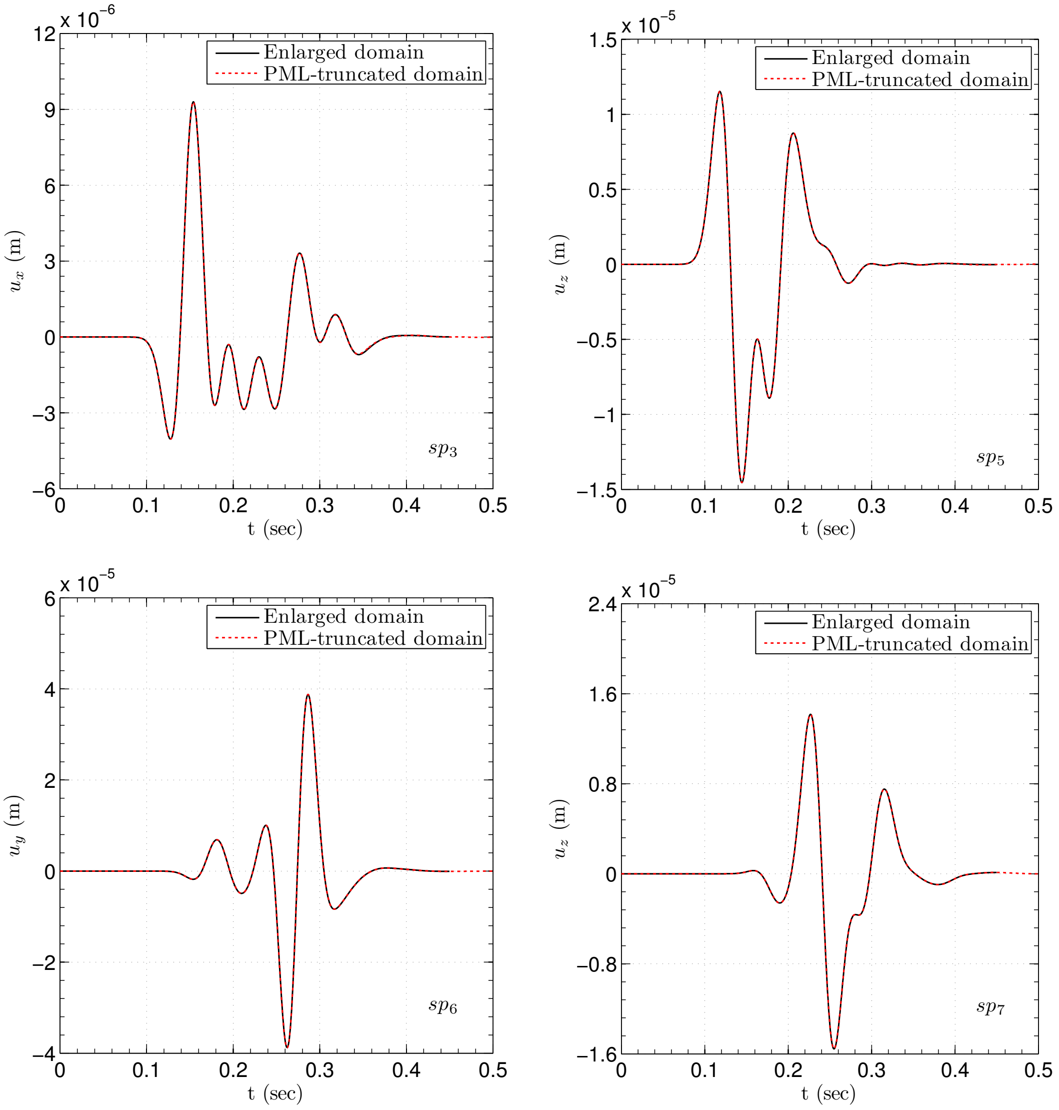

Figure 2.18: Comparison of displacement time histories between the enlarged and PML-truncated domain solutions at the sp_3, sp_5, sp_6, and sp_7 sampling points (heterogeneous case).

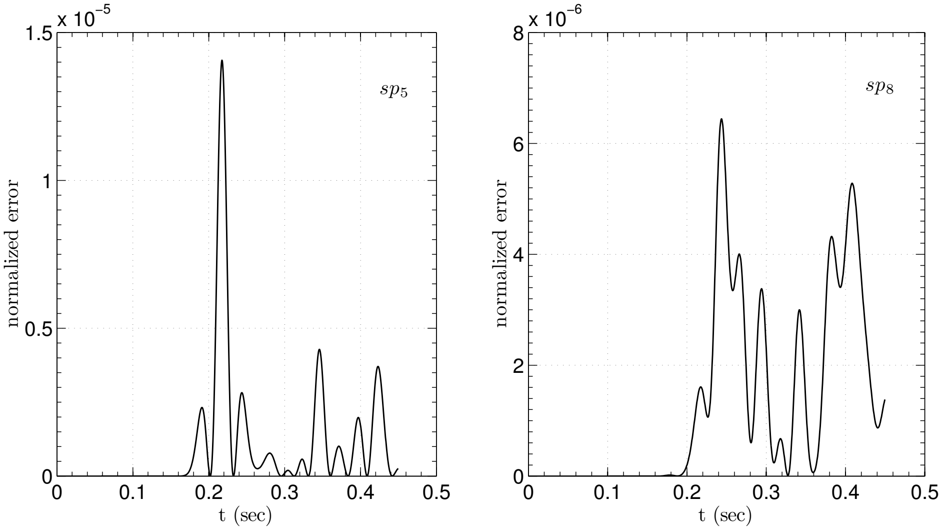

Figure 2.19: Relative error time history at various sampling points (heterogeneous case).

We compare the total energy decay within the regular domain between the PML and enlarged domain solutions. Due to the size of the enlarged domain model, the energy can only be computed up to 0.45 s. For the PML-truncated model, however, we allow the simulation to run for 2 s. The energy curves are presented in Fig. 2.20. The agreement between the enlarged domain solution and the PML curves is excellent. The reduction of the total energy is 14 orders of magnitude for $\beta_o = 500\ s^{-1}$; energy decay is sharp and smooth, with no sign of reflections, signifying satisfactory performance of the PML.

Finally, to illustrate the stability of the proposed scheme, we run the simulation for 125,000 time steps. The decay of the total energy is shown in Fig. 2.21 and shows no numerical instability during the simulation time.

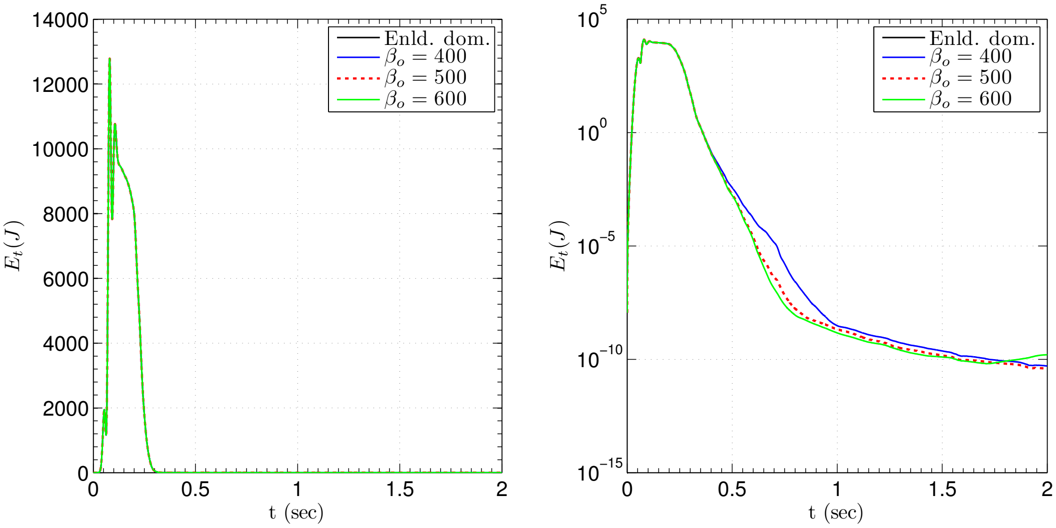

(a) normal scale

(b) logarithmic scale

Figure 2.20: Total decay of energy within the regular domain for various values of β_o (heterogeneous case).

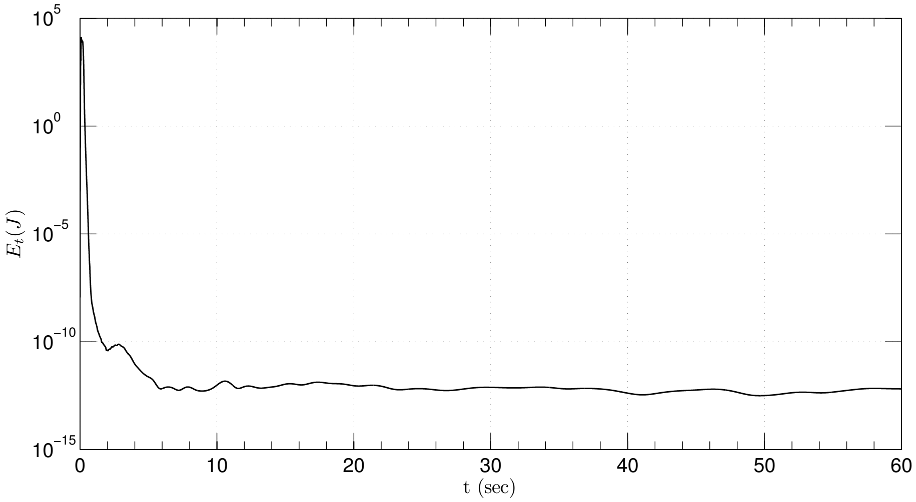

Figure 2.21: Total decay of energy within the regular domain for $\beta_o = 500$ s^{-1} (heterogeneous case).

2.7.3 Comparison of various formulations

In the previous numerical experiments, we utilized explicit time-stepping using spectral elements, which is well suited for solving large-scale problems on parallel computers. In this section, we compare alternative formulations and various time marching schemes, discussed earlier in Sections 2.3.2 and 2.5, using the same numerical experiment considered in [31]. Specifically, we use the standard Newmark method for the second-order in time forms (2.34, 2.35) using standard quadratic 20-noded elements. Next, we apply the extended Newmark method to the symmetric form (2.47) also discretized by standard quadratic 20-noded elements. We also compute the response of the system with explicit RK-4 scheme for both PML-truncated, and an enlarged domain using quadratic spectral elements. The size of the considered enlarged domain model allows simulation for up to 15 s, before reflections travel back to the interior domain. Results for PML-truncated domain models, however, are computed for 30 s. The numerical experiments are summarized in Table 2.4.

Table 2.4: Test cases for comparing various formulations and their corresponding relative error.

Case	Equation	Time-stepping	Element type	error (center)	error (corner)
UnSym-1	(2.34)-2$^{\text{nd}}$ order	standard Newmark	Lagrangian 20-noded	1.73×10^{-5}	2.31×10^{-4}
UnSym-2	(2.35)-2$^{\text{nd}}$ order	standard Newmark	Lagrangian 20-noded	1.73×10^{-5}	2.31×10^{-4}
Symmetric	(2.47)-3$^{\text{rd}}$ order	extended Newmark	Lagrangian 20-noded	1.73×10^{-5}	2.31×10^{-4}
Explicit	(2.36)-1$^{\text{st}}$ order	RK-4	Spectral 27-noded	5.03×10^{-6}	1.80×10^{-5}
Enld. dom. (no PML)	1$^{\text{st}}$ order	RK-4	Spectral 27-noded		

The problem consists of a half-space with shear wave velocity $c_s = 1$ m/s, Poisson's ratio $\nu = 0.25$, and mass density $\rho = 1$ kg/m^3, which, after truncation, is reduced to a 1.2 m × 1.2 m × 0.2 m regular domain, and 0.8 m-thick PML is placed on the sides and at the bottom of the truncation boundaries, as shown in Fig. 2.22. A uniform pressure, of the form considered in [2] (with characteristic parameters $t_d = 10$ s, $\omega_f = 3$ rad/s), as shown in Fig. 2.23, is applied on the surface over a region (-1 m $\leq x, y \leq 1$ m). Quadratic elements of size 0.2 m are used for discretizing both the interior domain and the PML buffer (i.e., quadratic-quadratic pairs of approximation for displacement and stress components in the PML). We consider $\alpha_o = 10$, $\beta_o = 20\ s^{-1}$, and $m = 2$ for the PML parameters, and $\Delta t = 0.05$ s for temporal discretization.

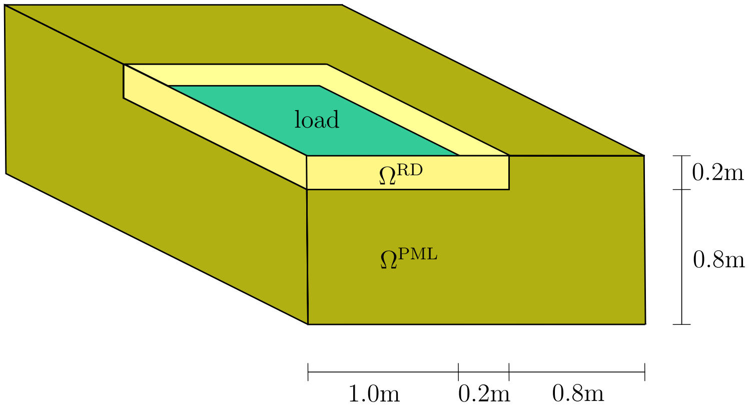

Figure 2.22: Quarter model of a PML-truncated semi-infinite homogeneous media.

Considering the enlarged domain solution as benchmark, we compute the maximum relative error given by (2.58) at the center and corner of the loading surface. These values are given in Table 2.4, and are very small, considering that PML was discretized only with four elements. The largest relative error is only 2.31×10^{-4}. The relative error for the cases using Newmark schemes are slightly greater than those using RK-4, as one would expect. The vertical component of

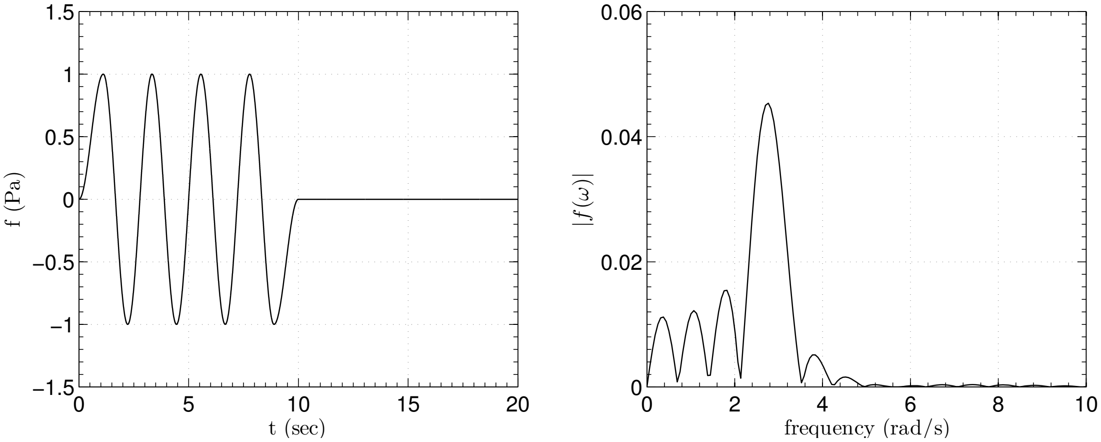

Figure 2.23: Surface load time history considered in Section 2.7.3 and its Fourier spectrum.

the displacement time history for the center and corner nodes is depicted in Fig. 2.24; the agreement is remarkable. Overall, all cases considered in Table 2.4 provide satisfactory results.

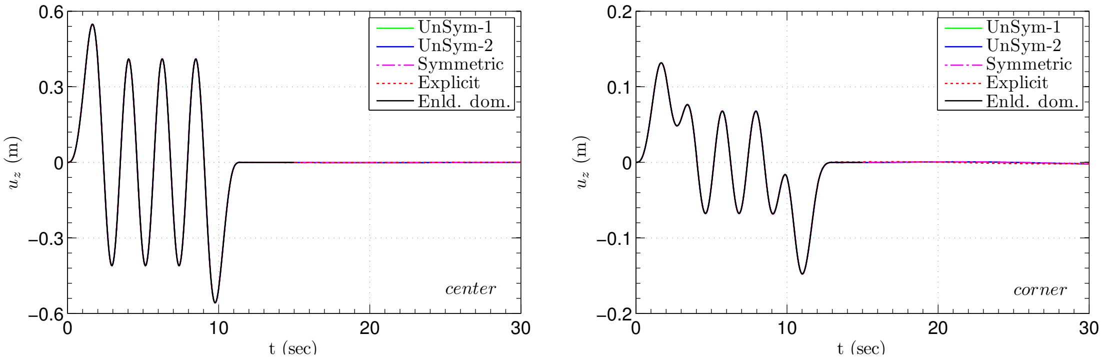

Figure 2.24: Comparison of displacement time histories for various cases considered in Table 2.4.

2.8 Summary

We presented various time-domain formulations for elastic wave propagation in arbitrarily heterogeneous PML-truncated media. The main contribution of this development over the earlier work [33] is the extension to three-dimensions of a hybrid formulation, endowed with explicit time integration and spectral elements. Our formulation is hybrid in the sense that it uses a displacement-stress formulation for the PML buffer, coupled with a standard displacement-only formulation for the interior domain, which results in optimal computational cost and allows for the ready incorporation of the PML in existing codes. Moreover, the mixed-field finite element scheme for the PML buffer does not require specialized elements for LBB-type stability.

The resulting semi-discrete form of the PML-truncated model is third-order-in-time. Several alternatives for time marching were discussed which may suit various applications. In particular, we discussed: (a) an explicit time stepping scheme utilizing the Runge-Kutta method; (b) time integration via the standard Newmark scheme by recasting the semi-discrete form into a second-order system; and (c) applying an extended Newmark scheme to a fully-symmetric, third-order-in-time, semi-discrete form. Numerical experiments demonstrate stability, efficacy, and satisfactory performance of the proposed schemes.

Chapter 3

The elastic inverse medium problem in three-dimensional PML-truncated domains

In this chapter, we address the inverse medium problem of finding the distributed elastic properties of an arbitrarily heterogeneous soil medium. To allow for this chapter to be self-contained, we discuss first the forward scheme we chose to use among those presented in the preceding chapter. Next, we discuss the mathematical and numerical aspects of the underlying inverse medium problem, where we derive the adjoint and control problems, and discuss strategies that invite robustness. We report on numerical experiments, using synthetic data, targeting the reconstruction of both smooth and sharp profiles. Lastly, we conclude with summary remarks.

3.1 The forward problem

Consider the forward problem first cast in (2.24)-(2.25). After integrating the equations once in time, there result:

$$\mathbf{div}\left\{\mu\left[\nabla\mathbf{u}+(\nabla\mathbf{u})^T\right]+\lambda(\operatorname{div}\mathbf{u})\mathfrak{I}\right\}+\mathbf{b}=\rho\ddot{\mathbf{u}} \qquad \text{in } \Omega^{\mathrm{RD}}\times\mathsf{J}, \tag{3.1a}$$

$$\mathbf{div}\left(\dot{\mathbf{S}}^T\Lambda_e+\mathbf{S}^T\Lambda_p+\bar{\mathbf{S}}^T\Lambda_w\right)=\rho\left(a\ddot{\mathbf{u}}+b\dot{\mathbf{u}}+c\mathbf{u}+d\bar{\mathbf{u}}\right) \qquad \text{in } \Omega^{\mathrm{PML}}\times\mathsf{J}, \tag{3.1b}$$

$$\begin{aligned}&a\ddot{\mathbf{S}}+b\dot{\mathbf{S}}+c\mathbf{S}+d\bar{\mathbf{S}}=\\&\mu\left[(\nabla\dot{\mathbf{u}})\Lambda_e+\Lambda_e(\nabla\dot{\mathbf{u}})^T+(\nabla\mathbf{u})\Lambda_p+\Lambda_p(\nabla\mathbf{u})^T+(\nabla\bar{\mathbf{u}})\Lambda_w+\Lambda_w(\nabla\bar{\mathbf{u}})^T\right]+\\&\lambda\left[\operatorname{div}(\Lambda_e\dot{\mathbf{u}})+\operatorname{div}(\Lambda_p\mathbf{u})+\operatorname{div}(\Lambda_w\bar{\mathbf{u}})\right]\mathfrak{I} \qquad \text{in } \Omega^{\mathrm{PML}}\times\mathsf{J}.\end{aligned} \tag{3.1c}$$

The system is initially at rest, and subject to the following boundary and interface conditions:

$$\left\{\mu\left[\nabla\mathbf{u}+(\nabla\mathbf{u})^T\right]+\lambda(\operatorname{div}\mathbf{u})\mathfrak{I}\right\}\mathbf{n}=\boldsymbol{g}_n \qquad \text{on } \Gamma_{\mathrm{N}}^{\mathrm{RD}}\times\mathsf{J}, \tag{3.2a}$$

$$(\dot{\mathbf{S}}^T\Lambda_e+\mathbf{S}^T\Lambda_p+\bar{\mathbf{S}}^T\Lambda_w)\mathbf{n}=\mathbf{0} \qquad \text{on } \Gamma_{\mathrm{N}}^{\mathrm{PML}}\times\mathsf{J}, \tag{3.2b}$$

$$\mathbf{u}=\mathbf{0} \qquad \text{on } \Gamma_{\mathrm{D}}^{\mathrm{PML}}\times\mathsf{J}, \tag{3.2c}$$

$$\mathbf{u}^{\mathrm{RD}}=\mathbf{u}^{\mathrm{PML}} \qquad \text{on } \Gamma^{\mathrm{I}}\times\mathsf{J}, \tag{3.2d}$$

$$\left\{\mu\left[\nabla\mathbf{u}+(\nabla\mathbf{u})^T\right]+\lambda(\operatorname{div}\mathbf{u})\mathfrak{I}\right\}\mathbf{n}=(\dot{\mathbf{S}}^T\Lambda_e+\mathbf{S}^T\Lambda_p+\bar{\mathbf{S}}^T\Lambda_w)\mathbf{n} \qquad \text{on } \Gamma^{\mathrm{I}}\times\mathsf{J}, \tag{3.2e}$$

where again, a bar ($\bar{\ }$) indicates history of the subtended variable[1].

Next, we seek a weak solution, corresponding to the strong form of (3.1) and (3.2), in the Galerkin sense, similarly to the steps followed in Section 2.3.1.

---

[1] For instance, $\bar{\mathbf{u}}(\mathbf{x},t)=\int_0^t\mathbf{u}(\mathbf{x},\tau)\,d\tau$.

Specifically, we take the inner products of (3.1a) and (3.1b) with (vector) test function $\tilde{\mathbf{w}}(\mathbf{x})$, and integrate by parts over their corresponding domains. Incorporating (3.2d-3.2e) eliminates the interface boundary terms and results in (3.3a). Next, we take the inner product of (3.1c) with (tensor) test function $\tilde{\mathbf{T}}(\mathbf{x})$; there results (3.3b). Accordingly, find $\mathbf{u} \in \mathbf{H}^1(\Omega) \times \mathsf{J}$, and $\mathbf{S} \in \mathcal{L}^2(\Omega) \times \mathsf{J}$, such that:

$$\int\limits_{\Omega^{\mathrm{RD}}} \nabla\tilde{\mathbf{w}} : \left\{\mu\left[\nabla\mathbf{u} + (\nabla\mathbf{u})^T\right] + \lambda(\operatorname{div}\mathbf{u})\mathcal{I}\right\}\,\mathrm{d}\Omega + \int\limits_{\Omega^{\mathrm{PML}}} \nabla\tilde{\mathbf{w}} : \left(\dot{\mathbf{S}}^T\Lambda_e + \mathbf{S}^T\Lambda_p + \bar{\mathbf{S}}^T\Lambda_w\right)\,\mathrm{d}\Omega$$
$$+ \int\limits_{\Omega^{\mathrm{RD}}} \tilde{\mathbf{w}}\cdot\rho\ddot{\mathbf{u}}\,\mathrm{d}\Omega + \int\limits_{\Omega^{\mathrm{PML}}} \tilde{\mathbf{w}}\cdot\rho\left(a\ddot{\mathbf{u}} + b\dot{\mathbf{u}} + c\mathbf{u} + d\bar{\mathbf{u}}\right)\,\mathrm{d}\Omega = \int\limits_{\Gamma^{\mathrm{RD}}_{\mathrm{N}}} \tilde{\mathbf{w}}\cdot\boldsymbol{g}_n\,\mathrm{d}\Gamma + \int\limits_{\Omega^{\mathrm{RD}}} \tilde{\mathbf{w}}\cdot\mathbf{b}\,\mathrm{d}\Omega, \tag{3.3a}$$

$$\int\limits_{\Omega^{\mathrm{PML}}} \tilde{\mathbf{T}} : \left(a\ddot{\mathbf{S}} + b\dot{\mathbf{S}} + c\mathbf{S} + d\bar{\mathbf{S}}\right)\,\mathrm{d}\Omega$$
$$= \int\limits_{\Omega^{\mathrm{PML}}} \tilde{\mathbf{T}} : \mu\left[(\nabla\dot{\mathbf{u}})\Lambda_e + \Lambda_e(\nabla\dot{\mathbf{u}})^T + (\nabla\mathbf{u})\Lambda_p + \Lambda_p(\nabla\mathbf{u})^T + (\nabla\bar{\mathbf{u}})\Lambda_w + \Lambda_w(\nabla\bar{\mathbf{u}})^T\right]$$
$$+ \tilde{\mathbf{T}} : \lambda\left[\operatorname{div}(\Lambda_e\dot{\mathbf{u}}) + \operatorname{div}(\Lambda_p\mathbf{u}) + \operatorname{div}(\Lambda_w\bar{\mathbf{u}})\right]\mathcal{I}\,\mathrm{d}\Omega, \tag{3.3b}$$

for every $\tilde{\mathbf{w}} \in \mathbf{H}^1(\Omega)$ and $\tilde{\mathbf{T}} \in \mathcal{L}^2(\Omega)$, where $\boldsymbol{g}_n \in \mathbf{L}^2(\Omega) \times \mathsf{J}$, and $\mathbf{b} \in \mathbf{L}^2(\Omega) \times \mathsf{J}$.

Then the following semi-discrete form results:

$$\mathbf{M}\ddot{\mathbf{d}}^{\mathrm{st}} + \mathbf{C}\dot{\mathbf{d}}^{\mathrm{st}} + \mathbf{K}\mathbf{d}^{\mathrm{st}} + \mathbf{G}\bar{\mathbf{d}}^{\mathrm{st}} = \mathbf{f}^{\mathrm{st}}, \tag{3.4a}$$
$$\bar{\mathbf{d}}^{\mathrm{st}} = \int_0^t \mathbf{d}^{\mathrm{st}}(\tau)|_{\mathrm{PML}}\,d\tau, \tag{3.4b}$$

where spatial and temporal dependencies are suppressed for brevity; $\mathbf{M}$, $\mathbf{C}$, $\mathbf{K}$, $\mathbf{G}$, are system matrices[2], $\mathbf{d}^{\text{st}} = (\mathbf{u}_h^T, \mathbf{S}_h^T)^T$ is the vector of nodal unknowns comprising displacements in $\bar{\Omega}^{\text{RD}} \cup \bar{\Omega}^{\text{PML}}$, and stress components only in $\bar{\Omega}^{\text{PML}}$, and $\mathbf{f}^{\text{st}}$ is the vector of applied forces. Equations (3.4) are identical to (2.32), which were derived following a different sequence of temporal operations. The superscript st is used here to designate the solution of the forward problem as the "state" solution, and contrast it with the solution of the adjoint problem, which is discussed in Section 3.2.1.2.

The matrix $\mathbf{M}$ has a block-diagonal structure, and can be diagonalized if one uses spectral elements, which then enables the explicit time integration of (3.4). In this regard, we express (3.4) as a first-order system

$$\frac{d}{dt}\begin{bmatrix} \mathbf{x}_0 \\ \mathbf{x}_1 \\ \mathbf{M}\mathbf{x}_2 \end{bmatrix} = \begin{bmatrix} \mathbf{0} & \mathbf{I} & \mathbf{0} \\ \mathbf{0} & \mathbf{0} & \mathbf{I} \\ -\mathbf{G} & -\mathbf{K} & -\mathbf{C} \end{bmatrix} \begin{bmatrix} \mathbf{x}_0 \\ \mathbf{x}_1 \\ \mathbf{x}_2 \end{bmatrix} + \begin{bmatrix} \mathbf{0} \\ \mathbf{0} \\ \mathbf{f}^{\text{st}} \end{bmatrix}, \tag{3.5}$$

where $\mathbf{x}_0 = \bar{\mathbf{d}}^{\text{st}}$, $\mathbf{x}_1 = \mathbf{d}^{\text{st}}$, and $\mathbf{x}_2 = \dot{\mathbf{d}}^{\text{st}}$. We then use an explicit fourth-order Runge-Kutta (RK-4) method for integrating (3.5) in time.

3.2 The inverse medium problem

Our goal is to find the distribution of the Lamé parameters $\lambda(\mathbf{x})$ and $\mu(\mathbf{x})$ within the elastic soil medium. We consider the sources, and the response recorded at receivers on the ground surface, as known. The inverse medium problem can thus be formulated as the minimization of the difference (or misfit) between the measured

---

[2] The definition of $\mathbf{M}$, $\mathbf{C}$, $\mathbf{K}$, and $\mathbf{G}$ are given in (2.31).

response at receiver locations, and a computed response corresponding to a trial distribution of the material parameters. The misfit minimization should honor the physics of the problem, as described by the forward problem of the preceding section. Mathematically, the inverse medium problem can be cast as a PDE-constrained optimization problem:

$$\min_{\lambda,\mu} \mathcal{J}(\lambda,\mu) := \frac{1}{2}\sum_{j=1}^{N_r}\int_0^T \int_{\Gamma_m} (\mathbf{u}-\mathbf{u}_m)\cdot(\mathbf{u}-\mathbf{u}_m)\ \delta(\mathbf{x}-\mathbf{x}_j)\,\mathrm{d}\Gamma\ dt + \mathcal{R}(\lambda,\mu), \quad (3.6)$$

where the minimization is constrained by the forward initial and boundary value problem (PDE-constrained). In (3.6), $\mathbf{u}$ is the solution of the forward problem governed by the initial- and boundary-value problem (3.1), (3.2), $\mathcal{J}$ is the objective functional[3], N_r denotes the total number of receivers, T is the total observation time, Γ_m is the part of the ground surface where the receiver response, $\mathbf{u}_m$, has been recorded, $\delta(\mathbf{x}-\mathbf{x}_j)$ is the Dirac delta function, which enables measurements at receiver locations $\mathbf{x}_j$, and $\mathcal{R}(\lambda,\mu)$ is the regularization term, which is discussed below.

Inverse problems suffer from solution multiplicity, which, in general, is due to the presence of insufficient data. This makes the problem ill-posed in the Hadamard sense. Regularization of the solution by using the Tikhonov (TN) [84], or, the Total Variation (TV) [85] scheme are among common strategies to alleviate ill-posedness.

---

[3] We use $\mathbf{J}$ to indicate the corresponding discrete objective functional. See [82, 83] for other possibilities.

The Tikhonov regularization, denoted by $\mathcal{R}^{TN}(\lambda, \mu)$, penalizes large material gradients and, thus, precludes spatially rapid material variations from becoming solutions to the inverse medium problem. It is defined as:

$$\mathcal{R}^{TN}(\lambda, \mu) = \frac{R_\lambda}{2} \int\limits_{\Omega^{\mathrm{RD}}} \nabla\lambda \cdot \nabla\lambda \, \mathrm{d}\Omega + \frac{R_\mu}{2} \int\limits_{\Omega^{\mathrm{RD}}} \nabla\mu \cdot \nabla\mu \, \mathrm{d}\Omega, \tag{3.7}$$

where R_λ and R_μ are the so-called λ- and μ-regularization factor, respectively, and control the amount of penalty imposed via (3.7) on the gradients of λ and μ. By construction, TN regularization results in material reconstructions with smooth variations. Consequently, sharp interfaces may not be captured well when using the TN scheme. The TV regularization, however, works better for imaging profiles involving sharp interfaces, as it typically preserves edges. It is defined as:

$$\mathcal{R}^{TV}(\lambda, \mu) = \frac{R_\lambda}{2} \int\limits_{\Omega^{\mathrm{RD}}} (\nabla\lambda \cdot \nabla\lambda + \epsilon)^{\frac{1}{2}} \, \mathrm{d}\Omega + \frac{R_\mu}{2} \int\limits_{\Omega^{\mathrm{RD}}} (\nabla\mu \cdot \nabla\mu + \epsilon)^{\frac{1}{2}} \, \mathrm{d}\Omega, \tag{3.8}$$

where the parameter ϵ makes $\mathcal{R}^{TV}$ differentiable when either $\nabla\lambda \cdot \nabla\lambda = 0$, or, $\nabla\mu \cdot \nabla\mu = 0$.

For computing the first-order optimality conditions for (3.6), we use the (formal) Lagrangian approach [86] to impose the PDE constraint in its weak form. These are necessary conditions that must be satisfied at a stationary point of (3.6). Specifically, we introduce Lagrange multiplier vector function $\mathbf{w} \in \mathbf{H}^1(\Omega)$, and Lagrange multiplier tensor function $\mathbf{T} \in \mathcal{L}^2(\Omega)$ to enforce the initial- and boundary-value problem (3.1), (3.2), which admits the weak form (3.3). The Lagrangian functional becomes

$$
\begin{aligned}
\mathcal{L}(\mathbf{u},\mathbf{S},\mathbf{w},\mathbf{T},\lambda,\mu) &= \frac{1}{2}\sum_{j=1}^{N_r}\int_0^T\int_{\Gamma_m}(\mathbf{u}-\mathbf{u}_m)\cdot(\mathbf{u}-\mathbf{u}_m)\,\delta(\mathbf{x}-\mathbf{x}_j)\,\mathrm{d}\Gamma\;dt+\mathcal{R}(\lambda,\mu)\\
&-\int_0^T\int\limits_{\Omega^{\mathrm{RD}}}\nabla\mathbf{w}:\left\{\mu\left[\nabla\mathbf{u}+(\nabla\mathbf{u})^T\right]+\lambda(\operatorname{div}\mathbf{u})\mathcal{I}\right\}\,\mathrm{d}\Omega\;dt\\
&-\int_0^T\int\limits_{\Omega^{\mathrm{PML}}}\nabla\mathbf{w}:\left(\dot{\mathbf{S}}^T\Lambda_e+\mathbf{S}^T\Lambda_p+\bar{\mathbf{S}}^T\Lambda_w\right)\,\mathrm{d}\Omega\;dt-\int_0^T\int\limits_{\Omega^{\mathrm{RD}}}\mathbf{w}\cdot\rho\ddot{\mathbf{u}}\,\mathrm{d}\Omega\;dt\\
&-\int_0^T\int\limits_{\Omega^{\mathrm{PML}}}\mathbf{w}\cdot\rho\,(a\ddot{\mathbf{u}}+b\dot{\mathbf{u}}+c\mathbf{u}+d\bar{\mathbf{u}})\,\mathrm{d}\Omega\;dt+\int_0^T\int\limits_{\Gamma_{\mathrm{N}}^{\mathrm{RD}}}\mathbf{w}\cdot\boldsymbol{g}_n\,\mathrm{d}\Gamma\;dt\\
&+\int_0^T\int\limits_{\Omega^{\mathrm{RD}}}\mathbf{w}\cdot\mathbf{b}\,\mathrm{d}\Omega\;dt-\int_0^T\int\limits_{\Omega^{\mathrm{PML}}}\mathbf{T}:\left(a\ddot{\mathbf{S}}+b\dot{\mathbf{S}}+c\mathbf{S}+d\bar{\mathbf{S}}\right)\,\mathrm{d}\Omega\;dt\\
&+\int_0^T\int\limits_{\Omega^{\mathrm{PML}}}\mathbf{T}:\mu\Big((\nabla\dot{\mathbf{u}})\Lambda_e+\Lambda_e(\nabla\dot{\mathbf{u}})^T+(\nabla\mathbf{u})\Lambda_p+\Lambda_p(\nabla\mathbf{u})^T+(\nabla\bar{\mathbf{u}})\Lambda_w\\
&+\Lambda_w(\nabla\bar{\mathbf{u}})^T\Big)+\mathbf{T}:\lambda\left[\operatorname{div}(\Lambda_e\dot{\mathbf{u}})+\operatorname{div}(\Lambda_p\mathbf{u})+\operatorname{div}(\Lambda_w\bar{\mathbf{u}})\right]\mathcal{I}\,\mathrm{d}\Omega\;dt, \qquad (3.9)
\end{aligned}
$$

where now $\mathbf{u}$, $\mathbf{S}$, λ, and μ are treated as independent variables.

3.2.1 Optimality system

We use the Lagrangian functional (3.9) as a tool to compute the optimality system for (3.6). To this end, the Gâteaux derivative[4] (or first variation) of the Lagrangian functional with respect to all variables must vanish. This process is

---

[4] See Appendix C for the definition and notation.

discussed next.

3.2.1.1 The state problem

Taking the derivatives of the Lagrangian functional $\mathcal{L}$ with respect to $\mathbf{w}$ and $\mathbf{T}$ in directions $\tilde{\mathbf{w}} \in \mathbf{H}^1(\Omega)$ and $\tilde{\mathbf{T}} \in \mathcal{L}^2(\Omega)$, and setting it to zero, results in the state problem, which is identical to (3.3). That is

$$\mathcal{L}'(\mathbf{u}, \mathbf{S}, \mathbf{w}, \mathbf{T}, \lambda, \mu)(\tilde{\mathbf{w}}, \tilde{\mathbf{T}}) = 0. \tag{3.10}$$

3.2.1.2 The adjoint problem

We now take the derivative of $\mathcal{L}$ with respect to $\mathbf{u}$ and $\mathbf{S}$ in directions $\tilde{\mathbf{u}} \in \mathbf{H}^1(\Omega)$ and $\tilde{\mathbf{S}} \in \mathcal{L}^2(\Omega)$. This yields

$$
\begin{aligned}
\mathcal{L}'(\mathbf{u},&\mathbf{S},\mathbf{w},\mathbf{T},\lambda,\mu)(\tilde{\mathbf{u}},\tilde{\mathbf{S}}) = \sum_{j=1}^{N_r}\int_0^T \int_{\Gamma_m} \tilde{\mathbf{u}}\cdot(\mathbf{u}-\mathbf{u}_m)\ \delta(\mathbf{x}-\mathbf{x}_j)\,\mathrm{d}\Gamma\ dt \\
&- \int_0^T \int\limits_{\Omega^{\mathrm{RD}}} \nabla\mathbf{w} : \left\{\mu\left[\nabla\tilde{\mathbf{u}} + (\nabla\tilde{\mathbf{u}})^T\right] + \lambda(\operatorname{div}\tilde{\mathbf{u}})\mathcal{I}\right\}\ \mathrm{d}\Omega\ dt \\
&- \int_0^T \int\limits_{\Omega^{\mathrm{PML}}} \nabla\mathbf{w} : \left(\dot{\tilde{\mathbf{S}}}^T\Lambda_e + \tilde{\mathbf{S}}^T\Lambda_p + \bar{\tilde{\mathbf{S}}}^T\Lambda_w\right)\ \mathrm{d}\Omega\ dt - \int_0^T \int\limits_{\Omega^{\mathrm{RD}}} \mathbf{w}\cdot\rho\ddot{\tilde{\mathbf{u}}}\,\mathrm{d}\Omega\ dt \\
&- \int_0^T \int\limits_{\Omega^{\mathrm{PML}}} \mathbf{w}\cdot\rho\left(a\ddot{\tilde{\mathbf{u}}} + b\dot{\tilde{\mathbf{u}}} + c\tilde{\mathbf{u}} + d\bar{\tilde{\mathbf{u}}}\right)\ \mathrm{d}\Omega\ dt \\
&- \int_0^T \int\limits_{\Omega^{\mathrm{PML}}} \mathbf{T} : \left(a\ddot{\tilde{\mathbf{S}}} + b\dot{\tilde{\mathbf{S}}} + c\tilde{\mathbf{S}} + d\bar{\tilde{\mathbf{S}}}\right)\ \mathrm{d}\Omega\ dt \\
&+ \int_0^T \int\limits_{\Omega^{\mathrm{PML}}} \mathbf{T} : \mu\Big((\nabla\dot{\tilde{\mathbf{u}}})\Lambda_e + \Lambda_e(\nabla\dot{\tilde{\mathbf{u}}})^T + (\nabla\tilde{\mathbf{u}})\Lambda_p + \Lambda_p(\nabla\tilde{\mathbf{u}})^T + (\nabla\bar{\tilde{\mathbf{u}}})\Lambda_w \\
&+ \Lambda_w(\nabla\bar{\tilde{\mathbf{u}}})^T\Big) + \mathbf{T} : \lambda\left[\operatorname{div}(\Lambda_e\dot{\tilde{\mathbf{u}}}) + \operatorname{div}(\Lambda_p\tilde{\mathbf{u}}) + \operatorname{div}(\Lambda_w\bar{\tilde{\mathbf{u}}})\right]\mathcal{I}\,\mathrm{d}\Omega\ dt.
\end{aligned}
\tag{3.11}
$$

Setting the above derivative to zero, and performing integration by parts in time, results in the statement of the weak form of the adjoint problem. That is, find $\mathbf{w} \in \mathbf{H}^1(\Omega)\times \mathsf{J}$, and $\mathbf{T} \in \mathcal{L}^2(\Omega)\times \mathsf{J}$, such that:

$$
\begin{aligned}
&\int\limits_{\Omega^{\mathrm{RD}}} \nabla\tilde{\mathbf{u}} : \left\{\mu\left[\nabla\mathbf{w} + (\nabla\mathbf{w})^T\right] + \lambda(\operatorname{div}\mathbf{w})\mathcal{I}\right\}\,\mathrm{d}\Omega + \\
&+ \int\limits_{\Omega^{\mathrm{RD}}} \tilde{\mathbf{u}}\cdot\rho\ddot{\mathbf{w}}\,\mathrm{d}\Omega + \int\limits_{\Omega^{\mathrm{PML}}} \tilde{\mathbf{u}}\cdot\rho\left(a\ddot{\mathbf{w}} - b\dot{\mathbf{w}} + c\mathbf{w} - d\bar{\mathbf{w}}\right)\,\mathrm{d}\Omega \\
&- \int\limits_{\Omega^{\mathrm{PML}}} \nabla\tilde{\mathbf{u}} : \mu\left[-\dot{\mathbf{T}}\Lambda_e - \dot{\mathbf{T}}^T\Lambda_e + \mathbf{T}\Lambda_p + \mathbf{T}^T\Lambda_p - \bar{\mathbf{T}}\Lambda_w - \bar{\mathbf{T}}^T\Lambda_w\right] \\
&+ \lambda\left[-\dot{\mathbf{T}} : \operatorname{div}(\Lambda_e\tilde{\mathbf{u}}) + \mathbf{T} : \operatorname{div}(\Lambda_p\tilde{\mathbf{u}}) - \bar{\mathbf{T}} : \operatorname{div}(\Lambda_w\tilde{\mathbf{u}})\right]\mathcal{I}\,\mathrm{d}\Omega \\
&= \sum_{j=1}^{N_r} \int_{\Gamma_m} \tilde{\mathbf{u}}\cdot(\mathbf{u} - \mathbf{u}_m)\;\delta(\mathbf{x} - \mathbf{x}_j)\,\mathrm{d}\Gamma, \qquad (3.12a)
\end{aligned}
$$

$$
\int\limits_{\Omega^{\mathrm{PML}}} \nabla\dot{\mathbf{w}} : \tilde{\mathbf{S}}^T\Lambda_e - \nabla\mathbf{w} : \tilde{\mathbf{S}}^T\Lambda_p + \nabla\bar{\mathbf{w}} : \tilde{\mathbf{S}}^T\Lambda_w\,\mathrm{d}\Omega = \int\limits_{\Omega^{\mathrm{PML}}} \tilde{\mathbf{S}} : \left(a\ddot{\mathbf{T}} - b\dot{\mathbf{T}} + c\mathbf{S} - d\bar{\mathbf{T}}\right)\,\mathrm{d}\Omega \tag{3.12b}
$$

for every $\tilde{\mathbf{u}} \in \mathbf{H}^1(\Omega)$ and $\tilde{\mathbf{S}} \in \mathcal{L}^2(\Omega)$, where $\mathbf{w}(\mathbf{x}, T) = \mathbf{0}$, and $\mathbf{T}(\mathbf{x}, T) = \mathbf{0}$.

We remark that the adjoint problem (3.12) is a final-value problem and, thus, is solved backwards in time[5]; it is driven by the misfit between a computed response, and the measured response at receiver locations. Moreover, the operators implicated in the adjoint problem are very similar to those of the state problem: they involve transposition of the system matrices, and sign reversal for terms involving history, and first-order time derivatives. In this regard, we obtain the following semi-discrete form for the adjoint problem:

---

[5] See [87] for other possibilities, and [88–90] for alternative approaches.

$$\mathbf{M}\ddot{\mathbf{d}}^{\mathrm{adj}} - \mathbf{C}^T\dot{\mathbf{d}}^{\mathrm{adj}} + \mathbf{K}^T\mathbf{d}^{\mathrm{adj}} - \mathbf{G}^T\bar{\mathbf{d}}^{\mathrm{adj}} = \mathbf{f}^{\mathrm{adj}}, \tag{3.13a}$$

$$\bar{\mathbf{d}}^{\mathrm{adj}} = \int_0^t \mathbf{d}^{\mathrm{adj}}(\tau)|_{\mathrm{PML}}\, d\tau, \tag{3.13b}$$

where superscript "adj" refers to the adjoint problem, $\mathbf{d}^{\mathrm{adj}} = (\mathbf{w}_h^T, \mathbf{T}_h^T)^T$ is the vector of nodal unknowns comprising discrete values of $\mathbf{w}$ in $\bar{\Omega}^{\mathrm{RD}} \cup \bar{\Omega}^{\mathrm{PML}}$ and discrete values of $\mathbf{T}$ only in $\bar{\Omega}^{\mathrm{PML}}$, and $\mathbf{f}^{\mathrm{adj}}$ is a vector comprising the misfit at receiver locations. Moreover, system matrices $\mathbf{M}$, $\mathbf{C}$, $\mathbf{K}$, $\mathbf{G}$, are identical to those of the forward problem and, thus, with minor adjustments, an implementation of the forward problem can also be used for the solution of the adjoint problem.

The matrix $\mathbf{M}$ in (3.13) can be diagonalized by using spectral elements, similar to what we did in (3.5). We rewrite (3.13) as a first-order system

$$\frac{d}{dt}\begin{bmatrix}\mathbf{y}_0\\ \mathbf{y}_1\\ \mathbf{M}\mathbf{y}_2\end{bmatrix} = \begin{bmatrix}\mathbf{0} & \mathbf{I} & \mathbf{0}\\ \mathbf{0} & \mathbf{0} & \mathbf{I}\\ \mathbf{G}^T & -\mathbf{K}^T & \mathbf{C}^T\end{bmatrix}\begin{bmatrix}\mathbf{y}_0\\ \mathbf{y}_1\\ \mathbf{y}_2\end{bmatrix} + \begin{bmatrix}\mathbf{0}\\ \mathbf{0}\\ \mathbf{f}^{\mathrm{adj}}\end{bmatrix}, \tag{3.14}$$

where $\mathbf{y}_0 = \bar{\mathbf{d}}^{\mathrm{adj}}$, $\mathbf{y}_1 = \mathbf{d}^{\mathrm{adj}}$, $\mathbf{y}_2 = \dot{\mathbf{d}}^{\mathrm{adj}}$, with final values $\mathbf{y}_0(T) = \mathbf{0}$, $\mathbf{y}_1(T) = \mathbf{0}$, and $\mathbf{y}_2(T) = \mathbf{0}$. We use an explicit RK-4 method to integrate (3.14) in time. The scheme is outlined in Appendix B.3.

3.2.1.3 The control problems

Lastly, we take the derivative of $\mathcal{L}$ with respect to λ and μ in directions $\tilde{\lambda}$ and $\tilde{\mu}$, which yields the reduced gradients with respect to λ and μ, respectively. We restrict the reduced gradients to Ω^{RD} (the material properties at the interfaces Γ^{I} are extended into the PML buffer). For the TN regularization, this yields

$$\mathcal{L}'(\mathbf{u},\mathbf{S},\mathbf{w},\mathbf{T},\lambda,\mu)(\tilde{\lambda}) = R_\lambda \int\limits_{\Omega^{\mathrm{RD}}} \nabla\tilde{\lambda}\cdot\nabla\lambda \,\mathrm{d}\Omega - \int_0^T \int\limits_{\Omega^{\mathrm{RD}}} \tilde{\lambda}\ \nabla\mathbf{w} :(\operatorname{div}\mathbf{u})\mathcal{I}\,\mathrm{d}\Omega\ dt, \tag{3.15a}$$

$$\mathcal{L}'(\mathbf{u},\mathbf{S},\mathbf{w},\mathbf{T},\lambda,\mu)(\tilde{\mu}) = R_\mu \int\limits_{\Omega^{\mathrm{RD}}} \nabla\tilde{\mu}\cdot\nabla\mu \,\mathrm{d}\Omega - \int_0^T \int\limits_{\Omega^{\mathrm{RD}}} \tilde{\mu}\ \nabla\mathbf{u} : \left[\nabla\mathbf{w} + (\nabla\mathbf{w})^T\right]\ \mathrm{d}\Omega\ dt. \tag{3.15b}$$

Setting the above derivatives to zero, results in the control problems. Similarly, for the TV regularization, the control problems read

$$\mathcal{L}'(\mathbf{u},\mathbf{S},\mathbf{w},\mathbf{T},\lambda,\mu)(\tilde{\lambda}) = R_\lambda \int\limits_{\Omega^{\mathrm{RD}}} \frac{\nabla\tilde{\lambda}\cdot\nabla\lambda}{(\nabla\lambda\cdot\nabla\lambda+\epsilon)^{\frac{1}{2}}}\,\mathrm{d}\Omega - \int_0^T \int\limits_{\Omega^{\mathrm{RD}}} \tilde{\lambda}\ \nabla\mathbf{w} :(\operatorname{div}\mathbf{u})\mathcal{I}\,\mathrm{d}\Omega\ dt, \tag{3.16a}$$

$$\begin{aligned}\mathcal{L}'(\mathbf{u},\mathbf{S},\mathbf{w},\mathbf{T},\lambda,\mu)(\tilde{\mu}) = R_\mu &\int\limits_{\Omega^{\mathrm{RD}}} \frac{\nabla\tilde{\mu}\cdot\nabla\mu}{(\nabla\mu\cdot\nabla\mu+\epsilon)^{\frac{1}{2}}}\,\mathrm{d}\Omega \\ &- \int_0^T \int\limits_{\Omega^{\mathrm{RD}}} \tilde{\mu}\ \nabla\mathbf{u} : \left[\nabla\mathbf{w} + (\nabla\mathbf{w})^T\right]\ \mathrm{d}\Omega\ dt.\end{aligned} \tag{3.16b}$$

Discretization of either (3.15) or (3.16) result in the following form

$$\tilde{\mathbf{M}}\mathbf{g}^\lambda = R_\lambda\ \mathbf{g}^\lambda_{\mathrm{reg}} + \mathbf{g}^\lambda_{\mathrm{mis}}, \tag{3.17a}$$

$$\tilde{\mathbf{M}}\mathbf{g}^\mu = R_\mu\ \mathbf{g}^\mu_{\mathrm{reg}} + \mathbf{g}^\mu_{\mathrm{mis}}, \tag{3.17b}$$

where $\tilde{\mathbf{M}}$ is a mass-like matrix, $\mathbf{g}^\lambda$ and $\mathbf{g}^\mu$ is the vector of discrete values of the (reduced) gradient for λ and μ, respectively, and $\mathbf{g}^\lambda_{\text{reg}}$, $\mathbf{g}^\mu_{\text{reg}}$ and $\mathbf{g}^\lambda_{\text{mis}}$, $\mathbf{g}^\mu_{\text{mis}}$ are the associated vectors corresponding to the regularization-part and misfit-part of $\mathbf{g}^\lambda$ and $\mathbf{g}^\mu$. We refer to Appendix A.4 for matrix and vector definitions, and discretization details.

3.2.2 The inversion process

A solution of (3.6) requires simultaneous satisfaction of the state problem (3.5), the adjoint problem (3.14), and the control problems (3.17). This approach –a full-space method– is, in principle, possible [91]; however, the associated computational cost can be substantial. Alternatively, a reduced-space method may be adopted, in which, discrete material properties are updated iteratively, using a gradient-based minimization scheme. The latter approach is employed here, and is discussed next.

We start with an assumed initial spatial distribution of the control parameters (λ and μ), and solve the state problem (3.5) to obtain $\mathbf{d}^{\text{st}} = (\mathbf{u}_h^T, \mathbf{S}_h^T)^T$. With the misfit known, we solve the adjoint problem (3.14) and obtain $\mathbf{d}^{\text{adj}} = (\mathbf{w}_h^T, \mathbf{T}_h^T)^T$. With $\mathbf{u}_h$ and $\mathbf{w}_h$ known, the (reduced) material gradients $\mathbf{g}^\lambda$ and $\mathbf{g}^\mu$, can be computed from (3.17). Thus, the vector of material values, at iteration $k+1$, can be computed by using a search direction via

$$\boldsymbol{\lambda}_{k+1} = \boldsymbol{\lambda}_k + \alpha_k^\lambda \; \boldsymbol{s}_k^\lambda, \tag{3.18a}$$

$$\boldsymbol{\mu}_{k+1} = \boldsymbol{\mu}_k + \alpha_k^\mu \; \boldsymbol{s}_k^\mu, \tag{3.18b}$$

where $\boldsymbol{\lambda}$ and $\boldsymbol{\mu}$ comprise the vector of discrete values for λ and μ, respectively, α_k^λ, α_k^μ are step lengths, and $\boldsymbol{s}_k^\lambda$, $\boldsymbol{s}_k^\mu$ are the search directions for $\boldsymbol{\lambda}_k$ and $\boldsymbol{\mu}_k$. Herein, we use the L-BFGS method to compute the search directions [92][6]. Moreover, to ensure sufficient decrease of the objective functional at each inversion iteration, we employ an Armijo backtracking line search [92], which is outlined in Algorithm 1. The inversion process discussed thus far is summarized in Algorithm 2.

Algorithm 1 Backtracking line search.

```
Choose $\alpha^\lambda$, $\alpha^\mu$, $c_1$, $\rho$        ▷ e.g., $\alpha^\lambda = 1$, $\alpha^\mu = 1$, $c_1 = 10^{-4}$, $\rho = 0.5$
while $\mathbf{J}(\boldsymbol{\lambda}_k + \alpha^\lambda \; \boldsymbol{s}_k^\lambda, \boldsymbol{\mu}_k + \alpha^\mu \; \boldsymbol{s}_k^\mu) \geq \mathbf{J}(\boldsymbol{\lambda}_k, \boldsymbol{\mu}_k) + c_1(\alpha^\lambda \; \mathbf{g}_k^\lambda \cdot \boldsymbol{s}_k^\lambda + \alpha^\mu \; \mathbf{g}_k^\mu \cdot \boldsymbol{s}_k^\mu)$ do
    $\alpha^\lambda \leftarrow \rho\alpha^\lambda$
    $\alpha^\mu \leftarrow \rho\alpha^\mu$
end while
Terminate with $\alpha_k^\lambda = \alpha^\lambda$, $\alpha_k^\mu = \alpha^\mu$
```

We remark that for the reduced-space method, either (3.15) or (3.16) can also be expressed as

$$\mathcal{L}'(\mathbf{u}, \mathbf{S}, \mathbf{w}, \mathbf{T}, \lambda, \mu)(\tilde{\lambda}) = \mathscr{J}'(\lambda, \mu)(\tilde{\lambda}), \tag{3.19a}$$

$$\mathcal{L}'(\mathbf{u}, \mathbf{S}, \mathbf{w}, \mathbf{T}, \lambda, \mu)(\tilde{\mu}) = \mathscr{J}'(\lambda, \mu)(\tilde{\mu}), \tag{3.19b}$$

---

[6] In the numerical experiments that we perform, we store $m = 15$ L-BFGS vectors.

Algorithm 2 Inversion for Lamé parameters.

```
$k \leftarrow 0$
Set initial guess for material property vectors $\boldsymbol{\lambda}_k$, $\boldsymbol{\mu}_k$
Compute $\mathbf{J}(\boldsymbol{\lambda}_k, \boldsymbol{\mu}_k)$                                  ▷ Eq. (3.6)
Set convergence tolerance $tol$
while $\{\mathbf{J}(\boldsymbol{\lambda}_k, \boldsymbol{\mu}_k) > tol\}$ do
    Solve the state problem for $\mathbf{d}^{\mathrm{st}} = (\mathbf{u}_h^T, \mathbf{S}_h^T)^T$              ▷ Eq. (3.5)
    Solve the adjoint problem for $\mathbf{d}^{\mathrm{adj}} = (\mathbf{w}_h^T, \mathbf{T}_h^T)^T$          ▷ Eq. (3.14)
    Evaluate the discrete reduced gradients $\mathbf{g}_k^{\lambda}$, $\mathbf{g}_k^{\mu}$               ▷ Eqs. (3.17)
    Compute search directions $\boldsymbol{s}_k^{\lambda}$, $\boldsymbol{s}_k^{\mu}$                     ▷ L-BFGS
    Choose step lengths $\alpha_k^{\lambda}$, $\alpha_k^{\mu}$                                ▷ Algorithm 1
    Update material property vectors $\boldsymbol{\lambda}_k$, $\boldsymbol{\mu}_k$                  ▷ Eq. (3.18)
    $k \leftarrow k + 1$
end while
```

where the equality in (3.19) is due to the satisfaction of the state problem. Therefore, the reduced gradients in (3.17), are, indeed, the gradients of the objective functional with respect to λ and μ.

3.2.3 Buttressing schemes

Inverse medium problems are notoriously ill-posed. They suffer from solution multiplicity; that is, material profiles that are very different from each other, and, potentially non-physical, can become solutions to the misfit minimization problem. Regularization of the control parameters alleviates the ill-posedness; however, this alone, may not be adequate when dealing with large-scale complex problems. In this part, we discuss additional strategies that further assist the inversion process, outlined in Algorithm 2, in imaging complex profiles.

3.2.3.1 Regularization factor selection and continuation

Computation of the (reduced) gradients (3.17) necessitates selection of the regularization factors R_λ and R_μ. A common strategy is to use Morozov's discrepancy principle [93], where a constant value for the regularization factor is used throughout the inversion process. Here, we discuss a simple and practical approach that was initially developed for acoustic inversion [56], and, later, was successfully applied to problems involving elastic inversion [57].

We start by rewriting the discrete control problem (3.17), either for λ or μ, in the following generic form

$$\tilde{\mathbf{M}}\mathbf{g} = R\ \mathbf{g}_{\text{reg}} + \mathbf{g}_{\text{mis}}, \tag{3.20}$$

where $\mathbf{g}$ refers to the vector of discrete values of the (reduced) gradient, either for λ or μ, $\mathbf{g}_{\text{reg}}$ and $\mathbf{g}_{\text{mis}}$ are the associated vectors corresponding to the regularization-part and misfit-part of $\mathbf{g}$, and R is the regularization factor yet to be determined. The main idea is that the "size" of $R\ \mathbf{g}_{\text{reg}}$ should be proportional to that of $\mathbf{g}_{\text{mis}}$ at each inversion iteration. We define the following unit vectors for the two components of the gradient vector

$$\mathbf{n}_{\text{reg}} = \frac{\mathbf{g}_{\text{reg}}}{\|\mathbf{g}_{\text{reg}}\|}, \qquad \mathbf{n}_{\text{mis}} = \frac{\mathbf{g}_{\text{mis}}}{\|\mathbf{g}_{\text{mis}}\|}, \tag{3.21}$$

where $\|\cdot\|$ denotes the Euclidean norm. Equation (3.20) can then be written as

$$
\begin{aligned}
\tilde{\mathbf{M}}\mathbf{g} &= R\,\|\mathbf{g}_{\text{reg}}\|\;\mathbf{n}_{\text{reg}} + \|\mathbf{g}_{\text{mis}}\|\;\mathbf{n}_{\text{mis}} && \text{(3.22a)}\\
&= \|\mathbf{g}_{\text{mis}}\|\;\left(R\,\frac{\|\mathbf{g}_{\text{reg}}\|}{\|\mathbf{g}_{\text{mis}}\|}\;\mathbf{n}_{\text{reg}} + \mathbf{n}_{\text{mis}}\right)\\
&= \|\mathbf{g}_{\text{mis}}\|\;\Big(\wp\;\mathbf{n}_{\text{reg}} + \mathbf{n}_{\text{mis}}\Big), && \text{(3.22b)}
\end{aligned}
$$

where,

$$
\wp = R\,\frac{\|\mathbf{g}_{\text{reg}}\|}{\|\mathbf{g}_{\text{mis}}\|}. \tag{3.22c}
$$

In (3.22b), for the "size" of $\wp\;\mathbf{n}_{\text{reg}}$ to be proportional to $\mathbf{n}_{\text{mis}}$ throughout the entire inversion process, one may choose $0 < \wp \leq 1$. Once a value for $\wp$ has been decided, R can be computed via

$$
R = \wp\,\frac{\|\mathbf{g}_{\text{mis}}\|}{\|\mathbf{g}_{\text{reg}}\|}, \tag{3.23}
$$

where $\wp$ can take large values (e.g., 0.5) at early stages of the inversion process and, thus, narrow down the initial search space. As the inversion evolves, $\wp$ can be continuously reduced (e.g., down to 0.3) to allow for profile refinement.

3.2.3.2 Source-frequency continuation

Using loading sources with low-frequency content result in an overall image of the medium that lacks fine features. To allow for more details, and fine-tune the profile, one needs to probe with higher frequency content. Thus, the inversion process can be initiated with a signal having a low-frequency content and, then, the frequency range can be increased progressively as inversion evolves. This can be achieved by using a set of probing signals, ordered such that each signal has a broader range of frequencies than the previous ones. The inversion process then begins with using the first signal. Upon convergence, the profile is used as a starting point for the second signal, and the process is repeated for all signals.

3.2.3.3 Biased search direction for λ

Simultaneous inversion for both λ and μ is remarkably challenging [61]. As we demonstrate in Section 3.3.2, the objective functional (3.6) is more sensitive to μ, than to λ. Consequently, as the inversion evolves, the μ-profile converges faster than that of λ. In [57], a biasing scheme was proposed to accelerate the convergence of the λ-profile, such that, at the early stages of inversion, the search direction for λ is biased according to that of μ.

The main idea is that due to physical considerations, the λ-profile should be, more or less, similar to the μ-profile. Hence, during the early inversion iterations, the search direction for λ is biased according to

$$\boldsymbol{s}_k^{\lambda} \leftarrow \|\boldsymbol{s}_k^{\lambda}\| \left(W \frac{\boldsymbol{s}_k^{\mu}}{\|\boldsymbol{s}_k^{\mu}\|} + (1-W) \frac{\boldsymbol{s}_k^{\lambda}}{\|\boldsymbol{s}_k^{\lambda}\|} \right), \tag{3.24}$$

where W is a weight that imposes the biasing amount. We assign full weight ($W = 1$) on μ at the first inversion iteration, and reduce it linearly down to zero as iterates evolve (say at $k = 50$). After that, we let λ evolve on its own, according to the original, unbiased search direction.

3.3 Numerical experiments

We present numerical experiments[7] with increasing complexity to test the proposed inversion scheme. In the first example, we verify the accuracy of the gradients, computed by using Algorithm 2. Next, we focus on material profile reconstruction for heterogeneous hosts, using synthetic data at measurement locations. Specifically, we consider: (a) a medium with smoothly varying material properties along depth, to study various aspects of the inversion scheme; (b) a horizontally-layered profile with sharp interfaces; (c) a horizontally-layered profile with an ellipsoidal inclusion, using highly noisy data; and (d) a layered profile with three inclusions in an attempt to implicate arbitrary heterogeneity. Throughout, we use Gaussian pulses to probe the considered domains:

$$f(t) = e^{-(\frac{t-\bar{\mu}}{\bar{\sigma}})^2},$$

where the parameters that characterize the load are given in Table 3.1; $\bar{\mu}$ is the mean, $\bar{\sigma}$ is the deviation, f_{max} is the maximal frequency content of the pulse, t_{end} is the active duration of the Gaussian pulse, and the load has an amplitude of 1 kPa. The time history of the loads and their corresponding Fourier spectrum are shown in Figure 3.1.

---

[7] We developed a code in Fortran, using PETSc [81] to facilitate parallel implementation.

Table 3.1: Characterization of Gaussian pulses.

Name	f_{max}	$\bar{\mu}$	$\bar{\sigma}$	t_{end}
p_{20}	20	0.11	0.0014	0.20
p_{30}	30	0.08	0.0007	0.15
p_{40}	40	0.06	0.0004	0.12

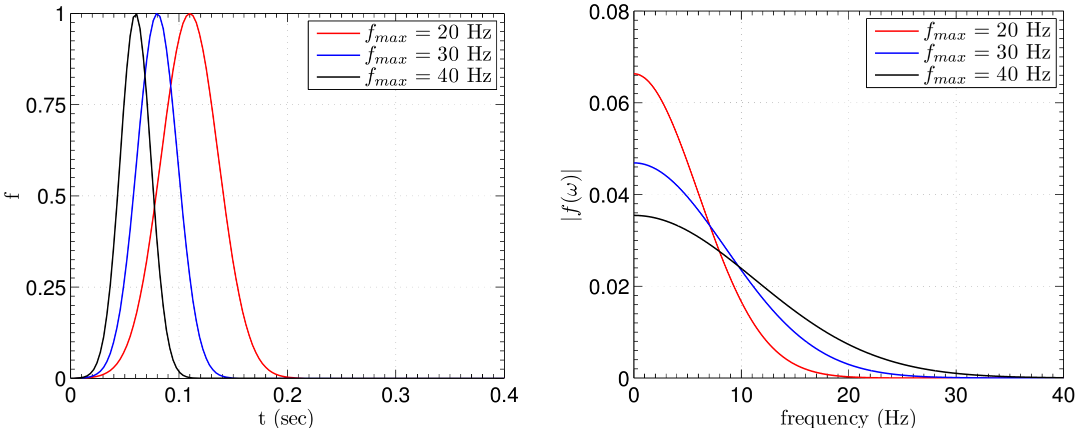

Figure 3.1: Time history of the Gaussian pulses and their Fourier spectrum.

3.3.1 Numerical verification of the material gradients

Accurate computation of the discrete gradients is crucial for the robustness of Algorithm 2. The gradients of the objective functional with respect to the control parameters can be computed either by the optimize-then-discretize, or, the discretize-then-optimize approach [68]. While the discretize-then-optimize method yields the exact discrete gradients of the discrete objective functional [94], this is not always the case with the optimize-then-discretize scheme [95].

In this part, through a numerical experiment, we demonstrate that the discrete gradients that we compute via the optimize-then-discretize technique, are accurate, and equal to the discrete gradients of the discrete objective functional. To this end, we consider a heterogeneous half-space with a smoothly varying material profile along depth, given in (3.27), and mass density $\rho = 2000$ kg/m^3, which, after truncation, is reduced to a cubic computational domain of length and width 24 m × 24 m, and 45 m depth. A 5 m-thick PML is placed at the truncation boundaries, as shown in Fig. 3.2. The material properties at the interfaces Γ^{I} are extended into the PML. The interior and PML domains are discretized by quadratic hexahedral spectral elements of size 1 m (i.e., 27-noded bricks, and quadratic-quadratic pairs of approximation for displacement and stress components in the PML, and, quadratic approximations for the material properties), and $\Delta t = 9 \times 10^{-4}$ s. Throughout, for the PML parameters, we choose $\alpha_o = 5$, $\beta_o = 400$ s^{-1}, and a quadratic profile for the attenuation functions, i.e., $m = 2$. To probe the medium, we consider vertical stress loads with Gaussian pulse temporal signatures (see Table 3.1), applied on the surface of the domain over a region (-11 m $\leq x, y \leq 11$ m), whereas receivers that collect displacement response $\mathbf{u}_m(\mathbf{x}, t)$ are also located in the same region, at every grid point. To obtain synthetic data at the receiver locations, we use a model with identical characteristics and dimensions as detailed above, but, with a refined discretization; i.e., element size of 0.5 m, and $\Delta t = 4.5 \times 10^{-4}$ s. The total duration of the simulation is $T = 0.5$ s. We compare directional finite differences of the discrete objective functional, with directional gradients obtained from (3.17). We start by defining the finite difference directional derivatives

$$d_h^{\text{fd}}(\boldsymbol{\lambda}, \boldsymbol{\mu})(\tilde{\boldsymbol{\lambda}}) := \frac{\mathbf{J}(\boldsymbol{\lambda} + h\tilde{\boldsymbol{\lambda}}, \boldsymbol{\mu}) - \mathbf{J}(\boldsymbol{\lambda}, \boldsymbol{\mu})}{h}, \tag{3.25a}$$

$$d_h^{\text{fd}}(\boldsymbol{\lambda}, \boldsymbol{\mu})(\tilde{\boldsymbol{\mu}}) := \frac{\mathbf{J}(\boldsymbol{\lambda}, \boldsymbol{\mu} + h\tilde{\boldsymbol{\mu}}) - \mathbf{J}(\boldsymbol{\lambda}, \boldsymbol{\mu})}{h}, \tag{3.25b}$$

where $\tilde{\boldsymbol{\lambda}}$ and $\tilde{\boldsymbol{\mu}}$ is the discrete direction vector for λ and μ, respectively. The directional derivatives obtained via the control problems (3.17) are

$$d^{\text{co}}(\boldsymbol{\lambda}, \boldsymbol{\mu})(\tilde{\boldsymbol{\lambda}}) = \tilde{\boldsymbol{\lambda}}\ \tilde{\mathbf{M}}\ \mathbf{g}^{\lambda}, \tag{3.26a}$$

$$d^{\text{co}}(\boldsymbol{\lambda}, \boldsymbol{\mu})(\tilde{\boldsymbol{\mu}}) = \tilde{\boldsymbol{\mu}}\ \tilde{\mathbf{M}}\ \mathbf{g}^{\mu}. \tag{3.26b}$$

Next, we verify that (3.25) and (3.26) produce identical values for several choices that we make for $\tilde{\boldsymbol{\lambda}}$ and $\tilde{\boldsymbol{\mu}}$, with regularization factors[8] $R_\lambda = R_\mu = 0$. We consider perturbations $\tilde{\boldsymbol{\lambda}}$ or $\tilde{\boldsymbol{\mu}}$: the unit vector is zero everywhere except at the

---

[8] Zero values are considered since convergence difficulties that may arise stem from the misfit part of the objective functional, and not from the regularization part. Nevertheless, we have also successfully verified the accuracy of the regularization component of the gradients.

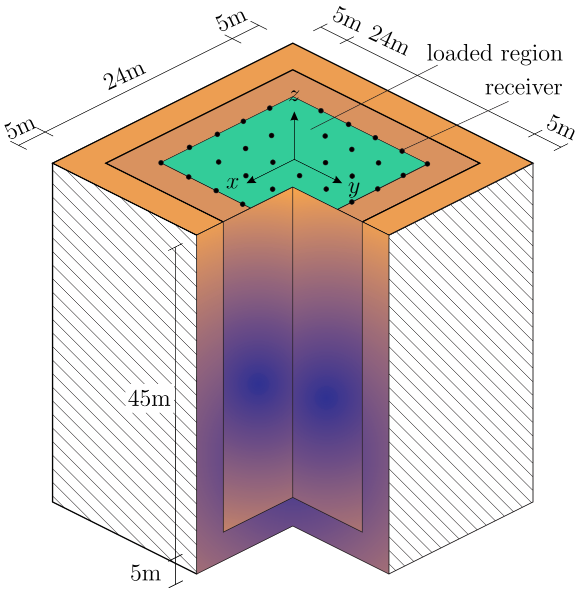

Figure 3.2: Problem configuration for the verification of the gradients.

component corresponding to coordinate (x, y, z) where the directional derivatives are being computed. The derivatives d^{co} and d_h^{fd} with respect to either λ or μ, for points with coordinates (x, y, z), are presented in Table 3.2. The digits to which d_h^{fd} agrees with d^{co} are shown in bold. Since pointwise perturbations result in small changes in the objective functional, numerical roundoff influences the accuracy of the finite difference directional derivatives, as it has also been reported in [95].

The agreement between the two derivatives is remarkable, both for cases 1-4, where the wavefield is well-resolved, and for cases 5 and 6, where only 10 points per wavelength are used for spatial discretization.

Table 3.2: Comparison of the directional derivatives.

Case	f_{max}	(x,y,z)	Pert. field	d^{co}		d_h^{fd}	
					$h = 10^{-3}$	$h = 10^{-4}$	$h = 10^{-5}$
1	20 Hz	(1,1,0)	λ	−3.03500e-9	**−3.03**416e-9	**−3.03**496e-9	**−3.03501**e-9
2	20 Hz	(1,1,0)	μ	−2.78908e-9	**−2.78**875e-9	**−2.789**17e-9	**−2.789**21e-9
3	20 Hz	(1,1,-40)	λ	−5.14848e-11	**−5.14**711e-11	**−5.14**647e-11	**−5.14**996e-11
4	20 Hz	(1,1,-40)	μ	+4.97666e-10	**+4.97**411e-10	**+4.97**512e-10	**+4.97**366e-10
5	40 Hz	(1,1,0)	λ	−1.07645e-9	**−1.076**23e-9	**−1.076**52e-9	**−1.076**56e-9
6	40 Hz	(1,1,0)	μ	−1.56155e-9	**−1.5615**3e-9	**−1.561**78e-9	**−1.561**80e-9

3.3.2 Smoothly varying heterogeneous medium

We consider a heterogeneous half-space with a smoothly varying material profile along depth, given by

$$\lambda(z) = \mu(z) = 80 + 0.45\ |z| + 35\ \exp\left(-\frac{(|z| - 22.5)^2}{150}\right)\ (\mathrm{MPa}), \tag{3.27}$$

and mass density $\rho = 2000$ kg/m^3, which, after truncation, is reduced to a cubic computational domain of length and width 40 m × 40 m, and 45 m depth. A 6.25 m-thick PML is placed at the truncation boundaries, as illustrated in Fig. 3.3. The target profiles are shown in Fig. 3.4. The material properties at the interfaces Γ^{I} are extended into the PML. The interior and PML domains are discretized by quadratic hexahedral spectral elements of size 1.25 m (i.e., 27-noded bricks, and quadratic-quadratic pairs of approximation for displacement and stress components in the PML, and, quadratic approximations for the material properties), and $\Delta t = 10^{-3}$ s. This leads to $3,578,136$ state unknowns, and $616,850$ material parameters. To probe the medium, we consider vertical stress loads with Gaussian pulse temporal signatures (see Table 3.1), applied on the surface of the domain over a region (-17.5 m $\leq\ x,\ y \leq 17.5$ m), whereas receivers that collect displacement response $\mathbf{u}_m(\mathbf{x}, t)$ are placed at every grid point, in the same region.

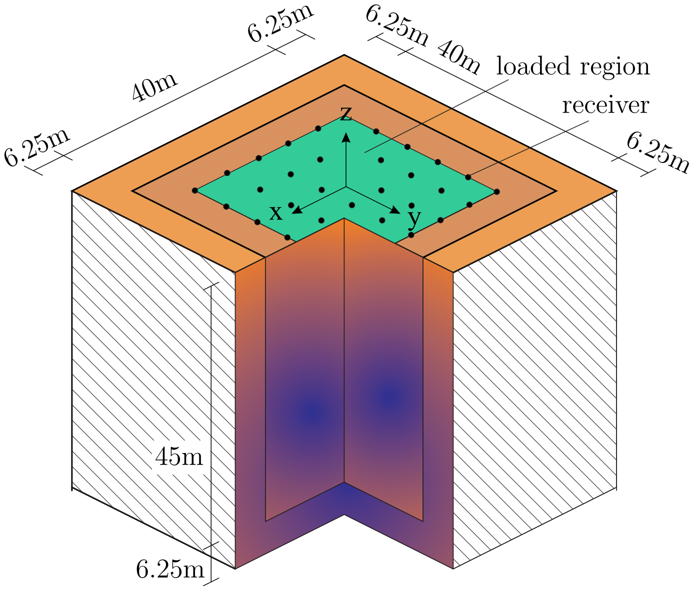

Figure 3.3: Problem configuration: material profile reconstruction of a smoothly varying medium.

Before attempting simultaneous inversion for the two Lamé parameters, we perform single parameter inversion for a) μ only, assuming λ is *a priori* known and fixing it to the target profile; and b) λ only, assuming the distribution of μ is known.

3.3.2.1 Single parameter inversion

First, we assume λ is *a priori* known, and fix it to the target profile. We start inverting for μ, with a homogeneous initial guess of 80 MPa, exploiting Tikhonov regularization for taming ill-posedness and solution multiplicity. We use the Gaussian

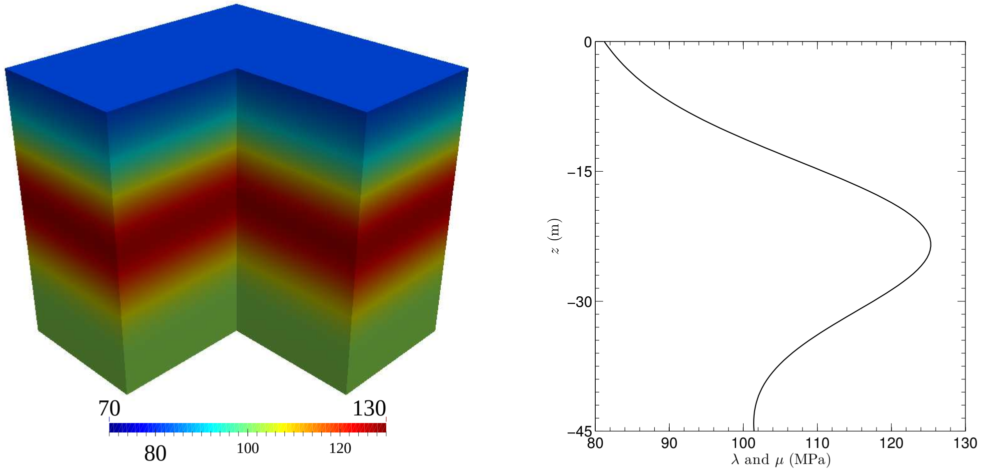

(a)

(b)

Figure 3.4: Smoothly varying medium: (a) target λ and μ (MPa); and (b) profile at $(x, y) = (0, 0)$.

pulse p_{20} with maximal frequency content $f_{max} = 20$ Hz (see Table 3.1) for 50 iterations, and, then, switch to p_{30} with $f_{max} = 30$ Hz. After 156 iterations, μ converges to the target profile, as shown in Fig. 3.5(b). We compare the inverted cross-sectional profiles of μ with the target profile at three different locations, as shown in Figs. 3.5(c), 3.5(d), and 3.5(e). The agreement between the two profiles is excellent. Reduction of the misfit functional with respect to inversion iterations is shown in Fig. 3.7(a) (almost 7 orders of magnitude).

Next, we fix μ to the target profile, and invert for λ, starting with a homogeneous initial guess of 80 MPa. We use the Gaussian pulse p_{20} for 160 iterations, p_{30} up to the 300$^{\text{th}}$ iteration, and then switch to p_{40}. After 456 iterations, the optimizer converges to the profile displayed in Fig. 3.6(a). The agreement between the target profile and the inverted profile is remarkable. We compare the two profiles at three

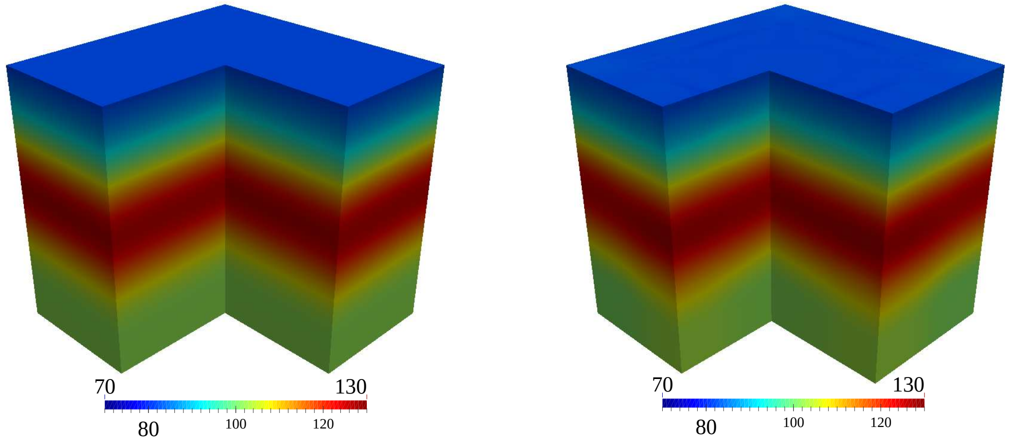

(a) λ (*a priori* known) (b) μ (inverted)

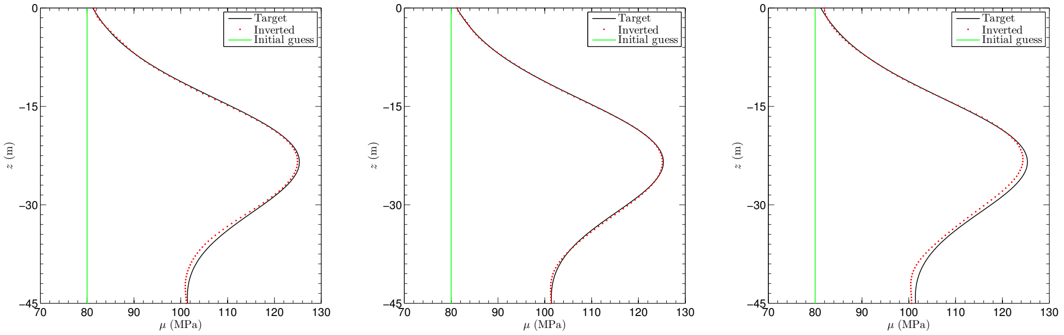

(c) μ at $(x, y) = (0, 0)$ (d) μ at $(x, y) = (10, 10)$ (e) μ at $(x, y) = (20, 20)$

Figure 3.5: Single-parameter inversion (μ only) for a smoothly varying medium.

different cross-sections shown in Figs. 3.6(c), 3.6(d), and 3.6(e): the agreement between the two profiles is excellent. The misfit history is shown in Fig. 3.7(b); the optimizer reduced the misfit almost 6 orders of magnitude.

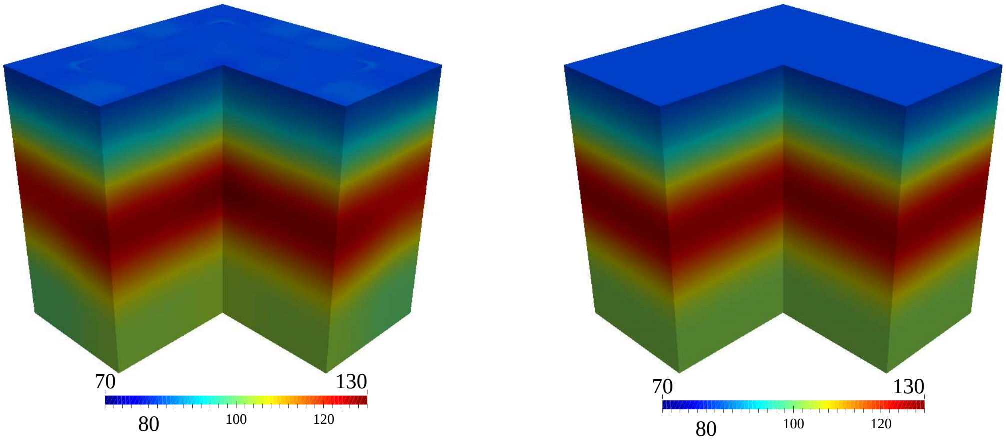

(a) λ (inverted)

(b) μ (*a priori* known)

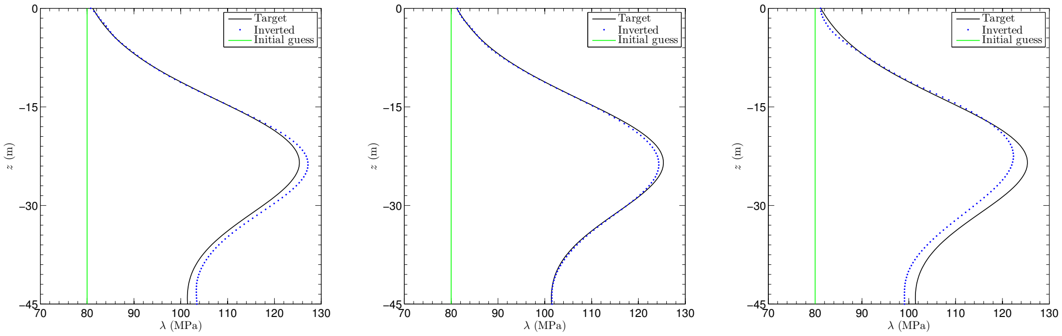

(c) λ at $(x, y) = (0, 0)$

(d) λ at $(x, y) = (10, 10)$

(e) λ at $(x, y) = (20, 20)$

Figure 3.6: Single-parameter inversion (λ only) for a smoothly varying medium.

We remark that the initial value of the misfit in the first experiment is almost 2 orders of magnitude more than that of the second experiment. This indicates that the objective functional is not equally sensitive to both control parameters, as it has

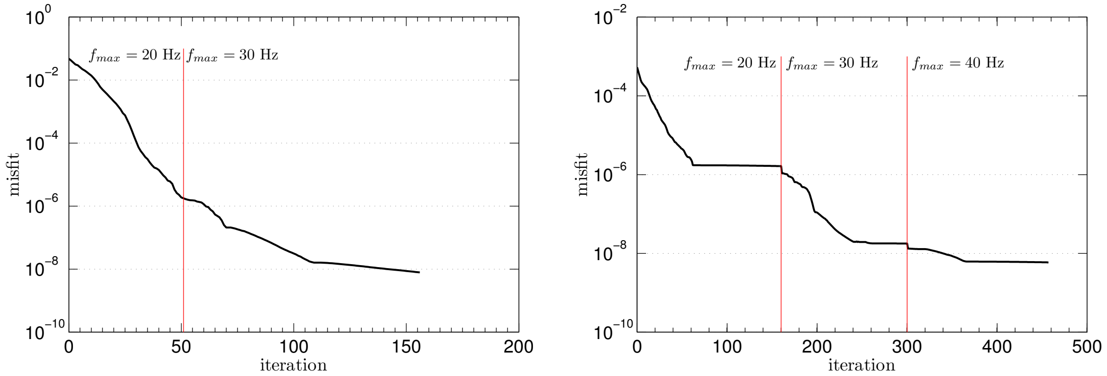

(a) reconstruction for μ only

(b) reconstruction for λ only

Figure 3.7: Variation of the misfit functional with respect to inversion iterations (single parameter inversion).

also been reported in [57]: the objective functional is more sensitive to μ.

3.3.2.2 Simultaneous inversion

We start with a homogeneous initial guess of 80 MPa for both λ and μ and attempt simultaneous inversion. The target profiles are shown in Fig. 3.4, and the inverted profiles are displayed in Figs. 3.8(a) and 3.8(b). We also compare the cross-sectional values of the target and inverted profiles at three different locations, shown in Fig. 3.9. Although the inverted μ profile agrees reasonably well with the target profile, inversion for λ is not satisfactory, and the inverted profile departs from the target as depth increases.

Due to the unsuccessful inversion of the λ profile in the case of simultaneous inversion, in the next experiment, we bias the search direction of λ based on that of μ, at the very early stages of inversion, according to the procedure detailed in Section 3.2.3.3. This leads to the successful reconstruction of the two profiles, as is shown in

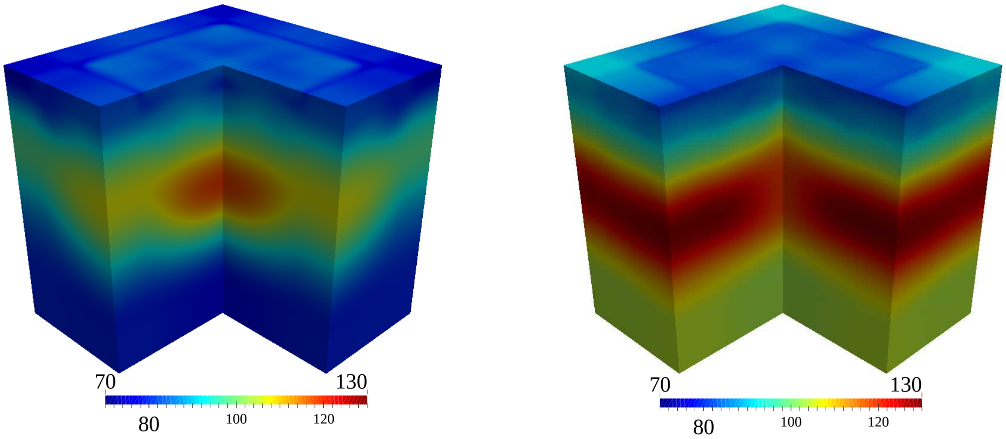

(a) λ (inverted) (b) μ (inverted)

Figure 3.8: Simultaneous inversion for λ and μ using unbiased search directions.

Figs. 3.10(a) and 3.10(b). In Fig. 3.11, we compare the cross-sectional values of the target and the inverted profiles. The agreement of the inverted μ profile with the target is remarkable. Moreover, the inverted λ profile agrees reasonably well with the target, with some discrepancies in depth. The misfit history is shown in Fig. 3.12(b), where the kink in the misfit curve at the 50^{th} iteration corresponds to the termination point of the biasing scheme.

We remark that in practical applications, one is more interested in the shear wave velocity (c_s) and compression wave velocity (c_p) profiles. Once the Lamé parameters have been determined, the wave velocities can be readily computed via

$$c_s = \sqrt{\frac{\mu}{\rho}}, \qquad c_p = \sqrt{\frac{\lambda + 2\mu}{\rho}}. \tag{3.28}$$

In Fig. 3.13, we compare the compressional wave velocities at three different cross-

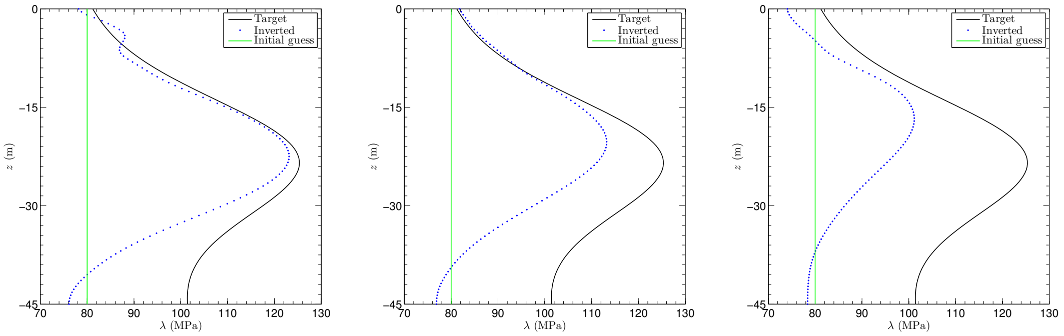

(a) λ at $(x, y) = (0, 0)$ (b) λ at $(x, y) = (10, 10)$ (c) λ at $(x, y) = (20, 20)$

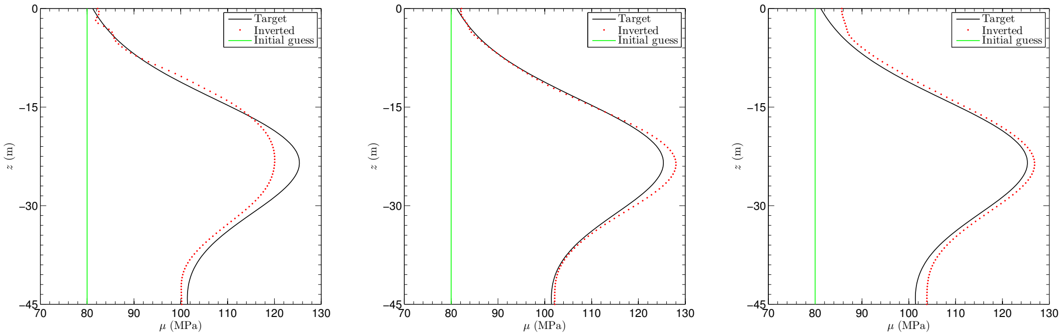

(d) μ at $(x, y) = (0, 0)$ (e) μ at $(x, y) = (10, 10)$ (f) μ at $(x, y) = (20, 20)$

Figure 3.9: Cross-sectional profiles of λ and μ using unbiased search directions.

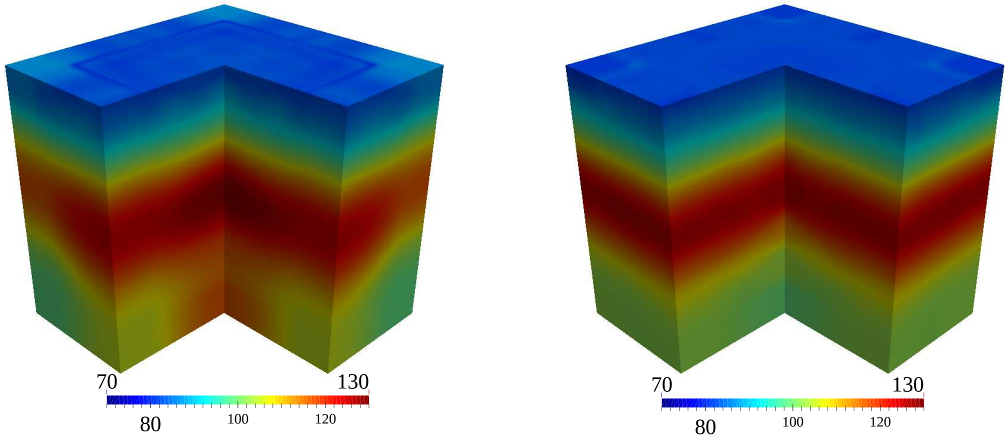

(a) λ (inverted)

(b) μ (inverted)

Figure 3.10: Simultaneous inversion for λ and μ using biased search directions.

sectional locations, where the agreement between the reconstructed c_p profile and the target is remarkable. The shear wave velocity does not depend on λ, and, therefore, its quality is similar to that of the μ profile.

3.3.3 Layered medium

We consider a 40 m × 40 m × 45 m layered medium, where a 6.25 m-thick PML is placed at its truncation boundaries. The properties of the medium are

$$\lambda(z) = \mu(z) = \begin{cases} 80 \text{ MPa}, & \text{for } -12 \text{ m} \le z \le 0 \text{ m}, \\ 101.25 \text{ MPa}, & \text{for } -27 \text{ m} \le z < -12 \text{ m}, \\ 125 \text{ MPa}, & \text{for } -50 \text{ m} \le z < -27 \text{ m}, \end{cases} \tag{3.29}$$

and are shown in Fig. 3.14, with mass density $\rho = 2000$ kg/m^3. The material properties at the interfaces Γ^{I} are extended into the PML buffer. The interior and PML domains are discretized by quadratic hexahedral spectral elements of size 1.25 m

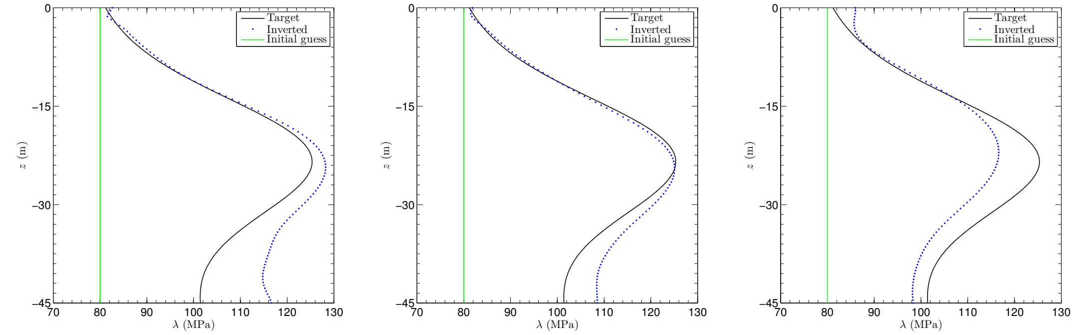

(a) λ at $(x, y) = (0, 0)$ (b) λ at $(x, y) = (10, 10)$ (c) λ at $(x, y) = (20, 20)$

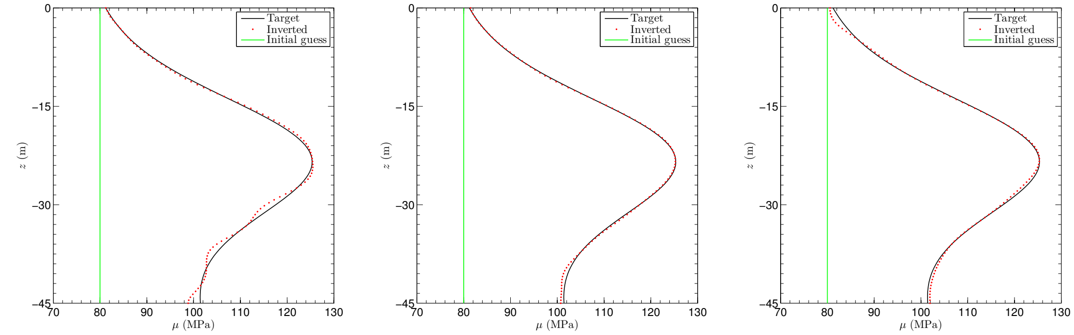

(d) μ at $(x, y) = (0, 0)$ (e) μ at $(x, y) = (10, 10)$ (f) μ at $(x, y) = (20, 20)$

Figure 3.11: Cross-sectional profiles of λ and μ using biased search directions.

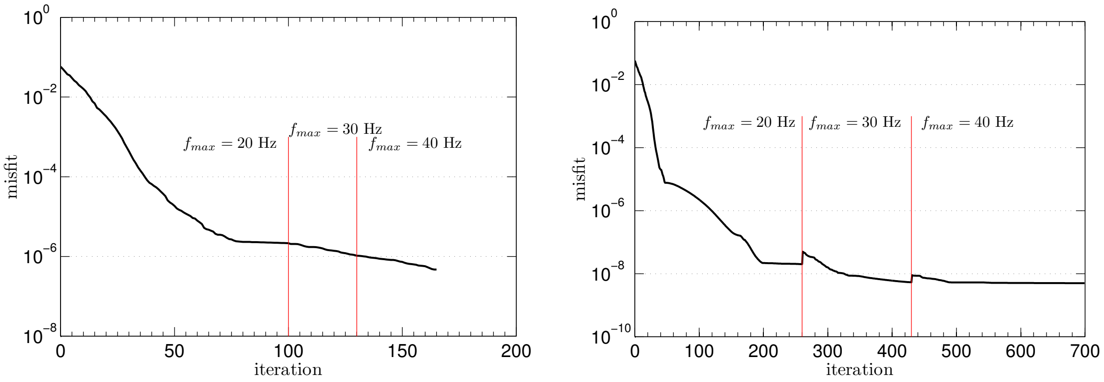

(a) unbiased search directions (b) biased search direction for λ

Figure 3.12: Variation of the misfit functional with respect to inversion iterations (simultaneous inversion).

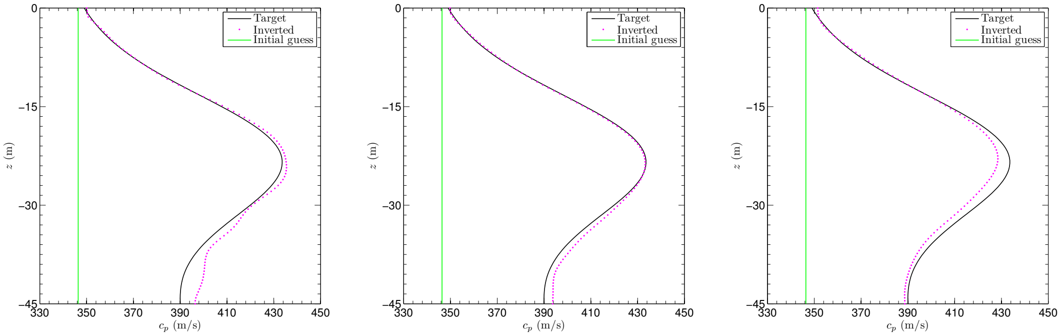

(a) c_p at $(x, y) = (0, 0)$ (b) c_p at $(x, y) = (10, 10)$ (c) c_p at $(x, y) = (20, 20)$

Figure 3.13: Cross-sectional profiles of c_p using biased search directions.

(i.e., 27-noded bricks, and quadratic-quadratic pairs of approximation for displacement and stress components in the PML, and, quadratic approximations for the material properties), and $\Delta t = 10^{-3}$ s. For probing the medium, we use vertical stress loads with Gaussian pulse temporal signatures, applied on the surface of the domain over a region ($-17.5\text{m} \leq x, y \leq 17.5\text{m}$), whereas receivers that collect displacement response $\mathbf{u}_m(\mathbf{x}, t)$ are also located in the same region, at every grid point.

We start the inversion process with a homogeneous initial guess of 80 MPa for the Lamé parameters, and attempt simultaneous inversion for both λ and μ, using the biasing scheme outlined in Section 3.2.3.3. We use the Total Variation regularization scheme, with $\epsilon = 0.01$, to capture the sharp interfaces of the target profiles. We use the Gaussian pulse p_{20}, with $f_{max} = 20$ Hz, and final simulation time $T = 0.45$ s, for 310 iterations. The resulting profiles are shown in Fig. 3.15(a) and 3.15(b), where the layering of the medium is clearly visible in the inverted profiles. To improve the quality of the inverted profiles, we use them as an initial guess with the Gaussian pulse p_{30}, and final simulation time of $T = 0.4$ s, for up to the 860th

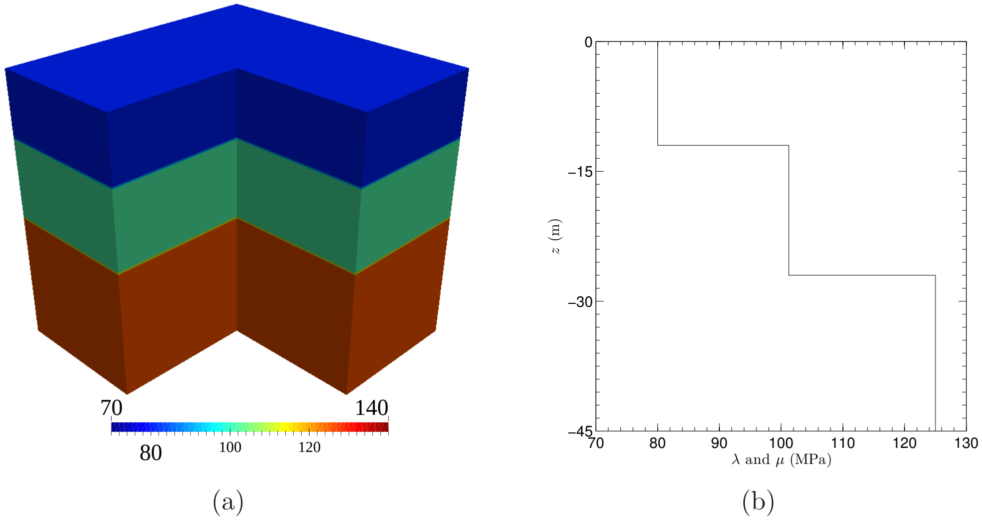

(a) (b)

Figure 3.14: Layered medium: (a) target λ and μ (MPa); and (b) profile at $(x, y) = (0, 0)$.

iteration, and, then, switch to p_{40}, with final simulation time of $T = 0.4$ s. After 1112 iterations, the optimizer converges to the profiles displayed in Fig. 3.15(c) and 3.15(d). There is excellent agreement between the inverted μ profile and the target profile. The inverted λ profile is also in good agreement with the target profile: the two top layers have been reconstructed quite well, whereas the bottom layer is slightly "stiffer" in its middle zone. We compare the inverted profiles with the targets at three different cross-sections, shown in Fig. 3.16. Due to the TV regularization, sharp interfaces have been captured quite successfully. In Fig. 3.17, we compare the c_p profile with the target, at the same cross-sections; the agreement between the two profiles is impressive. Figure 3.18 shows the misfit history: the optimizer reduced the misfit almost 7 orders of magnitude.

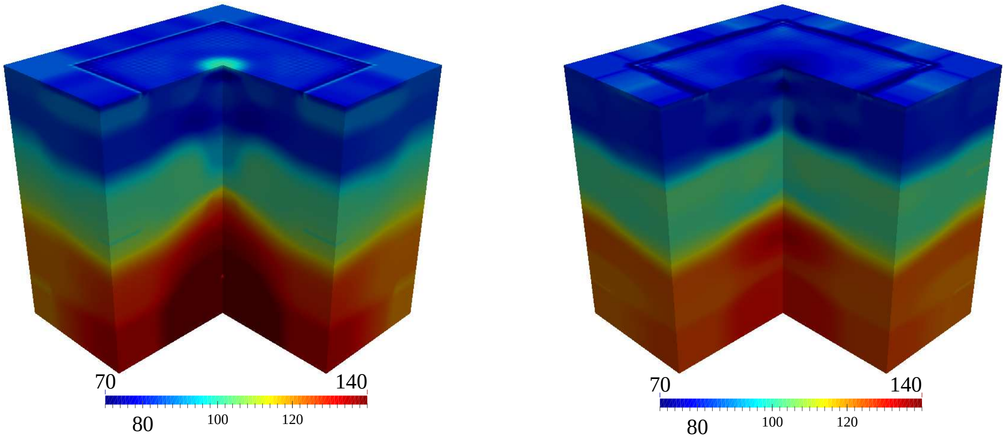

(a) λ ($f_{max} = 10$ Hz)   (b) μ ($f_{max} = 10$ Hz)

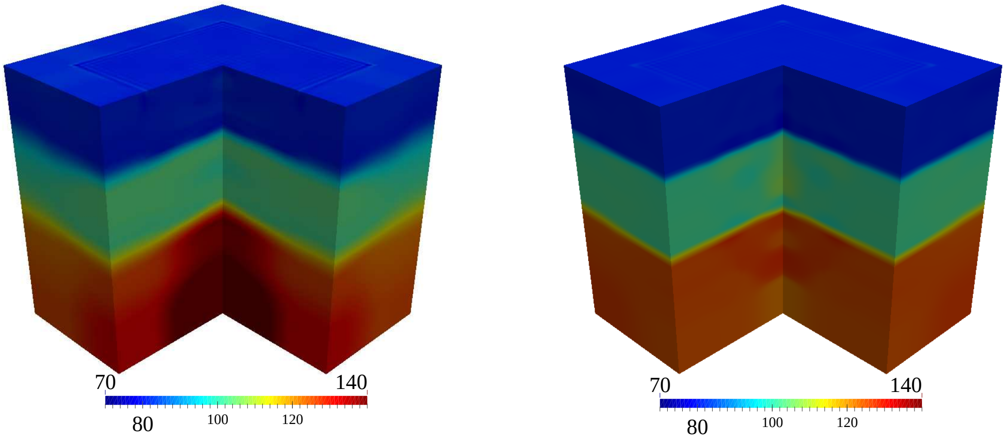

(c) λ ($f_{max} = 40$ Hz)   (d) μ ($f_{max} = 40$ Hz)

Figure 3.15: Simultaneous inversion for λ and μ (layered medium).

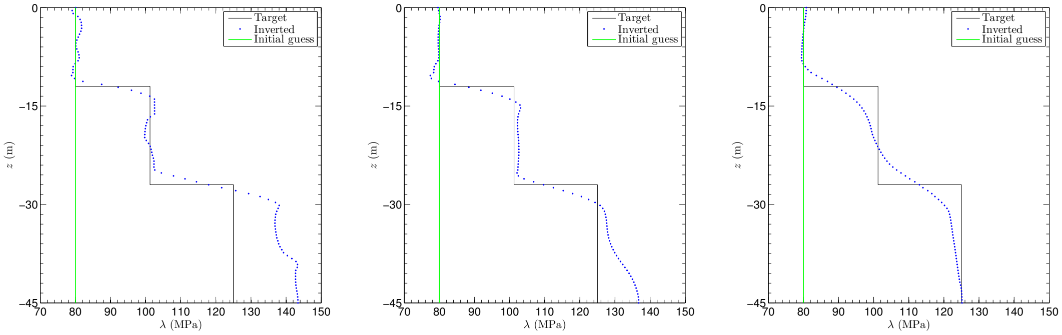

(a) λ at $(x, y) = (0, 0)$ (b) λ at $(x, y) = (10, 10)$ (c) λ at $(x, y) = (20, 20)$

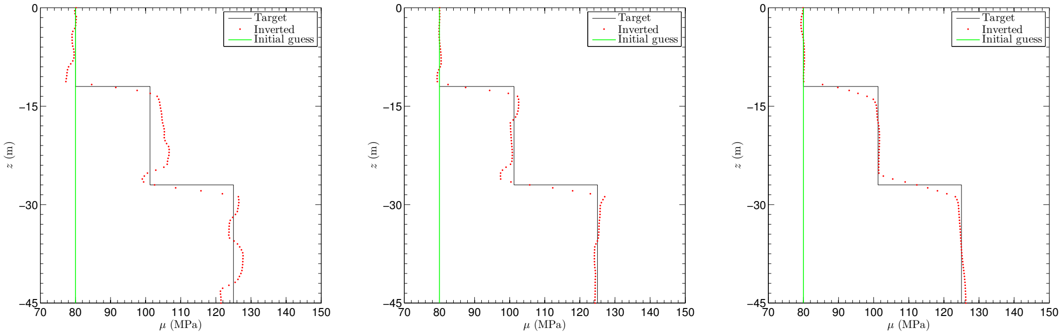

(d) μ at $(x, y) = (0, 0)$ (e) μ at $(x, y) = (10, 10)$ (f) μ at $(x, y) = (20, 20)$

Figure 3.16: Cross-sectional profiles of λ and μ (layered medium).

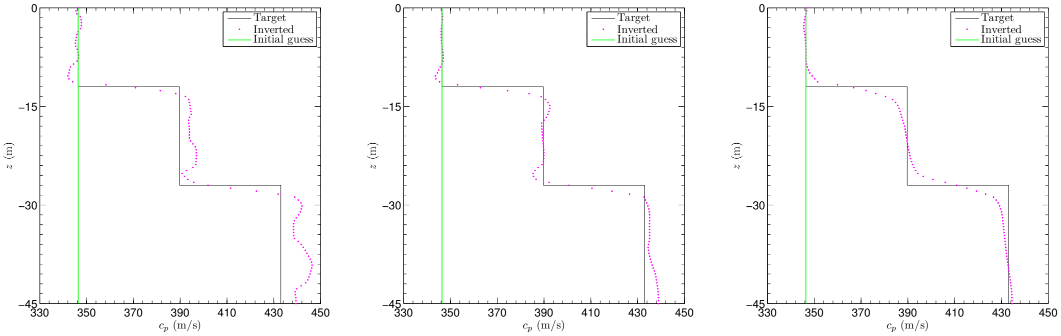

(a) c_p at $(x, y) = (0, 0)$ (b) c_p at $(x, y) = (10, 10)$ (c) c_p at $(x, y) = (20, 20)$

Figure 3.17: Cross-sectional profiles of c_p (layered medium).

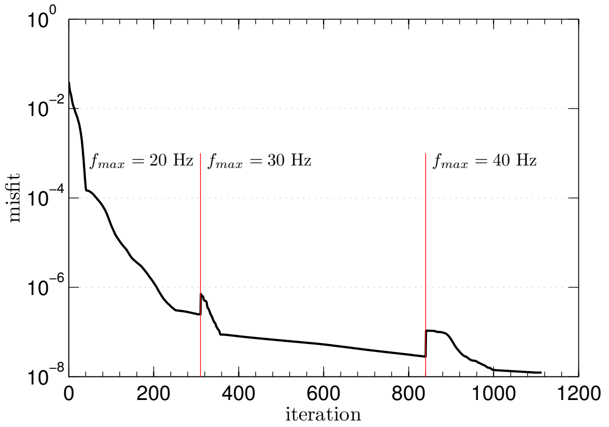

Figure 3.18: Variation of the misfit functional with respect to inversion iterations (layered medium).

3.3.4 Layered medium with inclusion

We consider a layered medium with an inclusion. The problem consists of a 40 m × 40 m × 45 m layered medium with an ellipsoidal inclusion, where a 6.25 m-thick PML is placed at its truncation boundaries. The material profiles are given by

$$\lambda(z) = \mu(z) = \begin{cases} 80 \text{ MPa}, & \text{for } -12 \text{ m} \leq z \leq 0 \text{ m}, \\ 101.25 \text{ MPa}, & \text{for } -27 \text{ m} \leq z < -12 \text{ m}, \\ 125 \text{ MPa}, & \text{for } -50 \text{ m} \leq z < -27 \text{ m}, \\ 156.8 \text{ MPa}, & \text{for ellipsoidal inclusion}, \end{cases} \tag{3.30}$$

and are shown in Fig. 3.19, with constant mass density $\rho = 2000$ kg/m^3. The ellipsoidal inclusion occupies the region $(\frac{x-7.5}{7.5})^2 + (\frac{y}{5})^2 + (\frac{z+12}{5.5})^2 \leq 1$. The material properties at the interfaces Γ^{I} are extended into the PML buffer. The interior and PML domains are discretized by quadratic hexahedral spectral elements of size

1.25 m, and $\Delta t = 10^{-3}$ s. To illuminate the domain, we use vertical stress loads with Gaussian pulse temporal signatures, applied on the surface of the medium over a region ($-17.5\text{m} \leq x, y \leq 17.5\text{m}$), whereas the receivers are also placed at every grid point in the same region.

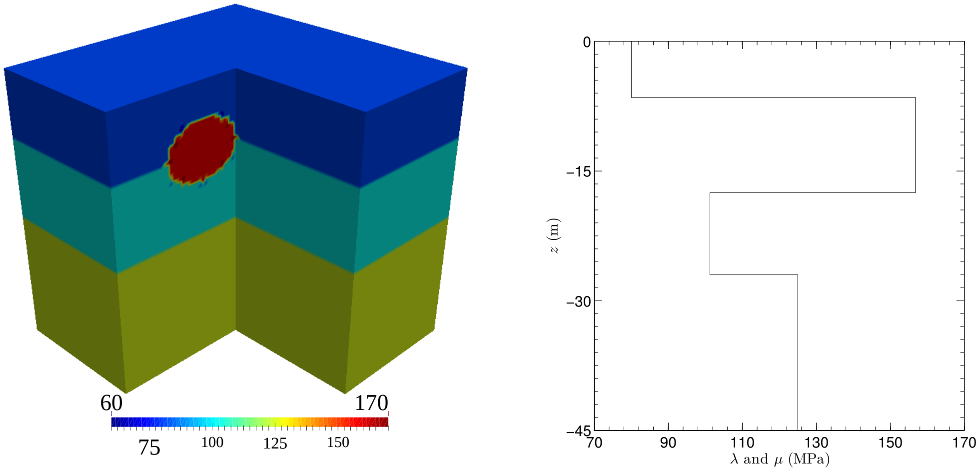

(a) (b)

Figure 3.19: Layered medium with inclusion: (a) target λ and μ; and (b) profile at $(x, y) = (7.5, 0)$.

We use the Total Variation regularization scheme to alleviate ill-posedness and solution multiplicity, with $\epsilon = 0.01$. Similar to the previous examples, we use a source-frequency continuation scheme, starting with the Gaussian pulse p_{20} with maximal frequency content of 20 Hz for $T = 0.45$ s, and, when updates in the material profiles become practically insignificant, we switch to the next load in Table 3.1, which contains a broader range of frequencies, and, therefore, is able to image finer features. Figure 3.20(a) and 3.20(b) show the material profiles after 410 iterations, which adequately capture the layering of the domain as well as the ellipsoidal inclusion. To improve the quality of the reconstructed profiles, we use them as an initial guess with the Gaussian pulse p_{30}, and final simulation time of $T = 0.4$ s, for up to the 730^{th} iteration, and, then, switch to p_{40}, with final simulation time of $T = 0.4$ s. Figure 3.20(c) and 3.20(d) show the inverted profiles after 1160 iterations. The sharp interfaces between the three layers and around the ellipsoidal inclusion are very well captured for the μ profile. The λ profile agrees reasonably well with the target, showing some "stiff" features at the center of the bottom layer, similar to the previous example.

Figures 3.21 and 3.22 compare the inverted profiles with the target profiles at three different cross-sectional lines of the domain, indicating successful imaging of both the layering and the inclusion. Variation of the misfit functional with respect to the inversion iterations is shown in Fig. 3.22, where, again, a kink at the 50^{th} iteration of the misfit curve, corresponds to the termination point of the biasing scheme.

Encouraged by the successful performance of the proposed inversion algorithm with noise-free data, next, we consider adding different levels of Gaussian noise to the measured synthetic response at the receiver locations, and investigate its effect on the inversion. Figures 3.24(a)-3.24(d) show the measured displacement response of the system at $(x, y, z) = (3.125, \text{-}13.75, 0)$ m, subjected to the p_{20} pulse, contaminated with 1%, 5%, 10%, and 20% Gaussian noise, respectively. Using the source-frequency continuation scheme, the optimizer converges after 811 and 751 iterations, respectively, for cases corresponding to the 1% and 5% Gaussian noise levels. The inverted profiles are shown in Fig. 3.25. The reconstruction is successful, with minor dis-

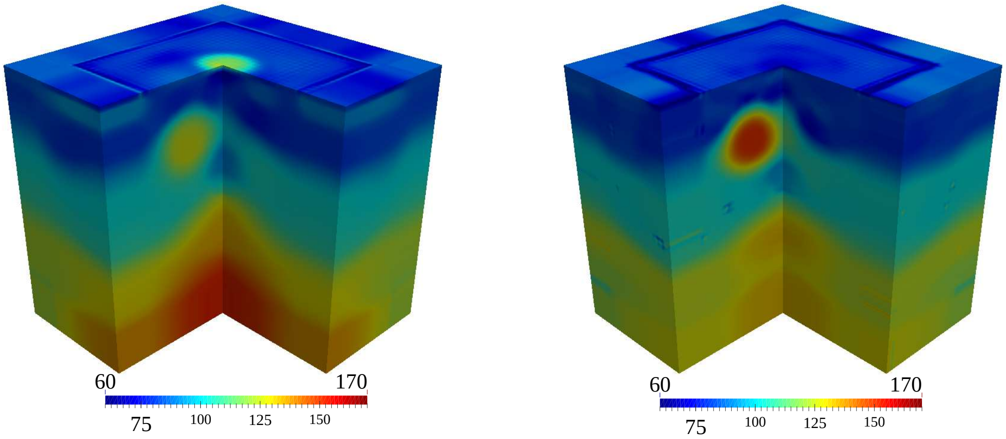

(a) λ ($f_{max} = 10$ Hz)

(b) μ ($f_{max} = 10$ Hz)

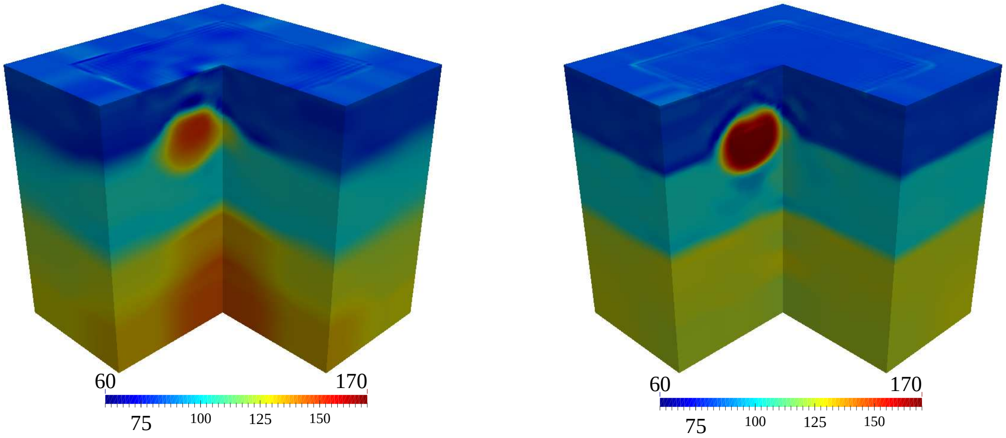

(c) λ ($f_{max} = 40$ Hz)

(d) μ ($f_{max} = 40$ Hz)

Figure 3.20: Simultaneous inversion for λ and μ (layered medium with inclusion).

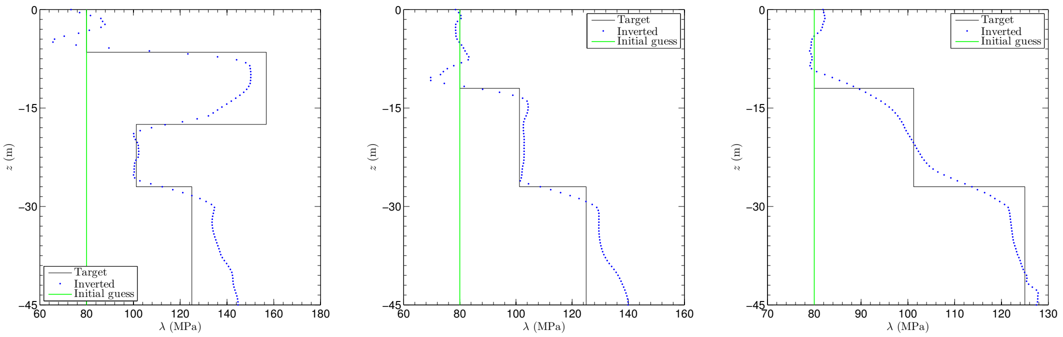

(a) λ at $(x, y) = (7.5, 0)$ (b) λ at $(x, y) = (7.5, 10)$ (c) λ at $(x, y) = (20, 20)$

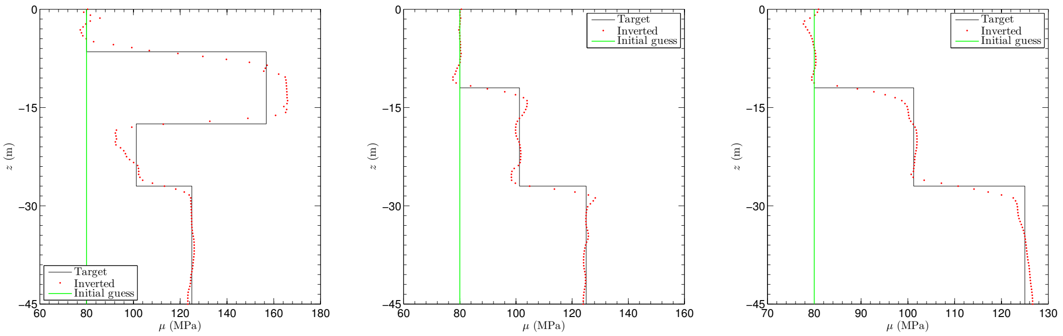

(d) μ at $(x, y) = (7.5, 0)$ (e) μ at $(x, y) = (7.5, 10)$ (f) μ at $(x, y) = (20, 20)$

Figure 3.21: Cross-sectional profiles of λ and μ (layered medium with inclusion).

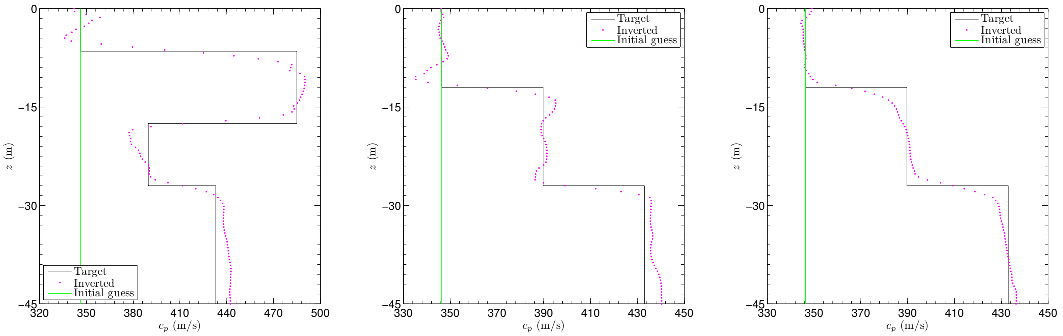

(a) c_p at $(x, y) = (7.5, 0)$ (b) c_p at $(x, y) = (7.5, 10)$ (c) c_p at $(x, y) = (20, 20)$

Figure 3.22: Cross-sectional profiles of c_p (layered medium with inclusion).

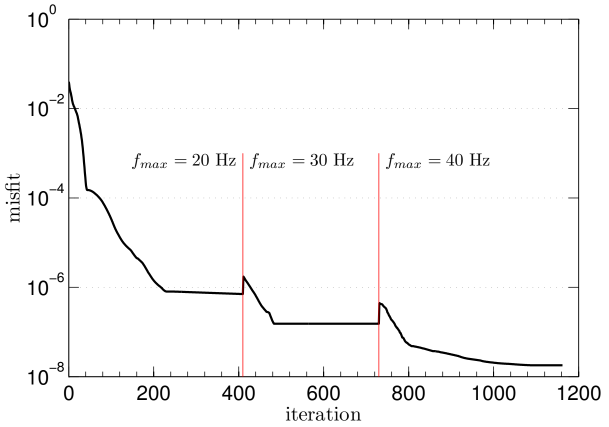

Figure 3.23: Variation of the misfit functional with respect to inversion iterations (layered medium with inclusion).

crepancies on the top surface. Next, we increase the noise level to 10% and 20%, and attempt inversion; after 770 and 674 iterations, respectively, we converge to the profiles shown in Fig. 3.26. The quality of the inverted profiles decreases as the noise level increases. However, similarly to the previous case, except for a thin layer on the top surface, inversion is successful. In Fig. 3.27, we compare cross-sectional profiles of λ and μ with the target, at different noise levels, at $(x, y) = (7.5, 0)$ m, which passes through the center of the ellipsoidal inclusion. Sharp interfaces are captured remarkably well for the μ profile, even at the presence of 20% noise. The inversion for λ is also satisfactory.

3.3.5 Layered medium with three inclusions

In the last example, we consider a layered medium, with three inclusions, to study the performance of our inversion scheme for a more complex material profile. The problem consists of an 80 m × 80 m × 45 m medium, where a 6.25 m-thick

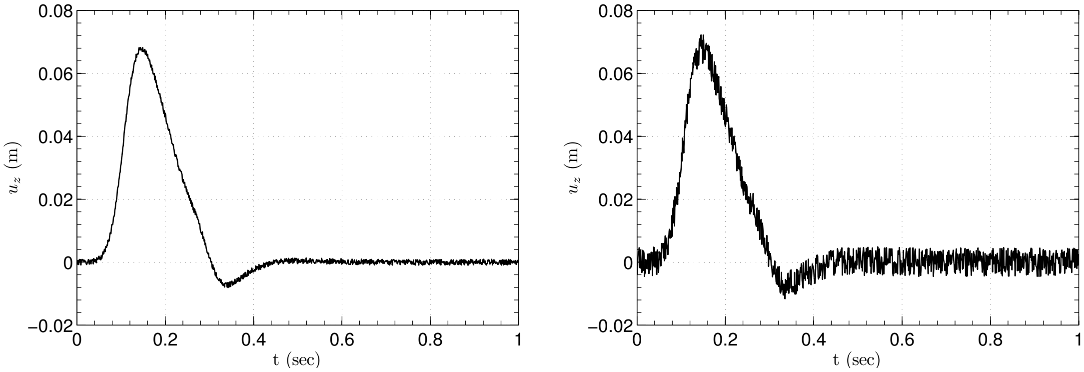

(a) with 1% Gaussian noise

(b) with 5% Gaussian noise

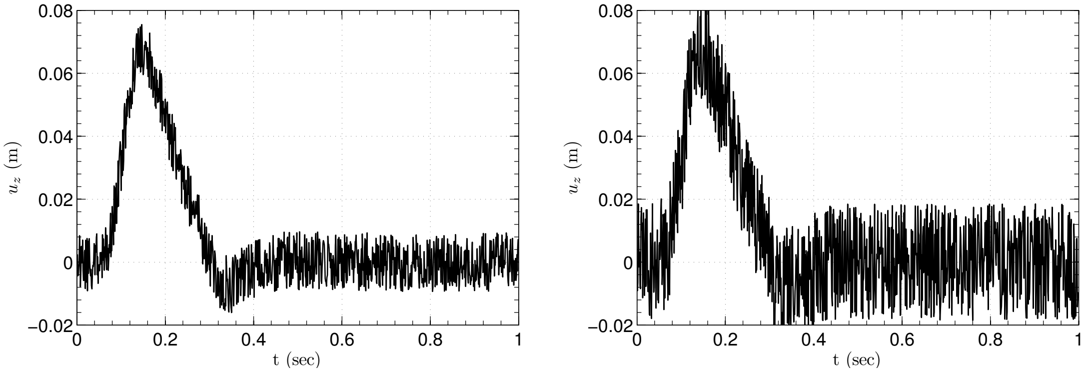

(c) with 10% Gaussian noise

(d) with 20% Gaussian noise

Figure 3.24: Measured displacement response of the layered medium with inclusion, at $(x, y, z) = (3.125, -13.75, 0)$ m, due to the Gaussian pulse p_{20}, contaminated with Gaussian noise.

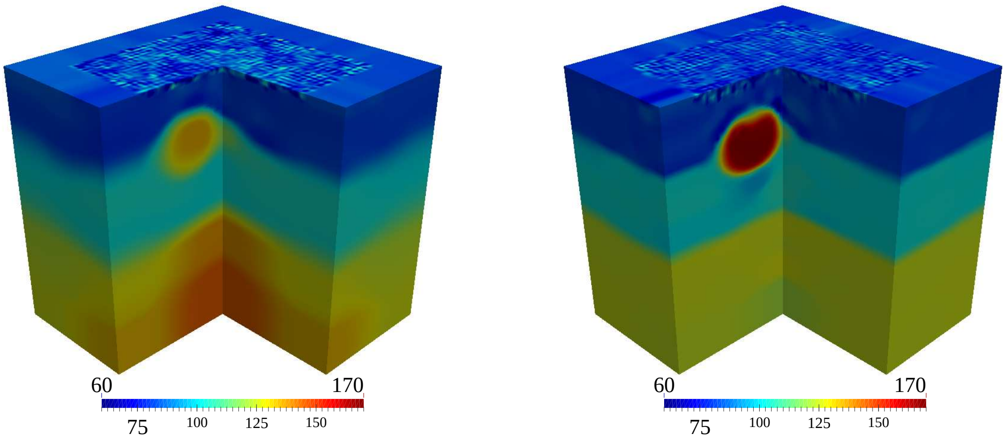

(a) λ (1% Gaussian noise) (b) μ (1% Gaussian noise)

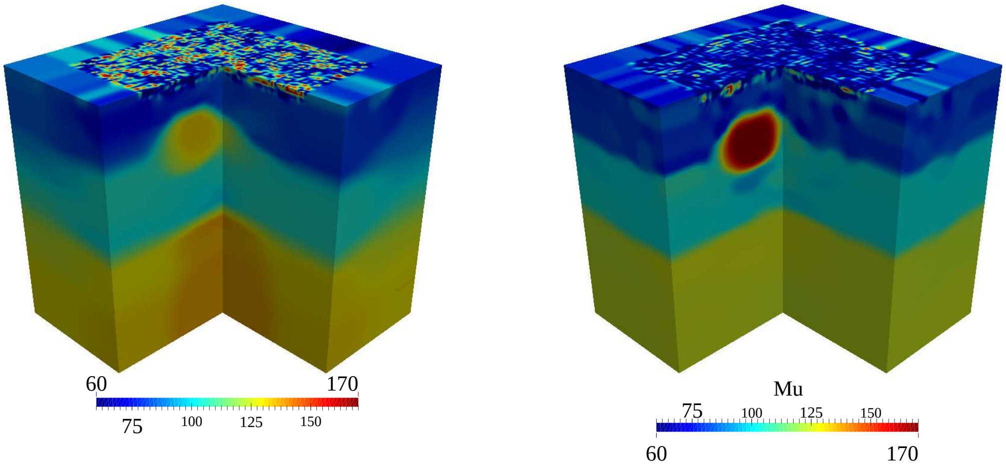

(c) λ (5% Gaussian noise) (d) μ (5% Gaussian noise)

Figure 3.25: Simultaneous inversion for λ and μ using measured data contaminated with 1% and 5% Gaussian noise (layered medium with inclusion).

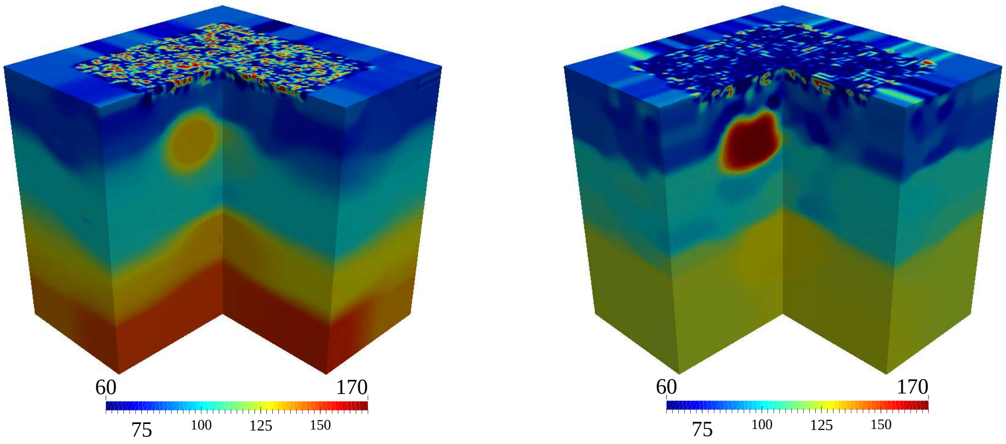

(a) λ (10% Gaussian noise)

(b) μ (10% Gaussian noise)

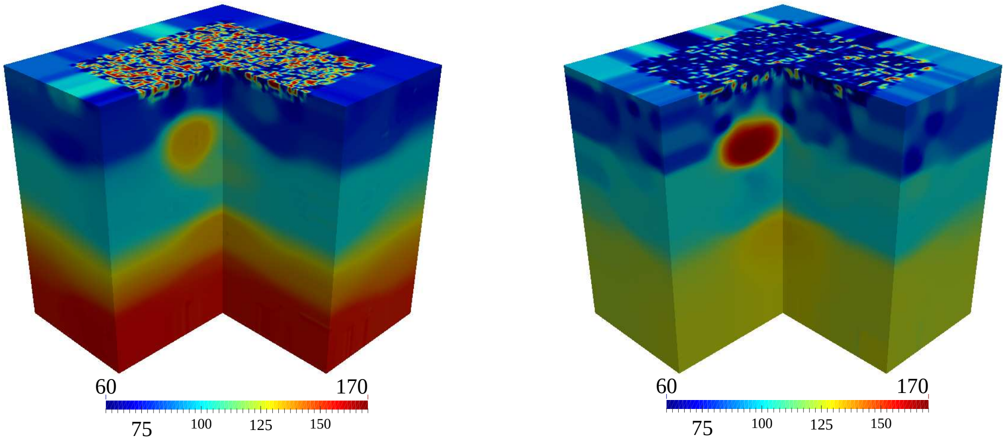

(c) λ (20% Gaussian noise)

(d) μ (20% Gaussian noise)

Figure 3.26: Simultaneous inversion for λ and μ using measured data contaminated with 10% and 20% Gaussian noise (layered medium with inclusion).

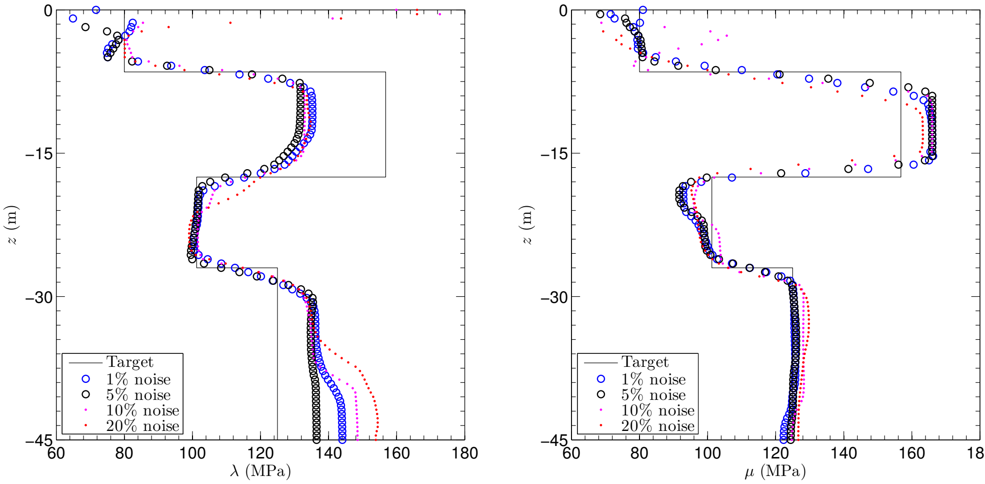

(a) λ at $(x, y) = (7.5, 0)$

(b) μ at $(x, y) = (7.5, 0)$

Figure 3.27: Cross-sectional profiles of λ and μ at different noise levels (layered medium with inclusion).

PML is placed at its truncation boundaries. The material profiles are given by

$$\lambda(z) = \mu(z) = \begin{cases} 80 \text{ MPa}, & \text{for } -15 \text{ m} \leq z \leq 0 \text{ m}, \\ 101.25 \text{ MPa}, & \text{for } -30 \text{ m} \leq z < -15 \text{ m}, \\ 125 \text{ MPa}, & \text{for } -50 \text{ m} \leq z < -30 \text{ m}, \\ 156.8 \text{ MPa}, & \text{for spheroidal: } (\frac{x+20}{3.75})^2 + (\frac{y+20}{20})^2 + (\frac{z+8.75}{3.75})^2 \leq 1, \\ 156.8 \text{ MPa}, & \text{for ellipsoidal: } (\frac{x-20}{15})^2 + (\frac{y-20}{7.5})^2 + (\frac{z+30}{5})^2 \leq 1, \\ 80 \text{ MPa}, & \text{for sphere: } (x-20)^2 + (y+20)^2 + (z+35)^2 \leq 6.25, \end{cases}$$

and are shown in Fig. 3.28, with constant mass density $\rho = 2000$ kg/m^3. Figures 3.29(a) and 3.29(b) depict the target profiles on a cross-section through the domain situated at 8.75 m and 35 m from the top surface, going through the ellipsoid's and sphere's midplane, respectively. In terms of the smallest wavelength[9] the prescribed

---

[9] The smallest wavelength is equal to the smallest velocity in the formation 200 m/s, divided by

geometry comprises a domain of $16 \times\ 16 \times\ 9$ wavelengths long, wide, and deep, a spherical inclusion with a diameter equal to 2.5 wavelengths, an ellipsoidal inclusion of $6 \times 3 \times 2$ wavelengths, and a spheroidal inclusion of $1.5 \times 8 \times 1.5$ wavelengths. The material properties at the interfaces Γ^{I} are extended into the PML buffer. The interior and PML domains are discretized by quadratic hexahedral spectral elements (i.e., 27-noded bricks, and quadratic-quadratic pairs of approximation for displacement and stress components in the PML, and, also, quadratic approximation for material properties) of size 1.25 m, and $\Delta t = 10^{-3}$ s. This leads to $9,404,184$ state unknowns, and $2,429,586$ material parameters. To illuminate the domain, we use vertical stress loads with Gaussian pulse temporal signatures, applied on the surface of the medium over a region ($-37.5 \text{ m} \leq x, y \leq 37.5$ m), whereas receivers are placed at every grid point, within the same region as the load.

To narrow the feasibility space and alleviate difficulties with solution multiplicity, we use the Total Variation regularization, with $\epsilon = 0.01$, combined with the regularization factor continuation scheme outlined in Section 3.2.3.1, the source-frequency continuation scheme in Section 3.2.3.2, and the biasing scheme for λ search directions in Section 3.2.3.3. Specifically, we use the regularization parameter $\varrho = 0.5$ when illuminating the medium with pulse p_{20} for 60 iterations. Next, we use $\varrho = 0.4$ with pulse p_{30} up to the 290^{th} iteration. Finally, we use $\varrho = 0.3$ with pulse p_{40} and stop at the 741^{st} iteration. In all the three cases, the total simulation time is $T = 0.7$ s.

---

the largest probing frequency 40 Hz, i.e., 5 m.

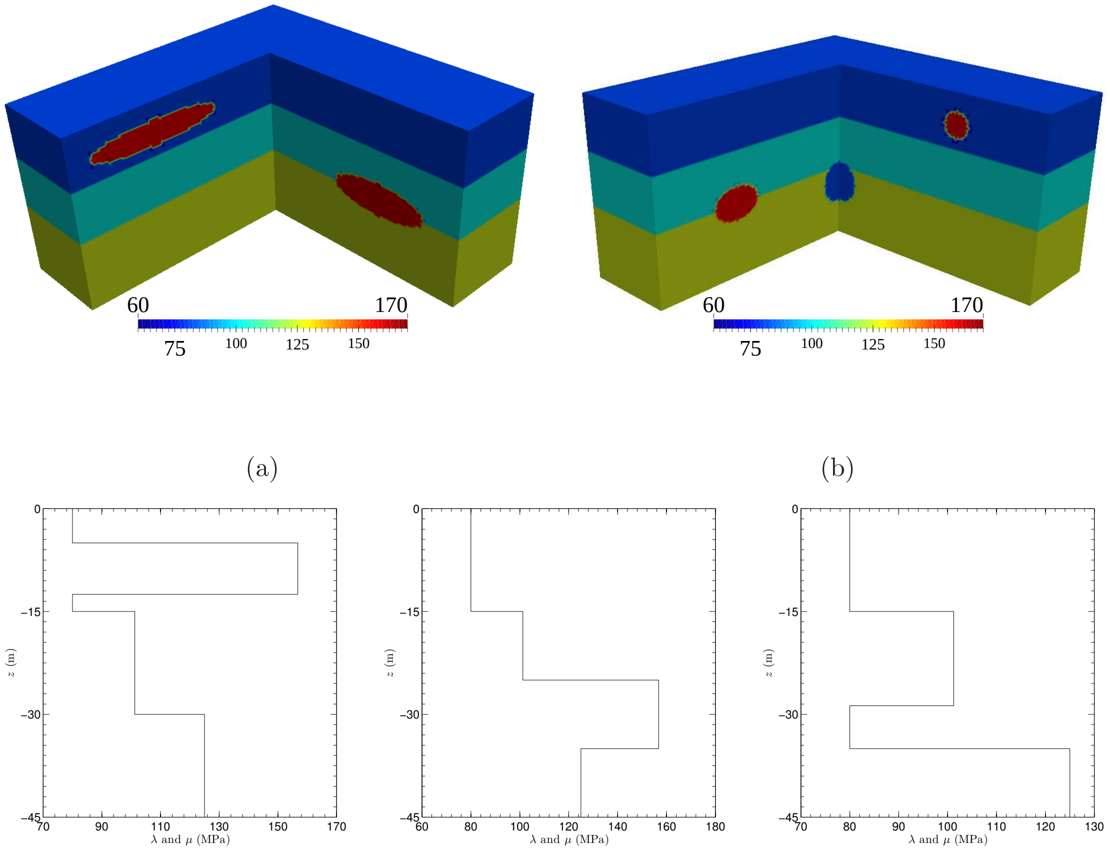

(a) (b)

(c) (d) (e)

Figure 3.28: Layered medium with three inclusions: target λ and μ (a) along a cross-section that cuts through the domain from $(x, y) = (\text{-}20, \text{-}46.5)$ to $(\text{-}20, 20)$ to $(46.5, 20)$; (b) along a cross-section that cuts through the medium from $(x, y) = (20, 46.5)$ to $(20, \text{-}20)$ to $(\text{-}46.5, \text{-}20)$; (c) profile at $(x, y) = (\text{-}20, \text{-}20)$; (d) profile at $(x, y) = (20, 20)$; and (e) profile at $(x, y) = (20, \text{-}20)$.

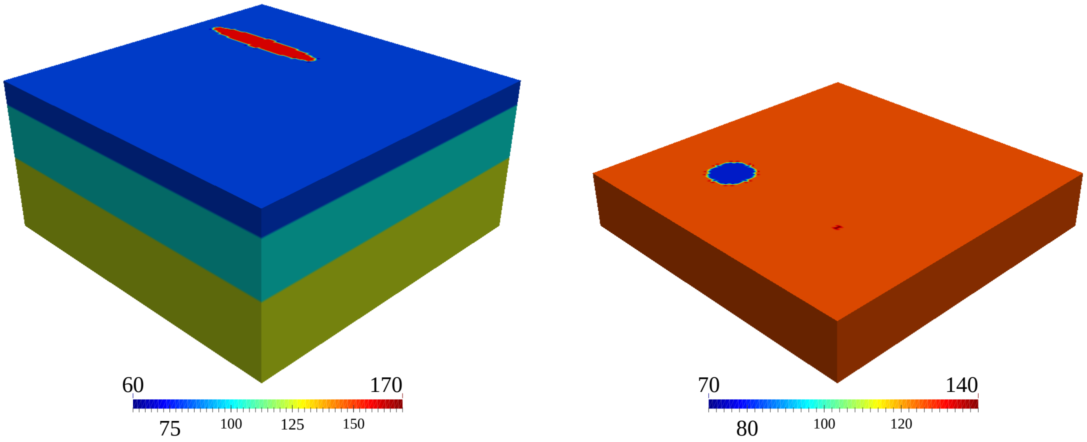

(a) (b)

Figure 3.29: Layered medium with three inclusions: target λ and μ on (a) the $z = -8.75$ m cross-section; and (b) the $z = -35$ m cross-section.

Figure 3.30 shows the inverted profile along a cross-section that cuts through the domain from (x, y) = (-20, -46.5) to (-20, 20) to (46.5, 20). The cross section passes through the larger semi-principal axes of both ellipsoids, and shows very good reconstruction of the μ profile, and satisfactory inversion of the λ profile. The layering is sharp, and the ellipsoids are captured well. In Fig. 3.31, a cross section of the inverted profiles from (x, y) = (20, 46.5) to (20, -20) to (-46.5, -20) is displayed, where it passes through the smaller semi-principal axes of the ellipsoids and the center of the sphere. The ellipsoids are well captured; however, the sphere, which consists of "soft" materials, can hardly be noticed, especially, in the λ profile. Figure 3.32(a) and 3.32(b) show the inverted profiles on a cross-section through the domain, situated at 8.75 m from the surface, going through the top ellipsoid's midplane, and show satisfactory reconstruction of the ellipsoid. To see the reconstruction of the sphere in more detail, we consider a cross-section, which goes through the sphere's midplane, situated at 35 m from the top surface; this is shown in Fig. 3.32(c) and 3.32(d). The sphere's footprint is visible in the λ profile, whereas it is more conspicuous in the μ profile.

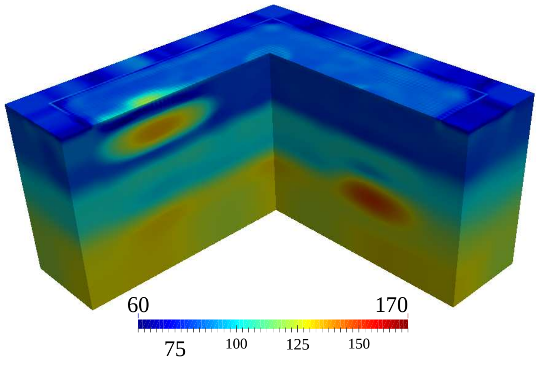

(a) λ ($f_{max} = 40$ Hz) (b) μ ($f_{max} = 40$ Hz)

Figure 3.30: Simultaneous inversion for λ and μ: cross-section cuts through the domain from (x, y) = (-20, -46.5) to (-20, 20) to (46.5, 20) (layered medium with three inclusions).

We also compare cross sections of the inverted profiles with the target along three different lines, which pass through the ellipsoids and the sphere. These are shown in Fig. 3.33. Overall, the inverted profiles are satisfactory.

3.4 Summary

We discussed a full-waveform-based inversion methodology for imaging the elastic properties of a soil medium in three-dimensional, arbitrarily heterogeneous,

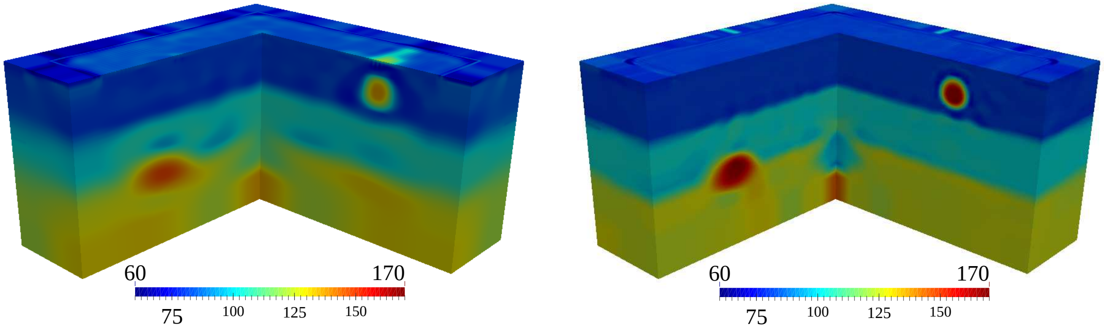

(a) λ ($f_{max} = 40$ Hz)

(b) μ ($f_{max} = 40$ Hz)

Figure 3.31: Simultaneous inversion for λ and μ: cross-section cuts through the domain from $(x, y) = (20, 46.5)$ to $(20, \text{-}20)$ to $(\text{-}46.5, \text{-}20)$ (layered medium with three inclusions).

semi-infinite domains. The problem typically arises in geotechnical site characterization and geophysical explorations, where high-fidelity imaging of the two Lamé parameters (or an equivalent pair) is of interest. Elastic waves are used as probing agents to interrogate the soil medium, and the response of the medium to these waves are collected at receivers located on the ground surface. The inversion process relies on minimizing a misfit between the collected response at receiver locations, and a computed response based on a trial distribution of the Lamé parameters. We used the apparatus of PDE-constrained optimization to impose the forward wave propagation equations to the minimization problem, directly in the time-domain. Moreover, PMLs were used to limit the extent of the computational domain.

To alleviate the ill-posedness, associated with inverse problems, we used reg-

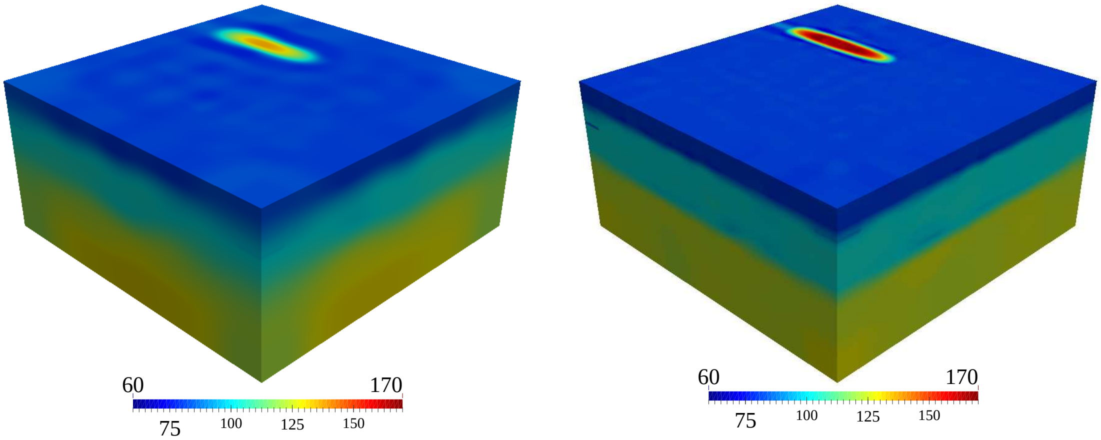

(a) λ (f_{max} = 40 Hz) (b) μ (f_{max} = 40 Hz)

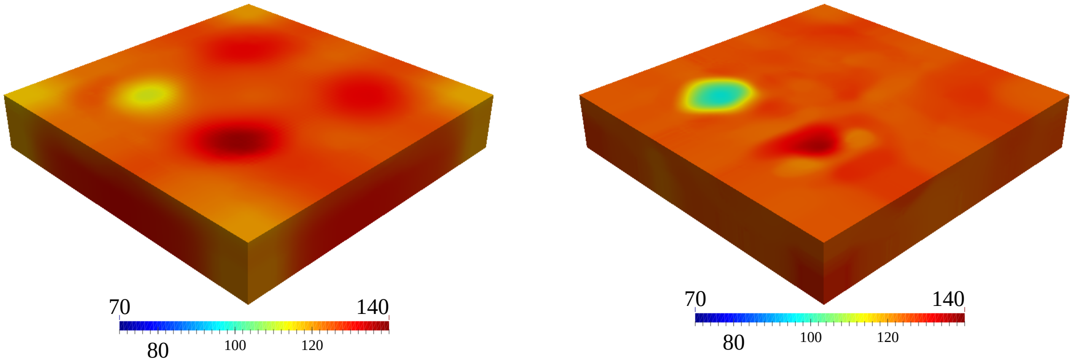

(c) λ (f_{max} = 40 Hz) (d) μ (f_{max} = 40 Hz)

Figure 3.32: Layered medium with three inclusions: (a) inverted λ profile on the z = -8.75 m cross-section; (b) inverted μ profile on the z = -8.75 m cross-section; (c) inverted λ profile on the z = -35 m cross-section; and (d) inverted μ profile on the z = -35 m cross-section.

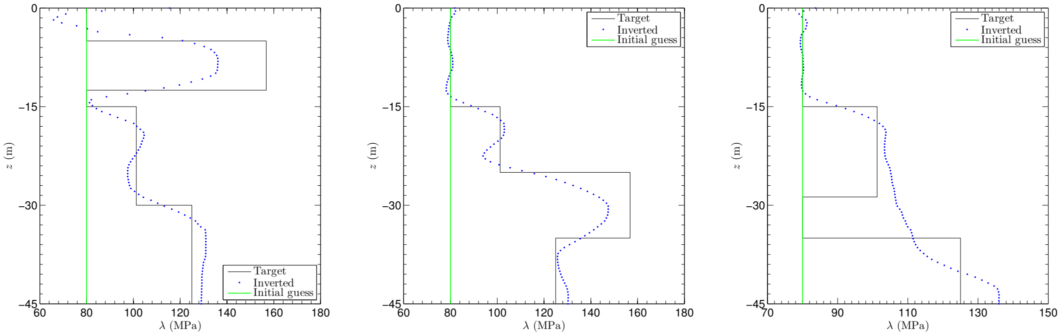

(a) λ at $(x, y) = (-20, -20)$ (b) λ at $(x, y) = (20, 20)$ (c) λ at $(x, y) = (20, -20)$

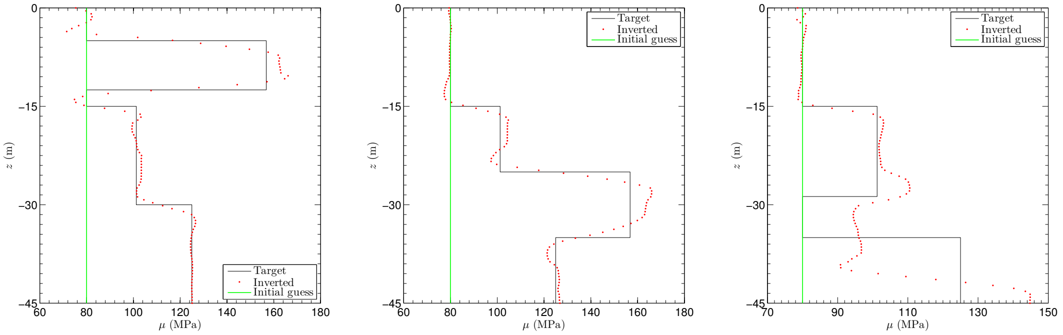

(d) μ at $(x, y) = (-20, -20)$ (e) μ at $(x, y) = (20, 20)$ (f) μ at $(x, y) = (20, -20)$

Figure 3.33: Cross-sectional profiles of λ and μ (layered medium with three inclusions).

ularization schemes, along with a regularization factor continuation scheme, which tunes the regularization factor adaptively at each inversion iteration. We discussed additional strategies to robustify the inversion algorithm: specifically, we used (a) a source-frequency continuation scheme such that the inversion process evolves by using low-frequency sources, and, gradually, we use sources with higher frequencies; and (b) a biasing scheme for the λ-profile, such that, at early iterations of inversion, the search direction for λ is biased based on that of μ. The latter strategy, in particular, improves the reconstruction of the material profiles when simultaneous inversion of the two Lamé parameters is exercised. To the best of our knowledge, this is the first attempt that the two Lamé parameters have been successfully reconstructed in three-dimensional PML-truncated domains.

By comparing directional finite differences of the discrete objective functional, and directional derivatives obtained via the control problems, we verified the accuracy and correctness of the material gradients. We reported numerical results demonstrating successful reconstruction of both Lamé parameters for smooth and sharp profiles. Overall, the framework discussed in this study seems robust, practical, and promising.

Chapter 4

Site characterization using full-waveform inversion

In the preceding chapters, we discussed the theoretical aspects of a full-waveform-inversion-based methodology for the imaging of the elastic properties of near-surface deposits. We also addressed the forward problem of numerically simulating the propagation of waves in PML-truncated, arbitrarily heterogeneous, elastic domains. We presented several PML formulations for the three-dimensional case, numerical results for the forward problem, as well as numerical results for the associated inverse medium problem using synthetic data.

In this chapter, we focus on the exercising of the developed methodology by real, as opposed to synthetic, data. There are several applications in engineering that stand to benefit from a robust full-waveform-inversion methodology: among these, our focus here is geotechnical site characterization. To this end, we use the data collected during two field experiments in an attempt to validate the theoretical development. Specifically, we consider two cases consistent with our code development cycle: firstly, we describe the design of a field experiment aimed at reproducing in the field plane-strain conditions, in order to allow us to exercise two-dimensional inversion codes. We describe the design, the pre-processing, the field data, and the inversion results. Moreover, we describe comparisons of the inverted full-waveform based profile against those by using two other imaging methods - the non-invasive SASW, as well as an invasive CPT test. Secondly, we describe the field experiment and associated inversion results obtained by exercising the three-dimensional inversion codes.

The remainder of this chapter is organized as follows: first, we review the mathematical and numerical aspects of the underlying inverse medium problem in two space dimensions. We remark that there are differences between the two- and three-dimensional formulation that merit a detailed discussion. The differences stem from the fact that the number of stretching functions for the PML equals the spatial dimensionality: this difference, in turn, affects the temporal complexity, and gives rise to alternative formulations, which could not be trivially obtained by simply reducing the three-dimensional formulations to two dimensions. The two-dimensional development preceded the research described in this dissertation [57]. However, algorithmic modifications/improvements, the field experiment, and the two-dimensional inversion results using the field data were all part of the work described herein. Next, we describe the design, data collection, and full-waveform inversion results based on a field experiment collected at the UCSB NEES site in Garner Valley, California in March 2012. Lastly, we conclude with summary remarks.

4.1 The inverse medium problem in two space dimensions

To fix ideas, we refer to the depiction of the driving application shown in Fig. 4.1: similarly to the three-dimensional case, here too we are interested in reconstructing the formation's profile shown in Fig. 4.1(a). Given the arbitrary heterogeneity of the domain of interest, the problem is inherently three-dimensional. Herein, we describe the methodology by focusing on the two-dimensional counterpart of the original problem, as depicted in Fig. 4.1(b): we accept arbitrary heterogeneity within a two-dimensional slice, but presume that the properties remain unchanged along the third dimension, i.e., a plane strain problem. While, the problem, as defined, departs from the true physical three-dimensional case[1], it still contains all the algorithmic and theoretical complexities associated with the three-dimensional problem. Figure 4.1(c) represents the mathematical idealization of the two-dimensional slice shown in Fig. 4.1(b): the semi-infinite (two-dimensional) physical domain has been truncated to a finite one, through the introduction of PMLs.

4.1.1 The forward problem

We use a hybrid approach for the simulation of the wave motion inside a two-dimensional PML-truncated elastic medium. We refer to [33] and references therein for the complete development of the method. Here, we repeat only the resulting coupled system of equations. Accordingly, find $\mathbf{u}(\mathbf{x}, t)$ in $\Omega^{\mathrm{RD}} \cup \Omega^{\mathrm{PML}}$, and $\mathbf{S}(\mathbf{x}, t)$ in Ω^{PML} (see Fig. 4.2 for domain and boundary designations), where $\mathbf{u}$ and $\mathbf{S}$ reside in appropriate functional spaces and:

---

[1] The problem is still valid in the case of horizontal layers, or even in the case of inclined layers, or even in the case of arbitrary plane heterogeneity.

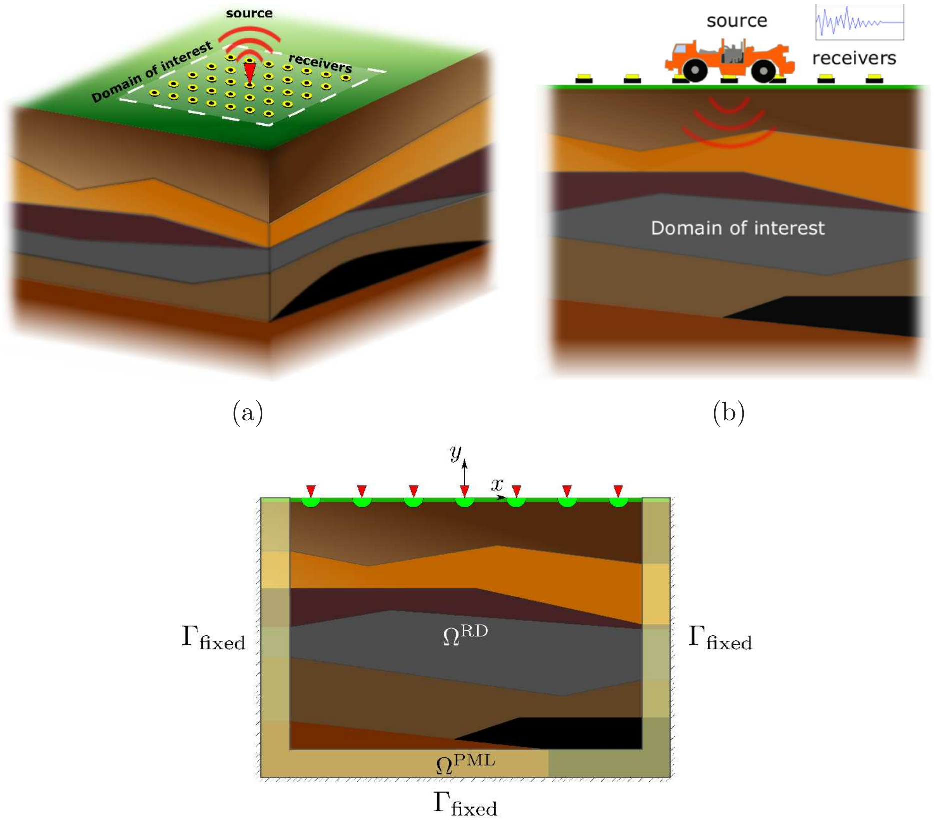

(a) (b)

(c)

Figure 4.1: Problem definition: (a) interrogation of a heterogeneous semi-infinite domain by an active source; (b) a 2D cross-section of the domain showing one source and multiple receivers; and (c) computational model truncated from the semi-infinite medium via the introduction of PMLs.

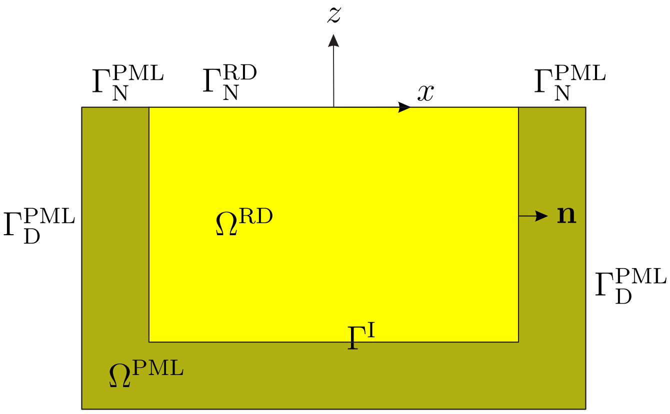

Figure 4.2: A PML-truncated semi-infinite domain in two dimensions.

$$\mathbf{div}\{\mu\ [\nabla\mathbf{u} + (\nabla\mathbf{u})^T] + \lambda(\text{div}\ \mathbf{u})\ \mathcal{I}\} + \mathbf{b} = \rho\ddot{\mathbf{u}}, \qquad \text{in } \Omega^{\rm RD} \times \mathsf{J}, \tag{4.1a}$$

$$\mathbf{div}\{\dot{\mathbf{S}}^T\tilde{\Lambda}_e + \mathbf{S}^T\tilde{\Lambda}_p\} = \rho\ (\ a\ddot{\mathbf{u}} + b\dot{\mathbf{u}} + c\mathbf{u}\ ), \qquad \text{in } \Omega^{\rm PML} \times \mathsf{J}, \tag{4.1b}$$

$$\mathcal{D}\ [\ a\ddot{\mathbf{S}} + b\dot{\mathbf{S}} + c\mathbf{S}\ ] = \frac{1}{2}\ [\ (\nabla\dot{\mathbf{u}})\tilde{\Lambda}_e + \tilde{\Lambda}_e(\nabla\dot{\mathbf{u}})^T + (\nabla\mathbf{u})\tilde{\Lambda}_p + \tilde{\Lambda}_p(\nabla\mathbf{u})^T\ ], \quad \text{in } \Omega^{\rm PML} \times \mathsf{J}. \tag{4.1c}$$

The system is initially at rest, and subject to the following boundary and interface conditions:

$$\{\mu\,[\nabla\mathbf{u} + (\nabla\mathbf{u})^T] + \lambda\,(\mathrm{div}\ \mathbf{u})\,\mathcal{I}\}\mathbf{n} = \boldsymbol{g}_n, \qquad \text{on } \Gamma_{\mathrm{N}}^{\mathrm{RD}} \times \mathsf{J}, \tag{4.2a}$$

$$\{\dot{\mathbf{S}}^T\tilde{\Lambda}_e + \mathbf{S}^T\tilde{\Lambda}_p\}\mathbf{n} = \mathbf{0}, \qquad \text{on } \Gamma_{\mathrm{N}}^{\mathrm{PML}} \times \mathsf{J}, \tag{4.2b}$$

$$\mathbf{u} = \mathbf{0}, \qquad \text{on } \Gamma_{\mathrm{D}}^{\mathrm{PML}} \times \mathsf{J}, \tag{4.2c}$$

$$\mathbf{u}^+ = \mathbf{u}^-, \qquad \text{on } \Gamma_{\mathrm{I}} \times \mathsf{J}, \tag{4.2d}$$

$$\{\mu\,[\nabla\mathbf{u} + (\nabla\mathbf{u})^T] + \lambda(\mathrm{div}\ \mathbf{u})\,\mathcal{I}\}\mathbf{n}^+ + \{\dot{\mathbf{S}}^T\tilde{\Lambda}_e + \mathbf{S}^T\tilde{\Lambda}_p\}\mathbf{n}^- = \mathbf{0}, \qquad \text{on } \Gamma_{\mathrm{I}} \times \mathsf{J}. \tag{4.2e}$$

In the above, $\tilde{\Lambda}_e$ and $\tilde{\Lambda}_p$ are the so-called stretch tensors corresponding to evanescent and propagating waves, respectively, $\mathcal{D}[\cdot]$ is the fourth-order elasticity compliance tensor, and a, b, c are products of certain elements of the stretch tensors [33, 96].

We remark that, while the three-dimensional PML formulation leads to third-order in time semi-discrete forms, due to the multiplication of three stretching functions, the two-dimensional formulation maintains the second-order temporal complexity typical of elastodynamics. Moreover, due to the different algebraic manipulation of the constitutive and kinematic equations in (4.1c) when compared to the approach followed in Chapter 2, the resulting semi-discrete form is symmetric, with a block tri-diagonal mass matrix.

Following a Galerkin approach, similar to what we described in Section 2.3.1, the following semi-discrete form results [33]:

$$\mathbf{M}_{\mathrm{2D}}\ddot{\mathbf{d}} + \mathbf{C}_{\mathrm{2D}}\dot{\mathbf{d}} + \mathbf{K}_{\mathrm{2D}}\mathbf{d} = \mathbf{f}, \tag{4.3}$$

where $\mathbf{M}_{2\mathrm{D}}, \mathbf{C}_{2\mathrm{D}}, \mathbf{K}_{2\mathrm{D}}$ are system matrices and are defined in Appendix A.5, $\mathbf{d}$ is the vector of nodal unknowns comprising displacements in $\bar{\Omega}^{\mathrm{RD}} \cup \bar{\Omega}^{\mathrm{PML}}$, and stress components only in $\bar{\Omega}^{\mathrm{PML}}$, and $\mathbf{f}$ is the vector of applied forces. Several methods can be used to integrate (4.3) in time; for example, application of the well-known family of Newmark methods would require for the $n+1$-th time step to solve:

$$\hat{\mathbf{K}}\mathbf{d}^{n+1} = \mathbf{f}^{n+1} + \mathbf{M}_{2\mathrm{D}}(a_0\mathbf{d}^n + a_2\dot{\mathbf{d}}^n + a_3\ddot{\mathbf{d}}^n) + \mathbf{C}_{2\mathrm{D}}(a_1\mathbf{d}^n + a_4\dot{\mathbf{d}}^n + a_5\ddot{\mathbf{d}}^n), \tag{4.4}$$

where the effective stiffness matrix is

$$\hat{\mathbf{K}} = a_0\mathbf{M}_{2\mathrm{D}} + a_1\mathbf{C}_{2\mathrm{D}} + \mathbf{K}_{2\mathrm{D}}, \tag{4.5}$$

and the velocity-like and acceleration-like updates are given by

$$\begin{aligned} \dot{\mathbf{d}}^{n+1} &= a_1(\mathbf{d}^{n+1} - \mathbf{d}^n) - a_4\dot{\mathbf{d}}^n - a_5\ddot{\mathbf{d}}^n, \\ \ddot{\mathbf{d}}^{n+1} &= a_0(\mathbf{d}^{n+1} - \mathbf{d}^n) - a_2\dot{\mathbf{d}}^n - a_3\ddot{\mathbf{d}}^n, \end{aligned} \tag{4.6}$$

in which a_0-a_5 are constants whose values depend on the choice of the particular Newmark method[2]. Given initial conditions $\mathbf{d}^0 = \mathbf{u}_0, \dot{\mathbf{d}}^0 = \mathbf{v}_0$, use of (4.4-4.6) allows the integration of the semi-discrete form. Alternatively, (4.4) and (4.6), supplemented by the initial conditions, can be cast in the following compact form:

$$\mathbf{Q}\hat{\mathbf{d}} = \hat{\mathbf{f}}, \tag{4.7}$$

---

[2] For instance, for a constant average acceleration scheme, $a_0 = 1/(\alpha\ \Delta t^2), a_1 = \delta/(\alpha\ \Delta t), a_2 = 1/(\alpha\ \Delta t), a_3 = 1/(2\ \alpha) - 1, a_4 = \delta/\alpha - 1, a_5 = (\delta/2\ \alpha - 1)\Delta t$, where $\delta = 1/2, \alpha = 1/4$.

where $\hat{\mathbf{d}} = [\mathbf{d}^0\ \dot{\mathbf{d}}^0\ \ddot{\mathbf{d}}^0\ \mathbf{d}^1\ \dot{\mathbf{d}}^1\ \ddot{\mathbf{d}}^1 \ldots \mathbf{d}^N\ \dot{\mathbf{d}}^N\ \ddot{\mathbf{d}}^N]^T$ corresponds to the space-time discretization of the unknown variables and their temporal derivatives (N is the number of time steps, and $\mathbf{d}^i$ are the spatial degrees of freedom at the i-th time step), and $\hat{\mathbf{f}} = [\mathbf{u}_0\ \mathbf{v}_0\ \mathbf{f}^0\ \mathbf{f}^1\ \mathbf{0}\ \mathbf{0} \ldots \mathbf{f}^N\ \mathbf{0}\ \mathbf{0}]^T$. The discrete forward operator $\mathbf{Q}$ is defined as:

$$\mathbf{Q} = \begin{bmatrix} \mathbf{I} & \mathbf{0} & \mathbf{0} & \mathbf{0} & \mathbf{0} & \mathbf{0} & \cdots & \mathbf{0} & \mathbf{0} & \mathbf{0} & \mathbf{0} & \mathbf{0} & \mathbf{0} \\ \mathbf{0} & \mathbf{I} & \mathbf{0} & \mathbf{0} & \mathbf{0} & \mathbf{0} & \cdots & \mathbf{0} & \mathbf{0} & \mathbf{0} & \mathbf{0} & \mathbf{0} & \mathbf{0} \\ \mathbf{K} & \mathbf{C} & \mathbf{M} & \mathbf{0} & \mathbf{0} & \mathbf{0} & \cdots & \mathbf{0} & \mathbf{0} & \mathbf{0} & \mathbf{0} & \mathbf{0} & \mathbf{0} \\ \mathbf{L}_1 & \mathbf{L}_2 & \mathbf{L}_3 & \hat{\mathbf{K}} & \mathbf{0} & \mathbf{0} & \cdots & \mathbf{0} & \mathbf{0} & \mathbf{0} & \mathbf{0} & \mathbf{0} & \mathbf{0} \\ a_1\mathbf{I} & a_4\mathbf{I} & a_5\mathbf{I} & -a_1\mathbf{I} & \mathbf{I} & \mathbf{0} & \cdots & \mathbf{0} & \mathbf{0} & \mathbf{0} & \mathbf{0} & \mathbf{0} & \mathbf{0} \\ a_0\mathbf{I} & a_2\mathbf{I} & a_3\mathbf{I} & -a_0\mathbf{I} & \mathbf{0} & \mathbf{I} & \cdots & \mathbf{0} & \mathbf{0} & \mathbf{0} & \mathbf{0} & \mathbf{0} & \mathbf{0} \\ \vdots & \vdots & \vdots & \vdots & \vdots & \vdots & \ddots & \vdots & \vdots & \vdots & \vdots & \vdots & \vdots \\ \mathbf{0} & \mathbf{0} & \mathbf{0} & \mathbf{0} & \mathbf{0} & \mathbf{0} & \cdots & \mathbf{L}_1 & \mathbf{L}_2 & \mathbf{L}_3 & \hat{\mathbf{K}} & \mathbf{0} & \mathbf{0} \\ \mathbf{0} & \mathbf{0} & \mathbf{0} & \mathbf{0} & \mathbf{0} & \mathbf{0} & \cdots & a_1\mathbf{I} & a_4\mathbf{I} & a_5\mathbf{I} & -a_1\mathbf{I} & \mathbf{I} & \mathbf{0} \\ \mathbf{0} & \mathbf{0} & \mathbf{0} & \mathbf{0} & \mathbf{0} & \mathbf{0} & \cdots & a_0\mathbf{I} & a_2\mathbf{I} & a_3\mathbf{I} & -a_0\mathbf{I} & \mathbf{0} & \mathbf{I} \end{bmatrix}, \tag{4.8}$$

where

$$\begin{aligned} \mathbf{L}_1 &= -a_0\mathbf{M}_{\mathrm{2D}} - a_1\mathbf{C}_{\mathrm{2D}}, \\ \mathbf{L}_2 &= -a_2\mathbf{M}_{\mathrm{2D}} - a_4\mathbf{C}_{\mathrm{2D}}, \\ \mathbf{L}_3 &= -a_3\mathbf{M}_{\mathrm{2D}} - a_5\mathbf{C}_{\mathrm{2D}}. \end{aligned}$$

We emphasize that (4.7) is precisely the Newmark algorithm written in a different form, which is better suited for the solution of the inverse medium problem at hand, as it will become apparent later. Notice that the first two rows of (4.8) recover the initial conditions, whereas the third row solves for $\ddot{\mathbf{d}}^0$. The fourth row solves for $\mathbf{d}^1$, and the fifth and sixth rows yield $\dot{\mathbf{d}}^1, \ddot{\mathbf{d}}^1$, respectively. Finally, the last three rows, solve for $\mathbf{d}^N$, and update $\dot{\mathbf{d}}^N, \ddot{\mathbf{d}}^N$, respectively.

4.1.2 The inverse problem

We consider the following PDE-constrained minimization problem:

$$\min_{\lambda,\mu} \mathcal{J}(\lambda,\mu) := \frac{1}{2}\sum_{j=1}^{N_r}\int_0^T \int_{\Gamma_m} (u-u_m)^2 \; \delta(x-x_j) \; ds(x) \; dt + \mathcal{R}^{TN}(\lambda,\mu), \quad (4.9)$$

subject to the (continuous) forward problem governed by the initial- and boundary-value problem (4.1a)-(4.2e).

In the above, u is the vertical component of the computed displacement, and u_m corresponds to the measured vertical displacement component (obtained via sensor data processing).

One may use the (formal) Lagrangian approach [86], whereby the forward problem (4.1a)-(4.2e) is imposed via Lagrange multipliers (adjoint variables) to the functional (4.9). One then seeks a stationary point to the resulting Lagrangian functional, by forcing the first-order optimality conditions to vanish. This approach was discussed in detail in Chapter 3, and is referred to as an *optimize-then-discretize* approach, since the optimality conditions are sought first in their continuous form, followed by spatial and temporal discretization steps[3].

Alternatively, one may discretize the continuous constrained optimization problem (4.9) first, and then compute the corresponding *discrete* optimality conditions [68, 94]. The procedure is referred to as a *discretize-then-optimize* approach

---

[3] See also [57].

[94]. The differences between the two approaches are summarized in the following diagram:

$$\begin{tikzcd}
\mathcal{J} \arrow[r, "discretize"] \arrow[d, "optimize"] & \mathbf{J} \arrow[d, "optimize"] \\
\mathcal{G} \arrow[r, "discretize"] & \mathbf{g}^{otd}, \mathbf{g}^{dto},
\end{tikzcd}$$

where $\mathbf{J}$ is the discrete objective functional, $\mathcal{G}$ is the continuous gradient of the continuous objective functional $\mathcal{J}$, $\mathbf{g}^{otd}$ refers to the discrete gradient obtained through the *optimize-then-discretize* approach, and $\mathbf{g}^{dto}$ is the discrete gradient computed through the *discretize-then-optimize* procedure.

Herein, we opt for the *discretize-then-optimize* approach for the following reasons: the *optimize-then-discretize* approach, oftentimes, yields an approximation of the gradient of the discrete functional (4.9), while the *discretize-then-optimize* approach yields the *exact* gradient of the discrete functional. Although both approaches involve approximation due to the discretization step, the *optimize-then-discretize* approach, sometimes[4], does not yield the exact gradient of either the continuous functional, or of the discretized functional [94]. Therefore, the *optimize-then-discretize* approach may result in inconsistent gradients, which, in turn, may cause numerical difficulties; for instance, a downhill direction as determined by the inconsistent gradient, may actually be an uphill direction of the functional. This may force the Armijo condition to be violated [92] and, eventually, force the optimizer to stop. The

---

[4] The inexact gradient is likely to manifest when the time integrator is “unsymmetric”, as in the case with the Newmark method [97].

discretize-then-optimize approach, however, is more robust and does not suffer from such problems (see, for example, Chapter 4 in [94] for a comprehensive discussion and [68] for a systematic treatment and a detailed example).

Discrete optimality conditions

Discretization of the objective functional (4.9) in space and time yields:

$$\min_{\boldsymbol{\lambda},\boldsymbol{\mu}} \mathbf{J}(\boldsymbol{\lambda},\boldsymbol{\mu}) := \frac{1}{2}(\hat{\mathbf{d}} - \hat{\mathbf{d}}_m)^T\bar{\mathbf{B}}(\hat{\mathbf{d}} - \hat{\mathbf{d}}_m) + \frac{R_\lambda}{2}\boldsymbol{\lambda}^T\mathbf{R}\,\boldsymbol{\lambda} + \frac{R_\mu}{2}\boldsymbol{\mu}^T\mathbf{R}\,\boldsymbol{\mu}, \qquad (4.10)$$

where $\hat{\mathbf{d}}$ satisfies the discrete forward problem (4.7). Here, $\boldsymbol{\lambda}$ and $\boldsymbol{\mu}$ are discrete material properties, $\hat{\mathbf{d}}_m$ are the discrete space-time measurement data, $\bar{\mathbf{B}}$ is the discretized (space-time) measurement operator[5], and $\mathbf{R}$ is the matrix corresponding to the discretization scheme used for the regularization terms. The discrete Lagrangian corresponding to (4.10) becomes:

$$\mathcal{L}(\hat{\mathbf{d}},\hat{\mathbf{p}},\boldsymbol{\lambda},\boldsymbol{\mu}) := \mathbf{J}(\boldsymbol{\lambda},\boldsymbol{\mu}) - \hat{\mathbf{p}}^T(\mathbf{Q}\hat{\mathbf{d}} - \hat{\mathbf{f}}), \qquad (4.11)$$

where $\hat{\mathbf{p}} = [\mathbf{r}^0\ \mathbf{q}^0\ \mathbf{p}^0\ \mathbf{r}^1\ \mathbf{q}^1\ \mathbf{p}^1 \ldots \mathbf{r}^N\ \mathbf{q}^N\ \mathbf{p}^N]^T$ is the *discrete* (space-time) Lagrange multiplier that enforces the *discrete* forward problem ($\mathbf{Q}\hat{\mathbf{d}} = \hat{\mathbf{f}}$) as a constraint[6]. The discrete optimality conditions for (4.11) are obtained by requiring that the derivatives of the Lagrangian with respect to each of the variables vanish. Taking the derivative

---

[5] $\bar{\mathbf{B}}$ is a block diagonal matrix with $\Delta t\ \mathbf{B}$ on the diagonal; Δt denotes the time step, and $\mathbf{B}$ is a square matrix that is zero everywhere except on the diagonals that correspond to a degree of freedom for which measured data are available.

[6] Though not necessary, $\mathbf{q}^i$ can be thought of as $\dot{\mathbf{p}}^i$, and $\mathbf{r}^i$ as $\ddot{\mathbf{p}}^i$ at the i-th time step.

with respect to the Lagrange multiplier $\hat{\mathbf{p}}$ recovers the discrete forward problem (4.7), which in this context, we refer to as the discrete state equation:

$$\mathcal{L}_{\hat{\mathbf{p}}}(\hat{\mathbf{d}}, \hat{\mathbf{p}}, \boldsymbol{\lambda}, \boldsymbol{\mu}) = -\mathbf{Q}\hat{\mathbf{d}} + \hat{\mathbf{f}} = \mathbf{0}. \tag{4.12}$$

We remark that equation (4.12) has the structure discussed earlier in section 4.1.1. The discrete adjoint equation is obtained by requiring that the derivative of the discrete Lagrangian with respect to $\hat{\mathbf{d}}$ vanish, that is,

$$\mathcal{L}_{\hat{\mathbf{d}}}(\hat{\mathbf{d}}, \hat{\mathbf{p}}, \boldsymbol{\lambda}, \boldsymbol{\mu}) = -\mathbf{Q}^T\hat{\mathbf{p}} + \mathbf{B}(\hat{\mathbf{d}} - \hat{\mathbf{d}}_m) = \mathbf{0}. \tag{4.13}$$

We remark that (4.13) involves the transpose of $\mathbf{Q}$, and hence, (4.13) is solved by marching backwards in time. For example, from the last two rows of (4.13), we obtain the final conditions:

$$\mathbf{p}^N = \mathbf{0}, \tag{4.14}$$
$$\mathbf{q}^N = \mathbf{0}, \tag{4.15}$$

respectively; and the third row from the bottom yields

$$\hat{\mathbf{K}}^T\mathbf{r}^N = \Delta t\mathbf{B}(\mathbf{d}^N - \mathbf{d}_m^N) + a_1\mathbf{q}^N + a_0\mathbf{p}^N, \tag{4.16}$$

which can be solved for $\mathbf{r}^N$. For time steps $n = N, N-1, \cdots, 2$, we deduce the following algorithm:

update:

$$\mathbf{p}^{n-1} = (a_3\mathbf{M}_{2\mathrm{D}}^T + a_5\mathbf{C}_{2\mathrm{D}}^T)\mathbf{r}^n - a_5\mathbf{q}^n - a_3\mathbf{p}^n,$$

$$\mathbf{q}^{n-1} = (a_2\mathbf{M}_{2\mathrm{D}}^T + a_4\mathbf{C}_{2\mathrm{D}}^T)\mathbf{r}^n - a_4\mathbf{q}^n - a_2\mathbf{p}^n. \tag{4.17a}$$

solve:

$$\begin{aligned}\hat{\mathbf{K}}^T\mathbf{r}^{n-1} = \Delta t\mathbf{B}(\mathbf{d}^{n-1} - \mathbf{d}_m^{n-1}) + a_1\mathbf{q}^{n-1} + a_0\mathbf{p}^{n-1}\\ + (a_0\mathbf{M}_{2\mathrm{D}}^T + a_1\mathbf{C}_{2\mathrm{D}}^T)\mathbf{r}^n - a_1\mathbf{q}^n - a_0\mathbf{p}^n.\end{aligned} \tag{4.17b}$$

Notice that contrary to the conventional application of the Newmark's method, here, we first update, and then solve. Finally, the first three rows of (4.13) result in the following equations:

solve:

$$\mathbf{M}_{2\mathrm{D}}^T\mathbf{p}^0 = (a_3\mathbf{M}_{2\mathrm{D}}^T + a_5\mathbf{C}_{2\mathrm{D}}^T)\mathbf{r}^1 - a_5\mathbf{q}^1 - a_3\mathbf{p}^1 \tag{4.18a}$$

update:

$$\mathbf{q}^0 = -\mathbf{C}_{2\mathrm{D}}^T\mathbf{p}^0 + (a_2\mathbf{M}_{2\mathrm{D}}^T + a_4\mathbf{C}_{2\mathrm{D}}^T)\mathbf{r}^1 - a_4\mathbf{q}^1 - a_2\mathbf{p}^1,$$

$$\mathbf{r}^0 = -\mathbf{K}_{2\mathrm{D}}^T\mathbf{p}^0 + (a_0\mathbf{M}_{2\mathrm{D}}^T + a_1\mathbf{C}_{2\mathrm{D}}^T)\mathbf{r}^1 - a_1\mathbf{q}^1 - a_0\mathbf{p}^1 + \Delta t\mathbf{B}(\mathbf{d}^0 - \mathbf{d}_m^0). \tag{4.18b}$$

The third discrete optimality condition is obtained by setting the derivative of (4.11) with respect to $\boldsymbol{\lambda}$ and $\boldsymbol{\mu}$ to zero. That is:

$$\mathcal{L}_{\boldsymbol{\lambda}}(\hat{\mathbf{d}}, \hat{\mathbf{p}}, \boldsymbol{\lambda}, \boldsymbol{\mu}) = R_\lambda \, \mathbf{R} \, \boldsymbol{\lambda} - \frac{\partial}{\partial \boldsymbol{\lambda}}(\hat{\mathbf{p}}^T \, \mathbf{Q} \, \hat{\mathbf{d}}) = \mathbf{0}, \tag{4.19}$$

$$\mathcal{L}_{\boldsymbol{\mu}}(\hat{\mathbf{d}}, \hat{\mathbf{p}}, \boldsymbol{\lambda}, \boldsymbol{\mu}) = R_\mu \, \mathbf{R} \, \boldsymbol{\mu} - \frac{\partial}{\partial \boldsymbol{\mu}}(\hat{\mathbf{p}}^T \, \mathbf{Q} \, \hat{\mathbf{d}}) = \mathbf{0}, \tag{4.20}$$

where the terms $\frac{\partial}{\partial \boldsymbol{\lambda}}(\hat{\mathbf{p}}^T \, \mathbf{Q} \, \hat{\mathbf{d}})$ and $\frac{\partial}{\partial \boldsymbol{\mu}}(\hat{\mathbf{p}}^T \, \mathbf{Q} \, \hat{\mathbf{d}})$ can be computed in a straightforward manner, as outlined in Appendix D.

Next, an iterative procedure may be used such that the discrete material properties are updated according to a gradient-based scheme. Here, we use a Fletcher-Reeves conjugate gradient scheme [57], endowed with an Armijo backtracking line search, to iteratively update the material profiles.

4.2 The field experiment - design considerations

In this section, we discuss the design of a field experiment that will provide us with field-measured data, which can then be used to exercise the two-dimensional inversion codes we developed/modified based on the preceding theory. To this end, we attempt to generate plane strain conditions in the field, so that we then attempt to invert for the properties of a two-dimensional site slice (Fig. 4.3c). Since the loads we can impart on the ground surface are really three-dimensional, plane strain conditions would require loading along densely populated lines (Fig. 4.3a) to emulate theoretical line loads. In this section, we discuss how this can be accomplished in a practical manner. Naturally, to replicate plane strain conditions in the field, the loading is only one of the difficulties: a key assumption we make here is that there is lateral material homogeneity, that is, the site slice may be, in plane, arbitrarily heterogeneous, but the properties do not change along the direction perpendicular to the slice. While restrictive, the assumption is realistic for layered sites, is a significant improvement upon pervasive one-dimensional assumptions of other methodologies, and, due to prior characterizations, it was a reasonable assumption to make for the specific field experiment site (Hornsby Bend in Austin, TX).

With these assumptions in mind, the question becomes: how can a line load be approximated by a sequence of loads in the field, which may resemble point loads, and are suitably spaced along straight lines whose extent remains finite (line loads are infinite in extent)? The question is depicted in Fig. 4.3. Therefore, we are interested in arriving at an estimate of the spacing between the loads, and an estimate of the finite extent of the line of loads. We focus next on these two questions of spatial load distribution, but, in parallel, we also address the temporal variability of the load signal. We sketch the process on the basis of a homogeneous halfspace by drawing on classical solutions; site-specific conditions will also have an effect on load spacing and load extent, but when the design is based on minimum expected wavelength, then the design is conservative.

Our methodology is based on the time-domain point-load analytical solutions in two-dimensional and three-dimensional space, that is, Lamb's problem and the Pekeris-Mooney's problem, respectively [98]. We use these solutions to derive the response of a two-dimensional or three-dimensional soil domain due to (temporally) arbitrary loads. In this way, the problem of designing the experiment reduces to a parametric study. We study first the effect of truncating the line load from extending to infinity by finding a suitable truncation length. Then, we replace the truncated

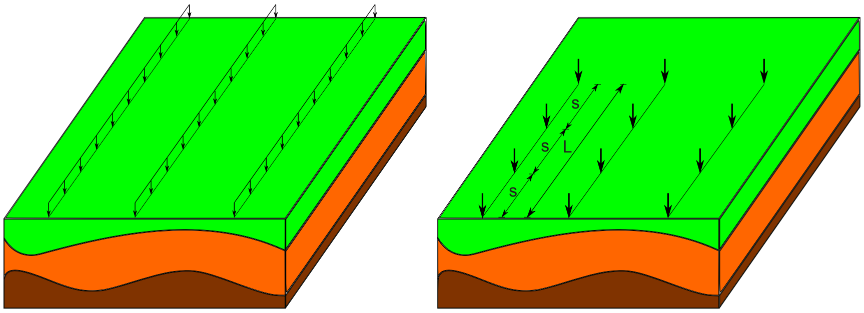

(a) 3D heterogeneous halfspace subjected to a series of line loads extending to infinity; heterogeneity is in plane only.

(b) 3D heterogeneous halfspace subjected to a finite number of point sources spaced apart by s, arranged along lines of L total length.

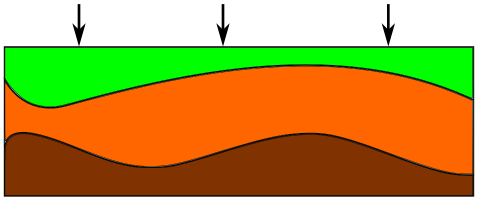

(c) Equivalent 2D halfplane subjected to concentrated sources.

Figure 4.3: Approximation of a 3D halfspace problem by a 2D halfplane problem.

load line with equivalent point sources and determine the appropriate spacing between them. Fig. 4.3 displays schematically this objective. Finally, we comment on designing signals that are appropriate for probing geotechnical sites and also discuss theoretical and practical issues that arise in such field experiments.

4.2.1 Line load truncation and spacing requirements

An impulsive in-plane point load is applied on the surface of a halfplane and the resulting displacements are sought. This plane strain problem is equivalent to an infinite line load applied on the surface of a halfspace. We denote the vertical displacement of a point $(x_1, 0)$ at time t by $G^{2D}(x_1, t)$, where G^{2D} stands for the Green's function, and the impulse load acts at the origin. The temporal dependence of the load can be described via the Dirac-delta function: exploiting superposition, we obtain the response due to any arbitrary time signal, denoted by $f^{2D}(t)$, via the following convolution integral:

$$u^{2D}(x_1, t) = \int_0^t f^{2D}(\tau) \; G^{2D}(x_1, t - \tau) \; d\tau. \tag{4.21}$$

The above relation allows us to compute the response of a halfplane subjected to any temporally arbitrary vertical force that acts on its surface. Special care must be taken when computing the integral since it has a singularity due to the arrival of the Rayleigh wave. Therefore, the integral should be interpreted in the Cauchy principal value sense. Details of the Green's function $G^{2D}(x_1, t)$ can be found in [98].

A vertical point source that varies as a step function in time is applied on the surface of a halfspace. The vertical displacement of a point $(x_1, x_2, 0)$ at time t

is denoted by $G^{3D}(x_1, x_2, t)$, and the load acts at the origin. Details of the Green's function G^{3D} are given in Appendix F. The time signal can be described via a Heaviside function. However, we are interested in obtaining the response due to any arbitrary load, not only those with a simple step-like signature. Hence, our first attempt in making this problem fit into our needs, is to represent any arbitrary load $f^{3D}(t)$ as a summation of Heaviside functions and denote this approximation by $f_n^{3D}(t)$. Indeed, given $n+1$ pairs $\{t_i, f_i = f^{3D}(t_i)\}, i = 0, 1, \cdots, n$, we have

$$\begin{aligned} f_n^{3D}(t) &= \frac{1}{2}(f_0 + f_1)(H_0 - H_1) + \frac{1}{2}(f_1 + f_2)(H_1 - H_2) + \cdots \\ &+ \frac{1}{2}(f_{n-1} + f_n)(H_{n-1} - H_n), \end{aligned} \tag{4.22}$$

where we used $H_i \equiv H(t - t_i)$ for notational simplicity, and t_i indicates time value at node i. Re-arranging the above relation yields the following more convenient form:

$$f_n^{3D}(t) = \sum_{i=0}^{n} h_i \; H(t - t_i), \tag{4.23}$$

where

$$h_i = \begin{cases} \frac{1}{2}(f_0 + f_1), & \text{for } i = 0, \\ -\frac{1}{2}(f_{n-1} + f_n), & \text{for } i = n, \\ \frac{1}{2}(f_{i+1} - f_{i-1}), & \text{otherwise.} \end{cases} \tag{4.24}$$

Next, we consider a uniform distribution of point sources, with a Heaviside time signature, along a line of finite length. Without loss of generality, we assume that the sources are positioned symmetrically about the origin, and occupy a total length of $2L$ along the x_2 axis (see Fig. 4.4). The response of the halfspace to this distribution, at any arbitrary point on the surface along the x_1 axis, at time t, is denoted by $G^{2L}(x_1, t)$, and is obtained by the following relation

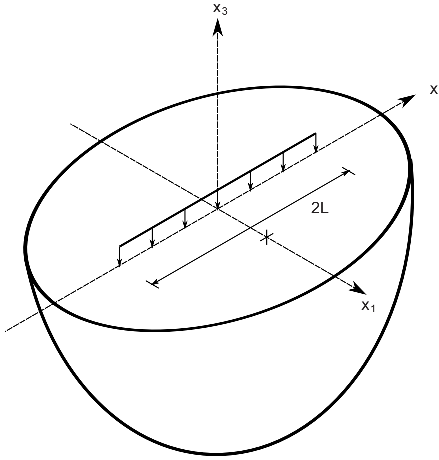

Figure 4.4: Line load with a finite length.

$$G^{2L}(x_1, t) = \int_{-L}^{L} G^{3D}(x_1, x_2, t)\ dx_2, \tag{4.25}$$

where $G^{2L}(x_1, t)$ may be interpreted as the Green's function of a truncated line load. We expect that, at the limit as $L \to \infty$, G^{2L} reduces to the solution of the corresponding plane strain problem in the $x_1 - x_3$ plane. Analytical expressions for the integral exist, and are discussed in detail in Appendix F. Finally, combining (4.23) and (4.25), we obtain the response of the halfspace due to any arbitrary in time, but uniform in space, load with a total length of $2L$ as:

$$u^{2L}(x_1, t) = \sum_{i=0}^{n} h_i\ G^{2L}(x_1, t - t_i). \tag{4.26}$$

Relation (4.26) can be compared against (4.21) to find the appropriate truncation length L.

Once L is determined, the next step is to replace the continuous line load, with point sources. This is readily available by combining $G^{3D}(x_1, x_2, t)$ with (4.23): if we consider $2m + 1$ point sources, symmetrically positioned along the x_2 axis, and spaced s distance apart such that $s = L/m$, the response of the halfspace at a point along the x_1 axis, may be obtained via:

$$u_s^{2L}(x_1, t) = \sum_{i=0}^{n} s\ h_i\ G^{3D}(x_1, 0, t - t_i) + 2 \sum_{j=1}^{m} \sum_{i=0}^{n} s\ h_i\ G^{3D}(x_1, js, t - t_i). \quad (4.27)$$

Relations (4.21) and (4.27) can be compared against each other to determine the appropriate spacing between point sources.

4.2.2 Verification

We consider two numerical experiments to verify the derivation and numerical implementation of (4.21) and (4.26). We consider the material properties summarized in Table 4.1 for the homogeneous, isotropic elastic medium under consideration (notice not all of these properties are independent).

P-wave velocity	$c_p = 346.4$ m/s
S-wave velocity	$c_s = 200.0$ m/s
R-wave velocity	$c_R = 183.9$ m/s
Poisson's ratio	$\nu = 0.25$

Table 4.1: Material properties used in load verification examples.

Lamb and Pekeris-Mooney's Green's functions are displayed in Fig. 4.5 where the observer is located at $x_1 = 20$ m away from the source. The P-wave arrives first, followed by the arrival of the S-wave with a change in slope. The Rayleigh surface wave comes next, and results in an infinite displacement that correspond to the singularity of the associated Green's function. Moreover, in the case of the Pekeris-Mooney's problem, the steady-state response that follows after the Rayleigh singularity corresponds to the Boussinesq's solution to a static load, acting on a halfspace.

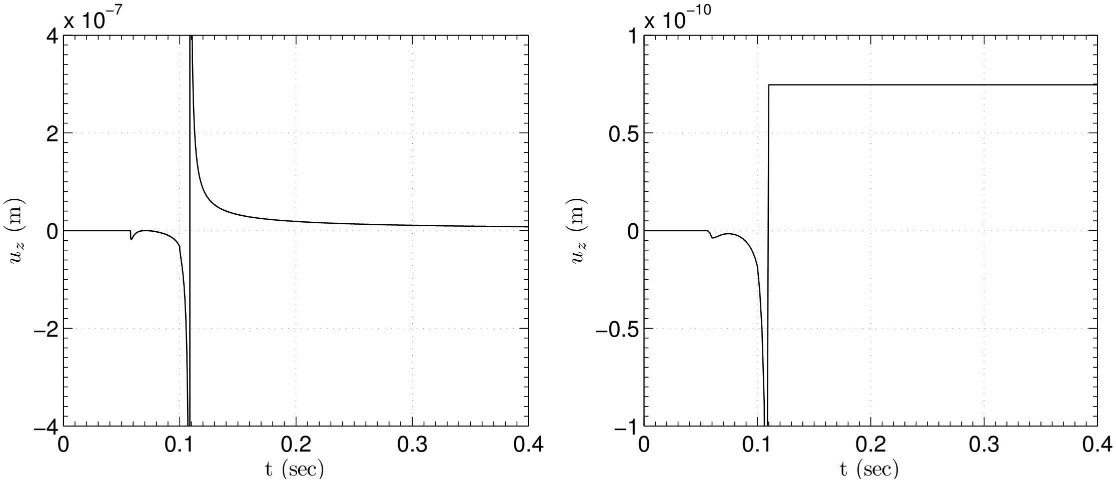

(a) Lamb's solution (b) Pekeris-Mooney's solution

Figure 4.5: 2D and 3D Green's functions.

Example 1. We consider a suddenly applied vertical load, with $f(t) = H(t)$. Then, in (4.21) we have $f^{2D}(t) = 1$, and only one term of the series in (4.26) is sufficient, namely $h_0 = 1$, while $t_0 = 0$.

Considering the value of the P-wave velocity, if we desire to plot the response up to 0.4 seconds, the farthest point from the observer that contributes to the response is located 140 m away. This means that taking $L = 140$ m should yield identical results when comparing (4.21) and (4.26). Indeed, this is the case as shown in Fig. 4.6. We also include the case of $L = 50$ m, which clearly deviates from the exact and the $L = 140$ m case. The deviation begins at $t \approx 0.14$ s, and is more pronounced at around $t = 0.27$ s. These times correspond to the arrival of the P and S-wave from the farthest loaded point (i.e. $x_2 = 50$ m), respectively. Finally, the response reached a steady state value at around 0.29 s, which corresponds to the arrival of the Rayleigh wave from the farthest point. Therefore, we conclude that for this example, the discrepancy can mostly be attributed to the arrival of Rayleigh waves from the farthest point, followed by the final arrival of the S-wave, whereas the P-wave has negligible effect in this regard.

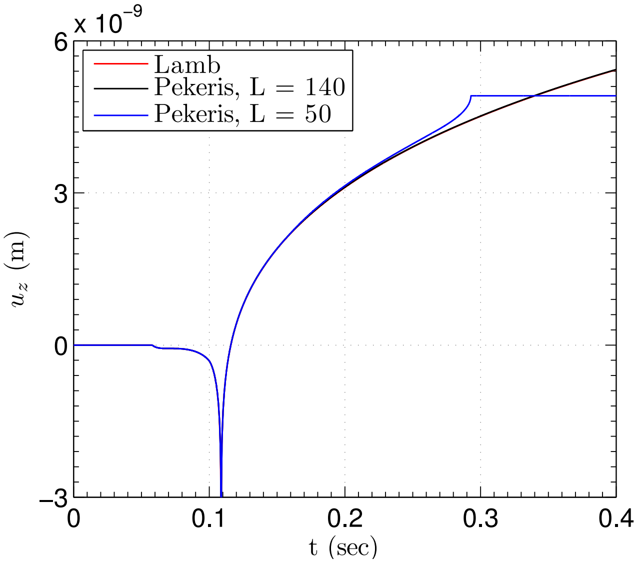

Figure 4.6: Comparison of 2D and 3D systems due to a suddenly applied load.

Example 2. We consider a rectangular pulse such that $f(t) = H(t) - H(t - 0.2)$. Hence, two terms of the series in (4.26) are sufficient, i.e., $h_0 = 1$, and $h_1 = -1$, while $t_0 = 0$, and $t_1 = 0.2$. We compare (4.21) and (4.26) for the same L values and observer location as in the previous example.

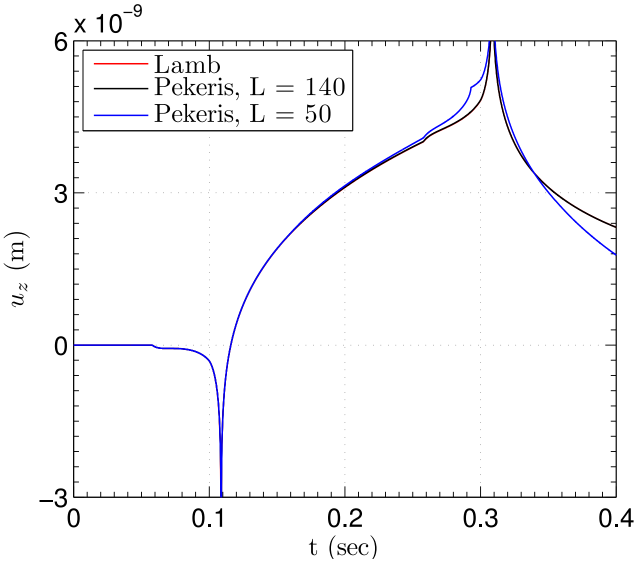

Figure 4.7: Comparison of 2D and 3D systems due to a rectangular pulse load.

Results are displayed in Fig. 4.7. The agreement is excellent between the two relations when L is sufficiently large; discrepancies result from choosing small values for L. We emphasize that the two singularities in the plot correspond to the particular character of the load which initiates and terminates sharply.

4.2.3 Signal design

In this section, we comment on the main features that must be considered in designing signals for site characterization applications based on full waveform-based inversion. For the field experiment we conducted we used the Vibroseis trucks of the NEES@UTexas site (National Science Foundation, Network for Earthquake

Engineering Simulation). In particular, we used T-Rex (tri-axial Vibroseis), and Liquidator (low-frequency Vibroseis) (Fig. 4.8).

Figure 4.8: NEES@UTexas Liquidator Vibroseis.

T-Rex can apply vertical loads with a maximum force amplitude of 267 kN within a frequency range from 12 Hz to about 180 Hz. It can also be used for applying loads outside this frequency range with a lower force amplitude. Liquidator is, however, more widely used when low frequency loading is desired. Liquidator is capable of applying loads within a frequency range of 1.3 Hz to 75 Hz, with a peak force amplitude of 89 kN. Thus, from a practical standpoint, the desired frequency content and amplitude of loading should be restricted within the aforementioned ranges. To record the motion on the ground surface we used 1 Hz geophones.

Our forward and inverse simulators are based on finite element discretization of the geotechnical site of interest. High frequency probing waves require a fine mesh resolution, and, thus, result in an increased computational cost. Therefore, they should be avoided whenever possible, unless fine features of the formation are of interest. Signals with long time duration require a longer observation period, thus also resulting in increased computation time, and increased storage requirements (the solution history must be stored at every time step for inverse problems [94]). Therefore, the time duration of a signal should be only long enough to effectively probe the depth of interest.

We favor signals that probe the geotechnical site of interest more effectively. Typically, these are signals that encompass a range of frequencies rather than containing only few isolated frequencies. The most commonly used class of these signals are chirps, and have shown their effectiveness in radar and geophysical applications. In this experiment, we use linear chirps of the form:

$$f(t) = \sin(2\pi\ (f_0 + \frac{kt}{2})\ t), \tag{4.28}$$

where f_0 is the starting frequency, and k is the chirp rate. With these two parameters, we can design a signal that has a desired frequency range. The starting frequency may be limited according to the geophone's resonant frequency, and k is determined according to the upper bound of the desired frequency range and total time duration of the signal. We consider four different chirp-type signals with an active and total time duration of 5 s and 8 s, respectively, which in total, span a frequency range of 3 Hz to 35 Hz. These are summarized in Table 4.2.

The dominant frequencies of the chirp lie between f_{min} and f_{max}. For example, Fig. 4.9 shows chirp's C-3-8 time dependence and frequency spectrum, where the strong components are clearly concentrated in the 3 Hz to 8 Hz range.

Chirp name	f_0	k	f_{min}	f_{max}
C-3-8	3	1	3	8
C-8-20	8	2.4	8	20
C-20-25	20	1	20	25
C-25-35	25	2	25	35

Table 4.2: Chirp signals used in the field experiment.

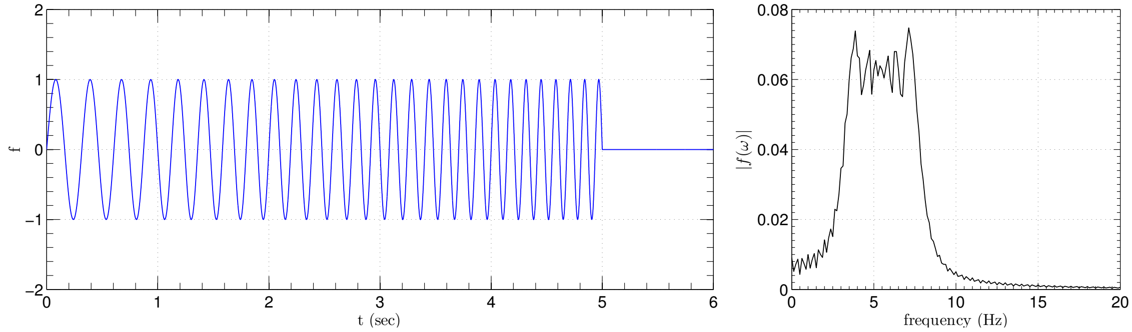

(a) Signal time-history

(b) Fourier spectrum

Figure 4.9: Chirp with dominant frequencies between 3 Hz and 8 Hz.

Finally, we remark that the signals in Table 4.2 cannot be applied on the ground surface by either T-rex or Liquidator in their exact form. Indeed, the equipment is only able to exert a load which is “close” to the design load. Therefore, it becomes necessary to measure the exact applied load due to its significance in the inversion process. This is done by installing accelerometers on the baseplate and reaction mass of the Vibroseis equipment. The actual applied load can be obtained by adding the products of the baseplate mass and the reaction mass by their corresponding measured accelerations.

4.2.4 Parametric studies

In the preceding sections, we developed all the tools we need for the parametric studies that we carry out in this section. We use (4.23) to represent signals considered in Table 4.2 with their corresponding Heaviside expansion. We then use (4.26) with a sufficiently large value for L to obtain the response of a 2D system and use it as benchmark to find smaller values for L that yield comparable results. Once an appropriate value for L is determined, (4.27) can be used to find out a suitable spacing between equivalent point sources.

In order to determine the appropriate length for the line load, we consider three representative values for L: 50 m, 100 m, and 150 m. We compare the response of these cases against the benchmark solution (large L value) due to the four loads considered in Table 4.2. This leads to twelve numerical experiments which provide insight on how the frequency content of the load may play a role in selecting L.

Results for the first two chirps of Table 4.2 are shown in Fig. 4.10. Each plot depicts two curves, one obtained using the infinite line load length, and the other obtained using a finite value for L. The agreement between the two curves is remarkable for all cases, considering that the observation period is 6 s, and the line load has a relatively short length. We note that for an exact match up to 6 s, a line load of length $L = 2100$ m is required. We also observe that larger values of L yield better results, which is indeed intuitive. Results of the last two chirps of Table 4.2 also follow a similar trend. We choose the case of $L = 100$ m for further investigations in the subsequent part.

We replace next the continuous line load with equivalent, equidistant point sources, spaced s apart. In particular, we consider two values for s, 5 m, and 10 m, respectively, and run numerical experiments with the chirp signals of Table 4.2. The results for the first two chirps of Table 4.2 are shown in Fig. 4.11 and demonstrate good agreement between the case of a line load of infinite length and that of point sources, positioned 5 meters apart from each other. The agreement is better for lower frequencies and deteriorates for higher frequencies. Hence, we choose $L = 100$ m with $s = 5$ m for the first two chirp signals of Table 4.2 in our field experiment (the 10 m spacing would lead to inaccuracies).

4.2.5 The experiment layout

We discuss next the actual field experiment aimed at a local characterization of the Hornsby Bend site located in Austin, Texas, using the field data, and the inversion methodology code discussed. As discussed already, a key assumption is that the site enjoys symmetry along the sensor plane, as displayed in Fig. 4.3. Our

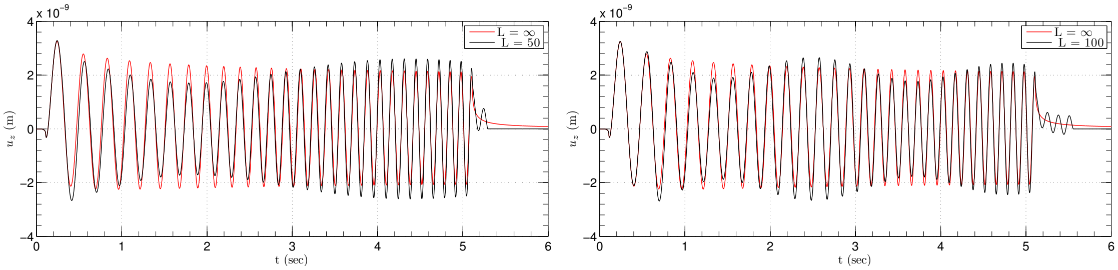

(a) L=50, L=∞ for Chirp C-3-8 (b) L=100, L=∞ for Chirp C-3-8

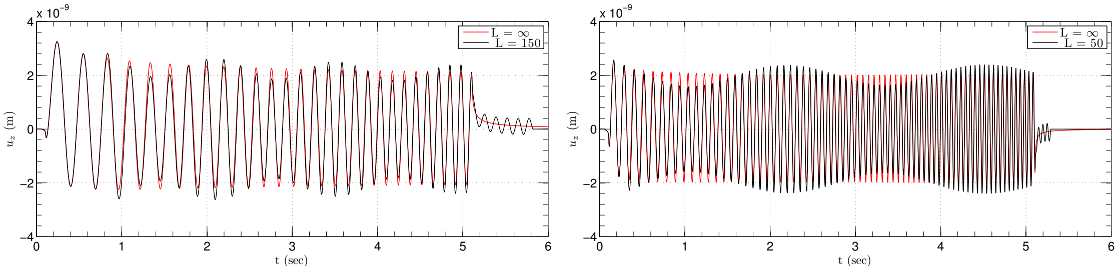

(c) L=150, L=∞ for Chirp C-3-8 (d) L=50, L=∞ for Chirp C-8-20

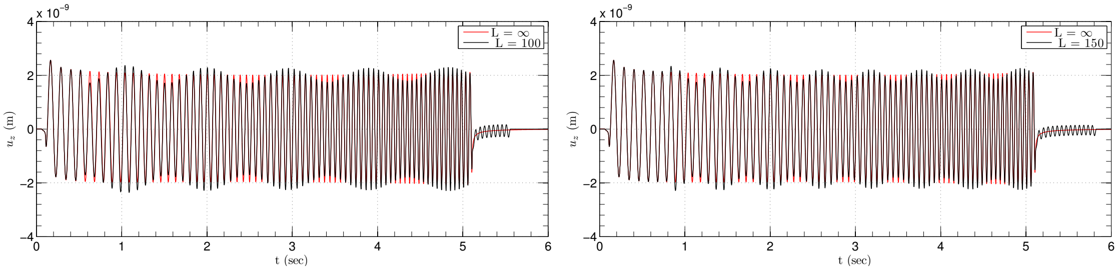

(e) L=100, L=∞ for Chirp C-8-20 (f) L=150, L=∞ for Chirp C-8-20

Figure 4.10: Line load truncation effect for different chirps.

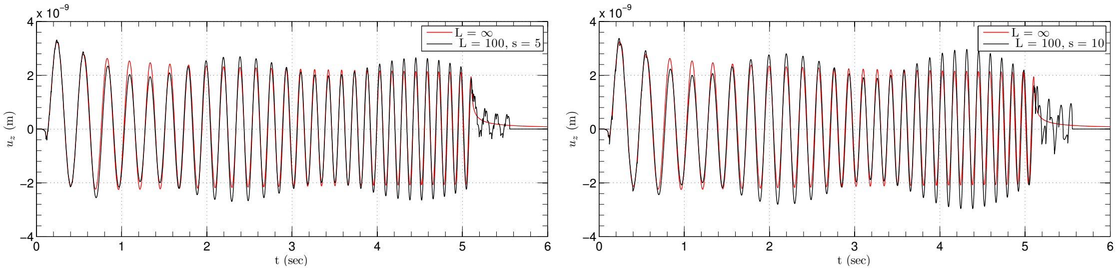

(a) s =5, chirp C-3-8 (b) s =10, chirp C-3-8

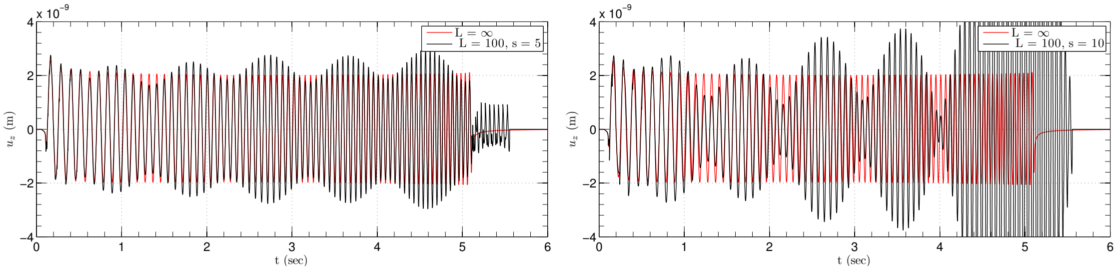

(c) s =5, chirp C-8-20 (d) s =10, chirp C-8-20

Figure 4.11: Comparison of infinite line load ($L = \infty$), a continuous line load of finite length ($L = 100$ m), and a series of point loads spaced s meters apart over a distance of 100 m.

objective is to explore a site of length 200 m along this plane. We place sensors every 5 m. These are shown in Fig. 4.12 with bullets. We consider sources, also spaced 5 m apart from each other, indicated by squares, which are placed along five lines of length 100 m. Due to the symmetry assumptions, we consider sources only on one side of the sensor plane, and assume that if we had sources on the mirror side, they would have yielded the same response as their existing counterparts. The experiment was performed in Austin, TX, Hornsby Bend in October 2010 (Fig. 4.13).

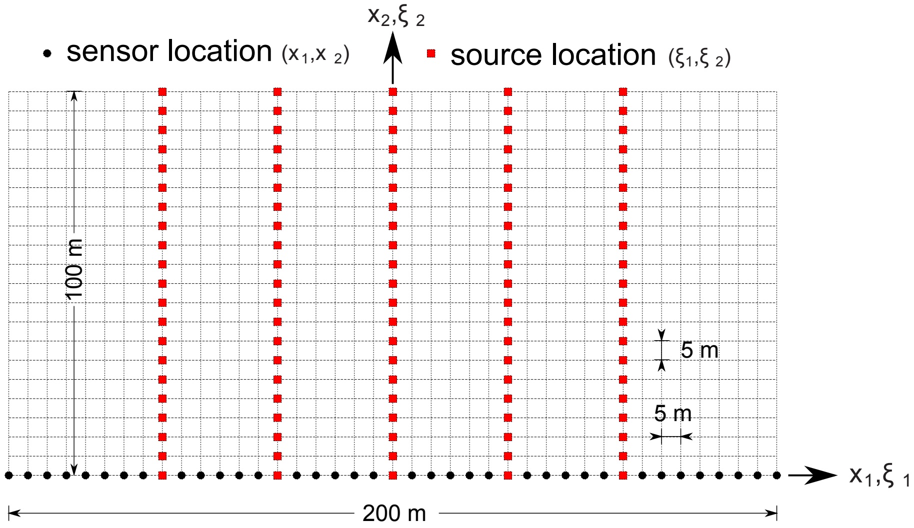

Figure 4.12: The field experiment layout.

4.3 Field experiment records and data processing

In this section, we discuss a subset of the field recorded data, and outline the data processing procedure. The latter consists of two main parts. First, identification and reduction of noise effects associated with the recorded data, and, secondly, integrating the data in such a way that they readily fit the requirements of our

(a) (b)

Figure 4.13: Hornsby Bend field experiment: (a) instrumentation van; and (b) T-rex at the site.

two-dimensional inversion codes.

4.3.1 Signal processing

Our records are inevitably contaminated by noise, which may distort the signals both at high and low frequencies. Our aim is to identify the parts of a signal (in the frequency domain), where the signal to noise ratio is low, and filter out these parts from the records. This is particularly important when dealing with low frequency noise, since the noise gets amplified when the velocity record is integrated to yield displacement time-history. The latter, may look unphysical and necessitate baseline adjustment [99], which will have serious consequences in the inversion process. On the other hand, high frequency noise may be less of a concern due to the regularization terms in the inversion algorithm: the regularization terms make the objective functional less sensitive to the high frequency noise [93].

A sampling frequency of 820 Hz is used for digital data collection. Assuming the highly unlikely event that data being contaminated by noise up to a range of 100 Hz (noise was observed up to 70 Hz), a sampling rate of 200 Hz could prevent aliasing effects according to the Nyquist sampling theorem [100]. In this sense, we oversampled the data, which causes no harm. Moreover, in order to reduce the effects of ambient noise, we repeated each loading five times, and use the average in our analysis.

We favor finite-impulse-response (FIR) filters since they preserve a signal's phase information (linear phase), and do not result in phase distortion, as commonly occurs in more popular infinite-impulse-response (IIR) filters [100]. We use Matlab's equiripple bandpass filter, with high and low cuts of 2.5 Hz and 12 Hz, respectively, and high and low slopes of 60 dB/octave and 38 db/octave, for the C-3-8 chirp (see Table 4.2). For the C-8-20 chirp, we use the same type of filter, with high and low cuts of 2.5 Hz and 25 Hz, and high and low slopes of 60 dB/octave and 26 db/octave, respectively.

Next, we present some of the field experiment records both in their unprocessed and processed form. For example, Fig. 4.14 shows the C-3-8 chirp, applied by Liquidator at $(\xi_1, \xi_2) = (0, 0)$. The record may be compared with the record in Fig. 4.9, which is the corresponding theoretical curve. Notice that the applied load lies mainly within the design frequency range, except for the relatively small-component high-frequency noise, which probably originates with the Liquidator's engine and hydraulics.

Figures 4.15, 4.16, and 4.17 depict a subset of the recorded sensor data: both

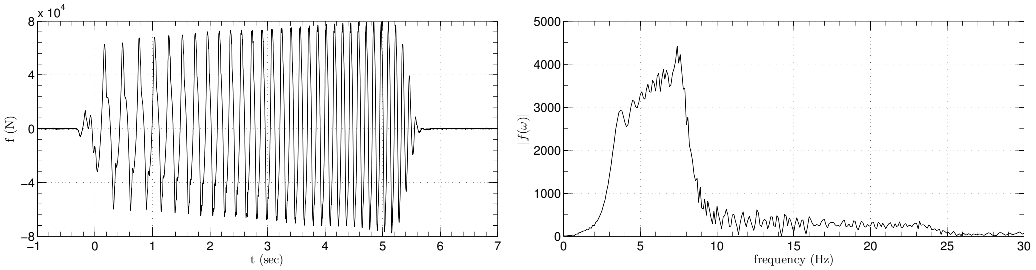

(a) Time-history (recorded) (b) Fourier spectrum (recorded)

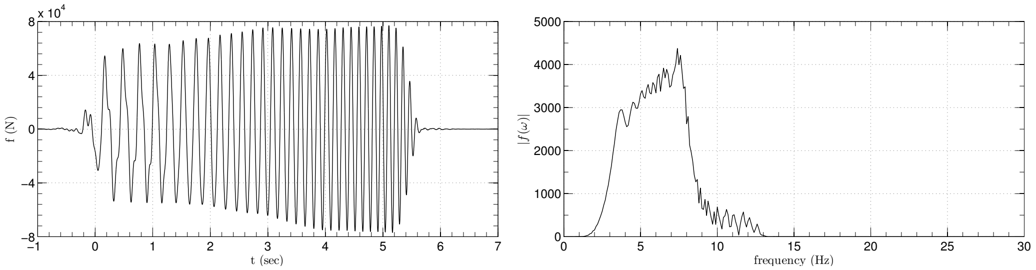

(c) Time-history (filtered) (d) Fourier spectrum (filtered)

Figure 4.14: Force (chirp C-3-8) applied by Liquidator at $(\xi_1, \xi_2) = (0, 0)$.

unprocessed and processed (filtered) velocity records are shown for various sensor locations due to different loads. In all cases shown, the load is the chirp C-3-8, as shown earlier in Fig. 4.14. Shown in Figs. 4.15-4.17 are the velocity time-histories at $(-5, 0, 0)$, while the load is applied at $(0, 0, 0)$, $(0, -5, 0)$, and $(0, -10, 0)$, respectively. Geometric decay is noticeable and amplitude reduction in velocity time-history is observed as distance between the source and observer increases.

4.3.2 Data integration

In this section, we address how we use the, essentially, three-dimensional field data, in order to obtain records suitable for exercising our two-dimensional codes. We follow the same lines as in the experiment design. Similarly to what we did in

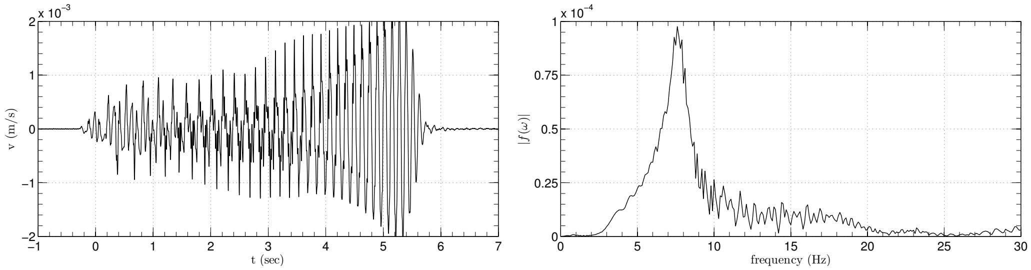

(a) Time-history (recorded) (b) Fourier spectrum (recorded)

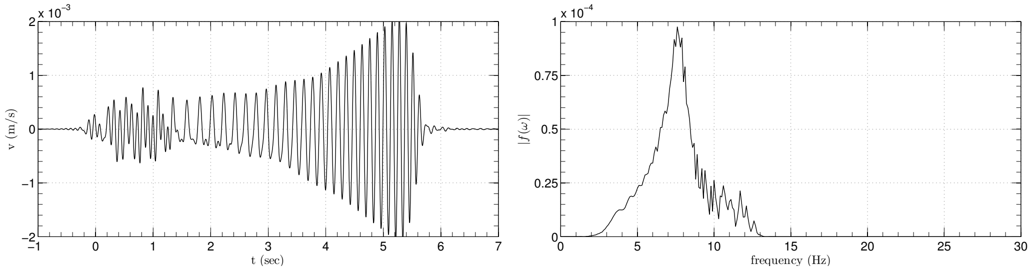

(c) Time-history (filtered) (d) Fourier spectrum (filtered)

Figure 4.15: Velocity (due to force C-3-8 at $(0, 0, 0)$) measured at $(-5, 0, 0)$.

(4.27), we obtain the following equivalent two-dimensional velocity time history v^{2L} from the three-dimensional field-recorded $v^{3D} := v^{3D}(x_1, x_2, t; \xi_1, \xi_2)$:

$$v^{2L}(x_1, t;\ \xi_1, \xi_2) = v^{3D}(x_1, 0, t;\ \xi_1, 0) + 2\sum_{j=1}^{m} v^{3D}(x_1, 0, t; \xi_1, js), \tag{4.29}$$

where x_1 denotes a geophone's location along the x_1 axis, (ξ_1, ξ_2) denotes the load location, m (=20) is the number of source locations for which $x_2 > 0$, and $s = 5$ m is the distance between the loads. v^{2L} is the equivalent two-dimensional velocity record, which can then be integrated in time to yield the displacement time history. Similarly, for the equivalent two-dimensional force time history, we obtain:

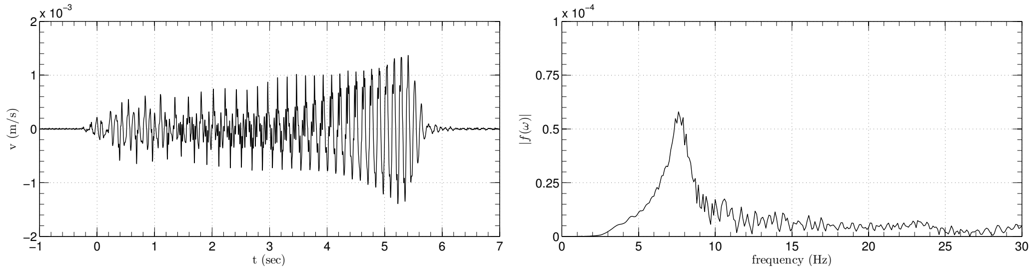

(a) Time-history (recorded) (b) Fourier spectrum (recorded)

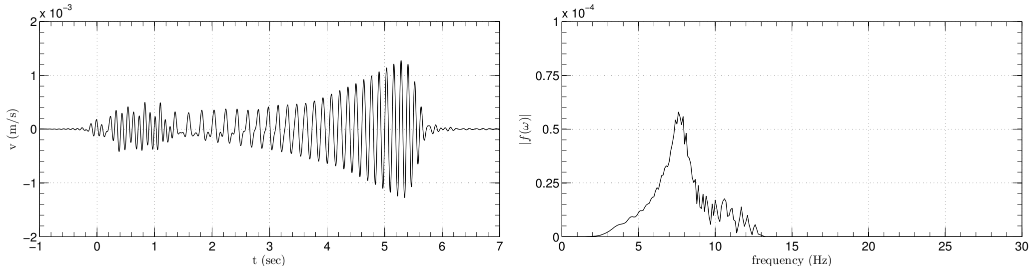

(c) Time-history (filtered) (d) Fourier spectrum (filtered)

Figure 4.16: Velocity (due to force C-3-8 at $(0, -5, 0)$) measured at $(-5, 0, 0)$.

$$f^{2L}(\xi_1, t) = \frac{1}{(2m+1)s}\left[f^{3D}(\xi_1, 0, t) + 2\sum_{j=1}^{m} f^{3D}(\xi_1, js, t)\right], \qquad (4.30)$$

where $f^{3D}(\xi_1, \xi_2, t)$ denotes the measured force applied at any given location (ξ_1, ξ_2). For example, the equivalent line load corresponding to chirp C-3-8, applied at $\xi_1 = 0$, and the resulting velocity time history at $x_1 = -5$ m are depicted in Fig. 4.18. The data, both measured force and recorded response, with the aid of (4.29) and (4.30), can now be readily used for inversion.

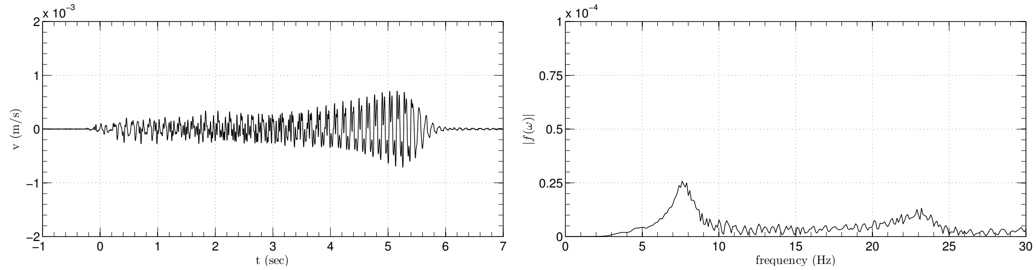

(a) Time-history (recorded)

(b) Fourier spectrum (recorded)

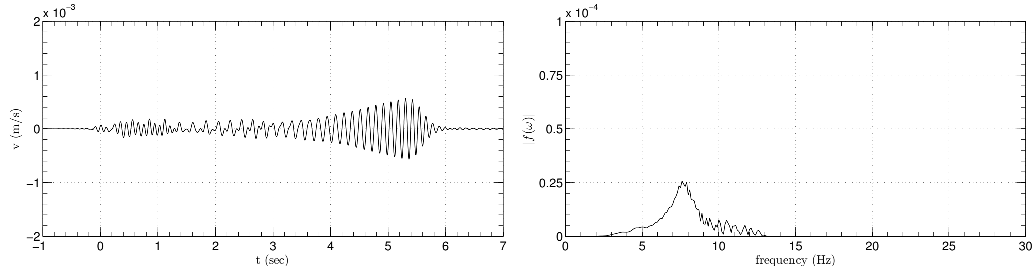

(c) Time-history (filtered)

(d) Fourier spectrum (filtered)

Figure 4.17: Velocity (due to force C-3-8 at $(0, -10, 0)$) measured at $(-5, 0, 0)$.

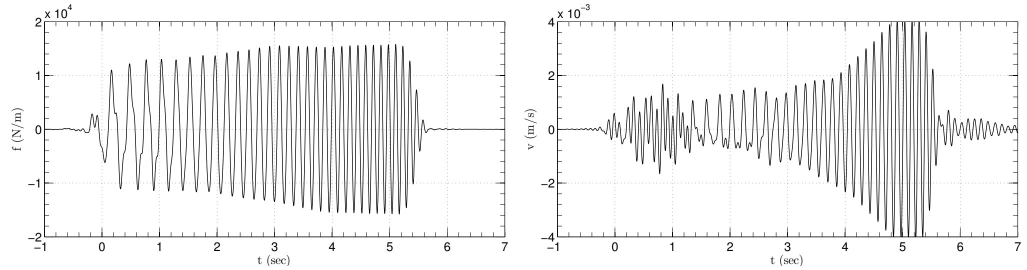

(a) Force time-history

(b) Velocity time-history

Figure 4.18: Equivalent line load (chirp C-3-8) applied at $\xi_1 = 0$ m, and corresponding response at $x_1 = -5$ m.

4.4 Inversion results using field experiment data

In this section, we use the inversion theory discussed earlier, along with measured data from the field experiment, to arrive at an estimate of the spatial distribution of the P and S wave velocities at the target site (Hornsby Bend).

The target domain is a two-dimensional slice, 200 m wide and 48 m deep. The domain is surrounded on its sides and bottom by a 10 m-thick PML to absorb outgoing waves. We use bilinear quadrilateral elements with element size of 1 m when applying the C-3-8 chirp (see Table 4.2), whereas 8-noded serendipity elements of the same size are used for higher frequency chirps. In all cases, we use 1 m × 1 m bilinear quadrilateral elements to interpolate the material properties.

According to the experiment layout in Fig. 4.12, we apply loads at every 5 m along five lines. T-Rex was used for loading along the lines $x_1 = -60$ m, $+30$ m, and $+60$ m, whereas Liquidator was used to load along $x_1 = -30$ m, and 0 m. We used 36 geophones with a resonant frequency of 1 Hz at every 5 m, along the x_1 axis. After processing the recorded data, per the discussion of the preceding section, we proceeded with the inversion process.

4.4.1 Inversion process

The inversion process begins with an initial profile for both of the Lamé parameters (linear in depth or homogeneous), and iteratively updates the profile until the misfit between the measured response and the computed response obtained at each inversion iteration is minimized. The convergence rate of the inversion process to the target profile, and even the success of the process itself, depends greatly on the initial guess, as is typically the case. An initial profile, which is close to the target profile, will likely need fewer number of iterations to converge, compared to an arbitrary initial profile. This fact can be exploited to speed up the convergence. If, for example, during a field experiment, an SASW experiment is performed in addition to the data collection for the full waveform inversion approach, then the SASW-rendered profile could be used as initial guess for the full waveform inversion. The SASW profile will be, by definition, horizontally layered, whereas the full waveform-based inverted profile will be, in general, arbitrarily heterogeneous.

We start the inversion process by applying the first (measured) equivalent force corresponding to chirp C-3-8 (see Table 4.2 for the theoretical curve and Fig. 4.18 for the actual, equivalent measured force). There are 5 loads at our disposal, and 36 measuring locations for every load. Owing to linearity, we apply all 5 loads simultaneously and add their corresponding responses at every sensor location. Other possibilities for combining the loads also exist [101, 102].

Due to the very construction of the chirp signals, their frequency increases linearly with time. This may be exploited to further regularize the inversion process, i.e., we start the inversion process by considering only a portion of the total chirp duration, arrive at an inverted profile, use the inverted profile as an initial guess to the next round of inversion, where we increase the duration of the same chirp signal, thus, gradually, bringing additional frequencies to bear on the inversion process (a, so-called, continuation scheme). For example, for the site under study, we start with the first 2 s of the signals, and progressively move up to 7 s duration, in increments of 1 s. A similar idea was discussed in [58, 103].

After 1900 iterations, the misfit between the measured response and the computed response becomes small enough, with no discernible update in the material properties. The corresponding compressional and shear wave velocity profiles for the Hornsby Bend site are shown in Fig. 4.19 (a constant mass density of $\rho = 2000$ kg/m^3 is considered for the soil medium throughout the analysis).

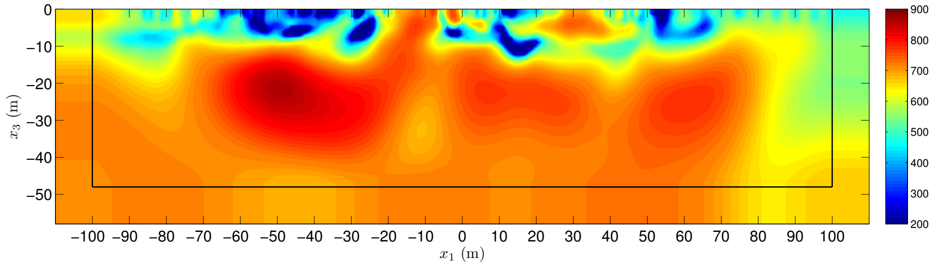

(a) c_p (m/s)

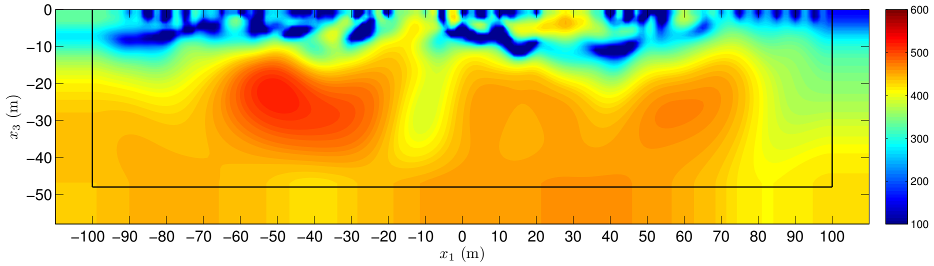

(b) c_s (m/s)

Figure 4.19: Inverted profiles for c_p and c_s at iteration 1900.

4.4.2 Comparison with SASW

Next, we compare our shear wave velocity (c_s) profile with that obtained via the SASW method. The Spectral-Analysis-of-Surface-Waves method relies on the dispersive nature of the Rayleigh wave velocity in layered media, i.e., the propagation speed of the surface waves depends on the frequency of the load [59]. Measuring this wave speed for different frequencies in a field experiment, results in the experimental dispersion curve. Next, a theoretical dispersion curve can be computed for a homogeneous elastic layered medium. The material properties for each layer are varied until a match is attained between the experimental and the theoretical dispersion curve (a comprehensive description of the SASW method can be found in [104]). The method assumes that the dominant portion of the wave energy is transported through Rayleigh waves, and disregards other wave types such as compressional and shear waves. The SASW is capable of rendering only horizontally layered profiles and only of the shear wave velocity. Despite its limitations it is widely used.

We performed three SASW experiments at our site: at the centerpoint $(x_1, x_2) = (0, 0)$ and close to the two end points of the domain $(x_1, x_2) = (\pm 90, 0)$. The c_s profile corresponding to the center point is shown in Fig. 4.20, whereas Fig. 4.21 compares the SASW profile with those obtained from the inversion process at the $x_1 = -90$ m, 0 m, and +90 m cross-sectional lines of the domain. In general, there is good agreement between the two methods. Discrepancies may be attributed to the three-dimensional nature of the physical problem. While in our study, we use a two-dimensional model for the full-waveform inversion, the model is one-dimensional for the SASW method. Whereas there may exist lateral property variability in the actual physical problem, these effects are completely neglected in the SASW method, and are only partially accounted for in the two-dimensional inversion process. We also observe that while the SASW method predicts sharp profile changes in depth, the inversion process yields profiles that vary gradually. Indeed, this is due to the Tikhonov regularization scheme, which precludes high gradients in the material profile while allowing smooth spatial variations.

We also compute time-history results corresponding to numerical simulation of the medium based on profiles obtained from the inversion process and the SASW method, and compare them with the actual field measurements at a few locations. To this end, since the SASW method only yields the shear wave velocity of the soil medium, we supplemented it with an estimation of the compressional wave velocity, by assuming that the Poisson's ratio decreases from 0.35 on the ground surface to 0.25 at a depth of −50 m. This allowed us to compute the response at the ground surface using the SASW-rendered profile. Due to the small variability between the three SASW profiles, we use their average in the time-history analysis for simplicity. Displacement time-histories at $x_1 = -80$ m, -40 m, $+5$ m, $+35$ m, and $+70$ m are shown in Fig. 4.22. Excellent agreement can be observed between the time histories computed based on the full-waveform inverted profile and the true recorded motion, whereas the SASW-based time histories exhibit significant amplitude discrepancies. We should mention, however, that since the full-waveform inversion process forces time-history matching, this may not be a fair comparison.

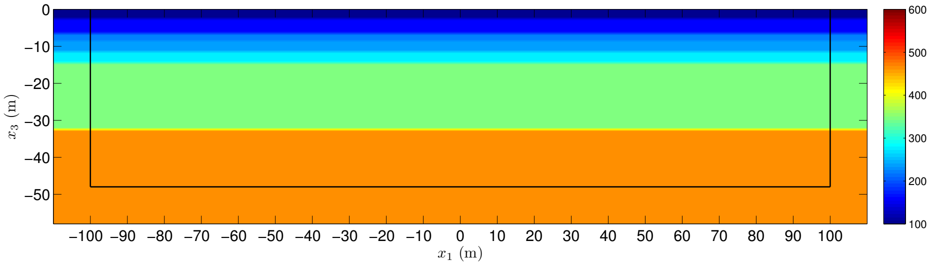

Figure 4.20: Inverted profile for c_s via the SASW method.

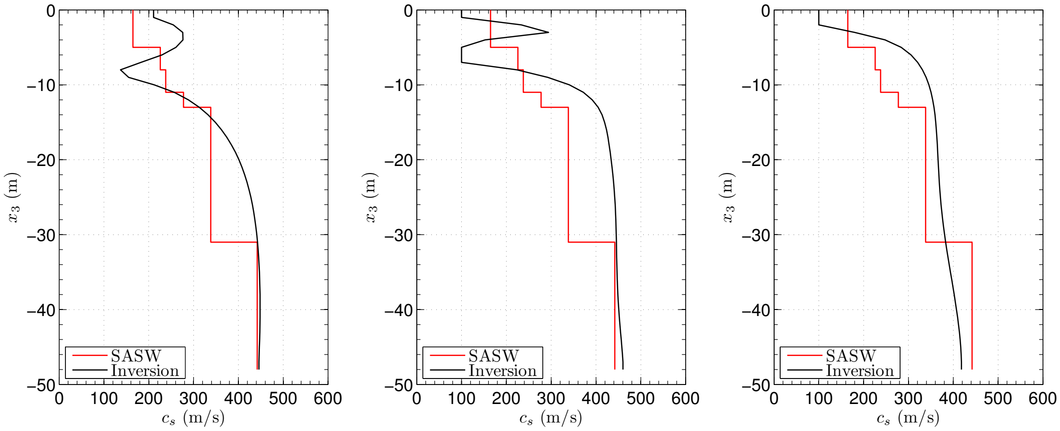

(a) $x_1 = -90$ m (b) $x_1 = \pm 0$ m (c) $x_1 = +90$ m

Figure 4.21: Shear wave velocity profiles obtained via SASW and full-waveform-based inversion.

4.4.3 Comparison with cone penetration test (CPT) results

The cone-penetration-test (CPT) is an intrusive field experiment, which provides information on soil properties and the soil's stratification. A rod with a cone-shaped ending is forced into the ground at a constant rate, while two load cells measure the required load that drives the rod into the ground. The first load cell measures the force that acts directly on the cone and yields the cone resistance, which is obtained by dividing the force over the cone's area. The second load cell measures the force that acts on the lateral sides of the rod, immediately past the cone, and provides sleeve friction [105]. Unfortunately, CPT results cannot be correlated with elastic properties of the soil. However, the cone resistance is an indicator of soil stiffness, and the depth at which the cone cannot be forced further into the ground, corresponds to a stiff layer. We present CPT results at the same site, and consider mainly the qualitative information that the test provides.

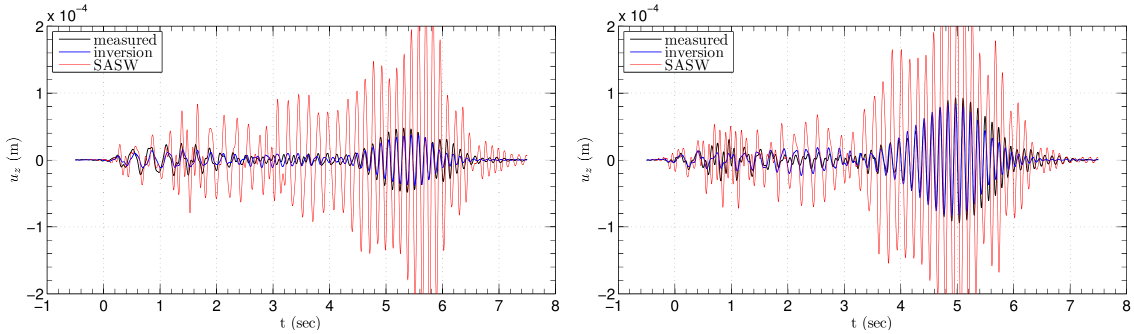

(a) $x_1 = -80$ m (b) $x_1 = -40$ m

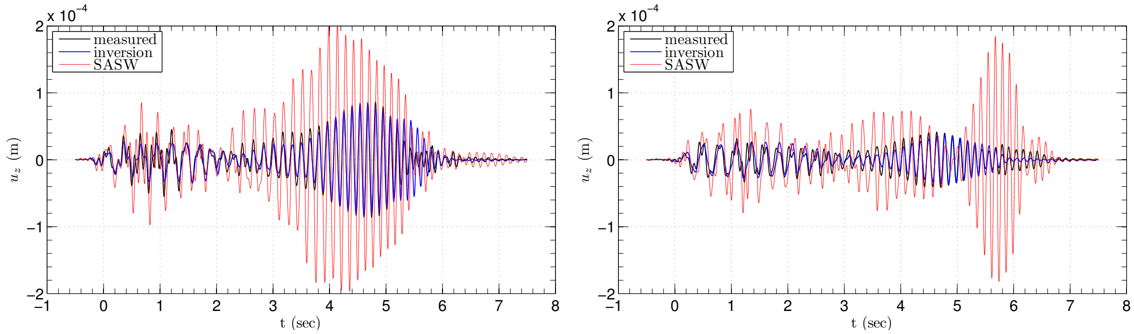

(c) $x_1 = +5$ m (d) $x_1 = +35$ m

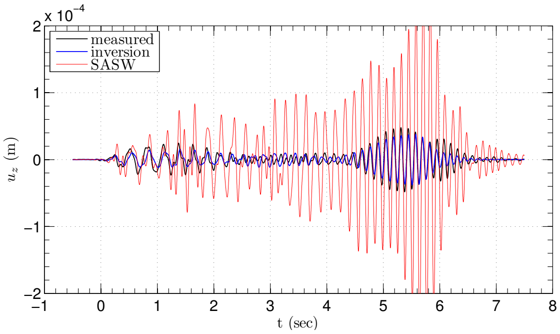

(e) $x_1 = +70$ m

Figure 4.22: Comparison of measured surface displacement time-histories against those resulting from the SASW and full-waveform-based inversion.

We performed CPT tests at four sample locations to investigate if they hit the stiff zones predicted by the inverted profile. These locations are at the $x_1 = -80$ m, -50 m, -8 m, and $+80$ m cross-sectional lines of the domain. The cone resistance along depth at these locations is shown in Fig. 4.23, along with the inverted c_p and c_s profiles. It can be observed that the cone cannot be pushed any further once it reaches a zone where the shear wave velocity is approximately around 400 m/s. There is general agreement between the CPT results and the inverted profile. For instance, at $x_1 = -80$ m, the cone resistance and the shear wave velocity have the same pattern in depth. At $x_1 = -50$ m, cone resistance has a spike at a shallow depth, reaches its minimum value at a depth of 5 m, and increases again after that. We observe a similar trend for both the shear and the compressional wave velocities. It is difficult to find a correlation at $x_1 = -8$ m and $+80$ m.

4.5 Three-dimensional site characterization

In this section, we report the design and data processing of a field experiment that we performed at the NEES@UCSB site in Garner Valley, CA. We use the field data in our three-dimensional full-waveform inversion code, to obtain the compressional wave velocity (c_p) and shear wave velocity (c_s) profiles of the site. The full-waveform-inversion-based c_s profile will then be compared against the profiling obtained from the SASW method.

We use the T-Rex seismic vibrator of the NEES@UTexas site for applying loads on the ground surface, and record the resulting ground motion by using 1 Hz geophones. We use a chirp signal with characteristic parameters $f_0 = 3$ Hz, and

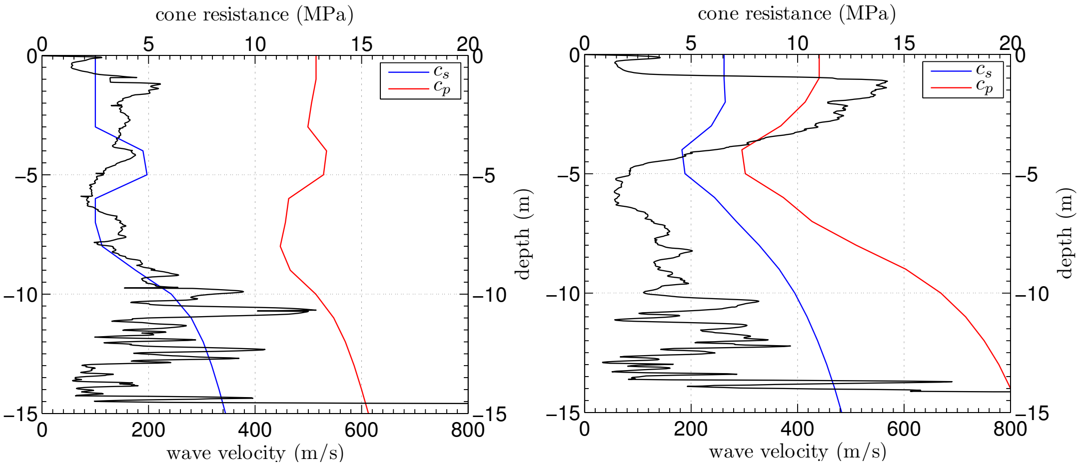

(a) $x_1 = -80$ m

(b) $x_1 = -50$ m

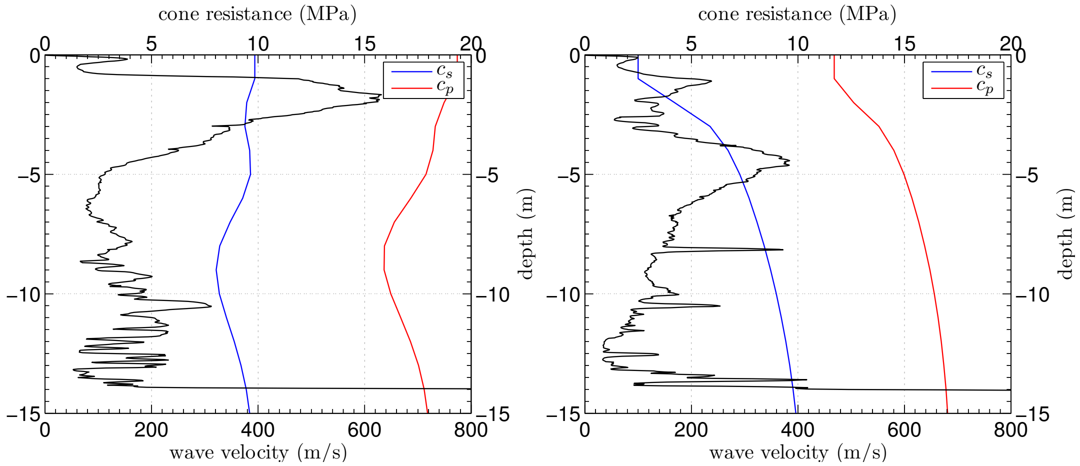

(c) $x_1 = -8$ m

(d) $x_1 = +80$ m

Figure 4.23: Juxtaposition of CPT results and the inverted profiles.

$k = 2.8$ (see (4.28)), and a total active duration of 2.5 s. This parameterization results in a loading with dominant frequencies between 3-10 Hz.

4.5.1 The experiment site and layout

The NEES Garner Valley Downhole Array research site in Southern California is located in a narrow valley, within the Peninsular Ranges batholith, 23 km east of Hemet, 20 km southwest of Palm Springs, and is just 7 km from the San Jacinto fault, and 35 km from the San Andreas fault.

We consider a portion of the site of length and width 126 m × 68 m, and 40 m depth. The experiment layout is displayed in Fig. 4.24. The main grid lines are 10 m apart. The sensors are shown with bullets and sources are indicated by squares. Overall, we "shake" at 24 locations, and record the site's response at 63 receiver locations. The experiment was performed on March 13th 2012 (Fig. 4.25).

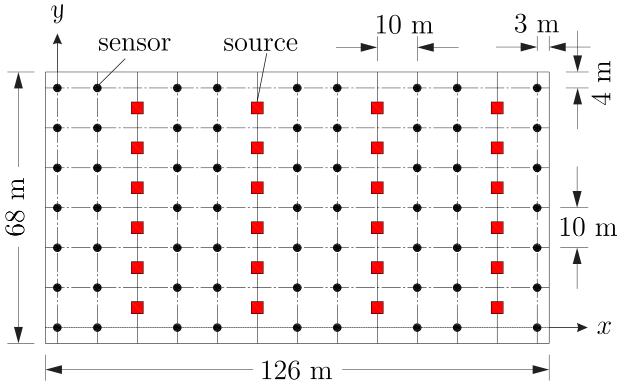

Figure 4.24: The field experiment layout.

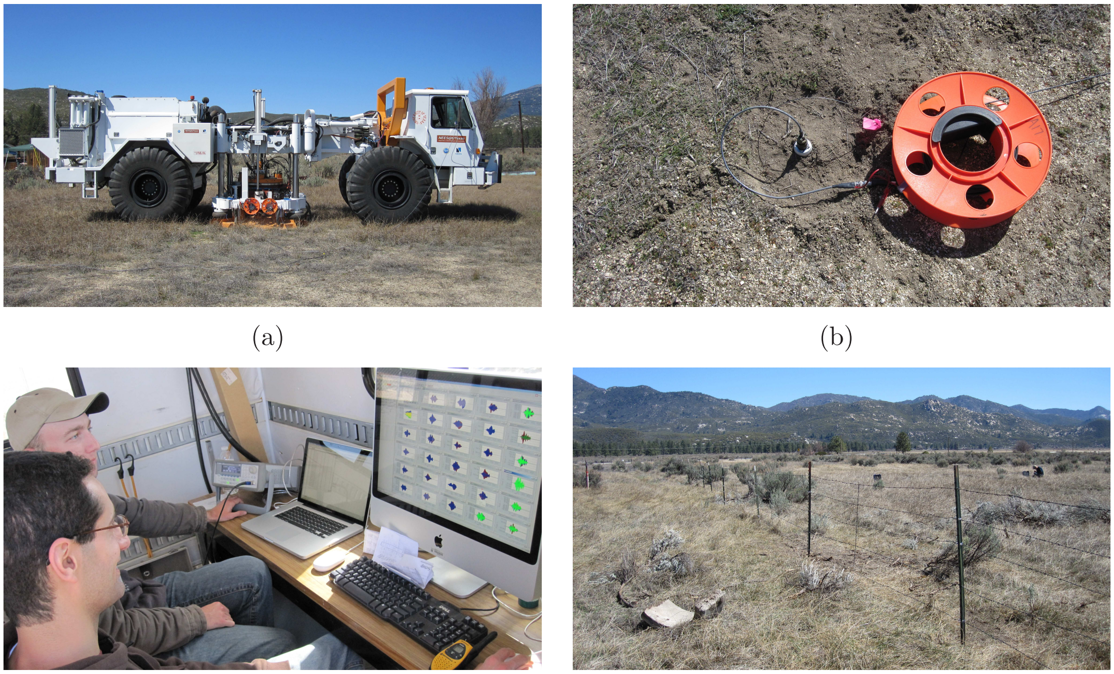

(a) (b) (c) (d)

Figure 4.25: Garner Valley field experiment: (a) T-rex at the site; (b) a buried geophone; (c) instrumentation van; and (d) the site.

4.5.2 Pre-processing the field data

We use a sampling frequency of 200 Hz for digital data collection, which, according to the Nyquist sampling theorem [100], is adequate, and prevents aliasing, if the recorded data are contaminated by noise up to 100 Hz. Moreover, to reduce the effects of ambient noise, we repeat each loading five times, and use the averaged recording for inversion. We then process the signal to eliminate the parts of the recorded motion with low signal to noise ratio, according to the procedure described in Section 4.3.1.

Next, we present a subset of the recorded motion at select sensor locations. Specifically, we consider the displacement time-history at four sensors, placed at $(x, y) = (30, 20), (30, 50), (70, 20), (70, 50)$ m, due to loading at $(x, y) = (50, 35)$ m. These sensors are shown with blue bullets in Fig. 4.26, and are labeled as "array 1". The considered sensors are equidistant from the source. We also study the recorded motion at sensors placed at $(x, y) = (10, 20), (10, 50), (90, 20), (90, 50)$ m, and label them as "array 2", which are shown with green bullets in Fig. 4.26. The displacement time-history at array 1 and array 2 sensors are shown in Figs. 4.27 and 4.28, respectively. Although there is general agreement between the time-history plots for the equidistant sensors of each array, there are differences: indicative of the heterogeneous character of the site.

4.5.3 Full-waveform inversion using field data

Based on the inversion framework discussed in the preceding chapter, we use the collected field data to compute the compressional wave velocity c_p and shear

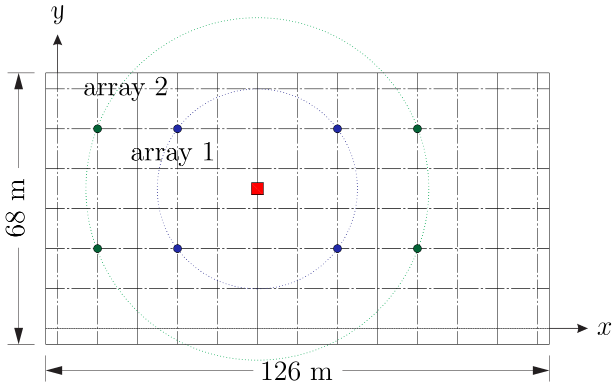

Figure 4.26: Location of array 1 and array 2 sensors.

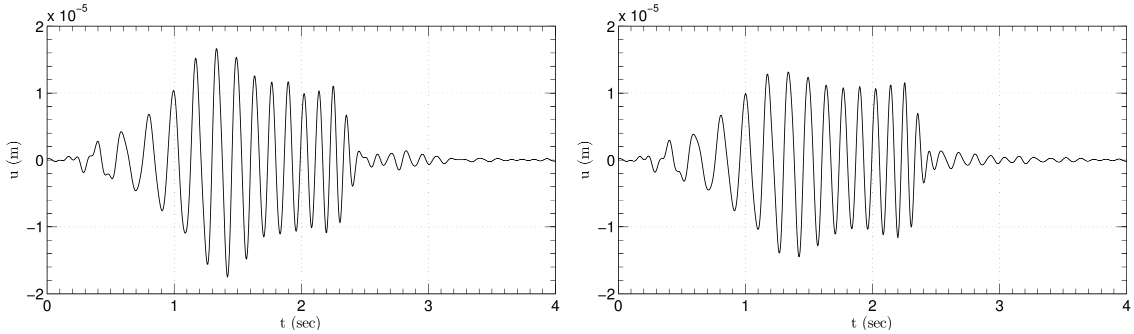

(a) $(x, y) = (30, 50)$ m (b) $(x, y) = (70, 50)$ m

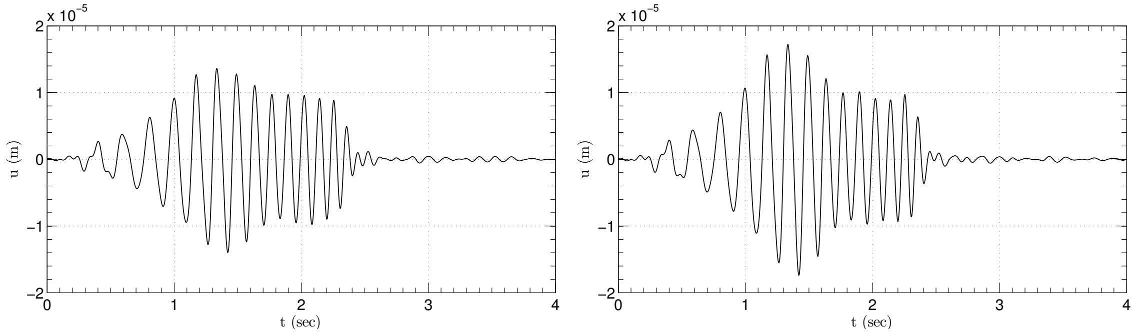

(c) $(x, y) = (30, 20)$ m (d) $(x, y) = (70, 20)$ m

Figure 4.27: Time-history of vertical displacement at sensors in array 1.

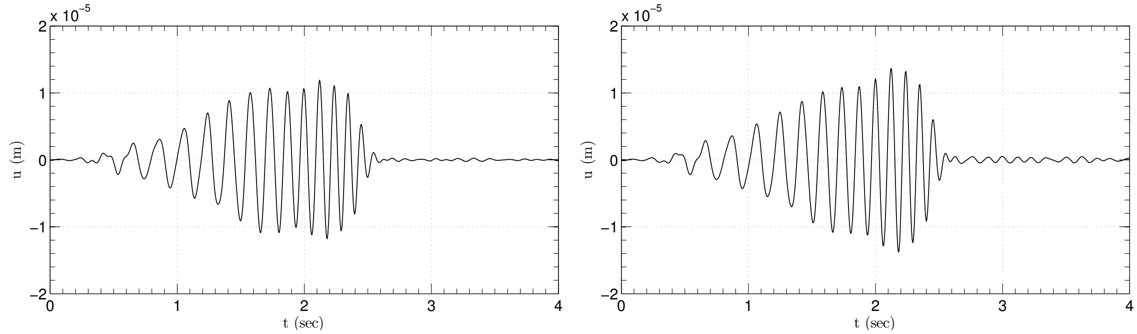

(a) $(x, y) = (10, 50)$ m (b) $(x, y) = (90, 50)$ m

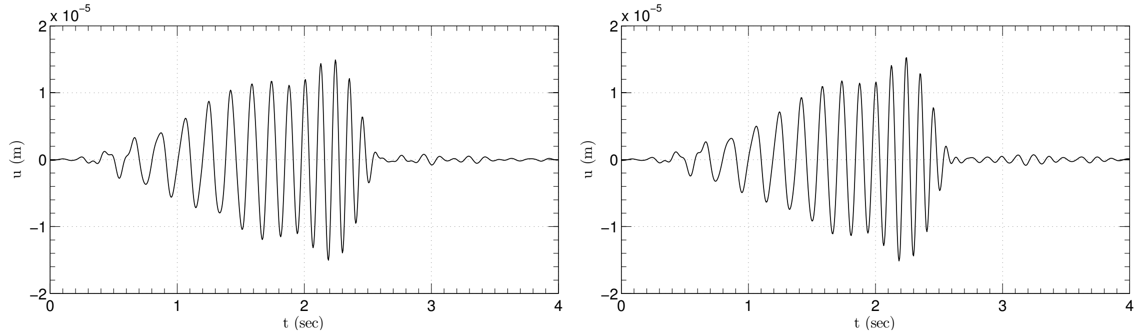

(c) $(x, y) = (10, 20)$ m (d) $(x, y) = (90, 20)$ m

Figure 4.28: Time-history of vertical displacement at sensors in array 2.

wave velocity c_s profiles of the probed site. We consider a cubic (regular) domain of length, width, and depth $126 \times 68 \times 40$ m. A 10 m-thick PML is placed at the truncation boundaries. For the PML parameters, we choose $\alpha_o = 5$, $\beta_o = 500\ s^{-1}$, and a quadratic profile for the attenuation functions, i.e., $m = 2$. The mass density is considered to be $\rho = 1760$ kg/m^3 for -2 m $\leq z \leq 0$, $\rho = 1880$ kg/m^3 for -4 m $\leq z \leq -2$ m, and $\rho = 2000$ kg/m^3 for -40 m $\leq z \leq -4$ m, according to prior investigations. The material properties at the interfaces Γ^{I} are extended into the PML. The interior and PML domains are discretized by quadratic hexahedral spectral elements of size 2 m, and $\Delta t = 10^{-3}$ s. This leads to $3,885,648$ state unknowns, and $718,566$ material parameters.

Owing to linearity, we apply all the 24 loads simultaneously, and consider their superimposed responses at each sensor location. We start the inversion process with only a portion of the signal, and as the inversion process evolves, we increase the temporal duration of the signal, thus, progressively introducing higher frequencies, which allows for profile refinement. We use a smoothed version of the profile obtained via the SASW method as the starting point of the inversion process.

After 4550 iterations, the misfit between the measured response and the computed response becomes reasonably small, with no strong update in the material profiles. The corresponding three-dimensional c_p and c_s profiles for the Garner Valley site are shown in Fig. 4.29, whereas Figs. 4.30-4.32 show the cross-sectional profiles of the velocity profiles at $x = 10, 60$, and 90 m. The profiles indicate that the site under investigation is heterogeneous, revealing the presence of a soft layer at a depth of about 25 m.

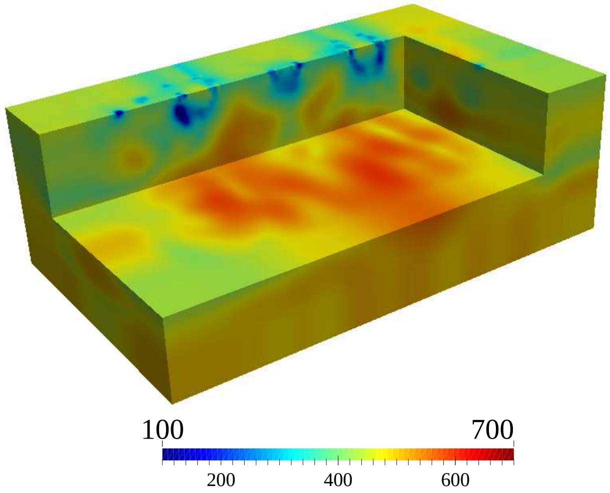

(a) c_p (m/s)

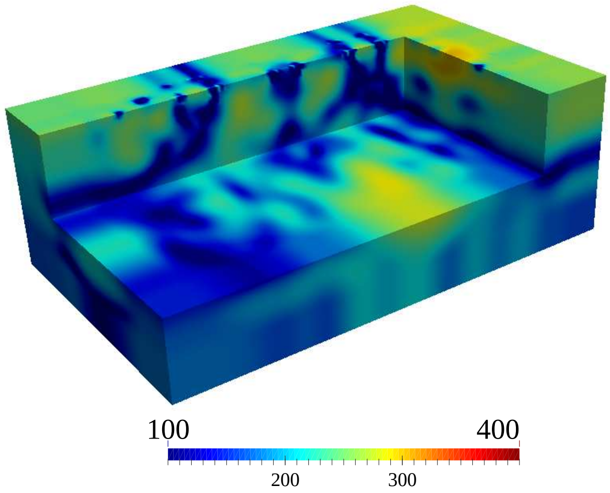

(b) c_s (m/s)

Figure 4.29: Inverted profiles for c_p and c_s at iteration 4550 (part of the domain is not shown to aid material visualization in depth).

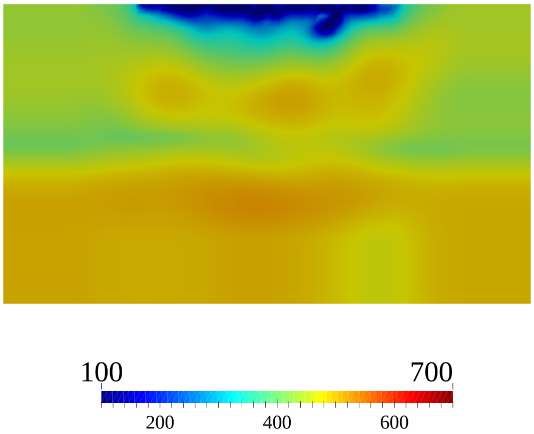

(a) c_p (m/s)

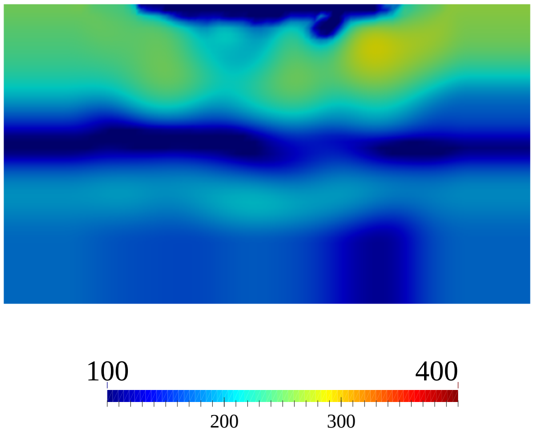

(b) c_s (m/s)

Figure 4.30: Inverted profiles for c_p and c_s at iteration 4550 ($x = 10$ m).

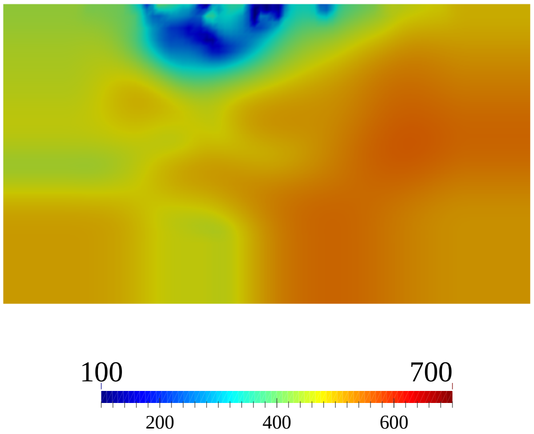

(a) c_p (m/s)

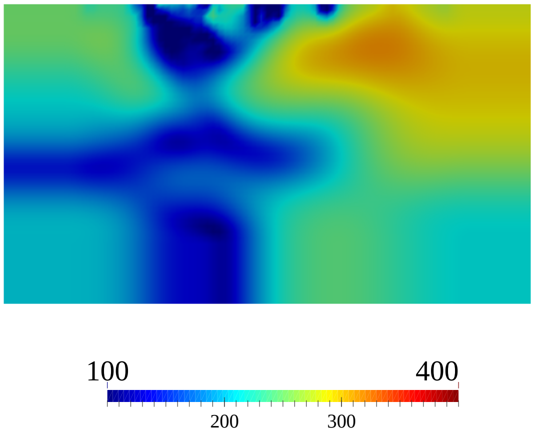

(b) c_s (m/s)

Figure 4.31: Inverted profiles for c_p and c_s at iteration 4550 ($x = 60$ m).

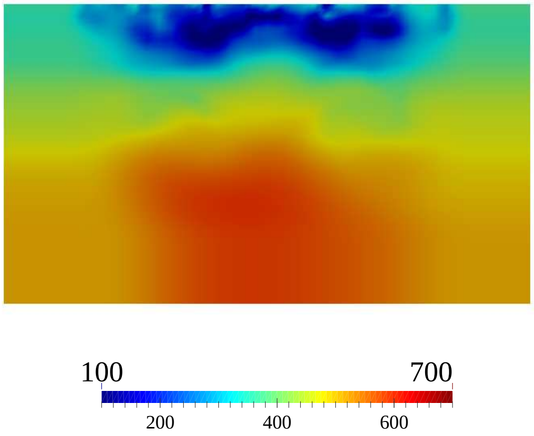

(a) c_p (m/s)

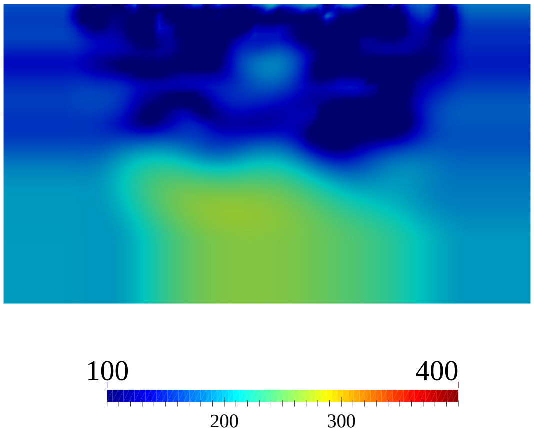

(b) c_s (m/s)

Figure 4.32: Inverted profiles for c_p and c_s at iteration 4550 ($x = 90$ m).

4.5.4 Profiling obtained from SASW

We performed field tests using the SASW method to obtain the shear wave velocity (c_s) profile of the site along three lines. The profiles are obtained along $x = 10$, 60, and 100 m, which are marked with red lines in Fig. 4.33, and are shown in Fig. 4.34. The c_s profiles obtained from the full-waveform inversion (FWI) at three different locations along these lines are also shown in the plots. There are considerable differences between the SASW profile and the FWI profiles along the $x = 10$ m and $x = 60$ m lines. However, there is general agreement between the profiles along the $x = 100$ m line.

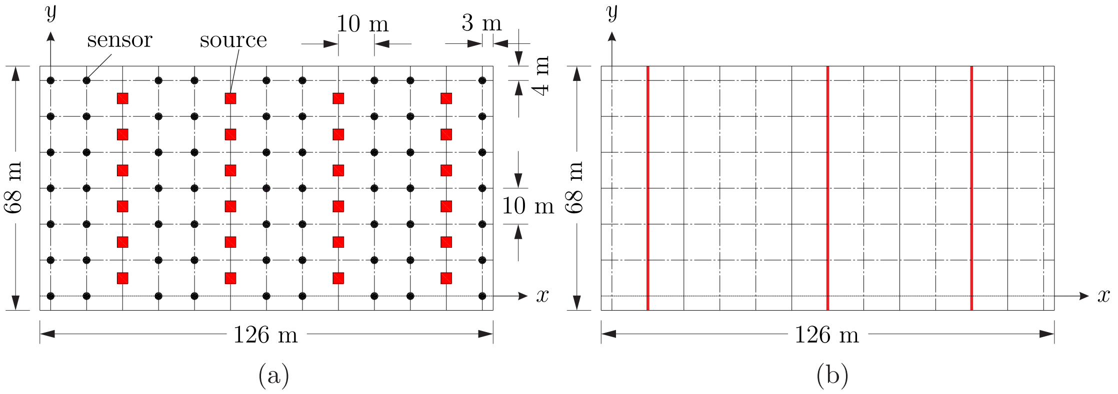

(a) (b)

Figure 4.33: Garner Valley experiment: (a) layout; and (b) SASW method test locations.

Next, we compute the time-history response corresponding to a forward wave simulation of the site, based on profiles obtained from full-waveform inversion and the SASW method[7] (Fig. 4.35), and compare them against the measured field re-

---

[7] We consider ν=0.3 to compute a c_p profile for the SASW method in order to exercise the forward code. Furthermore, since the SASW profiles along the three lines are almost identical, we use their average for time-history simulations.

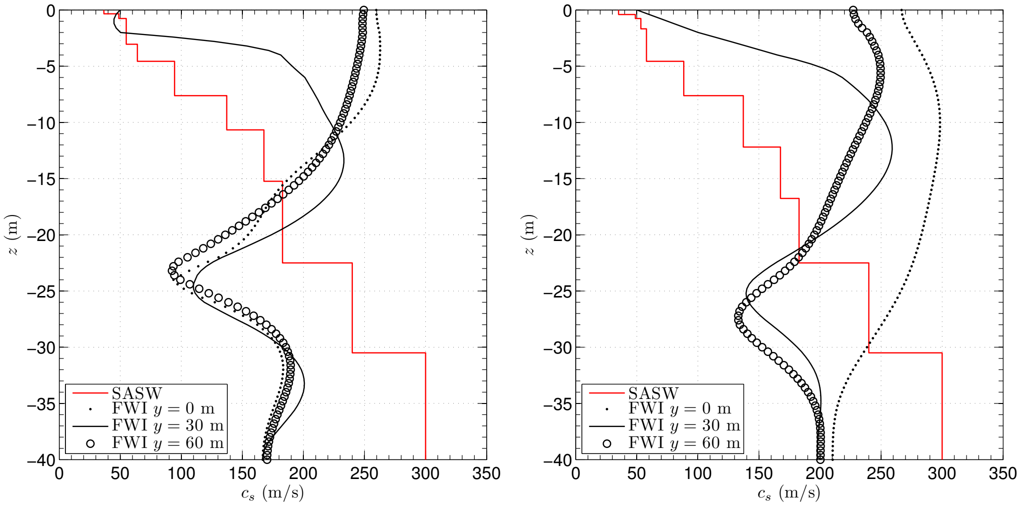

(a) $x = 10$ m (b) $x = 60$ m

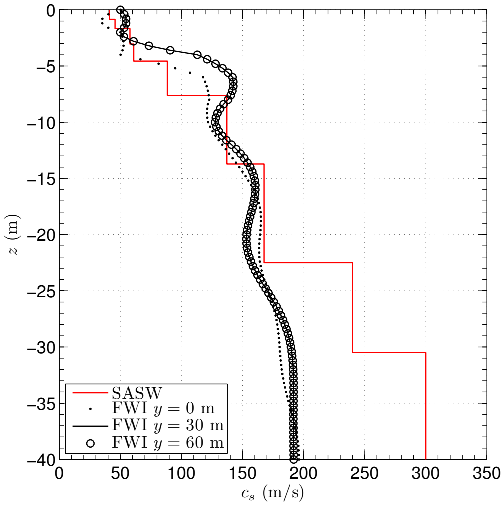

(c) $x = 100$ m

Figure 4.34: Shear wave velocity profiles of the NEES site obtained via SASW and full-waveform-based inversion (FWI).

sponse at select sensor locations. The sensors are placed along the $x = 10, 60, 90, 100$ m lines (Figs. 4.36-4.39). There is good agreement between the measured field response and the response computed based on using the full-waveform inversion profiles. The agreement is significantly better for sensors located along the $x = 90$, 100 m lines (Figs. 4.38-4.39). We remark that the full-waveform-inversion-based c_s profile also agrees better with that of the SASW profile for the $x = 100$ m line (Fig. 4.34(c)). The time-histories at the sensors, computed based on the SASW profiles, differ significantly from the recorded signals.

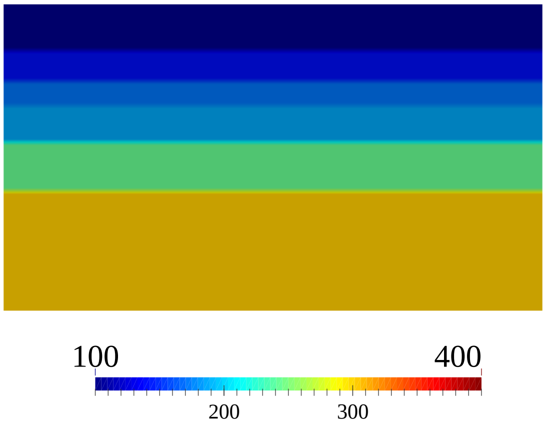

Figure 4.35: Inverted profile for c_s via the SASW method.

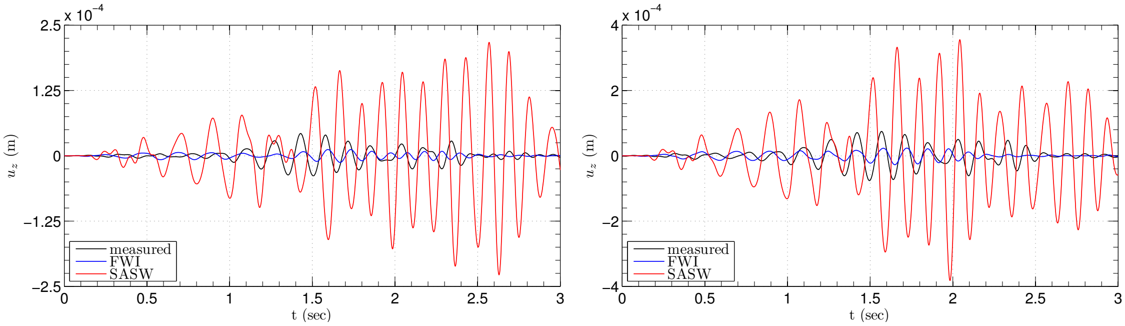

(a) $y = +60$ m (b) $y = +50$ m

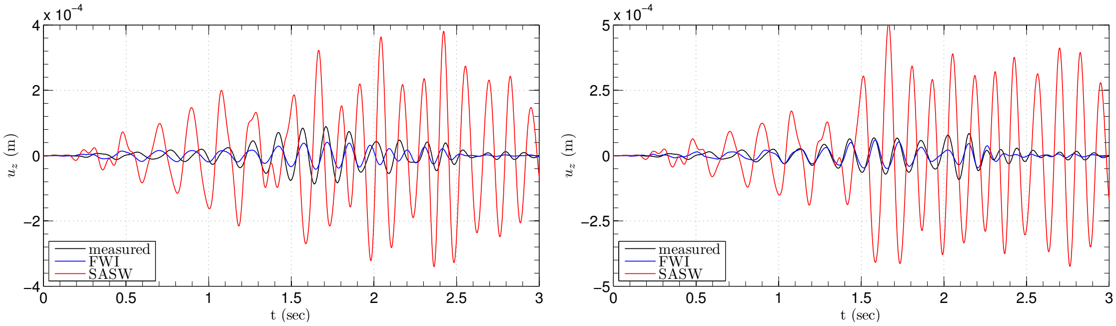

(c) $y = +40$ m (d) $y = +30$ m

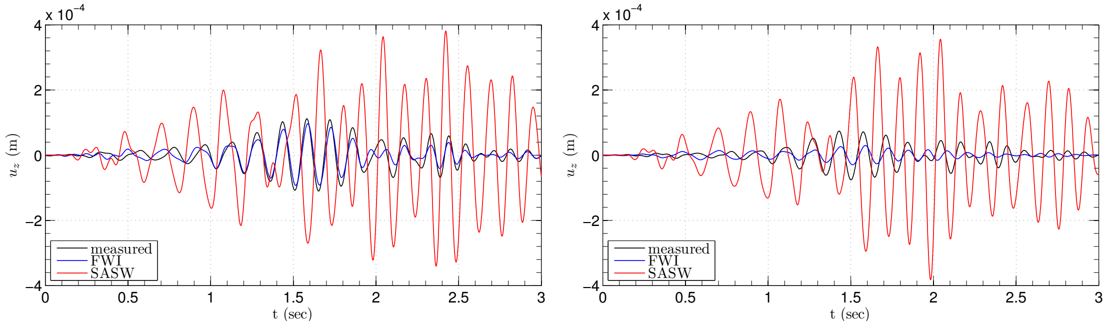

(e) $y = +20$ m (f) $y = +10$ m

Figure 4.36: Comparison of measured surface displacement time-histories against those resulting from the SASW and full-waveform-based inversion ($x = +10$m).

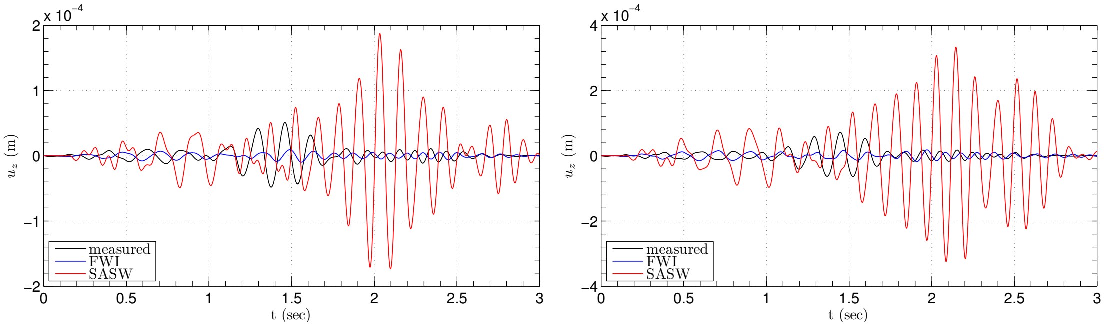

(a) $y = +60$ m (b) $y = +50$ m

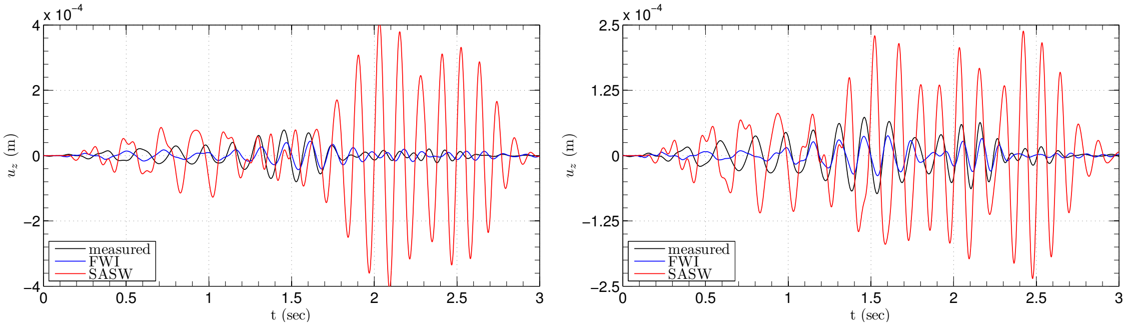

(c) $y = +40$ m (d) $y = +30$ m

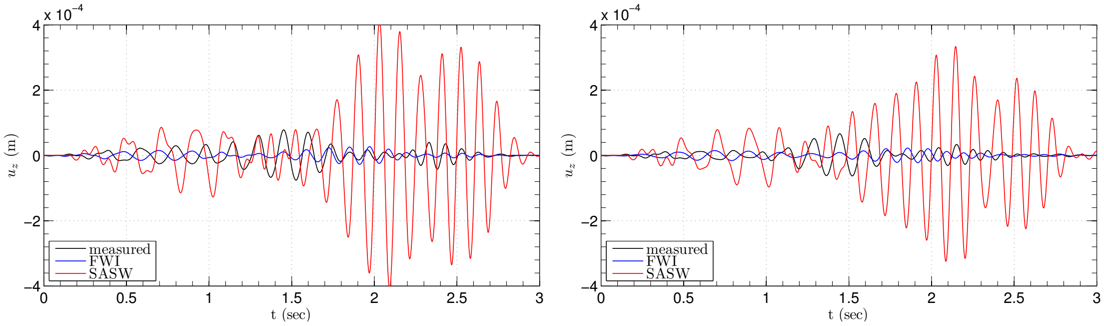

(e) $y = +20$ m (f) $y = +10$ m

Figure 4.37: Comparison of measured surface displacement time-histories against those resulting from the SASW and full-waveform-based inversion ($x = +60$m).

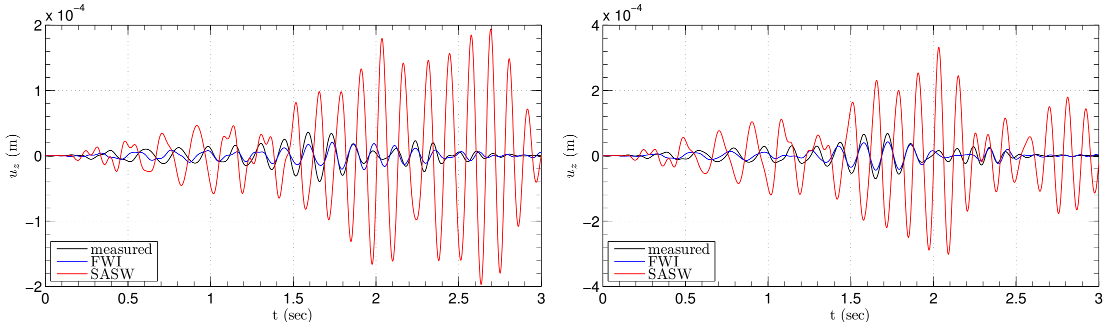

(a) $y = +60$ m (b) $y = +50$ m

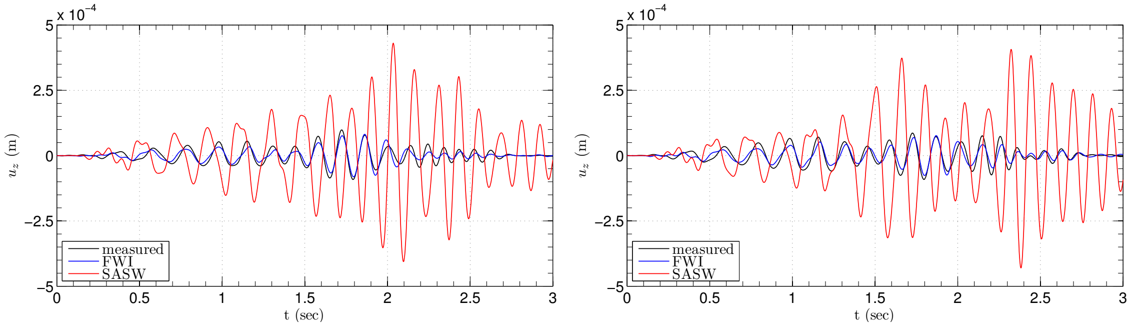

(c) $y = +40$ m (d) $y = +30$ m

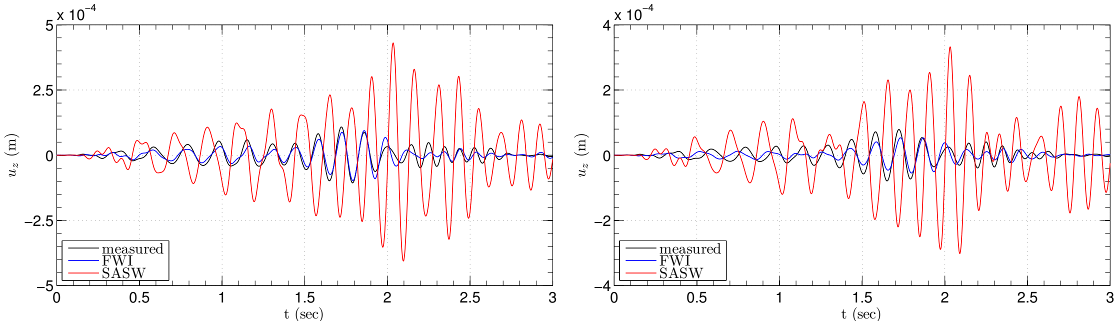

(e) $y = +20$ m (f) $y = +10$ m

Figure 4.38: Comparison of measured surface displacement time-histories against those resulting from the SASW and full-waveform-based inversion ($x = +90$m).

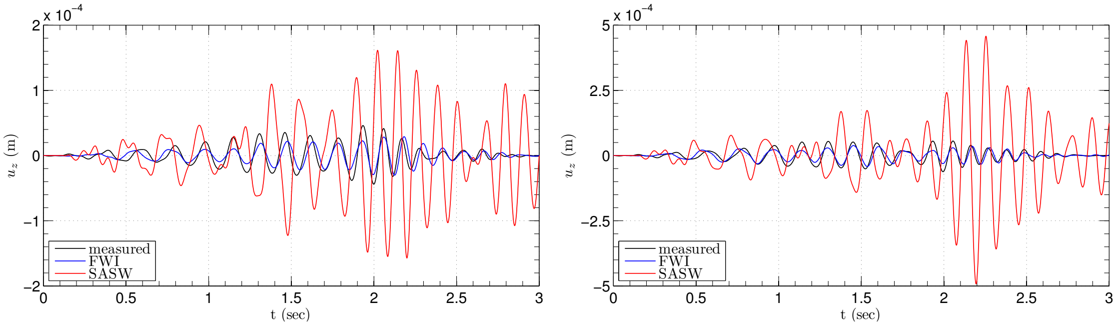

(a) $y = +60$ m (b) $y = +50$ m

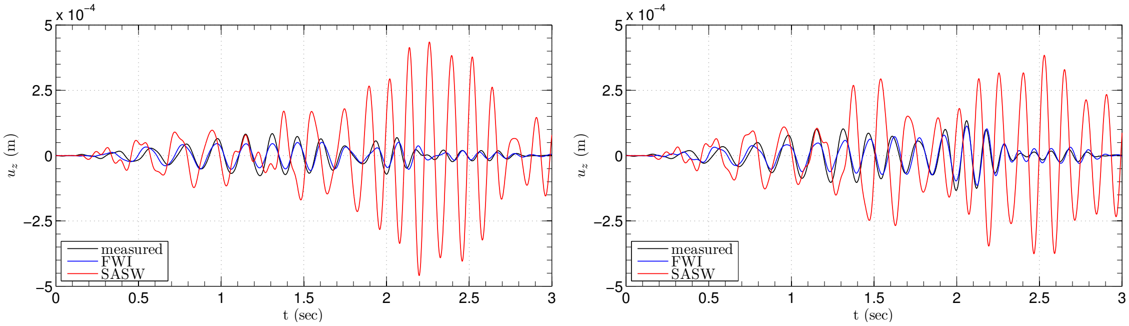

(c) $y = +40$ m (d) $y = +30$ m

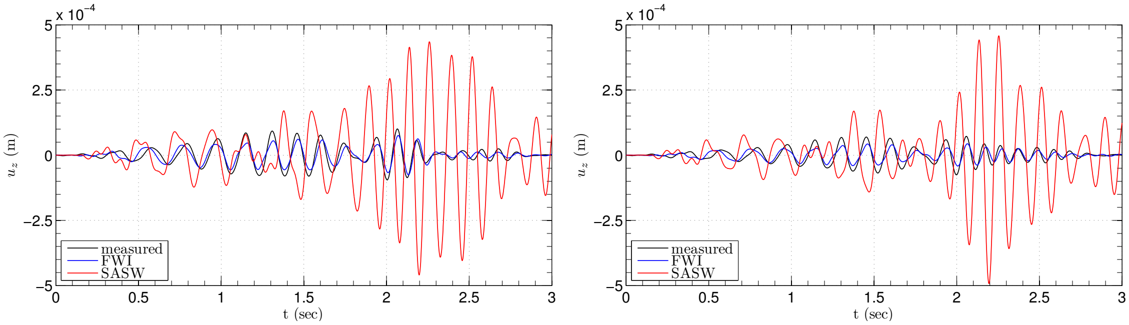

(e) $y = +20$ m (f) $y = +10$ m

Figure 4.39: Comparison of measured surface displacement time-histories against those resulting from the SASW and full-waveform-based inversion ($x = +100$m).

4.6 Summary

We discussed recent advances in the development of a general and robust methodology for geotechnical site characterization, based on full-waveform inversion, using actual field data.

We considered two field experiments consistent with our code development: firstly, we characterized the Hornsby Bend site in Austin, TX, by creating plane strain field conditions and by assuming homogeneity lateral to a two-dimensional slice. We discussed the design and post-processing needs of such field experiments, so that collected records can be seamlessly integrated in the software toolchain. Secondly, we reported the design of a field experiment aimed at the three-dimensional characterization of the NEES@UCSB site in Garner Valley, CA, using the developed three-dimensional inversion codes discussed in the preceding chapter.

Our results demonstrate the clear advantage of allowing for the imaging of arbitrarily heterogeneous sites. Overall, our full-waveform-inversion-based site characterization methodology seems robust and promising.

Chapter 5

Conclusions

5.1 Summary

We presented a robust methodology for site characterization using full-waveform inversion. We complemented the theory and the numerical implementation with results derived from synthetic, as well as field data.

We developed PMLs for domain truncation of three-dimensional, arbitrarily heterogeneous, elastic formations. The formulation is implemented in parallel, and uses scalable algorithms, which makes it suitable for tackling large-scale problems. Specifically, we use a displacement-stress formulation for the PML, coupled with a standard displacement-only formulation for the PML. This hybrid treatment leads to a cost-efficient computational scheme. We discuss several time-marching schemes, which can be used à la carte, depending on the application: a) an extended Newmark scheme for third-order in time, either unsymmetic or fully symmetric semi-discrete forms; b) a standard implicit Newmark for second-order, unsymmetric semi-discrete forms; and c) an explicit Runge-Kutta scheme for a first-order in time unsymmetric system. We also discuss how our formulation can accommodate M-PML with simple modifications. Using numerical experiments, we demonstrate stability and efficacy of the proposed formulation.

Armed with a parallel state-of-the-art forward-wave-solver, we considered the elastic inverse medium problem in three space dimensions. We cast the problem of finding the distributed Lamé parameters in an arbitrarily heterogeneous formation, as a PDE-constraint optimization problem: elastic waves are used as probing agents to interrogate the soil medium, and the response of the medium to these waves are collected at receivers located on the ground surface. The inversion process relies on minimizing a misfit between the collected response at receiver locations, and a computed response based on a trial distribution of the Lamé parameters. We used strategies to alleviate ill-posedness, and lend algorithmic robustness to the proposed inversion scheme. Specifically, we used (a) a regularization factor selection and continuation scheme, where the regularization factor is adaptively computed at each inversion iteration, based on a simple procedure; (b) a source-frequency continuation scheme such that the inversion process evolves by using low-frequency sources, and, gradually, we use sources with higher frequencies; and (c) a biasing scheme for the λ search direction, such that, at early iterations of inversion, the search direction for λ is biased based on that of μ. The latter strategy, in particular, improves the reconstruction of the material profiles when simultaneous inversion of the two Lamé parameters is exercised. After verifying the accuracy of the computed discrete gradients, by comparing them with directional finite differences, we reported results demonstrating successful reconstruction of the Lamé parameters for smooth and sharp profiles, using both noise-free and highly-noisy data.

We also considered the inverse medium problem in two space dimensions, followed by presenting a practical procedure to accommodate three-dimensional field data into two-dimensional codes. We then presented inversion results pertaining to a field experiment at the Hornsby Bend in Austin, TX, and compared them against profiles obtained from the non-invasive SASW, and from invasive CPT tests. Lastly, we used the methodology described in Chapter 3 for the three-dimensional site characterization of the NEES@UCSB site in Garner Valley, CA. Overall, the framework discussed in this study seems robust, practical, and promising.

5.2 Future directions

We suggest future directions that were outside the scope of this dissertation, but are perceived as significant steps toward improving the proposed inversion methodology.

- Validation: in an attempt to validate the proposed methodology, it is important for the full-waveform-inversion-based profiles, obtained from the field experiments, to be compared against invasive techniques that can also provide wave velocity profiles, such as borehole methods.
- Uncertainty quantification: it is desirable to quantify how much confidence one has in the inverted profiles. The Bayesian framework discussed in [106] seems to be applicable to the methodology discussed in this work for quantifying uncertainty in the inverted material profiles.
- Enhanced physics for wave simulation: reliable simulation of wave propagation in soils is remarkably challenging. Even though soil is a lossy, porous medium that is, oftentimes, partially saturated, it is usually idealized as an elastic solid.

Using models that can capture the complex physics of the soil more realistically, is a significant improvement toward high-fidelity subsurface imaging.

- Multi-scale approach for inversion: in order to alleviate the ill-posedness inherent in inverse problems, and to minimize the risk of local minima trapping, using a multi-scale approach, whereby the inversion process in carried out on a sequence of finer grids, seems to be a viable approach [47].

Appendices

Appendix A

Submatrix definitions

Subscripts in the shape functions indicate derivatives.

A.1 Submatrices in equation (2.31)

$$\begin{aligned}
\mathbf{K}_{\mathrm{RD}} &= \int\limits_{\Omega^{\mathrm{RD}}} \begin{bmatrix} \mathbf{K}_{xx} & \mathbf{K}_{xy} & \mathbf{K}_{xz} \\ \mathbf{K}_{yx} & \mathbf{K}_{yy} & \mathbf{K}_{yz} \\ \mathbf{K}_{zx} & \mathbf{K}_{zy} & \mathbf{K}_{zz} \end{bmatrix} \,\mathrm{d}\Omega, \\
\mathbf{K}_{xx} &= (\lambda + 2\mu)\mathbf{\Phi}_x\mathbf{\Phi}_x^T + \mu(\mathbf{\Phi}_y\mathbf{\Phi}_y^T + \mathbf{\Phi}_z\mathbf{\Phi}_z^T), \\
\mathbf{K}_{xy} &= \lambda\mathbf{\Phi}_x\mathbf{\Phi}_y^T + \mu\mathbf{\Phi}_y\mathbf{\Phi}_x^T, \\
\mathbf{K}_{xz} &= \lambda\mathbf{\Phi}_x\mathbf{\Phi}_z^T + \mu\mathbf{\Phi}_z\mathbf{\Phi}_x^T, \\
\mathbf{K}_{yx} &= \lambda\mathbf{\Phi}_y\mathbf{\Phi}_x^T + \mu\mathbf{\Phi}_x\mathbf{\Phi}_y^T, \\
\mathbf{K}_{yy} &= (\lambda + 2\mu)\mathbf{\Phi}_y\mathbf{\Phi}_y^T + \mu(\mathbf{\Phi}_x\mathbf{\Phi}_x^T + \mathbf{\Phi}_z\mathbf{\Phi}_z^T), \\
\mathbf{K}_{yz} &= \lambda\mathbf{\Phi}_y\mathbf{\Phi}_z^T + \mu\mathbf{\Phi}_z\mathbf{\Phi}_y^T, \\
\mathbf{K}_{zx} &= \lambda\mathbf{\Phi}_z\mathbf{\Phi}_x^T + \mu\mathbf{\Phi}_x\mathbf{\Phi}_z^T, \\
\mathbf{K}_{zy} &= \lambda\mathbf{\Phi}_z\mathbf{\Phi}_y^T + \mu\mathbf{\Phi}_y\mathbf{\Phi}_z^T, \\
\mathbf{K}_{zz} &= (\lambda + 2\mu)\mathbf{\Phi}_z\mathbf{\Phi}_z^T + \mu(\mathbf{\Phi}_x\mathbf{\Phi}_x^T + \mathbf{\Phi}_y\mathbf{\Phi}_y^T). \qquad \text{(A.1a)}
\end{aligned}$$

$$\mathbf{M}_{\mathrm{RD}} = \int\limits_{\Omega^{\mathrm{RD}}} \rho \,\mathrm{diag}(\mathbf{\Phi}\mathbf{\Phi}^T, \mathbf{\Phi}\mathbf{\Phi}^T, \mathbf{\Phi}\mathbf{\Phi}^T) \,\mathrm{d}\Omega. \qquad \text{(A.2a)}$$

$$\mathbf{M}_i = \int\limits_{\Omega^{\mathrm{RD}}} i \;\rho \,\mathrm{diag}(\mathbf{\Phi}\mathbf{\Phi}^T, \mathbf{\Phi}\mathbf{\Phi}^T, \mathbf{\Phi}\mathbf{\Phi}^T) \,\mathrm{d}\Omega, \quad i = a, b, c, d. \qquad \text{(A.2b)}$$

$$\mathbf{N}_i = \int\limits_{\Omega^{\mathrm{PML}}} i \,\mathrm{diag}(\mathbf{\Psi}\mathbf{\Psi}^T, \mathbf{\Psi}\mathbf{\Psi}^T, \mathbf{\Psi}\mathbf{\Psi}^T, 2\mathbf{\Psi}\mathbf{\Psi}^T, 2\mathbf{\Psi}\mathbf{\Psi}^T, 2\mathbf{\Psi}\mathbf{\Psi}^T) \,\mathrm{d}\Omega, \quad i = a, b, c, d. \qquad \text{(A.2c)}$$

$$\mathbf{A}_{iu} = \int\limits_{\Omega^{\mathrm{PML}}} \begin{bmatrix} \mathbf{\Phi}_x \mathbf{\Psi}^T \hat{\lambda}^i_{yz} & & & \mathbf{\Phi}_y \mathbf{\Psi}^T \hat{\lambda}^i_{xz} & \mathbf{\Phi}_z \mathbf{\Psi}^T \hat{\lambda}^i_{xy} & \\ & \mathbf{\Phi}_y \mathbf{\Psi}^T \hat{\lambda}^i_{xz} & & \mathbf{\Phi}_x \mathbf{\Psi}^T \hat{\lambda}^i_{yz} & & \mathbf{\Phi}_z \mathbf{\Psi}^T \hat{\lambda}^i_{xy} \\ & & \mathbf{\Phi}_z \mathbf{\Psi}^T \hat{\lambda}^i_{xy} & & \mathbf{\Phi}_x \mathbf{\Psi}^T \hat{\lambda}^i_{yz} & \mathbf{\Phi}_y \mathbf{\Psi}^T \hat{\lambda}^i_{xz} \end{bmatrix} \mathrm{d}\Omega,$$

$$i = e, w, p, \qquad \hat{\lambda}^e_{jk} = \alpha_j \alpha_k, \qquad \hat{\lambda}^p_{jk} = \alpha_j \beta_k + \beta_j \alpha_k, \qquad \hat{\lambda}^w_{jk} = \beta_j \beta_k, \qquad j, k = x, y, z. \tag{A.3a}$$

$$\mathbf{A}_{il} = \int\limits_{\Omega^{\mathrm{PML}}} \begin{bmatrix} \mathbf{A}_{x1} & \mathbf{A}_{x2} & \mathbf{A}_{x3} & \mathbf{A}_{x4} & \mathbf{A}_{x5} & \\ \mathbf{A}_{y1} & \mathbf{A}_{y2} & \mathbf{A}_{y3} & \mathbf{A}_{y4} & & \mathbf{A}_{y6} \\ \mathbf{A}_{z1} & \mathbf{A}_{z2} & \mathbf{A}_{z3} & & \mathbf{A}_{z5} & \mathbf{A}_{z6} \end{bmatrix} \mathrm{d}\Omega, \tag{A.4a}$$

$$\begin{aligned}
&\mathbf{A}_{x1} = (\lambda + 2\mu)\mathbf{\Phi}_x \mathbf{\Psi}^T \hat{\lambda}^i_{yz}, && \mathbf{A}_{y1} = \lambda \mathbf{\Phi}_y \mathbf{\Psi}^T \hat{\lambda}^i_{xz}, && \mathbf{A}_{z1} = \lambda \mathbf{\Phi}_z \mathbf{\Psi}^T \hat{\lambda}^i_{xy}, \\
&\mathbf{A}_{x2} = \lambda \mathbf{\Phi}_x \mathbf{\Psi}^T \hat{\lambda}^i_{yz}, && \mathbf{A}_{y2} = (\lambda + 2\mu)\mathbf{\Phi}_y \mathbf{\Psi}^T \hat{\lambda}^i_{xz}, && \mathbf{A}_{z2} = \lambda \mathbf{\Phi}_z \mathbf{\Psi}^T \hat{\lambda}^i_{xy}, \\
&\mathbf{A}_{x3} = \lambda \mathbf{\Phi}_x \mathbf{\Psi}^T \hat{\lambda}^i_{yz}, && \mathbf{A}_{y3} = \lambda \mathbf{\Phi}_y \mathbf{\Psi}^T \hat{\lambda}^i_{xz}, && \mathbf{A}_{z3} = (\lambda + 2\mu)\mathbf{\Phi}_z \mathbf{\Psi}^T \hat{\lambda}^i_{xy}, \\
&\mathbf{A}_{x4} = 2\mu \mathbf{\Phi}_y \mathbf{\Psi}^T \hat{\lambda}^i_{xz}, && \mathbf{A}_{y4} = 2\mu \mathbf{\Phi}_x \mathbf{\Psi}^T \hat{\lambda}^i_{yz}, && \mathbf{A}_{z5} = 2\mu \mathbf{\Phi}_x \mathbf{\Psi}^T \hat{\lambda}^i_{yz}, \\
&\mathbf{A}_{x5} = 2\mu \mathbf{\Phi}_z \mathbf{\Psi}^T \hat{\lambda}^i_{xy}, && \mathbf{A}_{y6} = 2\mu \mathbf{\Phi}_z \mathbf{\Psi}^T \hat{\lambda}^i_{xy}, && \mathbf{A}_{z6} = 2\mu \mathbf{\Phi}_y \mathbf{\Psi}^T \hat{\lambda}^i_{xz}, \\
&\hat{\lambda}^e_{jk} = \alpha_j \alpha_k, && \hat{\lambda}^p_{jk} = \alpha_j \beta_k + \beta_j \alpha_k, && \hat{\lambda}^w_{jk} = \beta_j \beta_k, \\
&i = e, w, p, && j, k = x, y, z. &&
\end{aligned} \tag{A.5a}$$

$$\mathbf{f}_{\mathrm{RD}} = \int\limits_{\Gamma^{\mathrm{RD}}_{\mathrm{N}}} \begin{bmatrix} \mathbf{\Phi}\ g_x(\mathbf{x}, t) \\ \mathbf{\Phi}\ g_y(\mathbf{x}, t) \\ \mathbf{\Phi}\ g_z(\mathbf{x}, t) \end{bmatrix} \mathrm{d}\Gamma + \int\limits_{\Omega^{\mathrm{RD}}} \begin{bmatrix} \mathbf{\Phi}\ b_x(\mathbf{x}, t) \\ \mathbf{\Phi}\ b_y(\mathbf{x}, t) \\ \mathbf{\Phi}\ b_z(\mathbf{x}, t) \end{bmatrix} \mathrm{d}\Omega. \tag{A.6a}$$

A.2 Submatrices for the symmetric PML formulation

$$\mathbf{N}_i = \int\limits_{\Omega^{\mathrm{PML}}} i \begin{bmatrix} \frac{\lambda+\mu}{\mu(3\lambda+2\mu)} \mathbf{\Psi}\mathbf{\Psi}^T & \frac{-\lambda}{2\mu(3\lambda+2\mu)} \mathbf{\Psi}\mathbf{\Psi}^T & \frac{-\lambda}{2\mu(3\lambda+2\mu)} \mathbf{\Psi}\mathbf{\Psi}^T & & & \\ \frac{-\lambda}{2\mu(3\lambda+2\mu)} \mathbf{\Psi}\mathbf{\Psi}^T & \frac{\lambda+\mu}{\mu(3\lambda+2\mu)} \mathbf{\Psi}\mathbf{\Psi}^T & \frac{-\lambda}{2\mu(3\lambda+2\mu)} \mathbf{\Psi}\mathbf{\Psi}^T & & & \\ \frac{-\lambda}{2\mu(3\lambda+2\mu)} \mathbf{\Psi}\mathbf{\Psi}^T & \frac{-\lambda}{2\mu(3\lambda+2\mu)} \mathbf{\Psi}\mathbf{\Psi}^T & \frac{\lambda+\mu}{\mu(3\lambda+2\mu)} \mathbf{\Psi}\mathbf{\Psi}^T & & & \\ & & & \frac{1}{\mu} \mathbf{\Psi}\mathbf{\Psi}^T & & \\ & & & & \frac{1}{\mu} \mathbf{\Psi}\mathbf{\Psi}^T & \\ & & & & & \frac{1}{\mu} \mathbf{\Psi}\mathbf{\Psi}^T \end{bmatrix} \mathrm{d}\Omega,$$

$$i = a, b, c, d. \tag{A.7a}$$

$$\mathbf{A}_i = \int\limits_{\Omega^{\mathrm{PML}}} \begin{bmatrix} \mathbf{\Phi}_x \mathbf{\Psi}^T \hat{\lambda}^i_{yz} & & & \mathbf{\Phi}_y \mathbf{\Psi}^T \hat{\lambda}^i_{xz} & \mathbf{\Phi}_z \mathbf{\Psi}^T \hat{\lambda}^i_{xy} & \\ & \mathbf{\Phi}_y \mathbf{\Psi}^T \hat{\lambda}^i_{xz} & & \mathbf{\Phi}_x \mathbf{\Psi}^T \hat{\lambda}^i_{yz} & & \mathbf{\Phi}_z \mathbf{\Psi}^T \hat{\lambda}^i_{xy} \\ & & \mathbf{\Phi}_z \mathbf{\Psi}^T \hat{\lambda}^i_{xy} & & \mathbf{\Phi}_x \mathbf{\Psi}^T \hat{\lambda}^i_{yz} & \mathbf{\Phi}_y \mathbf{\Psi}^T \hat{\lambda}^i_{xz} \end{bmatrix} \mathrm{d}\Omega,$$

$$i = e, w, p,$$

$$\hat{\lambda}^e_{jk} = \alpha_j \alpha_k, \qquad \hat{\lambda}^p_{jk} = \alpha_j \beta_k + \beta_j \alpha_k, \qquad \hat{\lambda}^w_{jk} = \beta_j \beta_k, \qquad j, k = x, y, z. \tag{A.8a}$$

A.3 Submatrices for M-PML

$$\mathbf{A}_{iu} = \int\limits_{\Omega^{\mathrm{PML}}} \begin{bmatrix} \mathbf{\Phi}_x \mathbf{\Psi}^T \hat{\lambda}^i_{yz} & & & \mathbf{\Phi}_y \mathbf{\Psi}^T \hat{\lambda}^i_{xz} & \mathbf{\Phi}_z \mathbf{\Psi}^T \hat{\lambda}^i_{xy} & \\ & \mathbf{\Phi}_y \mathbf{\Psi}^T \hat{\lambda}^i_{xz} & & \mathbf{\Phi}_x \mathbf{\Psi}^T \hat{\lambda}^i_{yz} & & \mathbf{\Phi}_z \mathbf{\Psi}^T \hat{\lambda}^i_{xy} \\ & & \mathbf{\Phi}_z \mathbf{\Psi}^T \hat{\lambda}^i_{xy} & & \mathbf{\Phi}_x \mathbf{\Psi}^T \hat{\lambda}^i_{yz} & \mathbf{\Phi}_y \mathbf{\Psi}^T \hat{\lambda}^i_{xz} \end{bmatrix} \mathrm{d}\Omega$$

$$+ \int\limits_{\Omega^{\mathrm{PML}}} \begin{bmatrix} \mathbf{\Phi} \mathbf{\Psi}^T \frac{\partial \hat{\lambda}^i_{yz}}{\partial x} & & & \mathbf{\Phi} \mathbf{\Psi}^T \frac{\partial \hat{\lambda}^i_{xz}}{\partial y} & \mathbf{\Phi} \mathbf{\Psi}^T \frac{\partial \hat{\lambda}^i_{xy}}{\partial z} & \\ & \mathbf{\Phi} \mathbf{\Psi}^T \frac{\partial \hat{\lambda}^i_{xz}}{\partial y} & & \mathbf{\Phi} \mathbf{\Psi}^T \frac{\partial \hat{\lambda}^i_{yz}}{\partial x} & & \mathbf{\Phi} \mathbf{\Psi}^T \frac{\partial \hat{\lambda}^i_{xy}}{\partial z} \\ & & \mathbf{\Phi} \mathbf{\Psi}^T \frac{\partial \hat{\lambda}^i_{xy}}{\partial z} & & \mathbf{\Phi} \mathbf{\Psi}^T \frac{\partial \hat{\lambda}^i_{yz}}{\partial x} & \mathbf{\Phi} \mathbf{\Psi}^T \frac{\partial \hat{\lambda}^i_{xz}}{\partial y} \end{bmatrix} \mathrm{d}\Omega,$$

$$i = e, w, p, \qquad \hat{\lambda}^e_{jk} = \alpha_j \alpha_k, \qquad \hat{\lambda}^p_{jk} = \alpha_j \beta_k + \beta_j \alpha_k, \qquad \hat{\lambda}^w_{jk} = \beta_j \beta_k, \qquad j, k = x, y, z. \tag{A.9a}$$

A.4 Discretization of the control problems

In Section 3.2.1.3, we discussed the λ- and μ-control problems. In this part, we consider their spatial discretization. We use the basis function $\mathbf{\Phi}$ for the spatial discretization of $\mathbf{w}(\mathbf{x}, t)$ and $\mathbf{u}(\mathbf{x}, t)$, and $\boldsymbol{\chi}$ is the basis function for discretizing $\lambda(\mathbf{x})$ and $\mu(\mathbf{x})$. For instance, if we approximate $\lambda(\mathbf{x})$ with $\lambda_h(\mathbf{x})$, then $\lambda_h(\mathbf{x}) = \boldsymbol{\chi}^T \boldsymbol{\lambda}$, where $\boldsymbol{\lambda}$ comprises the vector of nodal values for λ. In the following, subscripts in the shape functions indicate derivatives, and $\mathbf{u}_h = (\mathbf{u}_x^T, \mathbf{u}_y^T, \mathbf{u}_z^T)^T$ and $\mathbf{w}_h = (\mathbf{w}_x^T, \mathbf{w}_y^T, \mathbf{w}_z^T)^T$ is the vector of discrete values of the state and adjoint variables, respectively. Accordingly

$$\tilde{\mathbf{M}} = \int\limits_{\Omega^{\mathrm{RD}}} \boldsymbol{\chi} \boldsymbol{\chi}^T \, \mathrm{d}\Omega. \tag{A.10a}$$

For Tikhonov regularization:

$$\mathbf{g}_{\text{reg}}^{\lambda} = \int\limits_{\Omega^{\text{RD}}} (\boldsymbol{\chi}_x \boldsymbol{\chi}_x^T + \boldsymbol{\chi}_y \boldsymbol{\chi}_y^T + \boldsymbol{\chi}_z \boldsymbol{\chi}_z^T) \boldsymbol{\lambda} \, \mathrm{d}\Omega, \tag{A.10b}$$

$$\mathbf{g}_{\text{reg}}^{\mu} = \int\limits_{\Omega^{\text{RD}}} (\boldsymbol{\chi}_x \boldsymbol{\chi}_x^T + \boldsymbol{\chi}_y \boldsymbol{\chi}_y^T + \boldsymbol{\chi}_z \boldsymbol{\chi}_z^T) \boldsymbol{\mu} \, \mathrm{d}\Omega. \tag{A.10c}$$

For Total Variation regularization:

$$\mathbf{g}_{\text{reg}}^{\lambda} = \int\limits_{\Omega^{\text{RD}}} \frac{(\boldsymbol{\chi}_x \boldsymbol{\chi}_x^T + \boldsymbol{\chi}_y \boldsymbol{\chi}_y^T + \boldsymbol{\chi}_z \boldsymbol{\chi}_z^T) \boldsymbol{\lambda}}{\Big(\boldsymbol{\lambda}^T (\boldsymbol{\chi}_x \boldsymbol{\chi}_x^T + \boldsymbol{\chi}_y \boldsymbol{\chi}_y^T + \boldsymbol{\chi}_z \boldsymbol{\chi}_z^T) \boldsymbol{\lambda} + \epsilon \Big)^{\frac{1}{2}}} \, \mathrm{d}\Omega, \tag{A.10d}$$

$$\mathbf{g}_{\text{reg}}^{\mu} = \int\limits_{\Omega^{\text{RD}}} \frac{(\boldsymbol{\chi}_x \boldsymbol{\chi}_x^T + \boldsymbol{\chi}_y \boldsymbol{\chi}_y^T + \boldsymbol{\chi}_z \boldsymbol{\chi}_z^T) \boldsymbol{\mu}}{\Big(\boldsymbol{\mu}^T (\boldsymbol{\chi}_x \boldsymbol{\chi}_x^T + \boldsymbol{\chi}_y \boldsymbol{\chi}_y^T + \boldsymbol{\chi}_z \boldsymbol{\chi}_z^T) \boldsymbol{\mu} + \epsilon \Big)^{\frac{1}{2}}} \, \mathrm{d}\Omega. \tag{A.10e}$$

Moreover,

$$\mathbf{g}_{\text{mis}}^{\lambda} = -\int_0^T \int\limits_{\Omega^{\text{RD}}} \boldsymbol{\chi} \; (\boldsymbol{\Phi}_x^T \mathbf{w}_x + \boldsymbol{\Phi}_y^T \mathbf{w}_y + \boldsymbol{\Phi}_z^T \mathbf{w}_z)(\boldsymbol{\Phi}_x^T \mathbf{u}_x + \boldsymbol{\Phi}_y^T \mathbf{u}_y + \boldsymbol{\Phi}_z^T \mathbf{u}_z) \, \mathrm{d}\Omega \; dt, \tag{A.10f}$$

$$\begin{aligned} \mathbf{g}_{\text{mis}}^{\mu} = -\int_0^T \int\limits_{\Omega^{\text{RD}}} \boldsymbol{\chi} \; \Big(& 2 \; (\boldsymbol{\Phi}_x^T \mathbf{w}_x \; \boldsymbol{\Phi}_x^T \mathbf{u}_x + \boldsymbol{\Phi}_y^T \mathbf{w}_y \; \boldsymbol{\Phi}_y^T \mathbf{u}_y + \boldsymbol{\Phi}_z^T \mathbf{w}_z \; \boldsymbol{\Phi}_z^T \mathbf{u}_z) \\ & + (\boldsymbol{\Phi}_y^T \mathbf{w}_x + \boldsymbol{\Phi}_x^T \mathbf{w}_y)(\boldsymbol{\Phi}_x^T \mathbf{u}_y + \boldsymbol{\Phi}_y^T \mathbf{u}_x) + (\boldsymbol{\Phi}_z^T \mathbf{w}_x + \boldsymbol{\Phi}_x^T \mathbf{w}_z)(\boldsymbol{\Phi}_x^T \mathbf{u}_z + \boldsymbol{\Phi}_z^T \mathbf{u}_x) \\ & + (\boldsymbol{\Phi}_z^T \mathbf{w}_y + \boldsymbol{\Phi}_y^T \mathbf{w}_z)(\boldsymbol{\Phi}_y^T \mathbf{u}_z + \boldsymbol{\Phi}_z^T \mathbf{u}_y) \Big) \, \mathrm{d}\Omega \; dt. \end{aligned} \tag{A.10g}$$

In (A.10a), upon using spectral elements with LGL quadrature rule, $\tilde{\mathbf{M}}$ becomes diagonal; thus, its inverse can be computed easily.

A.5 Submatrices in equation (4.3)

The two-dimensional PML formulation discussed in Chapter 4, results in the semi-discrete form (4.3), with the following definition for the system matrices:

$$\mathbf{M}_{\mathrm{2D}} = \begin{bmatrix} \bar{\mathbf{M}}_{\mathrm{RD}} + \bar{\mathbf{M}}_a & \mathbf{0} \\ \mathbf{0} & -\mathbf{N}_a \end{bmatrix}, \qquad \mathbf{C}_{\mathrm{2D}} = \begin{bmatrix} \bar{\mathbf{M}}_b & \bar{\mathbf{A}}_e \\ \bar{\mathbf{A}}_e^T & -\mathbf{N}_b \end{bmatrix}, \tag{A.11a}$$

$$\mathbf{K}_{\mathrm{2D}} = \begin{bmatrix} \bar{\mathbf{K}}_{\mathrm{RD}} + \bar{\mathbf{M}}_c & \bar{\mathbf{A}}_p \\ \bar{\mathbf{A}}_p^T & -\mathbf{N}_c \end{bmatrix}, \tag{A.11b}$$

where a bar denotes matrix extension to encompass all the displacement degrees-of-freedom. The submatrices in (A.11) are defined below:

$$\mathbf{K}_{\mathrm{RD}} = \int\limits_{\Omega^{\mathrm{RD}}} \begin{bmatrix} (\lambda+2\mu)\boldsymbol{\Phi}_x\boldsymbol{\Phi}_x^T + \mu\boldsymbol{\Phi}_y\boldsymbol{\Phi}_y^T & \lambda\boldsymbol{\Phi}_x\boldsymbol{\Phi}_y^T + \mu\boldsymbol{\Phi}_y\boldsymbol{\Phi}_x^T \\ \lambda\boldsymbol{\Phi}_y\boldsymbol{\Phi}_x^T + \mu\boldsymbol{\Phi}_x\boldsymbol{\Phi}_y^T & (\lambda+2\mu)\boldsymbol{\Phi}_y\boldsymbol{\Phi}_y^T + \mu\boldsymbol{\Phi}_x\boldsymbol{\Phi}_x^T \end{bmatrix} \mathrm{d}\Omega, \tag{A.12a}$$

$$\mathbf{M}_{\mathrm{RD}} = \int\limits_{\Omega^{\mathrm{RD}}} \rho \ \mathrm{diag}(\boldsymbol{\Phi}\boldsymbol{\Phi}^T, \boldsymbol{\Phi}\boldsymbol{\Phi}^T) \, \mathrm{d}\Omega, \tag{A.12b}$$

$$\mathbf{M}_i = \int\limits_{\Omega^{\mathrm{RD}}} i \ \rho \ \mathrm{diag}(\boldsymbol{\Phi}\boldsymbol{\Phi}^T, \boldsymbol{\Phi}\boldsymbol{\Phi}^T) \, \mathrm{d}\Omega, \quad i = a, b, c, \tag{A.12c}$$

$$\mathbf{N}_i = \int\limits_{\Omega^{\mathrm{PML}}} i \begin{bmatrix} \frac{\lambda+2\mu}{4\mu(\lambda+\mu)}\boldsymbol{\Psi}\boldsymbol{\Psi}^T & \frac{-\lambda}{4\mu(\lambda+\mu)}\boldsymbol{\Psi}\boldsymbol{\Psi}^T & \\ \frac{-\lambda}{4\mu(\lambda+\mu)}\boldsymbol{\Psi}\boldsymbol{\Psi}^T & \frac{\lambda+2\mu}{4\mu(\lambda+\mu)}\boldsymbol{\Psi}\boldsymbol{\Psi}^T & \\ & & \frac{1}{\mu}\boldsymbol{\Psi}\boldsymbol{\Psi}^T \end{bmatrix} \mathrm{d}\Omega, \quad i = a, b, c, \tag{A.12d}$$

$$\mathbf{A}_i = \int\limits_{\Omega^{\mathrm{PML}}} \begin{bmatrix} \boldsymbol{\Phi}_x\boldsymbol{\Psi}^T\hat{\lambda}_y^i & & \boldsymbol{\Phi}_y\boldsymbol{\Psi}^T\hat{\lambda}_x^i \\ & \boldsymbol{\Phi}_y\boldsymbol{\Psi}^T\hat{\lambda}_x^i & \boldsymbol{\Phi}_x\boldsymbol{\Psi}^T\hat{\lambda}_y^i \end{bmatrix} \mathrm{d}\Omega, \quad i = e, p, \quad \hat{\lambda}_j^e = \alpha_j, \ \hat{\lambda}_j^p = \beta_j, \ j = x, y, \tag{A.12e}$$

where $a = \alpha_x\alpha_y$, $b = \alpha_x\beta_y + \alpha_y\beta_x$, and $c = \beta_x\beta_y$.

Appendix B

Time-integration schemes

B.1 Fourth-order Runge-Kutta method

In Section 2.3.2 we discussed various time marching schemes for integrating (2.32). Our preferred scheme is the explicit 4th-order Runge-Kutta method (RK-4), which is outlined below.

Upon using spectral elements, with Legendre-Gauss-Lobatto quadrature rule, the mass-like matrix **M** becomes diagonal; therefore, its inverse can be readily computed. We define the following variables:

$$\hat{\mathbf{C}} = \mathbf{M}^{-1}\ \mathbf{C}, \qquad \hat{\mathbf{K}} = \mathbf{M}^{-1}\ \mathbf{K}, \tag{B.1a}$$

$$\hat{\mathbf{G}} = \mathbf{M}^{-1}\ \mathbf{G}, \qquad \hat{\mathbf{f}} = \mathbf{M}^{-1}\ \mathbf{f}. \tag{B.1b}$$

Using the above notation, (2.36) becomes:

$$\frac{d}{dt}\begin{bmatrix}\mathbf{x}_0\\ \mathbf{x}_1\\ \mathbf{x}_2\end{bmatrix} = \begin{bmatrix}\mathbf{0} & \mathbf{I} & \mathbf{0}\\ \mathbf{0} & \mathbf{0} & \mathbf{I}\\ -\hat{\mathbf{G}} & -\hat{\mathbf{K}} & -\hat{\mathbf{C}}\end{bmatrix}\begin{bmatrix}\mathbf{x}_0\\ \mathbf{x}_1\\ \mathbf{x}_2\end{bmatrix} + \begin{bmatrix}\mathbf{0}\\ \mathbf{0}\\ \hat{\mathbf{f}}\end{bmatrix}. \tag{B.2}$$

The explicit RK-4 scheme entails computing the following vectors:

$$
\begin{aligned}
\mathbf{k}_{10} &= \mathbf{x}_1^n, \\
\mathbf{k}_{11} &= \mathbf{x}_2^n, \\
\mathbf{k}_{12} &= -\hat{\mathbf{C}}\mathbf{x}_2^n - \hat{\mathbf{K}}\mathbf{x}_1^n - \hat{\mathbf{G}}\mathbf{x}_0^n + \hat{\mathbf{f}}^n, \\
\mathbf{k}_{20} &= \mathbf{x}_1^n + \frac{\Delta t}{2}\ \mathbf{k}_{11}, \\
\mathbf{k}_{21} &= \mathbf{x}_2^n + \frac{\Delta t}{2}\ \mathbf{k}_{12}, \\
\mathbf{k}_{22} &= -\hat{\mathbf{C}}(\mathbf{x}_2^n + \frac{\Delta t}{2}\ \mathbf{k}_{12}) - \hat{\mathbf{K}}(\mathbf{x}_1^n + \frac{\Delta t}{2}\ \mathbf{k}_{11}) - \hat{\mathbf{G}}(\mathbf{x}_0^n + \frac{\Delta t}{2}\ \mathbf{k}_{10}) + \hat{\mathbf{f}}^{n+\frac{1}{2}}, \\
\mathbf{k}_{30} &= \mathbf{x}_1^n + \frac{\Delta t}{2}\ \mathbf{k}_{21}, \\
\mathbf{k}_{31} &= \mathbf{x}_2^n + \frac{\Delta t}{2}\ \mathbf{k}_{22}, \\
\mathbf{k}_{32} &= -\hat{\mathbf{C}}(\mathbf{x}_2^n + \frac{\Delta t}{2}\ \mathbf{k}_{22}) - \hat{\mathbf{K}}(\mathbf{x}_1^n + \frac{\Delta t}{2}\ \mathbf{k}_{21}) - \hat{\mathbf{G}}(\mathbf{x}_0^n + \frac{\Delta t}{2}\ \mathbf{k}_{20}) + \hat{\mathbf{f}}^{n+\frac{1}{2}}, \\
\mathbf{k}_{40} &= \mathbf{x}_1^n + \Delta t\ \mathbf{k}_{31}, \\
\mathbf{k}_{41} &= \mathbf{x}_2^n + \Delta t\ \mathbf{k}_{32}, \\
\mathbf{k}_{42} &= -\hat{\mathbf{C}}(\mathbf{x}_2^n + \Delta t\ \mathbf{k}_{32}) - \hat{\mathbf{K}}(\mathbf{x}_1^n + \Delta t\ \mathbf{k}_{31}) - \hat{\mathbf{G}}(\mathbf{x}_0^n + \Delta t\ \mathbf{k}_{30}) + \hat{\mathbf{f}}^{n+1}.
\end{aligned}
$$

Finally, the solution at time step $(n+1)$ can be updated via

$$
\begin{bmatrix} \mathbf{x}_0 \\ \mathbf{x}_1 \\ \mathbf{x}_2 \end{bmatrix}^{n+1} = \begin{bmatrix} \mathbf{x}_0 \\ \mathbf{x}_1 \\ \mathbf{x}_2 \end{bmatrix}^{n} + \frac{\Delta t}{6} \begin{bmatrix} \mathbf{k}_{10} + 2\ \mathbf{k}_{20} + 2\ \mathbf{k}_{30} + \mathbf{k}_{40} \\ \mathbf{k}_{11} + 2\ \mathbf{k}_{21} + 2\ \mathbf{k}_{31} + \mathbf{k}_{41} \\ \mathbf{k}_{12} + 2\ \mathbf{k}_{22} + 2\ \mathbf{k}_{32} + \mathbf{k}_{42} \end{bmatrix}. \tag{B.4}
$$

B.2 Extended Newmark method

In this part, we are concerned with the time integration of the following semi-discrete equation, discussed in Sections 2.3.2 and 2.5:

$$\mathbf{M}\ddot{\mathbf{d}} + \mathbf{C}\dot{\mathbf{d}} + \mathbf{K}\mathbf{d} + \mathbf{G}\bar{\mathbf{d}} = \mathbf{f}, \tag{B.5a}$$

$$\bar{\mathbf{d}} = \int_0^t \mathbf{d}(\tau)|_{\text{PML}}\ d\tau. \tag{B.5b}$$

We discuss an extension of the Newmark method [107] for time integration of this equation. The scheme is implicit, and can be applied to problems with either symmetric, or unsymmetric matrices. We start with Taylor series-like expansion of the following quantities

$$\bar{\mathbf{d}}^{n+1} = \bar{\mathbf{d}}^n + \Delta t\ \mathbf{d}^n + \frac{\Delta t^2}{2}\dot{\mathbf{d}}^n + (\frac{1}{6} - \alpha)\Delta t^3\ \ddot{\mathbf{d}}^n + \alpha\ \Delta t^3\ \ddot{\mathbf{d}}^{n+1}, \tag{B.6a}$$

$$\mathbf{d}^{n+1} = \mathbf{d}^n + \Delta t\ \dot{\mathbf{d}}^n + (\frac{1}{2} - \beta)\Delta t^2\ \ddot{\mathbf{d}}^n + \beta\ \Delta t^2\ \ddot{\mathbf{d}}^{n+1}, \tag{B.6b}$$

$$\dot{\mathbf{d}}^{n+1} = \dot{\mathbf{d}}^n + (1 - \gamma)\Delta t\ \ddot{\mathbf{d}}^n + \gamma\ \Delta t\ \ddot{\mathbf{d}}^{n+1}, \tag{B.6c}$$

where Δt denotes the time step, superscripts (n) and $(n+1)$ indicate current and next time steps, β and γ are the classic Newmark parameters, and α is a new parameter. Substitution of (B.6) in (B.5) at the $(n+1)^{\text{th}}$ time step, results in the following linear system of equations

$$\hat{\mathbf{K}}\ \ddot{\mathbf{d}}^{n+1} = \hat{\mathbf{R}}^{n+1}, \tag{B.7a}$$

where

$$\hat{\mathbf{K}} = \mathbf{M} + \gamma \ \Delta t \ \mathbf{C} + \beta \ \Delta t^2 \ \mathbf{K} + \alpha \ \Delta t^3 \ \mathbf{G}, \tag{B.7b}$$

$$\begin{aligned} \hat{\mathbf{R}}^{n+1} &= \mathbf{f}^{n+1} \\ &- \mathbf{C} \left[\dot{\mathbf{d}}^n + (1-\gamma) \ \Delta t \ \ddot{\mathbf{d}}^n \right] \\ &- \mathbf{K} \left[\mathbf{d}^n + \Delta t \ \dot{\mathbf{d}}^n + (\frac{1}{2} - \beta) \ \Delta t^2 \ \ddot{\mathbf{d}}^n \right] \\ &- \mathbf{G} \left[\bar{\mathbf{d}}^n + \Delta t \ \mathbf{d}^n + \frac{\Delta t^2}{2} \mathbf{d}^n + (\frac{1}{6} - \alpha) \ \Delta t^3 \ \ddot{\mathbf{d}}^n \right]. \end{aligned} \tag{B.7c}$$

Upon solving for $\ddot{\mathbf{d}}^{n+1}$ from (B.7a), $\bar{\mathbf{d}}^{n+1}$, $\mathbf{d}^{n+1}$, and $\dot{\mathbf{d}}^{n+1}$ can be updated using (B.6). Average-, and linear-acceleration schemes correspond to taking (α, β, γ) equal to $(\frac{1}{12}, \frac{1}{4}, \frac{1}{2})$, and $(\frac{1}{24}, \frac{1}{6}, \frac{1}{2})$, respectively. Numerical results reported in Section 2.7.3 were computed using the average-acceleration scheme.

B.3 The adjoint problem time-integration scheme

We outline the explicit 4^{th}-order Runge-Kutta method (RK-4) for the reverse time-integration of the adjoint problem. Upon using spectral elements, with Legendre-Gauss-Lobatto (LGL) quadrature rule, the mass-like matrix $\mathbf{M}$ becomes diagonal; therefore, its inverse can be readily computed. We use the following notation:

$$\hat{\mathbf{C}} = \mathbf{C} \ \mathbf{M}^{-1}, \qquad \hat{\mathbf{K}} = \mathbf{K} \ \mathbf{M}^{-1}, \tag{B.8a}$$

$$\hat{\mathbf{G}} = \mathbf{G} \ \mathbf{M}^{-1}, \qquad \hat{\mathbf{f}} = \mathbf{M}^{-1} \ \mathbf{f}^{\text{adj}}. \tag{B.8b}$$

Using (B.8), (3.14) becomes:

$$\frac{d}{dt}\begin{bmatrix}\mathbf{y}_0\\ \mathbf{y}_1\\ \mathbf{y}_2\end{bmatrix} = \begin{bmatrix}\mathbf{0} & \mathbf{I} & \mathbf{0}\\ \mathbf{0} & \mathbf{0} & \mathbf{I}\\ \hat{\mathbf{G}}^T & -\hat{\mathbf{K}}^T & \hat{\mathbf{C}}^T\end{bmatrix}\begin{bmatrix}\mathbf{y}_0\\ \mathbf{y}_1\\ \mathbf{y}_2\end{bmatrix} + \begin{bmatrix}\mathbf{0}\\ \mathbf{0}\\ \hat{\mathbf{f}}\end{bmatrix}. \tag{B.9}$$

The scheme entails computing the following vectors:

$$\begin{aligned}
\mathbf{k}_{10} &= \mathbf{y}_1^n,\\
\mathbf{k}_{11} &= \mathbf{y}_2^n,\\
\mathbf{k}_{12} &= \hat{\mathbf{C}}\mathbf{y}_2^n - \hat{\mathbf{K}}\mathbf{y}_1^n + \hat{\mathbf{G}}\mathbf{y}_0^n + \hat{\mathbf{f}}^n,\\
\mathbf{k}_{20} &= \mathbf{y}_1^n - \frac{\Delta t}{2}\,\mathbf{k}_{11},\\
\mathbf{k}_{21} &= \mathbf{y}_2^n - \frac{\Delta t}{2}\,\mathbf{k}_{12},\\
\mathbf{k}_{22} &= \hat{\mathbf{C}}(\mathbf{y}_2^n - \frac{\Delta t}{2}\,\mathbf{k}_{12}) - \hat{\mathbf{K}}(\mathbf{y}_1^n - \frac{\Delta t}{2}\,\mathbf{k}_{11}) + \hat{\mathbf{G}}(\mathbf{y}_0^n - \frac{\Delta t}{2}\,\mathbf{k}_{10}) + \hat{\mathbf{f}}^{n-\frac{1}{2}},\\
\mathbf{k}_{30} &= \mathbf{y}_1^n - \frac{\Delta t}{2}\,\mathbf{k}_{21},\\
\mathbf{k}_{31} &= \mathbf{y}_2^n - \frac{\Delta t}{2}\,\mathbf{k}_{22},\\
\mathbf{k}_{32} &= \hat{\mathbf{C}}(\mathbf{y}_2^n - \frac{\Delta t}{2}\,\mathbf{k}_{22}) - \hat{\mathbf{K}}(\mathbf{y}_1^n - \frac{\Delta t}{2}\,\mathbf{k}_{21}) + \hat{\mathbf{G}}(\mathbf{y}_0^n - \frac{\Delta t}{2}\,\mathbf{k}_{20}) + \hat{\mathbf{f}}^{n-\frac{1}{2}},\\
\mathbf{k}_{40} &= \mathbf{y}_1^n - \Delta t\,\mathbf{k}_{31},\\
\mathbf{k}_{41} &= \mathbf{y}_2^n - \Delta t\,\mathbf{k}_{32},\\
\mathbf{k}_{42} &= \hat{\mathbf{C}}(\mathbf{y}_2^n - \Delta t\,\mathbf{k}_{32}) - \hat{\mathbf{K}}(\mathbf{y}_1^n - \Delta t\,\mathbf{k}_{31}) + \hat{\mathbf{G}}(\mathbf{y}_0^n - \Delta t\,\mathbf{k}_{30}) + \hat{\mathbf{f}}^{n-1}.
\end{aligned}$$

Finally, the solution at time step $(n-1)$ can be updated via

$$\begin{bmatrix}\mathbf{y}_0\\ \mathbf{y}_1\\ \mathbf{y}_2\end{bmatrix}^{n-1} = \begin{bmatrix}\mathbf{y}_0\\ \mathbf{y}_1\\ \mathbf{y}_2\end{bmatrix}^{n} - \frac{\Delta t}{6}\begin{bmatrix}\mathbf{k}_{10} + 2\,\mathbf{k}_{20} + 2\,\mathbf{k}_{30} + \mathbf{k}_{40}\\ \mathbf{k}_{11} + 2\,\mathbf{k}_{21} + 2\,\mathbf{k}_{31} + \mathbf{k}_{41}\\ \mathbf{k}_{12} + 2\,\mathbf{k}_{22} + 2\,\mathbf{k}_{32} + \mathbf{k}_{42}\end{bmatrix}. \tag{B.11}$$

Appendix C

Gradient of a functional

The gradient of a functional $\mathcal{F} : \mathcal{H} \to \mathbb{R}$, where $\mathcal{H}$ is a Hilbert space, is defined as the Riesz-representation of the derivative $\mathcal{F}'(\mathbf{q})(\tilde{\mathbf{q}})$, such that

$$(\ \mathcal{G}(\mathbf{q}), \tilde{\mathbf{q}} \ )_{\mathcal{H}} = \mathcal{F}'(\mathbf{q})(\tilde{\mathbf{q}}) \qquad \forall \tilde{\mathbf{q}} \in \mathcal{H}, \tag{C.1}$$

where $\mathcal{G}$ denotes the gradient, and we use the following notation for the Gâteaux derivative of $\mathcal{F}$ at $\mathbf{q}$ in a direction $\tilde{\mathbf{q}}$:

$$\mathcal{F}'(\mathbf{q})(\tilde{\mathbf{q}}) = \lim_{h \to 0} \frac{\mathcal{F}(\mathbf{q} + h\tilde{\mathbf{q}}) - \mathcal{F}(\mathbf{q})}{h}. \tag{C.2}$$

With this definition, it is not possible to talk about the gradient, without specifying the inner-product utilized to represent the derivative [108].

Appendix D

On the third discrete optimality condition

We discuss the derivation of the discrete control equations, i.e., of the third discrete optimality condition, given in (4.19) and (4.20). We take the derivative of $\mathcal{L}$ with respect to $\boldsymbol{\lambda}$ and $\boldsymbol{\mu}$ over the interior domain only, since the values of the Lamé parameters at the interface nodes are extended into the PML domain, without any variation along the direction of projection [57]. This assumption greatly simplifies the derivation and implementation of the control equations.

The $\boldsymbol{\lambda}$ control problem

Equation (4.1a) governs the interior domain, denoted by Ω^{RD}, where $\lambda,\ \mu$ only contribute to terms in the $\mathbf{K}$ matrix of (4.3), which contributes to $\mathbf{Q}$ in (4.7). We denote the part of $\mathbf{K}$ that belongs to the interior domain by $\mathbf{K}^{\mathrm{RD}}$: it is the stiffness matrix of the interior problem, and is given by [33]:

$$
\begin{aligned}
\mathbf{K}^{\mathrm{RD}} = \int_{\Omega^{\mathrm{RD}}} \Bigg[& \begin{array}{ll} (\boldsymbol{\lambda}^T\boldsymbol{\chi} + 2\,\boldsymbol{\mu}^T\boldsymbol{\chi})\ \boldsymbol{\Phi}_{x_1}\boldsymbol{\Phi}_{x_1}^T + (\boldsymbol{\mu}^T\boldsymbol{\chi})\ \boldsymbol{\Phi}_{x_3}\boldsymbol{\Phi}_{x_3}^T & \dots \\ (\boldsymbol{\lambda}^T\boldsymbol{\chi})\ \boldsymbol{\Phi}_{x_3}\boldsymbol{\Phi}_{x_1}^T + (\boldsymbol{\mu}^T\boldsymbol{\chi})\ \boldsymbol{\Phi}_{x_1}\boldsymbol{\Phi}_{x_3}^T & \dots \end{array} \\
& \begin{array}{ll} \dots & (\boldsymbol{\lambda}^T\boldsymbol{\chi})\ \boldsymbol{\Phi}_{x_1}\boldsymbol{\Phi}_{x_3}^T + (\boldsymbol{\mu}^T\boldsymbol{\chi})\ \boldsymbol{\Phi}_{x_3}\boldsymbol{\Phi}_{x_1}^T \\ \dots & (\boldsymbol{\lambda}^T\boldsymbol{\chi} + 2\,\boldsymbol{\mu}^T\boldsymbol{\chi})\ \boldsymbol{\Phi}_{x_3}\boldsymbol{\Phi}_{x_3}^T + (\boldsymbol{\mu}^T\boldsymbol{\chi})\ \boldsymbol{\Phi}_{x_1}\boldsymbol{\Phi}_{x_1}^T \end{array} \Bigg] d\Omega, \qquad \text{(D.1)}
\end{aligned}
$$

where $\boldsymbol{\chi}$ is the vector of interpolation functions for the Lamé parameters, $\boldsymbol{\Phi}$ are the displacement interpolants, and subscripts x_1, x_3 denote differentiation with respect to x_1, and x_3, respectively. Taking the derivative of $\boldsymbol{K}^{\mathrm{RD}}$ with respect to $\boldsymbol{\lambda}$, yields

$$\frac{\partial \mathbf{K}^{\mathrm{RD}}}{\partial \boldsymbol{\lambda}} = \int_{\Omega^{\mathrm{RD}}} \begin{bmatrix} \boldsymbol{\Phi}_{x_1} \boldsymbol{\Phi}_{x_1}^T \boldsymbol{\chi} & \boldsymbol{\Phi}_{x_1} \boldsymbol{\Phi}_{x_3}^T \boldsymbol{\chi} \\ \boldsymbol{\Phi}_{x_3} \boldsymbol{\Phi}_{x_1}^T \boldsymbol{\chi} & \boldsymbol{\Phi}_{x_3} \boldsymbol{\Phi}_{x_3}^T \boldsymbol{\chi} \end{bmatrix} d\Omega^{\mathrm{RD}}, \tag{D.2}$$

which are the building blocks of $\frac{\partial}{\partial \boldsymbol{\lambda}}(\hat{\mathbf{p}}^T \ \mathbf{Q} \ \hat{\mathbf{d}})$ in (4.19), thus enabling its computation.

The $\boldsymbol{\mu}$ control problem

In a way similar to what we did above, we take the derivative of $\mathbf{K}^{\mathrm{RD}}$ with respect to $\boldsymbol{\mu}$ to obtain

$$\frac{\partial \mathbf{K}^{\mathrm{RD}}}{\partial \boldsymbol{\mu}} = \int_{\Omega^{\mathrm{RD}}} \begin{bmatrix} \left[2 \ \boldsymbol{\Phi}_{x_1} \boldsymbol{\Phi}_{x_1}^T + \boldsymbol{\Phi}_{x_3} \boldsymbol{\Phi}_{x_3}^T\right] \boldsymbol{\chi} & \boldsymbol{\Phi}_{x_3} \boldsymbol{\Phi}_{x_1}^T \boldsymbol{\chi} \\ \boldsymbol{\Phi}_{x_1} \boldsymbol{\Phi}_{x_3}^T \boldsymbol{\chi} & \left[2 \ \boldsymbol{\Phi}_{x_3} \boldsymbol{\Phi}_{x_3}^T + \boldsymbol{\Phi}_{x_1} \boldsymbol{\Phi}_{x_1}^T\right] \boldsymbol{\chi} \end{bmatrix} d\Omega^{\mathrm{RD}}, \tag{D.3}$$

thus allowing the computation of $\frac{\partial}{\partial \boldsymbol{\mu}}(\hat{\mathbf{p}}^T \ \mathbf{Q} \ \hat{\mathbf{d}})$ in (4.20).

Appendix E

On the singular convolution integral (4.21)

Due to the arrival of Raleigh waves, the integrand in (4.21) exhibits singularity. In this part, we consider the integral in the Cauchy principal value sense, investigate the type of singularity, and comment on the numerical evaluation of the integral. We repeat (4.21) with a small change in notation:

$$u^{2D}(x,t) = \int_0^t f^{2D}(t-t')\; G^{2D}(x,t')\; dt', \tag{E.1}$$

where $G^{2D}(x,t)$ is the Lamb Green's function:

$$G^{2D}(x,t) = \frac{c_s}{\pi\mu|x|} \begin{cases} 0, & \tau < a \\ \frac{-(2\tau^2-1)^2\sqrt{\tau^2-a^2}}{(2\tau^2-1)^4+16\tau^4(\tau^2-a^2)(1-\tau^2)}, & a \le \tau \le 1 \\ \frac{-\sqrt{\tau^2-a^2}}{(2\tau^2-1)^2-4\tau^2\sqrt{\tau^2-a^2}\sqrt{\tau^2-1}}, & \tau > 1, \end{cases}$$

where c_s is shear wave velocity, μ is shear modulus, $\tau = \frac{tc_s}{|x|}$ is dimensionless time, $a = \sqrt{\frac{1-2\nu}{2-2\nu}}$ indicates the ratio of shear wave velocity to that of the compressional wave, and ν is Poisson's ratio.

In this section, we consider $\tau > 1$, which contains the arrival time of the Rayleigh wave, denoted by t_R. Evaluation of (E.1) when $\tau \le 1$ is straightforward. We split the integral into two parts, the *regular* part and the *singular* part

$$u^{2D}(x,t) = \int_{t\setminus B(t_R,\epsilon)} f^{2D}(t-t')\; G^{2D}(x,t')\; dt' + \int_{B(t_R,\epsilon)} f^{2D}(t-t')\; G^{2D}(x,t')\; dt', \tag{E.2}$$

where the singularity is isolated inside the ball $B(t_R,\epsilon) = (t_R - \epsilon, t_R + \epsilon)$, where $\epsilon > 0$ is “small”. We focus on the *singular* integral. Since ϵ is “small”, we use the following approximation

$$\int_{B(t_R,\epsilon)} f^{2D}(t-t')\; G^{2D}(x,t')\; dt' \approx f^{2D}(t-t_R) \int_{B(t_R,\epsilon)} G^{2D}(x,t')\; dt'. \tag{E.3}$$

Next, we evaluate the following integral in the Cauchy principal value sense

$$\widehat{I_s} = \lim_{\epsilon\to 0} \int_{B(t_R,\epsilon)} G^{2D}(x,t')\; dt', \tag{E.4}$$

where

$$G^{2D}(x,t') = \frac{c_s}{\pi\mu|x|} \frac{-\sqrt{\tau^2-a^2}}{(2\tau^2-1)^2 - 4\tau^2\sqrt{\tau^2-a^2}\sqrt{\tau^2-1}}. \tag{E.5}$$

We rewrite the singular kernel (E.5) in the following form

$$G^{2D}(x,t') = \frac{Q}{L-R} = \frac{Q(L+R)}{(L-R)(L+R)}, \tag{E.6}$$

where

$$Q = \frac{-c_s}{\pi\mu|x|}\sqrt{\tau^2-a^2}, \tag{E.7a}$$

$$L = (2\tau^2-1)^2, \tag{E.7b}$$

$$R = 4\tau^2\sqrt{\tau^2-a^2}\sqrt{\tau^2-1}. \tag{E.7c}$$

We investigate the case when $L-R$ in (E.6) vanishes, i.e., $(L-R)(L+R)=0$. We exploit the following representation

$$(L-R)(L+R)=\alpha(\tau^2-\xi_1^2)(\tau^2-\xi_2^2)(\tau^2-\xi_3^2), \tag{E.8}$$

where $\xi_i^2,\ i=1,2,3$, are the roots of the corresponding polynomial on the left-hand-side, and α is a scaling parameter. We associate ξ_3 to the arrival time of the Rayleigh wave, and rewrite (E.6), using (E.8), as follows

$$G^{2D}(x,t')=\frac{Q(L+R)}{\alpha(\tau^2-\xi_1^2)(\tau^2-\xi_2^2)(\tau+\xi_3)(\tau-\xi_3)}=\frac{\phi(\tau)}{\tau-\xi_3}, \tag{E.9}$$

where

$$\phi(\tau)=\frac{Q(L+R)}{\alpha(\tau^2-\xi_1^2)(\tau^2-\xi_2^2)(\tau+\xi_3)}. \tag{E.10}$$

We remark that the above representation is considered in $B(t_R,\epsilon)$. Thus, $\phi(\tau)$ is continuous, and may be approximated with the following second order polynomial

$$\phi(\tau)=\phi(\frac{t\ c_s}{|x|})\approx a_0+a_1t+a_2t^2,\quad t\in B(t_R,\epsilon). \tag{E.11}$$

Thus, (E.4) becomes

$$\widehat{I_s}\approx\frac{|x|}{c_s}\lim_{\epsilon\to 0}\int_{t_R-\epsilon}^{t_R+\epsilon}\frac{a_0+a_1t+a_2t^2}{t-t_R}dt. \tag{E.12}$$

It can be shown that the above integral vanishes when evaluated in the Cauchy principal value sense, i.e., the singularity is "weak".

Next, we focus on the numerical evaluation of (E.1). In computer arithmetic, one cannot approach infinitely close to the singular point. Thus, our strategy is to approximate the *singular* integral analytically, inside a larger ball. To make the idea precise, let $\delta > \epsilon$, and $B(t_R, \delta) \supset B(t_R, \epsilon)$, where δ has the same order of magnitude that the time discretization has in the numerical evaluation of the *regular* integral. Let $t_1 = \inf B(t_R, \delta)$, and $t_2 = \sup B(t_R, \delta)$. Then, along the same lines, we have

$$u^{2D}(x,t) = \int_{t \setminus B(t_R,\delta)} f^{2D}(t-t')\ G^{2D}(x,t')\ dt' + \int_{B(t_R,\delta)} f^{2D}(t-t')\ G^{2D}(x,t')\ dt'. \tag{E.13}$$

We define

$$I_s = \int_{B(t_R,\delta)} f^{2D}(t-t')\ G^{2D}(x,t')\ dt'. \tag{E.14}$$

Thus,

$$I_s = \int_{t_1}^{t_R-\epsilon} \cdots + \int_{B(t_R,\epsilon)} \cdots + \int_{t_R+\epsilon}^{t_2} \cdots\,, \tag{E.15}$$

where $\cdots$ represents the integrand in (E.14). The second integral vanishes when evaluated in the Cauchy principal value sense, as was shown earlier. It can be shown that the remaining terms can be approximated as

$$I_s \approx f^{2D}(t - t_R) \frac{|x|}{c_s} \Bigg\{ ln|\frac{t_2 - t_R}{t_1 - t_R}|(b_0 + b_1 \; t_R + b_2 \; t_R^2) \\ + (t_2 - t_1) \Bigg(b_1 + b_2 \; (t_R + \frac{t_2 + t_1}{2}) \Bigg) \Bigg\}, \quad \text{(E.16)}$$

where b_0, b_1, and b_2 are the coefficients of the polynomial that approximates $\phi(\tau)$ in $B(t_R, \delta)$. When dealing with floating point arithmetic, the best approximation occurs when $t_R = \frac{1}{2}(t_1 + t_2)$, where the logarithmic term vanishes.

Appendix F

On the spatial integration of (4.25)

We assume that the line load is applied along the x_2 axis with a total length of $2L$, and that the observer is positioned along the x_1 axis. We make the following change of variable to ease the analytical integration:

$$G^{2L}(x_1,t) = \int_{-L}^{L} G^{3D}(x_1,x_2,t)\ dx_2 = 2\int_{x_1}^{r_L} G^{3D}(r,t)\ \frac{r}{\sqrt{r^2-x_1^2}}\ dr, \tag{F.1}$$

where, $r=\sqrt{x_1^2+x_2^2}$, $r_L=\sqrt{x_1^2+L^2}$, and the Green's function G^{3D} is given as:

$$G^{3D}(r,t) = B(r)\begin{cases} 0 & \tau < a \\ u_1 & a \le \tau \le 1 \\ u_2^* & 1 \le \tau \le \xi_3 \\ 1 & \tau > \xi_3 \end{cases}. \tag{F.2}$$

We have the following definitions:

$$B(r) = \frac{1}{r}B^* = \frac{1}{r}\frac{1-\nu}{2\pi\mu}, \quad \tau = t\frac{c_s}{r},$$

$$u_1 = \frac{1}{2} - \frac{1}{2}\sum_{i=3}^{3}\frac{A_i}{\sqrt{|\tau^2-\xi_i^2|}}, \quad u_2^* = 1 - \frac{A_3}{\sqrt{\xi_3^2-\tau^2}},$$

$$a = \sqrt{\frac{1-2\nu}{2-2\nu}}, \quad A_i = \frac{(1-2\xi_i^2)^2\sqrt{|a^2-\xi_i^2|}}{4(\xi_i^2-\xi_j^2)(\xi_i^2-\xi_k^2)},$$

where ν is Poisson's ration, μ is shear modulus, c_s is shear wave velocity, and ξ_i are the roots of the Rayleigh function:

$$R(\xi^2) = (2\xi^2 - 1)^2 + 4\sqrt{\xi^2 - a^2}\sqrt{\xi^2 - 1} = 0.$$

The above relations are valid when $\nu < 0.2631$. In such a case, all roots are real and satisfy $0 < \xi_1^2 < \xi_2^2 < a^2 < 1 < \xi_3^2$ [98]. Making use of Heaviside functions, we rewrite (F.2) as follows

$$\begin{aligned} G^{3D}(r,t) = B(r)\Big\{ &-u_1 H\left(r - \frac{tc_s}{a}\right) + (u_1 - u_2^*) H\left(r - \frac{tc_s}{1}\right) + \\ &(u_2^* - 1) H\left(r - \frac{tc_s}{\xi_3}\right) + 1 \Big\}. \end{aligned} \tag{F.3}$$

Substituting (F.3) into (F.1) yields

$$G^{2L}(x_1,t) = 2\ (I_1 + I_2 + I_3 + I_4), \tag{F.4}$$

where

$$I_1 = \frac{1}{2}B^*\{\int_{x_1}^{r_L} \frac{-H(r - \frac{tc_s}{a})}{\sqrt{r^2 - x_1^2}} + \sum_{i=1}^{3}\int_{x_1}^{r_L} \frac{A_i\ r\ H(r - \frac{tc_s}{a})}{\xi_i\sqrt{(\frac{t^2c_s^2}{\xi_i^2} - r^2)(r^2 - x_1^2)}}\ dr\},$$

$$\begin{aligned} I_2 = \frac{1}{2}B^*\{&\int_{x_1}^{r_L} \frac{-H(r - \frac{tc_s}{1})}{\sqrt{r^2 - x_1^2}} - \sum_{i=1}^{2}\int_{x_1}^{r_L} \frac{A_i\ r\ H(r - \frac{tc_s}{1})}{\xi_i\sqrt{(\frac{t^2c_s^2}{\xi_i^2} - r^2)(r^2 - x_1^2)}}\ dr \\ &+ \int_{x_1}^{r_L} \frac{A_3\ r\ H(r - \frac{tc_s}{1})}{\xi_3\sqrt{(\frac{t^2c_s^2}{\xi_3^2} - r^2)(r^2 - x_1^2)}}\ dr\}, \end{aligned}$$

$$I_3 = B^*\int_{x_1}^{r_L} \frac{-A_3\ r\ H(r - \frac{tc_s}{\xi_3})}{\xi_3\sqrt{(\frac{t^2c_s^2}{\xi_3^2} - r^2)(r^2 - x_1^2)}}\ dr,$$

$$I_4 = B^* \int_{x_1}^{r_L} \frac{dr}{\sqrt{r^2-x_1^2}}.$$

It is easy to verify that I_1, I_2, I_3, and I_4 consist of the following integrals with the corresponding closed-form solution

$$F_1 = \int \frac{r\ H(r-\frac{tc_s}{\lambda})}{\sqrt{(r^2-\frac{t^2c_s^2}{\xi^2})(r^2-x_1^2)}}\ dr = \frac{1}{2}H\left(r-\frac{tc_s}{\lambda}\right)\times$$
$$\ln\left\{\frac{(r^2-x_1^2)+(r^2-\frac{t^2c_s^2}{\xi^2})+2\sqrt{(r^2-\frac{t^2c_s^2}{\xi^2})(r^2-x_1^2)}}{(\frac{t^2c_s^2}{\lambda^2}-x_1^2)+(\frac{t^2c_s^2}{\lambda^2}-\frac{t^2c_s^2}{\xi^2})+2\sqrt{(\frac{t^2c_s^2}{\lambda^2}-\frac{t^2c_s^2}{\xi^2})(\frac{t^2c_s^2}{\lambda^2}-x_1^2)}}\right\},$$

$$\begin{aligned}
F_2 &= \int \frac{r\ H(r-\frac{tc_s}{\lambda})}{\sqrt{-(r^2-\frac{t^2c_s^2}{\xi^2})(r^2-x_1^2)}}\ dr \\
&= -\frac{1}{2}H\left(r-\frac{tc_s}{\lambda}\right)\tan^{-1}\left\{\frac{(\frac{t^2c_s^2}{\xi^2}-r^2)+(x_1^2-r^2)}{2\sqrt{(\frac{t^2c_s^2}{\xi^2}-r^2)(r^2-x_1^2)}}\right\} \\
&+\frac{1}{2}H\left(r-\frac{tc_s}{\lambda}\right)\tan^{-1}\left\{\frac{(\frac{t^2c_s^2}{\xi^2}-\frac{t^2c_s^2}{\lambda^2})+(x_1^2-\frac{t^2c_s^2}{\lambda^2})}{2\sqrt{(\frac{t^2c_s^2}{\xi^2}-\frac{t^2c_s^2}{\lambda^2})(\frac{t^2c_s^2}{\lambda^2}-x_1^2)}}\right\},
\end{aligned}$$

$$F_3 = \int \sqrt{r^2-x_1^2}dr = \ln(r+\sqrt{r^2-x_1^2}),$$

$$F_4 = \int H\left(r-\frac{tc_s}{\lambda}\right)\sqrt{r^2-x_1^2}\ dr = H\left(r-\frac{tc_s}{\lambda}\right)\left\{\frac{\ln(r+\sqrt{r^2-x_1^2})}{\ln(\frac{tc_s}{\lambda}+\sqrt{\frac{t^2c_s^2}{\lambda^2}-x_1^2})}\right\},$$

where λ takes the value of $a, 1$, or ξ_3. Clearly, by exploiting the above closed-form expressions, (4.25) can be evaluated accurately and efficiently.

Bibliography

[1] J. Bielak, R. W. Graves, K. B. Olsen, R. Taborda, L. Ramrez-Guzmn, S. M. Day, G. P. Ely, D. Roten, T. H. Jordan, P. J. Maechling, J. Urbanic, Y. Cui, and G. Juve. The shakeout earthquake scenario: Verification of three simulation sets. Geophysical Journal International, 180(1):375–404, 2010.

[2] U. Basu and A. K. Chopra. Perfectly matched layers for transient elastodynamics of unbounded domains. Int. J. Numer. Meth. Engng., 59:1039–1074, 2004.

[3] A. Fathi and V. Lotfi. Effects of reservoir length and rigorous fluid-foundation interaction on the frequency response functions of concrete gravity dams. Dam Engineering, XXI(3):213–233, January 2011.

[4] I. Epanomeritakis, V. Akcelik, O. Ghattas, and J. Bielak. A Newton-CG method for large-scale three-dimensional elastic full-waveform seismic inversion. Inverse Problems, 24(3):034015, 2008.

[5] C. Jeong, L.F. Kallivokas, S. Kucukcoban, W. Deng, and A. Fathi. Maximization of wave motion within a hydrocarbon reservoir for wave-based enhanced oil recovery. Journal of Petroleum Science and Engineering, doi:10.1016/j.petrol.2015.03.009, 2015.

[6] P. M. Karve, S. Kucukcoban, and L. F. Kallivokas. On an inverse source problem for enhanced oil recovery by wave motion maximization in reservoirs. Computational Geosciences, doi:10.1007/s10596-014-9462-7, 2014.

[7] P. M. Karve, , and L. F. Kallivokas. Wave energy focusing to subsurface poroelastic formations to promote oil mobilization. Geophysical Journal International, doi:10.1093/gji/ggv133, 2015.

[8] L.F. Kallivokas, A. Fathi, S. Kucukcoban, K.H. Stokoe II, J. Bielak, and O. Ghattas. Site characterization using full waveform inversion. Soil Dynamics and Earthquake Engineering, 47:62 – 82, 2013.

[9] I. Harari, M. Slavutin, and E. Turkel. Analytical and numerical studies of a finite element PML for the Helmholtz equation. Journal of Computational Acoustics, 8(1):121–137, 2000.

[10] D. Rabinovich, D. Givoli, and E. Bécache. Comparison of high-order absorbing boundary conditions and perfectly matched layers in the frequency domain. International Journal for Numerical Methods in Biomedical Engineering, 26(10):1351–1369, 2010.

[11] F. Collino and P. B. Monk. Optimizing the perfectly matched layer. Computer Methods in Applied Mechanics and Engineering, 164:157–171, 1998.

[12] P. G. Petropoulos. On the termination of the perfectly matched layer with local absorbing boundary conditions. Journal of Computational Physics, 143(2):665–673, 1998.

[13] J.-P. Bérenger. A perfectly matched layer for the absorption of electromagnetic waves. Journal of Computational Physics, 114:185–200, 1994.

[14] W. C. Chew, J. M. Jin, and E. Michielssen. Complex coordinate system as a generalized absorbing boundary condition. In Proc. 13th Annu. Rev. of Prog. Appl. Comp. Electromag., pages 909–914, Monterey,CA, 17-21 Mar. 1997. Vol. 2.

[15] W. C. Chew and W. H. Weedon. A 3D perfectly matched medium from modified Maxwell's equations with stretched coordinates. Micro. Opt. Tech. Lett., 7:599–604, 1994.

[16] F. L. Teixeira and W. C. Chew. Complex space approach to perfectly matched layers: a review and some new developments. Int. J. Numer. Model., 13:441–455, 2000.

[17] W. C. Chew and Q. H. Liu. Perfectly matched layers for elastodynamics: a new absorbing boundary condition. Journal of Computational Acoustics, 4(4):341–359, 1996.

[18] F. Collino and C. Tsogka. Application of the perfectly matched absorbing layer model to the linear elastodynamic problem in anisotropic heterogeneous media. Geophysics, 66(1):294–307, February 2001.

[19] F. Q. Hu. On absorbing boundary conditions for linearized Euler equations by a perfectly matched layer. Journal of Computational Physics, 129:201–219, 1996.

[20] Y. Q. Zeng, J. Q. He, and Q. H. Liu. The application of the perfectly matched layer in numerical modeling of wave propagation in poroelastic media. Geophysics, 66(4):1258–1266, 2001.

[21] S. D. Gedney. An anisotropic perfectly matched layer-absorbing medium for the truncation of FDTD lattices. IEEE Transactions on Antennas and Propagation, 44(12):1630–1639, December 1996.

[22] B. Gustafsson, H.-O. Kreiss, and J. Oliger. Time dependent problems and difference methods. John Wiley & Sons, Inc., New York, 1995.

[23] S. Abarbanel and D. Gottlieb. A mathematical analysis of the PML method. Journal of Computational Physics, 134(2):357 – 363, 1997.

[24] S. Abarbanel and D. Gottlieb. On the construction and analysis of absorbing layers in CEM. Applied Numerical Mathematics, 27(4):331 – 340, 1998. Special Issue on Absorbing Boundary Conditions.

[25] S. Abarbanel, D. Gottlieb, and J.S. Hesthaven. Long time behavior of the perfectly matched layer equations in computational electromagnetics. Journal of Scientific Computing, 17(1-4):405–422, 2002.

[26] K. Duru and G. Kreiss. A well-posed and discretely stable perfectly matched layer for elastic wave equations in second order formulation. Communications in Computational Physics, 11(5):1643 – 1672, 2012.

[27] E. Bécache, S. Fauqueux, and P. Joly. Stability of perfectly matched layers, group velocities and anisotropic waves. Journal of Computational Physics, 188:399–433, 2003.

[28] F. H. Drossaert and A. Giannopoulos. A nonsplit complex frequency-shifted PML based on recursive integration for FDTD modeling of elastic waves. Geophysics, 72(2):T9–T17, March-April 2007.

[29] D. Komatitsch and R. Martin. An unsplit convolutional perfectly matched layer improved at grazing incidence for the seismic wave equation. Geophysics, 72(5):SM155–SM167, September-October 2007.

[30] T. Wang and X. Tang. Finite-difference modeling of elastic wave propagation: A nonsplitting perfectly matched layer approach. Geophysics, 68(5):1749–1755, 2003.

[31] U. Basu. Explicit finite element perfectly matched layer for transient three-dimensional elastic waves. Int. J. Numer. Meth. Engng., 77:151–176, 2009.

[32] R. Martin, D. Komatitsch, and S. D. Gedney. A variational formulation of a stabilized unsplit convolutional perfectly matched layer for the isotropic or anisotropic seismic wave equation. CMES, 37(3):274–304, 2008.

[33] S. Kucukcoban and L. F. Kallivokas. A symmetric hybrid formulation for transient wave simulations in PML-truncated heterogeneous media. Wave Motion, 50:57–79, 2013.

[34] F. D. Hastings, J. B. Schneider, and S. L. Broschat. Application of the perfectly matched layer (PML) absorbing boundary condition to elastic wave propagation. J. Acoust. Soc. Am., 100(5):3061–3069, 1996.

[35] Q. H. Liu. Perfectly matched layers for elastic waves in cylindrical and spherical coordinates. J. Acoust. Soc. Am., 105(4):2075–2084, April 1999.

[36] E. Bécache, P. Joly, and C. Tsogka. Fictitious domains, mixed finite elements and perfectly matched layers for 2D elastic wave propagation. J. Comput. Acoust., 9(3):1175–1202, September 2001.

[37] G. Festa and S. Nielsen. PML absorbing boundaries. Bulletin of the Seismological Society of America, 93(2):891–903, April 2003.

[38] D. Komatitsch and J. Tromp. A perfectly matched layer absorbing boundary condition for the second-order seismic wave equation. Geophysical Journal International, 154:146–153, 2003.

[39] G. Cohen and S. Fauqueux. Mixed spectral finite elements for the linear elasticity system in unbounded domains. SIAM J. Sci. Comput., 26(3):864–884, 2005.

[40] G. Festa and J.-P. Vilotte. The Newmark scheme as velocity-stress time-staggering: an efficient PML implementation for spectral element simulations of elastodynamics. Geophys. J. Int., 161:789–812, 2005.

[41] K. C. Meza-Fajardo and A. S. Papageorgiou. A nonconvolutional, split-field, perfectly matched layer for wave propagation in isotropic and anisotropic elastic media: Stability analysis. Bulletin of the Seismological Society of America, 98(4):1811–1836, August 2008.

[42] D. Correia and J.-M. Jin. Performance of regular PML, CFS-PML, and second-order PML for waveguide problems. Microwave and Optical Technology Letters, 48(10):2121–2126, October 2006.

[43] M.N. Dmitriev and V.V. Lisitsa. Application of M-PML reflectionless boundary conditions to the numerical simulation of wave propagation in anisotropic media. part I: Reflectivity. Numerical Analysis and Applications, 4(4):271–280, 2011.

[44] M.N. Dmitriev and V.V. Lisitsa. Application of M-PML absorbing boundary conditions to the numerical simulation of wave propagation in anisotropic media. part II: Stability. Numerical Analysis and Applications, 5(1):36–44, 2012.

[45] K. C. Meza-Fajardo and A. S. Papageorgiou. Study of the accuracy of the multiaxial perfectly matched layer for the elastic-wave equation. Bulletin of the Seismological Society of America, 102(6):2458–2467, December 2012.

[46] P. Ping, Y. Zhang, and Y. Xu. A multiaxial perfectly matched layer (M-PML) for the long-time simulation of elastic wave propagation in the second-order equations. Journal of Applied Geophysics, 101:124 – 135, 2014.

[47] C. Bunks, F. Saleck, S. Zaleski, and G. Chavent. Multiscale seismic waveform inversion. Geophysics, 60(5):1457–1473, 1995.

[48] R. E. Plessix. Introduction: Towards a full waveform inversion. Geophysical Prospecting, 56(6):761–763, 2008.

[49] A. Tarantola. Inversion of seismic reflection data in the acoustic approximation. *Geophysics*, 49(8):1259–1266, 1984.

[50] A. Fichtner, J. Trampert, P. Cupillard, E. Saygin, T. Taymaz, Y. Capdeville, and A. Villaseor. Multiscale full waveform inversion. *Geophysical Journal International*, 2013.

[51] Q. Liu and Y. J. Gu. Seismic imaging: From classical to adjoint tomography. *Tectonophysics*, 566–567(0):31 – 66, 2012.

[52] P. Mora. Nonlinear two-dimensional elastic inversion of multioffset seismic data. *Geophysics*, 52(9):1211–1228, 1987.

[53] N. Rawlinson, S. Pozgay, and S. Fishwick. Seismic tomography: A window into deep earth. *Physics of the Earth and Planetary Interiors*, 178(34):101 – 135, 2010.

[54] B. Banerjee, T. F. Walsh, W. Aquino, and M. Bonnet. Large scale parameter estimation problems in frequency-domain elastodynamics using an error in constitutive equation functional. *Comp. Meth. Appl. Mech. Eng.*, 253:60–72, 2013.

[55] A. Gholami, A. Mang, and G Biros. Image-driven parameter estimation for low grade gliomas. *arXiv*, 2014.

[56] J. W. Kang and L. F. Kallivokas. The inverse medium problem in heterogeneous PML-truncated domains using scalar probing waves. *Comput. Methods Appl. Mech. Engrg.*, 200:265–283, 2011.

[57] S. Kucukcoban. *The inverse medium problem in PML-truncated elastic media*. Ph.D. thesis, The University of Texas at Austin, 2010.

[58] S.-W. Na and L. F. Kallivokas. Direct time-domain soil profile reconstruction for one-dimensional semi-infinite domains. Soil Dynamics and Earthquake Engineering, 29:1016–1026, 2009.

[59] K. H. Stokoe II, S. G. Wright, J. A. Bay, and J. M. Roësset. Characterization of geotechnical sites by SASW method. In R. D. Woods, editor, Geophysical Characterization of Sites, pages 15–25. Oxford & IBH Pub. Co., New Delhi, India, 1994.

[60] U. Albocher, P. E. Barbone, M. S. Richards, A. A. Oberai, and I. Harari. Approaches to accommodate noisy data in the direct solution of inverse problems in incompressible plane strain elasticity. Inverse Problems in Science and Engineering, 22(8):1307–1328, 2014.

[61] I. Epanomeritakis, V. Akcelik, O. Ghattas, and J. Bielak. A Newton-CG method for large-scale three-dimensional elastic full-waveform seismic inversion. Inverse Problems, 24(3):034015, 2008.

[62] A. A. Oberai, N. H. Gokhale, M. M. Doyley, and M. Bamber. Evaluation of the adjoint equation based algorithm for elasticity imaging. Physics in Medicine and Biology, 49:2955–2974, 2004.

[63] A. A. Oberai, N. H. Gokhale, and G. R. Feijo. Solution of inverse problems in elasticity imaging using the adjoint method. Inverse Problems, 19(2):297–313, 2003.

[64] K. T. Tran and M. McVay. Site characterization using Gauss-Newton inversion of 2-D full seismic waveform in the time domain. Soil Dynamics and Earthquake Engineering, 43(0):16 – 24, 2012.

[65] R. G. Pratt, C. Shin, and G. J. Hick. GaussNewton and full Newton methods in frequencyspace seismic waveform inversion. Geophysical Journal International, 133(2):341–362, 1998.

[66] J. Bramwell. A Discontinuous Petrov-Galerkin Method for Seismic Tomography Problems. Ph.D. thesis, The University of Texas at Austin, 2013.

[67] A. Fathi, B. Poursartip, and L. F. Kallivokas. Time-domain hybrid formulations for wave simulations in three-dimensional PML-truncated heterogeneous media. International Journal for Numerical Methods in Engineering, 101(3):165–198, 2015.

[68] N. Petra and G. Stadler. Model variational inverse problems governed by partial differential equations. ICES Report 11-05, The Institute for Computational Engineering and Sciences, The University of Texas at Austin, 2011.

[69] A. Fathi, L. F. Kallivokas, and B. Poursartip. Full-waveform inversion in three-dimensional PML-truncated elastic media. Computer Methods in Applied Mechanics and Engineering, (under review), 2015.

[70] A. Fathi, L. F. Kallivokas, K. H. Stokoe II, and B. Poursartip. Three-dimensional site characterization using full-waveform inversion: theory, computations, and field experiments. Soil Dynamics and Earthquake Engineering, (to be submitted), 2015.

[71] S. Kucukcoban and L.F. Kallivokas. Mixed perfectly-matched-layers for direct transient analysis in 2D elastic heterogeneous media. Computer Methods in Applied Mechanics and Engineering, 200(1-4):57–76, 2011.

[72] L. F. Kallivokas, J. Bielak, and R. C. MacCamy. A simple impedance-infinite element for the finite element solution of the three-dimensional wave equation in unbounded domains. Computer Methods in Applied Mechanics and Engineering, 147:235–262, 1997.

[73] F. Brezzi. A survey of mixed finite element methods. In D.L. Dwoyer, M.Y. Hussaini, and R.G. Voigt, editors, Finite Elements Theory and Application, pages 34–49. Springer-Verlag,

New York, 1988.

[74] A. Quarteroni, R. Sacco, and F. Saleri. Numerical Mathematics. Texts in Applied Mathematics. Springer, Berlin Heidelberg, second edition, 2007.

[75] A. Quarteroni and A. Valli. Numerical approximation of partial differential equations. Springer Series in Computational Mathematics. Springer, Berlin Heidelberg, 2008.

[76] H. Bao, J. Bielak, O. Ghattas, L. F. Kallivokas, D. R. O'Hallaron, J. R. Shewchuk, and J. Xu. Large-scale simulation of elastic wave propagation in heterogeneous media on parallel computers. Comput. Methods Appl. Mech. Engrg., 152:85–102, 1998.

[77] D. A. Kopriva. Implementing spectral methods for partial differential equations. Springer, 2009.

[78] L.C. Wilcox, G. Stadler, C. Burstedde, and O. Ghattas. A high-order discontinuous Galerkin method for wave propagation through coupled elastic-acoustic media. Journal of Computational Physics, 229:9373–9396, 2010.

[79] R. Matzen. An efficient finite element time-domain formulation for the elastic second-order wave equation: A non-split complex frequency shifted convolutional PML. International Journal for Numerical Methods in Engineering, 88(10):951–973, 2011.

[80] M. Benzi, G. H. Golub, and J. Liesen. Numerical solution of saddle point problems. Acta Numerica, pages 1–137, 2005.

[81] S. Balay, J. Brown, K. Buschelman, V. Eijkhout, W. D. Gropp, D. Kaushik, M. G. Knepley, L. C. McInnes, B. F. Smith, and H. Zhang. PETSc users manual. Technical Report ANL-95/11 - Revision 3.4, Argonne National Laboratory, 2013.

[82] E. Bozda, J. Trampert, and J. Tromp. Misfit functions for full waveform inversion based on instantaneous phase and envelope measurements. Geophysical Journal International, 185(2):845–870, 2011.

[83] B. Engquist and B. Froese. Application of the Wasserstein metric to seismic signals. Communications in Mathematical Science, 12(5):979–988, 2014.

[84] A. Tikhonov. Solution of incorrectly formulated problems and the regularization method. Soviet Math. Dokl., 5:1035/1038, 1963.

[85] L. I. Rudin, S. Osher, and E. Fatemi. Nonlinear total variation based noise removal algorithms. Phys. D, 60(1-4):259–268, November 1992.

[86] F. Tröltzsch. Optimal Control of Partial Differential Equations: Theory, Methods, and Applications, volume 112 of Graduate Studies in Mathematics. American Mathematical Society, 2010.

[87] Z. Xie, D. Komatitsch, R. Martin, and R. Matzen. Improved forward wave propagation and adjoint-based sensitivity kernel calculations using a numerically stable finite-element PML. Geophysical Journal International, 198(3):1714–1747, 2014.

[88] V. Monteiller, S. Chevrot, D. Komatitsch, and N. Fuji. A hybrid method to compute short-period synthetic seismograms of teleseismic body waves in a 3-D regional model. Geophysical Journal International, 192(1):230–247, 2013.

[89] P. Tong, C. W. Chen, D. Komatitsch, P. Basini, and Q. Liu. High-resolution seismic array imaging based on an SEM-FK hybrid method. Geophysical Journal International, 197(1):369–395, 2014.

[90] P. Tong, D. Komatitsch, T. L. Tseng, S. H. Hung, C. W. Chen, P. Basini, and Q. Liu. A 3-D spectral-element and frequency-wave number hybrid method for high-resolution seismic array imaging. Geophysical Research Letters, 2014.

[91] Y. Choi, C. Farhat, W. Murray, and M. Saunders. A practical factorization of a Schur complement for PDE-constrained distributed optimal control. arXiv, 2013.

[92] J. Nocedal and S. Wright. Numerical Optimization. Springer Series in Operations Research. Springer, New York, NY, second edition, 2006.

[93] C. R. Vogel. Computational Methods for Inverse Problems. Frontiers in Applied Mathematics. Society for Industrial and Applied Mathematics (SIAM), Philadelphia, PA, 2002.

[94] M. D. Gunzburger. Perspectives in Flow Control and Optimization. Advances in Design and Control. Society for Industrial and Applied Mathematics (SIAM), Philadelphia, PA, 2003.

[95] L. C. Wilcox, G. Stadler, T. Bui-Thanh, and O. Ghattas. Discretely exact derivatives for hyperbolic PDE-constrained optimization problems discretized by the discontinuous Galerkin method. arXiv, 2013.

[96] S. Kucukcoban and L. F. Kallivokas. Mixed perfectly-matched-layers for direct transient analysis in 2D elastic heterogeneous media. Comput. Methods Appl. Mech. Engrg., 200:57–76, 2011.

[97] G. Stadler. Personal communication, 2014.

[98] E. Kausel. Fundamental Solutions in Elastodynamics: a Compendium. Cambridge University Press, New York, NY, 2006.

[99] D. M. Boore and J. J. Bommer. Processing of strong-motion accelerograms: needs, options and consequences. Soil Dynamics and Earthquake Engineering, 25:93–115, 2005.

[100] J. G. Proakis and D. K. Manolakis. Digital Signal Processing. Prentice Hall, Englewood Cliffs, NJ, fourth edition, 2006.

[101] J. R. Krebs, J. E. Anderson, D. Hinkley, R. Neelamani, S. Lee, A. Baumstein, and M.-D. Lacasse. Fast full-wavefield seismic inversion using encoded sources. Geophysics, 74:WCC177–WCC188, 2009.

[102] L. A. Romero, D. C. Ghiglia, C. C. Ober, and S. A. Morton. Phase encoding of shot records in prestack migration. Geophysics, 65:426–436, 2000.

[103] G. Meles, S. Greenhalgh, J. van der Kruk, A. Green, and H. Mauerer. Taming the non-linearity problem in GPR full-waveform inversion for high contrast media. Journal of Applied Geophysics, 78:31–43, 2012.

[104] S. H. Joh. Advances in the data interpretation technique for spectral-analysis-of surface-waves (SASW) measurements. Ph.D. thesis, The University of Texas at Austin, 1996.

[105] T. Lunne, P. K. Robertson, and J.J.M. Powell. Cone Penetration Testing in Geotechnical Practice. Spon Press, London, 2002.

[106] T. Bui-Thanh, O. Ghattas, J. Martin, and G. Stadler. A computational framework for infinite-dimensional Bayesian inverse problems part I: The linearized case, with application to global seismic inversion. SIAM Journal on Scientific Computing, 35(6):A2494–A2523, 2013.

[107] D. Assimaki, L.F. Kallivokas, J.W. Kang, and S. Kucukcoban. Time-domain forward and inverse modeling of lossy soils with frequency-independent Q for near-surface applications. Soil Dynamics and Earthquake Engineering, 43:139–159, 2012.

[108] A. Borzi and V. Schulz. Computational Optimization of Systems Governed by Partial Differential Equations. Computational Science and Engineering. Society for Industrial and Applied Mathematics (SIAM), Philadelphia, PA, 2012.

Vita

Arash Fathi received his B.Sc. and M.Sc. degrees in Civil Engineering from Iran. He served in Iran Army Corps of Engineers as a structural engineer for a year and a half, and has three years of industrial experience with the dam and hydropower industry. In January 2009, he joined the Department of Civil, Architectural and Environmental Engineering of the University of Texas at Austin, to pursue a Ph.D. degree in Civil Engineering / Computational Mechanics, where he has been working as a research and teaching assistant. He is a finalist of the 26th annual Robert J. Melosh Medal competition for the best student paper on finite element analysis.

Permanent address: arash.fathi@utexas.edu.

This dissertation was typeset with LaTeX[†] by the author.

[†] LaTeX is a document preparation system developed by Leslie Lamport as a special version of Donald Knuth's TeX Program.